# Synthesis and Fabrication of Heterostructures of Novel Semiconductors for Device Application

A thesis submitted in partial fulfillment ofthe
requirements of the degree of

**Doctor of Philosophy**

*By*

**Gokul M. A**

**(Roll number 20173554)**

*to*


**INDIAN INSTITUTE OF SCIENCE EDUCATION AND RESEARCH (IISER), Pune**

*July 18, 2023*

# Certificate

Certified that the work incorporated in the thesis entitled '**Synthesis and Fabrication of Heterostructures of Novel Semiconductors for Device Application'**, submitted by **Gokul M. A** was carried out by the candidate, under my supervision. The workpresented here or any part of it has not been included in any other thesis submit-ted previously for the award of any degree or diploma from any other University or institution.

Pune-411008 **Dr. Atikur Rahman**

July 18, 2023 Supervisor

# Declaration

I declare that this written submission represents my ideas in my own words and where others' ideas have been included, I have adequately cited and referenced the original sources. I also declare that I have adhered to all principles of academic honesty and integrity and have not misrepresented or fabricated or falsified any idea/data/fact/source in my submission. I understand that violation of the above will be cause for disciplinary action by the Institute and can also evoke penal action from the sources which have thus not been properly cited or from whom proper permission has not been taken when needed.

Pune - 411008 **Gokul M. A**

July 18, 2023 **Roll No - 20173554**

*To my Sister, Mother, and Father*

# Acknowledgment

I would like to sincerely thank all the individuals who have played a vital role in the successful completion of this thesis chapter and have provided me with unwavering encouragement and support throughout the process. Their support, guidance, and collaboration have been invaluable to me throughout my research journey.

First and foremost, I would like to extend my deepest appreciation to my advisor, Professor Atikur Rahman. I am immensely grateful for his constant support and for providing me with the freedom to explore topics that deeply interested me. His guidance in setting up our lab has been an invaluable experience. He was always concerned over our physical and mental health and I am grateful for the stress-free research environment he has cultivated. I also thank him for his encouragement and guidance throughout my scientific endeavor.

I would also like to thank my RAC advisory committee members, Professor Mukul Kabir and Professor Arup Kumar Rath, for their valuable suggestions, critical feedback, thoughtful questions, and comments. Their extensive knowledge and constructive feedback have significantly enhanced the quality of my research and contributed to the overall improvement of this thesis chapter. I am grateful for the fellowship provided by UGC that supported me financially during my PhD.

I would like to express my sincere thanks to Dr. Vrinda Narayan, who has been a wonderful friend and an exceptional lab mate since the beginning of my PhD journey. I am grateful for our collaborative work and her constant support throughout this research endeavor.

I would like to express my gratitude to Dr. Divya Nechiyil, a postdoctoral researcher in our lab, for her help, guidance, and being an amazing friend. I would like to acknowledge the contributions of my juniors Suraj Lakhchaura, and Manisha, for their support and positive contributions to the lab environment. I would like to express my thanks to all the juniors, lab mates, and project students who have been part of our research group and kept a wonderful research atmosphere. Their

discussions and vibrant presence have contributed to a stimulating research environment.

I would like to extend my appreciation to Ankit Kumar for his companionship and the fun times we shared during the initial two years of my PhD. I am thankful to Priyanka Yadav, a summer student, for her assistance in setting up the UV curing setup. Working with her on fabricating microfluidic channels using PDMS was a delightful experience. I would also like to thank Diana She, another summer student, for the enjoyable moments and our collaboration on the exfoliation of van der Waals crystals. My gratitude goes to Clément Poulet for his help in setting up the transient photocurrent measurement system. I also thank Umesh Bansode for teaching me the fabrication of perovskite solar cells.

I would like to acknowledge and appreciate the collaborations with Dr. Shailendrakumar Chaubey, who not only contributed to our research efforts but also became a good friend. I would also like to thank other collaborators, Professor G.V. Pavan Kumar, Professor Angshuman Nag, Professor Gautham Sheet, Professor Stéphane Berciaud, Dr. Sooyeon Hwang, Monika Bhakar, Ashutosh Shukla, Dr. Sunny Tiwari, Dr. Chetna Taneja, Aditi Raman Moghe, Dr. Rayan Chakraborty, Parikshit Kumar Rajput, Habibul Arfin, Navita Jakhar, and Dr. Tariq Sheikh, for their scientific collaborations and insightful discussions.

I would like to express my gratitude to the technical staff at IISER Pune, Department of Physics, Nilesh Dumbre, Sudhir Lone, Anil Prathamshetti, and Parveen Nasa, and Megha Paygude for their invaluable assistance. My thanks go to the staff of the Physics Office, Prabhakar Anagare, and Dhanashree Sheth, for their support throughout my academic journey. I am also grateful to the administrative staff, Tushar, Nayana, Anjali, and Swapnil, for making the academic work easier.

I would like to thank all my seniors in the Physics Department, for their advice and insightful discussions.

I would like to express my heartfelt appreciation to my batchmates and friends, including Bhumika Kansal, Sarvotham Sing, Priya Batra, Sneha Kachhara, Sushanth, Pranab, Kushal, Umashankar, Naveen Joseph Roy, Amal Vijay, Markose Joshy, Benjamin Abraham, Sreeraam, Dhiya Vargeese, Ardra Shailendra, and many others, for their unwavering support and friendship throughout my research journey. A

special thanks to Arjun K. M. for all the trekking events he organized and fun times.

I am also thankful to Dr. Ayesha Rahman for the wonderful hospitality and the delicious food she made for us. The stories shared by Professor Atikur and Dr. Ayesha Rahman about their experiences were always fun to listen to.

Lastly, I am grateful to my family members, especially my sister, mother, and father, for their unwavering support throughout my life.

Thank you all for your invaluable contributions and support.

# Abstract

This thesis presents a comprehensive investigation into the synthesis and fabrication of heterostructures comprising transition metal dichalcogenides (TMDs) and lead halide perovskite materials. The research focuses on exploring the growth mechanism, material properties and the potential applications of heterostructures of these materials in the field of optoelectronics.

The study begins with a thorough examination of the synthesis routes for TMDs and perovskites, aiming to develop novel methods that enable the controlled growth of these materials with good optical and electrical properties. Special emphasis is placed on the synthesis of monolayer TMDs, leveraging growth promoters and optimizing chemical vapor deposition parameters to achieve improved control and reproducibility. Additionally, novel solvothermal methods are invented to grow lead halide perovskites with ultra-low dark currents. The thesis also discusses a technique to perform photolithography on water-soluble materials, enabling the fabrication of electrical devices out of water-soluble $CsPbBr_3$.

The final phase of the research focuses on the realization of heterostructures by combining TMDs and perovskites. A Transfer technique was developed for the successful transfer of 2D as well as perovskite materials. By employing this technique, we successfully fabricated photodiodes and LEDs out of the TMD perovskite heterostructures.

Overall, this thesis provides a comprehensive understanding of the synthesis and fabrication of heterostructures involving TMDs and perovskites. The results obtained demonstrate the potential for these heterostructures in optoelectronic applications, including photodetectors, light-emitting diodes, and sensors. The research contributes to the ongoing efforts in developing advanced materials and devices for the next generation of optoelectronic technologies.

# Abbreviations

- **2D** : Two Dimensional
- **TMDs** : Transition Metal Dichalcogenides
- **CVD** : Chemical Vapor Deposition
- **FET** : Field Effect Transistor
- **XRD**: X-Ray diffraction
- **XPS**: X-Ray Photoelectron Spectroscopy
- **FESEM** : Field Emission Scanning Electron Microscope
- **HRTEM** : High-Resolution Transmission Electron Microscope
- **SAED** : Selected Area Electron Diffraction
- **AFM** : Atomic Force Microscope
- **PFM** : Piezoresponse Force Microscope
- **PL** : Photoluminescence
- **SHG** : Second Harmonic Generation
- **LED** : Light Emitting Diode
- **IPA** : Isopropyl Alcohol
- **TVD** : Thermal Vapor Deposition
- **MSD** : Magnetron Sputter Deposition
- **RIE** : Reactive Ion Etching
- **PCB** : Printed Circuit Board
- **CCR** : Closed Cycle Refrigerator
- **OM** : Optical Microscope
- **PET** : Polyethylene terephthalate
- **WG** : Water glass (sodium silicate)
- **rpm** : Rounds per minute
- **ITO** : Indium doped Tin Oxide
- **HI** : Hot Injection
- **sccm** : Standard Cubic Centimeters per Minute
- **D.U.T** : Device under test

# List of Publications

(Included in the thesis)

- **Gokul M A**, Narayanan V and Rahman A 2020 "Modulating flow near substrate surface to grow clean and large-area monolayer MoS2" *Nanotechnology* **31** 415706
- **M A G** and Rahman A 2022 "Phase evolution of all-inorganic perovskite nanowires during its growth from quantum dots" *Nanotechnology* **33** 085706
- **Gokul M A** and Rahman A 2023 "Fabrication of High-Performance Devices on Water-Soluble Lead Halide Perovskites Using Water-Based Photolithography" *Adv. Mater. Interfaces* **10** 2201749
- Divya Nechiyil, **Gokul M. A**, Ashutosh Shukla, G. V. Pavan Kumar, and Atikur Rahman. 2023 "Strain-Induced Activation of Defects and Lowering of defect Migration Energy in MoS 2 monolayers" *2D Mater*. **10**, 045009
- **Gokul M. A**, Vrinda Narayanan P, Aditi Moghe, Shailendra K Chaubey, G. V. Pavan Kumar, Prasenjit Ghosh, St´ephane Berci- aud, Sooyeon Hwang, and Atikur Rahman. "Conformal growth of high-quality monolayer TMDs- Towards novel devices via morphology control" (Submitted).
- **Gokul M. A,** Monika Bhakar, Chetna Taneja, Sooyeon Hwang, G. V. Pavan Kumar, Goutam Sheet, and Atikur Rahman. "Near room temperature solvothermal growth of ferroelectric $CsPbBr_3$ Nanoplatelets with ultralow dark current" (Submitted).
- **Gokul M. A,** and Atikur Rahman. "$MoS_2$ $CsPbBr_3$ photodiodes" (work in progress).
- **Gokul M. A**, Shailendra K Chaubey, G. V. Pavan Kumar, and Atikur Rahman. "$WS_2$ $CsPbBr_3$ LED" (work in progress).

## **Contributed Works** (not included in the thesis)

- Narayanan V, **M A G** and Rahman A 2019 "How to train your CVD to grow large-area 2D materials *Mater. Res. Express* 2019, **6**(12), 125002

- Chaubey S K, **A G M**, Paul D, Tiwari S, Rahman A and Kumar G V P 2021 "Directional Emission from Tungsten Disulfide Monolayer Coupled to Plasmonic Nanowire-on-Mirror Cavity" *Adv. Photonics Res*. **2** 2100002

- Narayanan P. V, **M. A. G**, Chowdhury T, Singh C K, Chaubey S K, Taniguchi T, Watanabe K, Kabir M, Kumar G V P and Rahman A 2022 "Giant Photoresponse Enhancement in Mixed-Dimensional Van der Waals Heterostructure through Dielectric Engineering" *Adv. Mater. Interfaces* **9** 2102054

- Chowdhury T, Paul D, Nechiyil D, **M A G**, Watanabe K, Taniguchi T, Kumar G V P and Rahman A 2021 "Modulation of trion and exciton formation in monolayer WS 2 by dielectric and substrate engineering" *2D Mater*. **8** 045032

- Chaubey S K, Tiwari S, Shukla A, **Gokul M A**, Rahman A and Kumar G V P 2022 "Directing monolayer tungsten disulfide photoluminescence using a bent-plasmonic nanowire on a mirror cavity" *Eur. Phys. J. Spec. Top*. **231** 807–13

- Narayanan P V, **Anilkumar G M**, Rajput M and Rahman A 2022 "Role of Defects in the Transport Properties and Photoresponse of a Silicon–MoS 2 Mixed-Dimensional Van der Waals Heterostructure" *ACS Appl. Electron. Mater*. **4** 6038–46

- Chaubey S K, Tiwari S, **M. A. G**, Paul D, Rahman A and Pavan Kumar G V. 2022 "Mirror-coupled microsphere can narrow the angular distribution of photoluminescence from WS 2 monolayers" *Appl. Phys. Lett*. **120** 261109

- Chakraborty R, Rajput P K, **Anilkumar G M**, Maqbool S, Das R, Rahman A, Mandal P and Nag A 2023 "Rational Design of Non-Centrosymmetric Hybrid Halide Perovskites" *J. Am. Chem. Soc*. **145** 1378–88

- Sheikh T, **Anilkumar G M**, Das T, Rahman A, Chakraborty S and Nag A 2023 "Combining π-Conjugation and Cation−π Interaction for Water-Stable and Photoconductive One-Dimensional Hybrid Lead Bromide" *J. Phys. Chem. Lett.* **14** 1870–6

## Patents

- **Gokul M A** and Rahman A "PROCESS FOR SYNTHESIS OF MONOLAYER TRANSITION METAL DICHALOCOGENIDE" (WO2023148626A1)
- **Gokul M A** and Rahman A "A METHOD FOR SYNTHESIS OF METAL HALIDE PEROVSKITE ($CsPbBr_3$) NANO/MICROCRYSTALS "(Filed)

## Conference presentations

- "Observing the In-situ growth of perovskite nanowires",

  **Gokul M. A (Presenting author)**, Atikur Rahman, *Energy Day*, IISER Pune, 2019 (Oral presentation)

- "In-situ growth and characterization of all-inorganic perovskite nanowires", **Gokul M. A (Presenting author)**, Atikur Rahman, *International Conference on Nano Science and Technology (ICONSAT)*, Kolkata, March 2020 (Poster Presentation)

- "Hetero-Structures of Perovskite and 2D Materials"

  **Gokul M. A (Presenting author)**, Atikur Rahman, *Materials Research Society Hybrid Fall Meeting and Exhibit*, 2021 (Oral presentation)

- "Vanderwals contact engineering in CsPbBr3 micro crystals for optoelectronic application", **Gokul M. A (Presenting author)**, Atikur Rahman, *APS March Meeting*, 2022 (Oral presentation)

# Contents

**List of Figures** **xvii**

**1 Introduction** **1**

1.1 Introduction ..... 1

1.2 Materials of interest ..... 1

1.2.1 Monolayer TMDs ..... 2

1.2.2 All-inorganic perovskites ..... 3

1.3 Strained monolayer TMDs ..... 5

1.4 Heterostructures ..... 6

1.5 Thesis outline ..... 7

Bibliography ..... 8

**2 Experimental Techniques** **15**

2.1 Introduction ..... 15

2.2 Material characterization ..... 16

2.2.1 X-ray Diffraction ..... 16

2.2.2 XPS ..... 18

2.2.3 Optical techniques ..... 20

2.2.4 AFM ..... 21

2.2.5 HRTEM ..... 22

2.2.6 SEM ..... 24

2.3 Device fabrication techniques ..... 25

2.3.1 Photolithography ..... 26

2.3.2 Physical vapor deposition ..... 27

2.3.3 Wire bonding ..... 30

2.4 Summary ..... 31

Bibliography ..... 31

**3 Instrumentation 35**

3.1 Introduction ..... 35

3.2 Setting up Instruments from scratch ..... 36

3.2.1 Powell lens ..... 36

3.2.2 Plasma cleaner ..... 37

3.2.3 UV lamp and intensity measurement system ..... 40

3.2.4 Transient photocurrent/voltage measurement system ..... 41

3.2.5 Environment control box ..... 43

3.2.6 Noise spectroscopy ..... 44

3.2.7 Probe station ..... 45

3.2.8 Reactive ion etching ..... 49

3.3 Chemical vapor deposition system ..... 53

3.4 Modification of CCR substrate holders ..... 54

3.5 Combining UV Microscope with a Spectrometer ..... 56

3.6 Summary ..... 57

Bibliography ..... 58

**4 Chemical Vapor Deposition for Monolayer 2D Materials: Fine-Tuning Flow 61**

4.1 Introduction ..... 61

4.2 Effect of flow on CVD growth of monolayer on flow ..... 63

4.2.1 Sensitivity of growth to subtle changes in flow ..... 63

4.3 Modulating flow near the substrate surface ..... 68

4.3.1 Blockades ..... 69

4.3.2 Calculating the Flow rate ..... 71

4.3.3 Computing flow using COMSOL ..... 72

4.3.4 Fine tuning the flow using blockades ..... 75

4.4 Characterization of $MoS_2$ films ..... 77

4.4.1 Optical Characteristics ..... 77

4.4.2 Transfer Characteristics ..... 79

4.5 Summary ..... 81

Bibliography ..... 81

**5 Sodium silicate as a growth promoter for TMD growth 88**

5.1 Introduction ..... 88

5.2 Sodium silicate as a growth promoter ..... 89

5.3 Reaction mechanism ..... 92

5.4 Computing the reaction energy ..... 95

5.5 Properties of the synthesized monolayers ..... 97

5.5.1 Field effect mobility and optical characterization ..... 97

5.5.2 HRTEM of $MoS_2$ ..... 99

5.6 Expanding the Scope of Synthesizing monolayers ..... 100

5.6.1 Characterization of the Monolayers ..... 101

5.7 Summary ..... 102

Bibliography ..... 103

**6 Straining $MoS_2$ monolayer – Effect of uniform and non-uniform strain 107**

6.1 Introduction ..... 107

6.2 Uniformly straining $MoS_2$ monolayers uniaxially ..... 108

6.2.1 Optical studies on flexible devices ..... 111

6.2.2 Electrical studies on flexible device ..... 111

6.3 Conformal growth of monolayer $MoS_2$ ..... 118

6.3.1 Preparation of textured substrates ..... 118

6.3.2 Optical properties of conformally grown $MoS_2$ ..... 122

6.4 Summary ..... 126

Bibliography ..... 126

**7 Unveiling the Phase Evolution of All-Inorganic Perovskite Nanowires 132**

7.1 Introduction ..... 132

7.2 Synthesizing QDs ..... 133

7.3 Modifying the HI process ..... 134

7.3.1 XRD of nanowires ..... 136

7.3.2 HRTEM of nanowires ..... 137

7.3.3 Electrical characterization of nanowires ..... 140

7.4 In-situ observation of growth ..... 141

7.4.1 Design of the heater box and controller ..... 142

7.4.2 Growth inside the chamber ..... 134

7.4.3 Observed growth ..... 135

7.4.4 The growth mechanism ..... 148

7.5 Summary ..... 149

Bibliography ..... 150

**8 Water-based Photolithography on water-soluble $CsPbBr_3$ 155**

8.1 Introduction ..... 155

8.2 Drop casting vs deposition for device fabrication ..... 157

8.3 Synthesis and Characterization of $CsPbBr_3$ ..... 158

8.4 Solubility of $CsPbBr_3$ and its effect on photolithography ..... 159

8.5 Sacrificial layer-assisted photolithography ..... 161

8.6 Devices of CsPbBr 3 crystals ..... 164

8.6.1 Contact material ..... 166

8.7 Damage to the crystal ..... 168

8.8 Summary ..... 170

Bibliography ..... 171

**9 Ferroelectric $CsPbBr_3$ Nanoplatelets 175**

9.1 Introduction ..... 175

9.2 A novel solvothermal technique ..... 176

9.2.1 Solubility of $PbI_2$ ..... 176

9.2.2 Growth of $CsPbBr_3$ nanoplatelets ..... 178

9.2.3 Reaction with other combinations of alcohol mixtures ..... 180

9.3 Characterization of the as-grown crystal ..... 181

9.4 Optical characterization of the crystals ..... 183

9.5 Electrical characterization of the crystal ..... 186

9.6 Piezoresponse Force Microscopy ..... 189

9.7 Summary ..... 190

Bibliography ..... 191

**10 Conclusions and Future Directions** **195**

10.1 Conclusions ..... 195

10.2 Future directions ..... 196

10.2.1 Controlled Transfer of Perovskite and TMDs ..... 197

10.2.2 $WS_2$ - $CsPbBr_3$ micro-LED ..... 199

10.2.3 $MoS_2$ - $CsPbBr_3$ Photodiodes ..... 200

10.2.4 The research objective ..... 201

Bibliography ..... 202

*This page intentionally left blank*

# Chapter 1

# Introduction

This chapter gives a brief introduction to the thesis comprising of most of the work done over the last six years.

## 1.1 Introduction

The invention of the transistor at bell labs in 1947 marked the dawn of the semiconductor era, ushering in a remarkable era of precise control over electrical current. Semiconductors have since become the lifeblood of our technological progress, serving as the fundamental building blocks for countless electronic devices that have transformed the way we communicate, compute, and engage with the world. These extraordinary materials have provided us with unprecedented abilities to manipulate the flow of electricity. From transistors to integrated circuits, semiconductors have played a pivotal role in shaping our modern society. Nevertheless, as we continue to push the boundaries of technology, there is a growing need to explore new realms of physics and materials to support and accelerate our progress. Our relentless pursuit of technological innovation demands ongoing exploration and innovation in semiconductor materials, as our future will be built on semiconductors.

We obtained unprecedented control over silicon and this has made immense contributions to the evolution of electronic devices. However, as the demands for faster, smaller, and more efficient devices increase, the limitations of conventional materials like silicon become more evident. Exploring new materials with unique properties and characteristics has become crucial to overcome these limitations and driving the next wave of technological advancements.

## 1.2 Materials of interest

In this thesis, we explore TMDs and lead halide perovskite different classes of materials both of which were in the limelight in the research community over the past decade. The renewed

interest in the case of TMDs arises because of their intriguing optoelectric properties that emerge at the monolayer limit which set them apart from their bulk counterparts and perovskite garnered interest because of its potential in energy harvesting capabilities and possible optical and electronic devices such as nanowire lasers, LEDs, photodetectors, etc.

### 1.2.1 Monolayer TMDs

The discovery of two-dimensional (2D) Van der Waals materials has ushered in a new era of physics, characterized by the emergence of intriguing properties that are prominent in the monolayer regime.[1][2] These materials not only showcase unique features but also offer unprecedented opportunities for encoding, processing, and storing information through the fields of valleytronics, spintronics, straintronics, and twistronics. [3–11] As a result, they hold immense promise for shaping the future of the semiconductor industry, potentially revolutionizing its landscape by introducing novel effects.

Among the 2D materials, monolayer transition metal dichalcogenides (TMDs) such as $MoS_2$, $MoSe_2$, $WS_2$, and $WSe_2$ are particularly noteworthy candidates for semiconducting 2D structures due to their direct band gap characteristics and fascinating optoelectric properties.[12–15] The monolayer form of TMDs, in particular, exhibits distinct characteristics that significantly deviate from their bulk counterparts. The properties of monolayer TMDs, including electronic structure, dipole moment, band gap, mobility, carrier density, and local charge distribution, critically depend on their morphology, which can be tailored through stretching, twisting, bending, or wrinkling.[16–20] This precise control over the morphology of 2D materials presents new possibilities for engineering material properties, such as enabling unconventional light-matter interactions in optical metasurfaces through subwavelength-scale morphological control of TMDs.

offer exciting opportunities for exploring novel physics and enabling enhanced control in device applications. These materials hold significant promise as emerging materials for future technological advancements. Figure 1.1, adapted from Lemme, M.C. *et al*, illustrates the potential of 2D materials and highlights the slowdown in silicon technologies.[21]

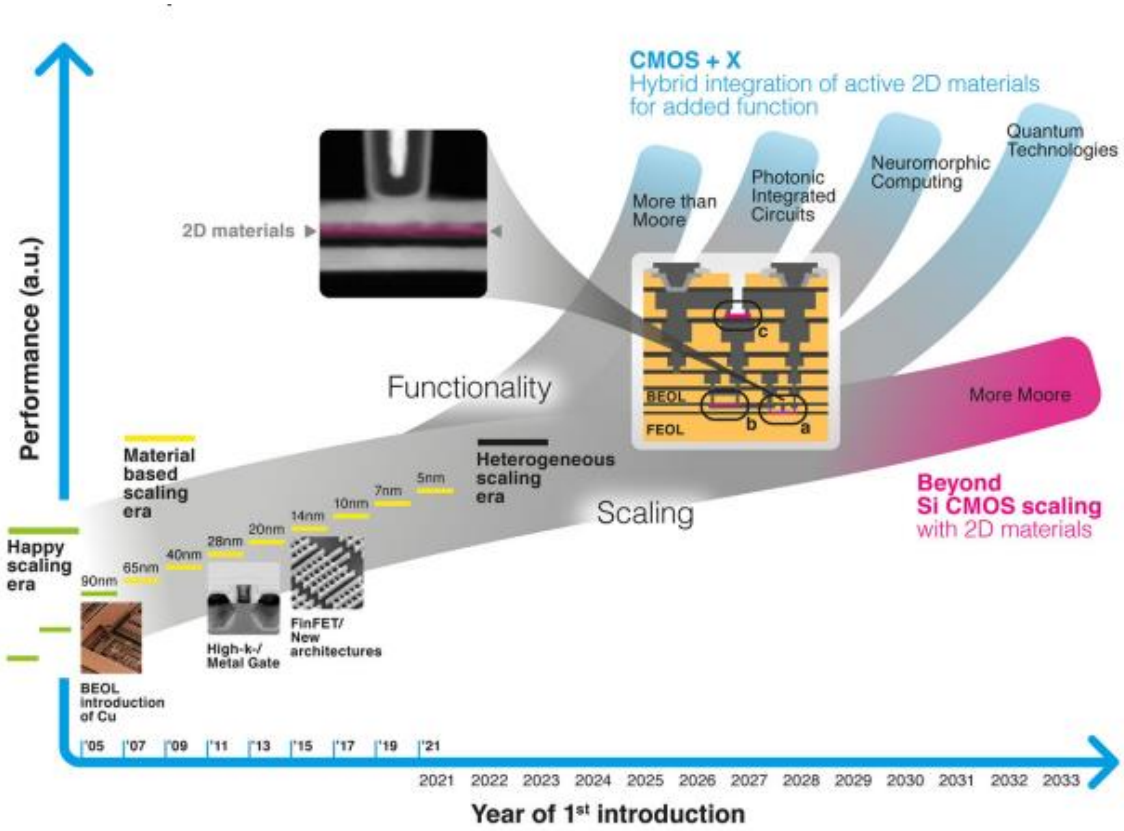


Figure 1.1: illustrates the evolution of silicon technology scaling and the future prospects of incorporating 2D materials in semiconductor processing.[21]

### 1.2.2 All inorganic perovskites

Metal halide perovskite materials have garnered significant attention due to their remarkable characteristics, including facile fabrication, low trap state density, high coefficient of optical absorption, low exciton binding energies, tunable bandgap, and long diffusion lengths of charge carriers.[22–27] These exceptional properties position them as highly desirable materials for a wide range of optoelectronic devices, such as solar cells, light-emitting diodes, lasers, and photodetectors.[28–32]

The organic-inorganic hybrid perovskites display inherent instability due to their sensitivity to moisture, heat, and oxygen.[33–38] But this limit was overcome by the introduction of all-inorganic components through cation substitution and has led to improved thermal stability.[39,40] The all-inorganic perovskites exhibit intriguing features, including high

photoluminescence (PL) quantum yield , narrow emission bandwidth, tunable optical and electrical properties, and adjustable electroluminescence emissions.[41–46] These properties enhance their attractiveness for a broad range of applications.

Thus metal halide perovskite materials have emerged as highly promising candidates for optoelectronic devices. The region where they have outshone every other material is their rise as a photovoltaic material. The schematic in Fig. 1.2 shows the evolution of conversion efficiencies of various technologies from 1985 to 2015. They have demonstrated an unprecedented rate of efficiency growth, surpassing any other technology in the history of photovoltaics. Their efficiency climbed from 3.9% in 2009 to a staggering 25.8% in 2021.[47]

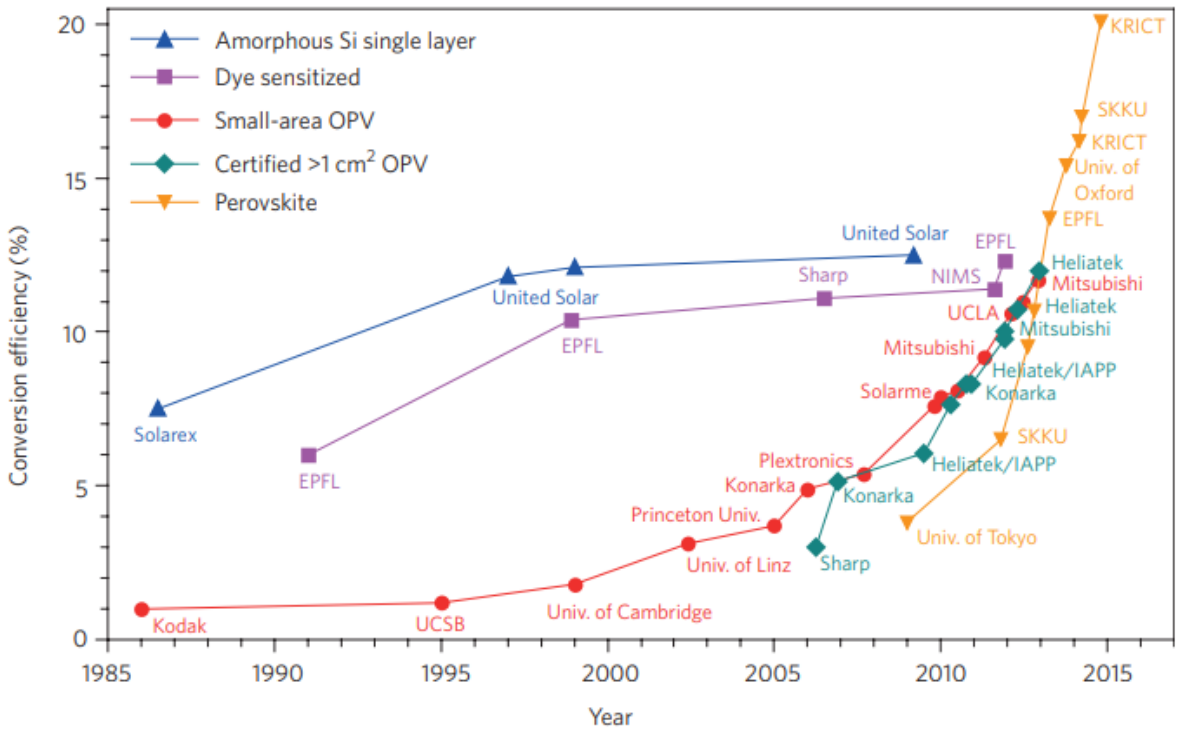


Figure 1.2: Schematic showing the efficiency improvements achieved in various thin-film photovoltaic technologies over the years. Among them, perovskite-based solar cells have demonstrated an unprecedented rate of efficiency growth, surpassing any other technology in the history of photovoltaics. Reproduced with permission from Ref. [48]

## 1.3 Strained monolayer TMDs

Theoretical studies have shown that the electron-phonon coupling in MoS2 is the main reason for its electrical resistance.[49] This limits the mobility of electron around 275 $cm^2/(V.s)$ at room temperature but by straining the monolayer by 3% we can completely decouple the phonons and improve the room temperature mobility to 1150 $cm^2/(V.s)$. The strength of the electron-phonon coupling increases with the doping density, but it decreases with strain. The change in electron-phonon coupling as a function of doping and strain is given in Fig. 1.3. The improvement in mobility with strain has been observed experimentally as well.[17][50]

Strain also effect the optical characterization of TMDs such as its PL and Raman signals. [51–54]. This makes strain a wonderful tool to tune the optoelectric properties of monolayer TMDs. The ability of monolayers like $MoS_2$ to withstand very high values of strains of about 11% also makes this all the more alluring. [55]

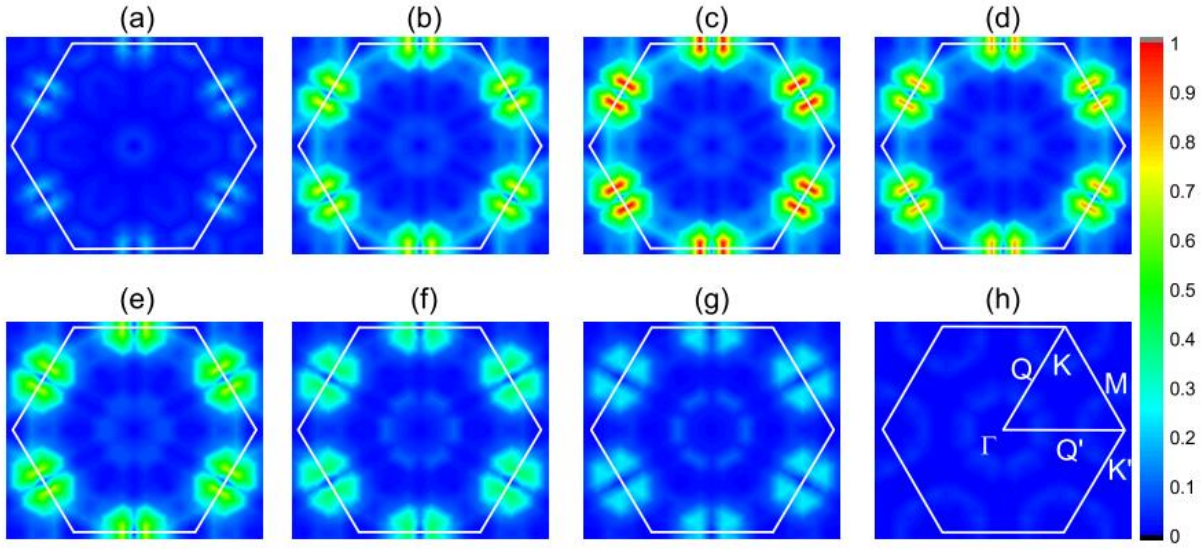


Figure 1.3: The distributions of the wave-vector-resolved electron-phonon coupling parameter $\lambda_{qtr}$ are mapped at various doping concentrations and tensile strains. (a) to (d) represent the maps of $\lambda_{qtr}$ at doping concentrations of $n_{2D}$ = 0.6, 1.6, 1.7, and 1.9 × $10^{14}$ $cm^{-2}$ under strain-free conditions. On the other hand, (e) to (h) depict the distributions of λqtr at tensile strains of ε = 0.4%, 0.8%, 1.2%, and 3.0% with a doping concentration of $n_{2D}$ = 1.7 × $10^{14}$ $cm^{-2}$. Reproduced with permission from Ref. [49]

Interesting effects like funnel effect and exciton to trion conversion happen in nonuniformly strained TMDs.[56][57] The effects cause diffusion of excitons from the unstrained region to the region of maximum strain caused by band bending. The exact mechanism in funneling and trion conversion slightly differs. However, the nonuniformly strained system in both cases produces an enhancement in PL which is interesting. As the nonuniformly strained region give rise to a continuous band modulation the system in itself is interesting. This thesis aims to touch upon these unique in-plane heterostructures due to their interesting nature.

## 1.4 Heterostructures

Semiconductor heterostructures, by combining different semiconductors with complementary properties, offer unique opportunities for engineering electronic and optoelectronic devices.[58] Semiconductor heterostructures, composed of distinct layers of semiconducting materials, enable precise control over band alignment, carrier confinement, and interface engineering. This control over the electronic and optical properties allows for the creation of devices with enhanced performance and novel functionalities. Heterostructures have led to a wide range of applications and devices, including diodes, transistors, lasers, photodetectors, and solar cells, among others.[59]

Recently, the emergence of 2D Van der Waals materials has garnered significant attention, as they can readily form great contact with other materials by simply placing them onto the material of interest. The Van der Waals nature of their bonds and their highly flexible nature are the crucial characteristics that enabled this ease of fabricating heterostructures.[60]

Perovskite 2D heterostructures represent a recent and exciting addition to the field of semiconductor heterostructures.[61][62] The perovskite 2D heterostructures exhibit intriguing properties arising from the combination of the constituent layers, including enhanced charge transport, improved stability, and tunable optoelectronic properties.

As both materials have very good optoelectric properties, the development of perovskite 2D heterostructures could open up new avenues for creating high-performance devices with advanced functionalities. Thus, their application in light-emitting diodes, photodetectors, and

transistors could revolutionize the field of optoelectronics. The exploration and utilization of perovskite 2D heterostructures hold great promise for the development of next-generation optoelectronic devices and pave the way for exciting advancements in the field of materials science.

## 1.5 Thesis outline

The thesis is organized into the following eleven chapters.

**Chapter 1** gives a brief introduction to semiconducting materials and introduces TMD monolayers and perovskites as upcoming semiconductors with good optoelectric capabilities. The chapter then briefly describes various semiconducting heterostructures and the possible applications of heterostructures are discussed.

**Chapter 2** presents the major characterization techniques used in the thesis to study the synthesized materials. The chapter also discusses the major device fabrication techniques used to make active devices for electrical characterization of these materials and their hetrostructures.

**Chapter 3** details the instrumentation done while setting up our lab.

**Chapter 4** discusses how sensitive the CVD growth of monolayer is to fluctuations in flow. We then used this sensitivity of growth to create a self-modulating effect that help in the growth of monolayers under conditions suited for the growth of bulk TMDs

**Chapter 5** Investigate a novel growth promoter sodium silicate, also known as water glass (WG) to synthesize MoS2 monolayers. The chapter then demonstrates how better WG is in synthesizing TMDs by comparing the growth and field effect mobility with that of salt.

**Chapter 6** examines the effect of strain on the optoelectronic properties of $MoS_2$. The strain caused by growing TMDs conformally on textured substrates led to an interesting modulation in their PL emission spectra.

**Chapter 7** discusses the growth of $CsPbI_3$ nanowires in the Hot Injection method wherein the mechanism of growth of nanowires is studied by a series of experiments involving the in-situ observation of the growth using an optical microscope.

**Chapter 8** demonstrates a sacrificial layer-assisted novel lithography technique that enabled the fabrication of electrical devices out of water-soluble perovskite crystal using traditional water-based photolithography.

**Chapter 9** presents a novel low-temperature solvothermal technique to grow $CsPbBr_3$ nanoplatelets with lateral dimensions in tens of micrometers and possessing ultralow dark currents. The method also led to the synthesis of ferroelectric $CsPbBr_3$ platelets.

**Chapter 10** concludes the thesis by outlining the future direction of the work done in this thesis which includes ongoing works on photodiodes of $CsPbBr_3$ and $MoS_2$ heterostructures and LEDs made using $WS_2$ $CsPbBr_3$ heterostructures.

**Bibliography**

[1] Schaibley J R, Yu H, Clark G, Rivera P, Ross J S, Seyler K L, Yao W and Xu X 2016 Valleytronics in 2D materials *Nat. Rev. Mater.* **1**

[2] Heine T 2015 Transition metal chalcogenides: Ultrathin inorganic materials with tunable electronic properties *Acc. Chem. Res.* **48** 65–72

[3] Xu X, Yao W, Xiao D and Heinz T F 2014 Spin and pseudospins in layered transition metal dichalcogenides *Nat. Phys.* **10** 343–50

[4] Mak K F, He K, Shan J and Heinz T F 2012 Control of valley polarization in monolayer MoS2 by optical helicity *Nat. Nanotechnol.* **7** 494–8

[5] Zeng H, Dai J, Yao W, Xiao D and Cui X 2012 Valley polarization in MoS 2 monolayers by optical pumping *Nat. Nanotechnol.* **7** 490–3

[6] Xiao D, Liu G Bin, Feng W, Xu X and Yao W 2012 Coupled spin and valley physics in monolayers of MoS 2 and other group-VI dichalcogenides *Phys. Rev. Lett.* **108**

[7] Carr S, Massatt D, Fang S, Cazeaux P, Luskin M and Kaxiras E 2017 Twistronics: Manipulating the electronic properties of two-dimensional layered structures through their twist angle *Phys. Rev. B* **95**

[8] Bhattacharyya S, Pandey T and Singh A K 2014 Effect of strain on electronic and

thermoelectric properties of few layers to bulk MoS 2 *Nanotechnology* **25** 465701

[9] Singh E, Singh P, Kim K S, Yeom G Y and Nalwa H S 2019 Flexible Molybdenum Disulfide (MoS 2 ) Atomic Layers for Wearable Electronics and Optoelectronics *ACS Appl. Mater. Interfaces* **11** 11061–105

[10] Wang H, Yuan H, Sae Hong S, Li Y and Cui Y 2015 Physical and chemical tuning of two-dimensional transition metal dichalcogenides *Chem. Soc. Rev.* **44** 2664–80

[11] Splendiani A, Sun L, Zhang Y, Li T, Kim J, Chim C-Y, Galli G and Wang F 2010 Emerging Photoluminescence in Monolayer MoS 2 *Nano Lett.* **10** 1271–5

[12] Mak K F F, Lee C, Hone J, Shan J and Heinz T F F 2010 Atomically thin MoS2: A new direct-gap semiconductor *Phys. Rev. Lett.* **105**

[13] Zhang Y, Chang T R, Zhou B, Cui Y T, Yan H, Liu Z, Schmitt F, Lee J, Moore R, Chen Y, Lin H, Jeng H T, Mo S K, Hussain Z, Bansil A and Shen Z X 2014 Direct observation of the transition from indirect to direct bandgap in atomically thin epitaxial MoSe2 *Nat. Nanotechnol.* **9** 111–5

[14] Lezama I G, Arora A, Ubaldini A, Barreteau C, Giannini E, Potemski M and Morpurgo A F 2015 Indirect-to-Direct Band Gap Crossover in Few-Layer MoTe2 *Nano Lett.* **15** 2336–42

[15] Zhao W, Ghorannevis Z, Chu L, Toh M, Kloc C, Tan P H and Eda G 2013 Evolution of electronic structure in atomically thin sheets of ws 2 and wse2 *ACS Nano* **7** 791–7

[16] Zhang R, Lai Y, Chen W, Teng C, Sun Y, Yang L, Wang J, Liu B and Cheng H-M 2022 Carrier Trapping in Wrinkled 2D Monolayer MoS 2 for Ultrathin Memory *ACS Nano* **16** 6309–16

[17] Liu T, Liu S, Tu K-H, Schmidt H, Chu L, Xiang D, Martin J, Eda G, Ross C A and Garaj S 2019 Crested two-dimensional transistors *Nat. Nanotechnol.* **14** 223–6

[18] Castellanos-Gomez A, Roldán R, Cappelluti E, Buscema M, Guinea F, van der Zant H S J and Steele G A 2013 Local Strain Engineering in Atomically Thin MoS 2 *Nano Lett.* **13** 5361–6

[19] Yang S, Wang C, Sahin H, Chen H, Li Y, Li S-S, Suslu A, Peeters F M, Liu Q, Li J and Tongay S 2015 Tuning the Optical, Magnetic, and Electrical Properties of ReSe 2 by Nanoscale Strain Engineering *Nano Lett.* **15** 1660–6

[20] Deng S, Che S, Debbarma R and Berry V 2019 Strain in a single wrinkle on an MoS 2 flake for in-plane realignment of band structure for enhanced photo-response *Nanoscale* **11** 504–11

[21] Lemme M C, Akinwande D, Huyghebaert C and Stampfer C 2022 2D materials for future heterogeneous electronics *Nat. Commun.* **13** 1392

[22] Shi D, Adinolfi V, Comin R, Yuan M, Alarousu E, Buin A, Chen Y, Hoogland S, Rothenberger A, Katsiev K, Losovyj Y, Zhang X, Dowben P A, Mohammed O F, Sargent E H and Bakr O M 2015 3、SCIENCE sciencemag.org **347** 6221

[23] Liu D and Kelly T L 2014 Perovskite solar cells with a planar heterojunction structure prepared using room-temperature solution processing techniques *Nat. Photonics* **8** 133–8

[24] Yin W J, Shi T and Yan Y 2014 Unique properties of halide perovskites as possible origins of the superior solar cell performance *Adv. Mater.* **26** 4653–8

[25] Weidman M C, Seitz M, Stranks S D and Tisdale W A 2016 Highly Tunable Colloidal Perovskite Nanoplatelets through Variable Cation, Metal, and Halide Composition *ACS Nano* **10** 7830–9

[26] Stranks S D, Eperon G E, Grancini G, Menelaou C, Alcocer M J P P, Leijtens T, Herz L M, Petrozza A and Snaith H J 2013 Electron-hole diffusion lengths exceeding 1 micrometer in an organometal trihalide perovskite absorber *Science (80-. ).* **342** 341–4

[27] Dong 2015 Electron-Hole diffusion length >175 nm *Sci. express* **43210** 1–8

[28] Liu M, Johnston M B and Snaith H J 2013 Efficient planar heterojunction perovskite solar cells by vapour deposition *Nature* **501** 395–8

[29] Green M A, Ho-Baillie A and Snaith H J 2014 The emergence of perovskite solar cells *Nat. Photonics* **8** 506–14

[30] Tan Z-K K, Moghaddam R S, Lai M L, Docampo P, Higler R, Deschler F, Price M,

Sadhanala A, Pazos L M, Credgington D, Hanusch F, Bein T, Snaith H J and Friend R H 2014 Bright light-emitting diodes based on organometal halide perovskite *Nat. Nanotechnol.* **9** 687–92

[31] Zhang Q, Ha S T, Liu X, Sum T C and Xiong Q 2014 Room-temperature near-infrared high-Q perovskite whispering-gallery planar nanolasers *Nano Lett.* **14** 5995–6001

[32] Dou L, Yang Y M, You J, Hong Z, Chang W H, Li G and Yang Y 2014 Solution-processed hybrid perovskite photodetectors with high detectivity *Nat. Commun.* **5**

[33] Cheng Z and Lin J 2010 Layered organic-inorganic hybrid perovskites: Structure, optical properties, film preparation, patterning and templating engineering *CrystEngComm* **12** 2646–62

[34] Noh J H, Im S H, Heo J H, Mandal T N and Seok S Il 2013 Nano Lett. 2013, 13, 1764−1769.pdf *Nano Lett.* **13** 1764−1769

[35] Divitini G, Cacovich S, Matteocci F, Cinà L, Di Carlo A and Ducati C 2016 In situ observation of heat-induced degradation of perovskite solar cells *Nat. Energy* **1** 1–12

[36] Nenon D P, Christians J A, Wheeler L M, Blackburn J L, Sanehira E M, Dou B, Olsen M L, Zhu K, Berry J J and Luther J M 2016 Structural and chemical evolution of methylammonium lead halide perovskites during thermal processing from solution *Energy Environ. Sci.* **9** 2072–82

[37] Deng W, Fang H, Jin X, Zhang X, Zhang X and Jie J 2018 Organic-inorganic hybrid perovskite quantum dots for light-emitting diodes *J. Mater. Chem. C* **6** 4831–41

[38] Kumar A, Bansode U, Ogale S and Rahman A 2020 Understanding the thermal degradation mechanism of perovskite solar cells via dielectric and noise measurements *Nanotechnology* **31** 365403

[39] Choi H, Jeong J, Kim H B, Kim S, Walker B, Kim G H and Kim J Y 2014 Cesium-doped methylammonium lead iodide perovskite light absorber for hybrid solar cells *Nano Energy* **7** 80–5

[40] Sun Q and Yin W J 2017 Thermodynamic Stability Trend of Cubic Perovskites *J. Am. Chem. Soc.* **139** 14905–8

[41] Koscher B A, Swabeck J K, Bronstein N D and Alivisatos A P 2017 Essentially Trap-Free CsPbBr3 Colloidal Nanocrystals by Postsynthetic Thiocyanate Surface Treatment *J. Am. Chem. Soc.* **139** 6566–9

[42] Di Stasio F, Christodoulou S, Huo N and Konstantatos G 2017 Near-Unity Photoluminescence Quantum Yield in CsPbBr3 Nanocrystal Solid-State Films via Postsynthesis Treatment with Lead Bromide *Chem. Mater.* **29** 7663–7

[43] Liu F, Zhang Y, Ding C, Kobayashi S, Izuishi T, Nakazawa N, Toyoda T, Ohta T, Hayase S, Minemoto T, Yoshino K, Dai S and Shen Q 2017 Highly Luminescent Phase-Stable CsPbI3 Perovskite Quantum Dots Achieving Near 100% Absolute Photoluminescence Quantum Yield *ACS Nano* **11** 10373–83

[44] Protesescu L, Yakunin S, Bodnarchuk M I, Krieg F, Caputo R, Hendon C H, Yang R X, Walsh A and Kovalenko M V 2015 Nanocrystals of Cesium Lead Halide Perovskites (CsPbX 3 , X = Cl, Br, and I): Novel Optoelectronic Materials Showing Bright Emission with Wide Color Gamut 1–5

[45] Lei T, Lai M, Kong Q, Lu D, Lee W, Dou L, Wu V, Yu Y and Yang P 2018 Electrical and Optical Tunability in All-Inorganic Halide Perovskite Alloy Nanowires *Nano Lett.* **18** 3538–42

[46] Song J, Li J, Li X, Xu L, Dong Y and Zeng H 2015 Quantum Dot Light-Emitting Diodes Based on Inorganic Perovskite Cesium Lead Halides (CsPbX3) *Adv. Mater.* **27** 7162–7

[47] George J, Joseph A P and Balachandran M 2022 Perovskites: Emergence of highly efficient third-generation solar cells *Int. J. Energy Res.* **46** 21856–83

[48] Leo K 2015 Signs of stability *Nat. Nanotechnol.* **10** 574–5

[49] Ge Y, Wan W, Feng W, Xiao D and Yao Y 2014 Effect of doping and strain modulations on electron transport in monolayer MoS2 *Phys. Rev. B* **90** 035414

[50] Datye I M, Daus A, Grady R W, Brenner K, Vaziri S and Pop E 2022 Strain-Enhanced Mobility of Monolayer MoS 2 *Nano Lett.* **22** 8052–9

[51] Li Z, Lv Y, Ren L, Li J, Kong L, Zeng Y, Tao Q, Wu R, Ma H, Zhao B, Wang D, Dang W, Chen K, Liao L, Duan X, Duan X and Liu Y 2020 Efficient strain modulation of 2D

materials via polymer encapsulation *Nat. Commun.* **11** 1151

[52] Sun Y, Wang R and Liu K 2017 Substrate induced changes in atomically thin 2-dimensional semiconductors: Fundamentals, engineering, and applications *Appl. Phys. Rev.* **4** 011301

[53] Zhu C R, Wang G, Liu B L, Marie X, Qiao X F, Zhang X, Wu X X, Fan H, Tan P H, Amand T and Urbaszek B 2013 Strain tuning of optical emission energy and polarization in monolayer and bilayer MoS2 *Phys. Rev. B* **88** 121301

[54] Yang S, Chen Y and Jiang C 2021 Strain engineering of two-dimensional materials: Methods, properties, and applications *InfoMat* **3** 397–420

[55] Bertolazzi S, Brivio J and Kis A 2011 Stretching and breaking of ultrathin MoS 2 *ACS Nano* **5** 9703–9

[56] Li H, Contryman A W, Qian X, Ardakani S M, Gong Y, Wang X, Weisse J M J M, Lee C H, Zhao J, Ajayan P M, Li J, Manoharan H C and Zheng X 2015 Optoelectronic crystal of artificial atoms in strain-textured molybdenum disulphide *Nat. Commun.* **6** 7381

[57] Harats M G, Kirchhof J N, Qiao M, Greben K and Bolotin K I 2020 Dynamics and efficient conversion of excitons to trions in non-uniformly strained monolayer WS2 *Nat. Photonics* **14** 324–9

[58] Liu R, Wang F, Liu L, He X, Chen J, Li Y and Zhai T 2021 Band Alignment Engineering in Two-Dimensional Transition Metal Dichalcogenide-Based Heterostructures for Photodetectors *Small Struct.* **2** 2000136

[59] Joseph S, Mohan J, Lakshmy S, Thomas S, Chakraborty B, Thomas S and Kalarikkal N 2023 A review of the synthesis, properties, and applications of 2D transition metal dichalcogenides and their heterostructures *Mater. Chem. Phys.* **297** 127332

[60] Fan S, Vu Q A, Tran M D, Adhikari S and Lee Y H 2020 Transfer assembly for two-dimensional van der Waals heterostructures *2D Mater.* **7** 022005

[61] Zhang Z, Wang S, Liu X, Chen Y, Su C, Tang Z, Li Y and Xing G 2021 Metal Halide Perovskite/2D Material Heterostructures: Syntheses and Applications *Small Methods* **5** 2000937

[62] Huo C, Liu X, Wang Z, Song X and Zeng H 2018 High-Performance Low-Voltage-Driven Phototransistors through CsPbBr 3 –2D Crystal van der Waals Heterojunctions *Adv. Opt. Mater.* **6** 1800152

# Chapter 2

# Experimental Techniques

This chapter discusses some of the experimental and characterization techniques used for material characterization and device fabrication used in this thesis.

## 2.1 Introduction

The field of materials science and engineering has witnessed remarkable advancements in recent years, leading to the development of novel materials and advancement in our technological prowess.[1,2] This trajectory is set to continue as ongoing discoveries in materials and physics fuel further advancements and breakthroughs in the field.[3–8] These advancements are often driven by a deep understanding of material properties and our ability to precisely tune them to suit our needs. The experimental and characterization techniques employed in material characterization and device fabrication play a crucial role in unraveling the mysteries of materials and harnessing their potential for technological applications. As a consequence, material characterization and device fabrication emerge as indispensable components within the realm of materials science.

This chapter discusses some of the experimental and characterization techniques utilized in the context of material characterization and device fabrication within the scope of this thesis. The objective of this chapter is to present a comprehensive overview of the diverse techniques employed in material characterization and device fabrication, emphasizing their relevance and impact on the research conducted in this thesis. Additionally, more experimental techniques are discussed in Chapter 3, which discusses the instrumentations done by us to establish our lab at IISER Pune.

Overall, this chapter serves as a comprehensive introduction to most of the experimental and characterization techniques used by us in material characterization and device fabrication within the scope of this thesis.

## 2.2 Material characterization

The materials explored in this thesis are mainly lead halide perovskites and monolayer TMDs both of which are crystalline direct bandgap materials. A range of characterization techniques has been utilized to investigate these materials after their growth, allowing for a comprehensive analysis of their structural, optical, and chemical properties.

One of the primary techniques employed for analyzing lead halide perovskite is X-ray diffraction (XRD), which provides valuable insights into the crystal structure, lattice parameters, and orientation of the materials. Raman spectroscopy played a pivotal role in the analysis of mainly monolayer TMDs, enabling the investigation of vibrational modes, strain effects, and disorder within the crystalline lattice. X-ray photoelectron spectroscopy (XPS) was implied in probing oxidation states, and surface chemistry of the TMDs.

Other techniques such as Photoluminescence (PL) spectroscopy, high-resolution transmission electron microscopy (HRTEM), Field-emission scanning electron microscopy (FESEM) and energy-dispersive X-ray spectroscopy (EDX) proved to be highly suitable for both materials.

### 2.2.1 X-ray diffraction

XRD is a powerful technique for evaluating the crystal structure of various crystals by analyzing the diffraction of X-rays caused by the periodic arrangement of atoms within a crystal lattice. The interatomic spacing of crystals is comparable to the wavelength of X-rays, this causes X-rays to diffract by seeing the crystal lattice as a grating giving rise to a diffraction pattern. The distance between the atoms results in specific angles at which the X-rays get diffracted. This phenomenon is described by Bragg's Law, formulated by Lawrence and William Bragg in the early 1900s, who were awarded the Nobel Prize in 1913 for their discovery.[9] The equation for diffraction, $2d \sin(\theta) = n \lambda$, forms the basis for X-ray analysis, where d represents the interatomic spacing.[10,11]

We used a Bruker D8 Advance X-ray diffractometer at room temperature using Cu-Kα radiation ($\lambda = 1.5406$ Å). The typical step size I use for my measurement is 0.02°. Fig. 2.1 a and b shows the photographs of the machine used for the XRD. Over the years, researchers have extensively utilized XRD to investigate known materials, resulting in the establishment of a comprehensive database of XRD patterns accessible to all. Notable contributions to this field include the

Inorganic Crystal Structure Database (ICSD) and the Crystallography Open Database (COD). The ICSD, which contains over 140,000 structures, can be accessed via the Chemical Database Service (CDS) hosted at the Daresbury Laboratory at http://cds.dl.ac.uk. On the other hand, the COD is an open-access repository that encompasses crystal structures of organic, inorganic, metal-organic compounds, and minerals (excluding biopolymers), and encourages registered users to contribute published and unpublished structures of small molecules and small to medium-sized unit cell crystals. Their open and collaborative nature, enables researchers worldwide to share and explore crystallographic data, facilitating advancements in various scientific domains.

A Crystallographic Information File (CIF) is a widely adopted file format utilized for the storage and exchange of crystallographic data. The CIF file corresponding to a crystal structure can be obtained from the Cambridge Crystallographic Data Centre (CCDC) website at https://www.ccdc.cam.ac.uk/structures/. The CCDC number, also known as the Cambridge Crystallographic Data Centre number, the CSD number, which refers to the Cambridge Structural Database, the ICSD number, associated with the Inorganic Crystal Structure Database, or the CSD reference number can all be utilized as search parameters when conducting queries in these databases. Alternatively, one can search the material project website https://next-gen.materialsproject.org/ to access calculated XRD patterns for numerous materials. The Materials Project is an online platform and database that provides comprehensive information and resources related to materials science and engineering. It offers researchers access to a vast collection of computed data, including XRD patterns and crystallographic information. Softwares like VESTA can be used to easily read these CIF Hence the XRD data from these sources can be used to compare the phase and structure of the synthesized crystals.

Fig. 2.1 c shows the XRD plots of the cubic and orthorhombic crystal structure of CsPbBr3 as obtained from the CIF files ICSD 97851 and ICSD 97852. The difference in their XRD pattern is obvious. Especially the twin peaks around 30 degrees makes it very easy to distinguish the cubic crystal from the orthorhombic crystal demonstrating the capability of XRD to distinguish polymorphs of different crystals. This helped us in identifying the crystal structures of perovskite crystals and played a major role in their characterizations.

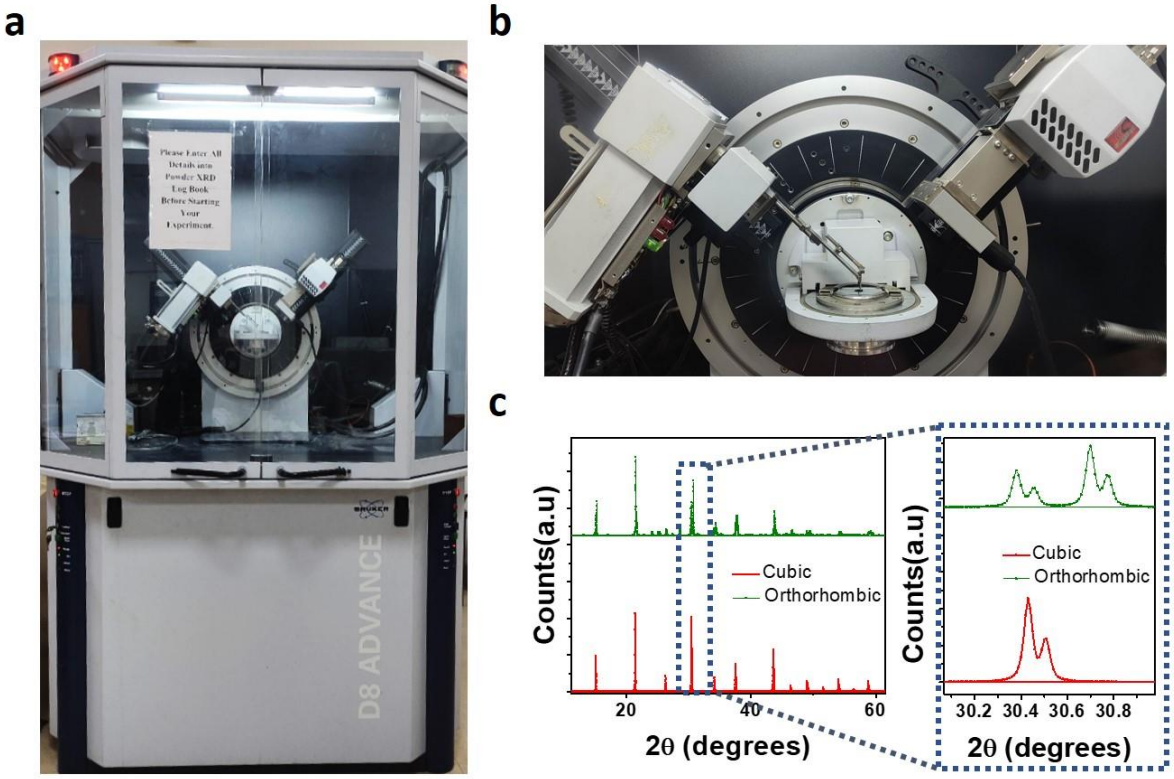


Figure 2.1: (a) and (b) are the photograph of the Bruker D8 Advance X-ray diffractometer. (c) XRD pattern of 2 different crystal structures of $CsPbBr_3$.

### 2.2.2 XPS

XPS is an invaluable analytical technique that can provide detailed information about the chemical composition and electronic structure of materials.[12] In this thesis, we used XPS for characterizing monolayer TMDs and the intermediate formed during its synthesis.

XPS involves irradiating the sample with soft x-rays, and then analyzing the kinetic energy of the emitted electrons. The energy transfer during this process is expressed by the equation:

$$BE = h\nu - KE - \varphi_{spe}$$

Where, $h\nu$ is the energy of the x-ray, $BE$ is the binding energy of the electron to the atom/orbital, $KE$ is the kinetic energy of the emitted electron, and $\varphi_{spe}$ is the spectrometer work function which is a constant value. In XPS, the binding energy is measured relative to the sample Fermi level. Photoelectron peaks are labeled based on the element and orbital from which they were ejected. The binding energy of an electron is a material property and remains constant regardless of the x-ray source used. However, the kinetic energy of the emitted

photoelectrons varies depending on the x-ray source. A schematic of the working of XPS is shown in Fig. 2.2.

XPS assumes a crucial role in the characterization of intermediates formed during the growth of TMDs. It provides valuable insights into the elemental composition and chemical states of both the intermediates and the resulting TMDs, thereby facilitating a deeper understanding of the growth process.

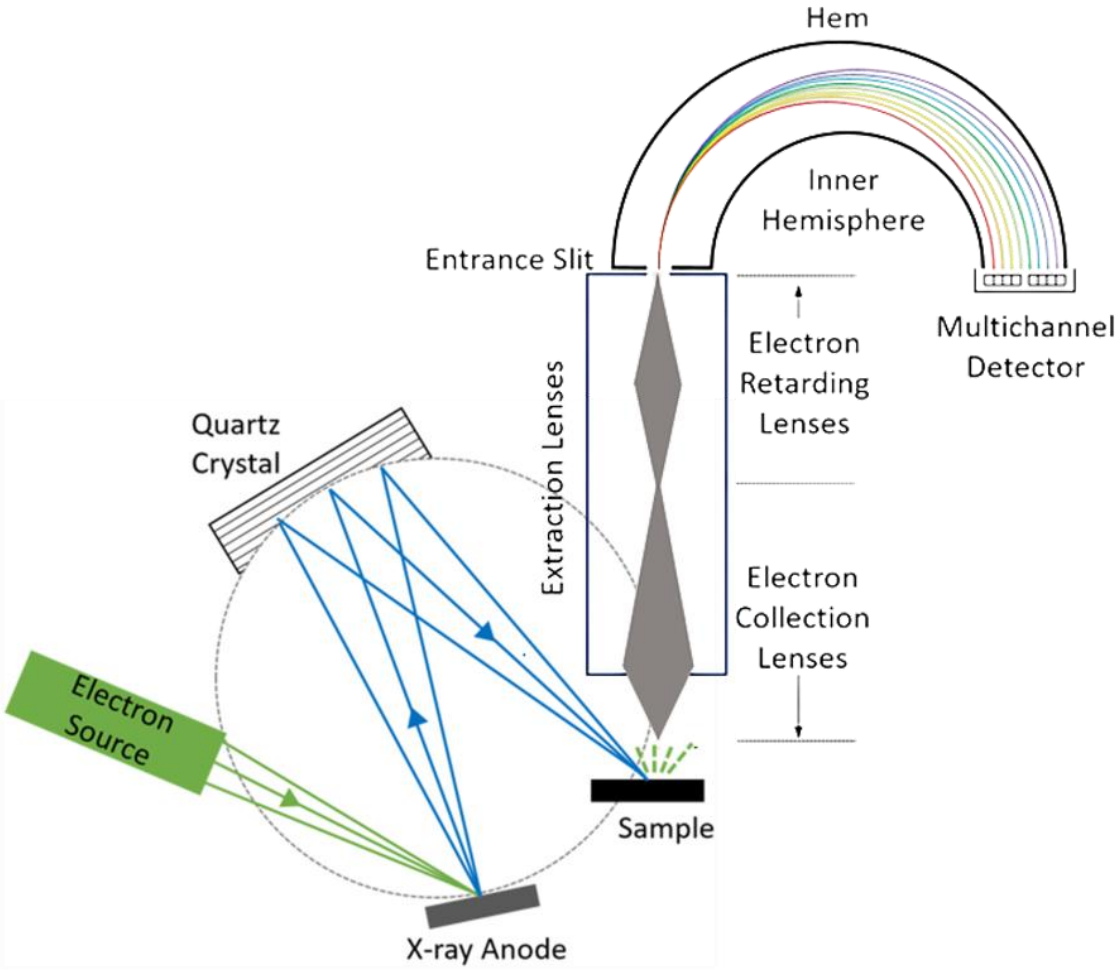


Figure 2.2: Schematic showing the working of an XPS measurement. Reproduced with permission from Ref. [12]

By irradiating the material with x-rays and measuring the kinetic energy of the emitted photoelectrons, XPS can precisely determine the atomic composition of the material surface and identify any impurities or contaminants present. It can discern between different oxidation states and reveal the presence of defects or surface modifications that may influence the

material's properties. This information is crucial for understanding the surface reactivity, stability, and potential interactions with other materials or environmental conditions.

### 2.2.3 Optical techniques

In this subsection, we discuss the characterization techniques of Raman spectroscopy, photoluminescence (PL) spectroscopy, and second harmonic generation (SHG), all of which are non-invasive means to study the properties of materials by exciting them with light. Raman spectroscopy, based on the principle of Raman scattering discovered by Sir C.V Raman, provides valuable insights into the vibrational modes of a system through inelastic scattering of light.[13] On the other hand, PL spectroscopy offers a means to study the optical properties of materials by exciting them with light and measuring the emitted photons.[14] The materials investigated in this thesis belong to the category of direct bandgap materials, which exhibit high photoluminescence. SHG, initially discovered by Frank et al. in 1961, is a nonlinear optical phenomenon that occurs in materials lacking inversion symmetry. [15,16] It involves the combination of two photons to generate a new photon with twice the frequency, resulting in an emission at precisely half the wavelength of the original light source. This intriguing process provides valuable insights into the optical properties of materials and is widely used for studying various phenomena in nonlinear optics and material science.

Monolayer TMDs and Perovskites are of interest as they possess a direct bandgap and host a diverse range of excitonic species and intriguing phenomena.[17] Photoluminescence serves as a powerful tool to explore and characterize these materials, enabling the investigation of various unique effects and phenomena associated with excitons. By utilizing photoluminescence spectroscopy, we can gain valuable insights into the optical properties and excitonic behavior of these direct bandgap materials, unraveling their fascinating attributes.

Raman spectroscopy is a powerful and non-destructive technique that enables the investigation of electronic and vibrational states. When light interacts with a substance, it undergoes various processes, including absorption, reflection, and scattering. Raman scattering occurs when the scattered light has frequencies different from the incident light, resulting in the emission of photons with altered frequencies. This inelastic scattering provides valuable information about the vibrational modes of the material. As the vibrational modes of different materials differ from one another Raman spectroscopy is regarded as the molecular fingerprint and is unique

for the materials that are Raman active.

Raman spectroscopy is widely employed in the study of various materials, including TMDs and perovskites, to gain insights into their vibrational properties, layer number, disorders, doping, and strain-induced effects. TMDs, such as $MoS_2$, exhibit unique Raman spectra that provide important signatures of their structural and vibrational properties. In the case of $MoS_2$, the Raman spectrum exhibits distinctive peaks corresponding to different vibrational modes, such as the out-of-plane relative motion of sulfur atoms ($A_{1g}$) and the in-plane opposing motion of molybdenum and sulfur atoms ($E_{2g}$). The ($A_{1g}$) peak provide information on doping and the ($E_{2g}$) provide valuable information on the strain in the films.[18]

In our study, we utilized Raman spectroscopy, PL spectroscopy and SHG to characterize the synthesized semiconductors. Raman spectroscopy was mainly performed using a 532 nm Continous Wave diode laser and a 100x objective with 0.95 NA, while PL spectroscopy involved the excitation of the samples using a 532 nm laser and the collection of emitted light through a 100x lens with 0.95 NA. The SHG studies were performed using a Ti-Sapphire Laser (operating at 140fs, 80 Hz), with an excitation wavelength of 810 nm. Most of the optical measurements were carried out in Dr. G. V Pavan Kumar's lab at IISER Pune and all the PL and Raman mapping were carried out in Dr. Stéphane Berciaud's lab at IPCMS, Strasbourg.

### 2.2.4 AFM

Atomic Force Microscopy (AFM), is a powerful scanning probe microscopy technique used to obtain topographical images of sample surfaces. G. Binnig and C. F. Quate at IBM developed the AFM by combining the principles of the scanning tunneling microscope and the stylus profilometer.[19] The AFM measurement involves the scanning of the surface using a sharp tip attached to a flexible cantilever, the atomic force between the surface and the tip causes the tip to deflect. The deflection is measured by using a laser beam focused onto the reflective-coated tip of the flexible cantilever as shown in Fig. 2.4, and the reflected beam is detected using a position-sensitive photodetector. The position-sensitive photodetector consists of multiple segments, and the position of the laser spot on these segments provides information about the deflection of the cantilever. By monitoring the position of the laser spot on the photodetector, the displacement of the cantilever can be determined. AFM offers atomic resolution and 3D

topographic imaging capabilities and can provide a lot more information depending on the AFM tip used. Some of the different AFM techniques include Magnetic AFM, Kelvin Probe Force Microscopy, Piezo Force Microscopy(PFM), and Conductive AFM.[20–23] It can be operated in different modes, such as contact mode or tapping mode, and can be used in ambient or controlled environments. AFM measurements in this thesis were performed using a Keysight 5500 AFM. The thesis also involves the measurement from PFM done by our collaborator Dr. Goutam Sheet's lab at IISER Mohali. PFM measurements were conducted using an Asylum Research AFM (MFP-3D) system equipped with a high-voltage amplifier. The sample was affixed to a conducting sample holder, which was directly linked to the amplifier's ground. A conductive AFM cantilever, with a Pt-Ir tip, was used to perform the PFM measurements.[24] In this thesis, AFM was employed to characterize the surface roughness and measure the thickness of perovskite platelets. Additionally, PFM was utilized to investigate the ferroelectric properties of the samples.

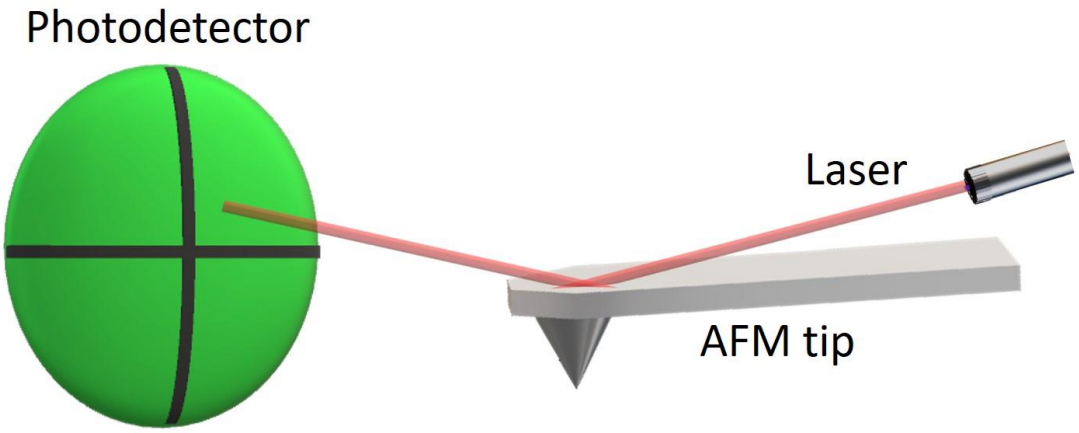


Figure 2.4: Schematic showing the working of an AFM

### 2.2.5 HRTEM

The development of electron microscopy revolutionized the field of microscopy by overcoming the fundamental limitations imposed by visible light on resolving objects. The smallest achievable angle θ between two circular point sources is the best obtainable resolution and is

given by the Rayleigh criteria

$$\Theta = 1.22\frac{\lambda}{d}$$

Where, $\lambda$ is the wavelength and d is the diameter of the circular aperture. This fundamental limit is imposed by diffraction and for an optical microscope the minimum resolution $R$ is given by

$$R = \frac{0.61 \times \lambda}{N.A}$$

Where, $N.A$ is the numerical aperture of the microscope objective. Using visible light, the shortest wavelength that we can see with the naked eye is close to 400 nm. However, using electron for imaging gives us the advantage of having an easy to control particle with tunable wavelength. The wavelength of the electron is governed by the de Broglie wavelength equation

$$\lambda = \frac{h}{m \times v}$$

Where, $h$ is the Planck's constant$m$ is the mass of the electron and $v$ is the velocity. It is easy to control the velocity of electrons by applying an electric field and thus its wavelength. The breakthrough in imaging capabilities using electrons was first demonstrated by G.P. Thomson in 1927 when he formed a transmission electron diffraction pattern using electrons that passed through a thin specimen.[25] The key principle behind HRTEM lies in the ability to focus electrons using electric or magnetic fields and Ernst Ruska made significant contributions to the development of electron lenses in the 1930s.[26] Ernst Ruska was awarded the Nobel Prize in Physics in 1986 for his groundbreaking contributions to the design and development of the electron microscope. Further advancements in electron lens technology led to the construction of transmission electron microscopes (TEMs), where electrons pass through a thin specimen and are then imaged using appropriate lenses. These early TEMs employed lenses arranged horizontally, but later designs adopted a vertical column arrangement to ensure better alignment and stability. [25] The electron source in TEMs utilizes a tungsten filament or a lanthanum hexaboride ($LaB_6$) crystal. These electron sources are chosen for their ability to emit a high-intensity electron beam with good stability and a long lifespan. By applying high voltages, the electron beams in electron microscopes are accelerated, allowing them to pass through thin samples with an extremely small wavelength. This enables electron microscopes to achieve

atomic-scale resolution, providing detailed imaging and analysis of the specimen at the atomic level.

HRTEM revolutionized materials characterization by enabling the examination of the materials at the atomic level. It provided direct visualization of lattice including crystalline defects. In this thesis, we use HRTEM to analyze Quantum dots (Q.D), nanowires, and monolayer TMDs. We use HRTEM (JEM-2100F, JEOL) for TEM imaging at IISER, and HAADF-STEM images were acquired with Hitachi HD2700C dedicated STEM with Cs probe corrector SAED patterns were obtained using Thermo-Fisher Talos F200X at BNL.

### 2.2.6 SEM

The scanning electron microscope (SEM) works with the same principles as a TEM. SEM has emerged as a powerful tool for examining relatively thick specimens, addressing a limitation of the TEM. In TEM, the specimen needs to be extremely thin for the successful transmission of electrons, which restricts its applicability. The development of SEM was driven by the need for an electron-beam instrument that offers improved spatial resolution with the advantage of working with bulk specimens.[25]

SEM operates by exploiting the phenomenon of electron scattering and secondary electron emission.[27,28] Instead of transmitting through the specimen, primary electrons can interact with atomic electrons within the solid, resulting in the release of secondary electrons. These secondary electrons are emitted with varying energies, making it challenging to focus them for imaging using electron lenses. However, SEM utilizes a scanning principle where a focused electron probe is scanned across the specimen using electrostatic or magnetic fields. By simultaneously scanning in two perpendicular directions, a raster pattern is formed, covering a square or rectangular area. Secondary electrons emitted from each point on the specimen are collected to generate an image of the area.

This raster-scanning approach is analogous to the generation and reception of television signals. The same principle is employed in the deflection of the electron beam within a cathode-ray tube (CRT) used for image recording.[25] In SEM, the image is produced sequentially, point by point, unlike the simultaneous image formation in TEM or light microscopy. Early prototypes

of SEM utilized field-emission electron sources, while later models adopted heated-filament sources, with electrostatic lenses focusing the electrons onto the specimen.

In this thesis, we use a Zeiss Ultra Plus FESEM with an integral charge compensator and embedded EsB and AsB detectors (Oxford X-max Instruments 80 mm2 (Carl Zeiss NTS, GmbH)). The FESEM is used to image the grown materials and textured substrates.

## 2.3 Device fabrication techniques

In the modern digital age, electronic devices have become an indispensable component of our daily lives, ranging from smartphones and personal computers to various gadgets. These devices consist of billions of individual components that work together to provide various functionalities. The fabrication of active devices using novel semiconductor materials plays a crucial role in advancing technology and meeting the demands of modern society.

The focus of this thesis is to synthesize and utilize novel semiconductor materials such as perovskites, TMDs and their heterostructures for device applications. The materials, often on the scale of a few tens of micrometers, possess unique electrical and optoelectronic properties that make them promising candidates for next-generation devices. To fully understand and harness their potential, it is essential to fabricate microscale devices on these materials and characterize their properties.

Fabrication techniques such as lithography and deposition play a vital role in the creation of these microscale devices. Lithography enables precise patterning and structuring of materials at the micro- and nanoscale, allowing for the creation of intricate device architectures. Deposition techniques, such as magnetron sputtering, provide a versatile method for depositing a wide variety of materials onto substrates, enabling the integration of different functional layers within a device structure.

We will discuss the techniques used in this thesis to fabricate devices and how they were integrated into a PCB for further characterization.

### 2.3.1 Photolithography

Lithography techniques serve as the cornerstone of semiconductor fabrication, playing a pivotal role in the production of advanced electronic devices. Photolithography dominates the semiconductor industry because of its high throughput. The method involves the use of a polymer compound which when light shines on causes a chemical change that prevents or allows it to be washed in a developer solution.[29]

Traditional lithography methods rely on masks, whereas direct laser writing lithography eliminates the need for a mask, offering increased flexibility and simplicity in the fabrication process. This not only reduces production costs but also enables rapid prototyping and design modifications.[30] Moreover, the scalability of direct laser writing lithography makes it suitable for both small-scale research projects and large-scale production applications. But the throughput of this would pale in comparison to traditional mask-based lithography as the process is more time-consuming.

However, direct laser writing offers distinct advantages, including maskless patterning, cost-effectiveness, and design scalability, making it a promising approach for sub-micron feature fabrication.[30] The key principle behind direct laser writing lithography involves utilizing a laser beam to directly expose and pattern a photosensitive material, such as a photoresist or a photopolymer, on a substrate. The laser intensity, controlled by factors such as laser power and exposure time, determines the degree of material modification and pattern resolution. The movement of the substrate stage at a defined speed, combined with the precise focusing of the laser beam, allows for the creation of intricate patterns with sub-micron dimensions.

We use S1813 positive photoresist which we spin coat on the substrate at 4000 rpm followed by baking at 110 0C for 1 min. The as-prepared substrate is loaded onto MICROTECH LW405 laser direct writer which uses a 405 nm laser to expose the resist according to our design. The resist is then washed in MF319 developer for 1 min washing off the exposed photoresist. The patterned substrate is then washed in deionized water followed by blow drying to complete the lithography.

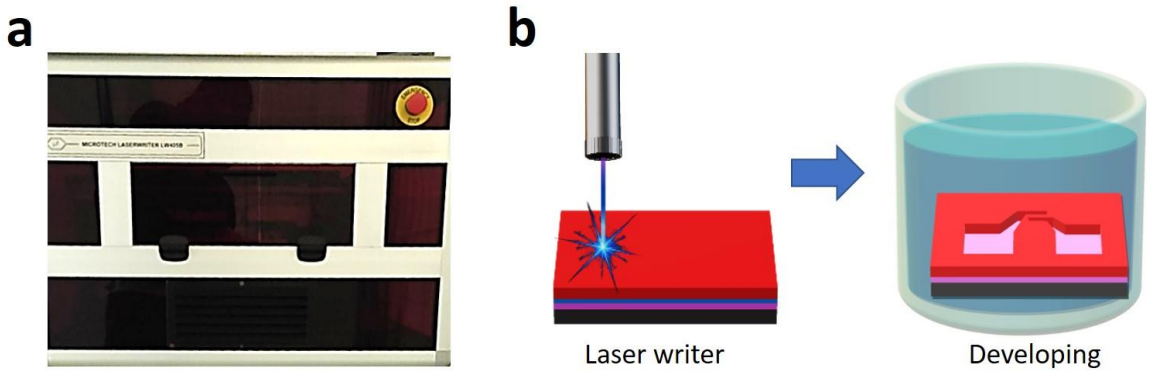


Figure 2.5: (a) Photograph of MICROTECH LW405 system used. (b) schematic of the lithography process.

### 2.3.2 Physical Vapor Deposition

Deposition techniques play a crucial role in device fabrication and thin film deposition for a wide range of applications. These techniques enable the controlled deposition of materials onto substrates, allowing the formation of thin films with desired properties and structures. Coupled with lithographic techniques you can create active devices from the nanoscale to the macro scale. Among the various deposition methods available, thermal vapor deposition (TVD) and magnetron sputter deposition (MSD) are widely used.

TVD offers precise control over film thickness and composition. One of the major advantages of TVD is its ability to deposit a wide range of materials, including metals, organic compounds, and inorganic compounds with low vaporization temperatures.[31] This method involves the evaporation of a solid material by heating it to its vaporization temperature, causing the atoms or molecules to enter the gas phase. The vaporized material then condenses onto a substrate, forming a thin film with desired properties.

TVD is typically performed under a vacuum to minimize the presence of impurities and ensure a controlled deposition environment. The vacuum environment eliminates the interference of air or other gases, which can affect film quality and purity.

Another advantage of TVD is its inherent directionality. When the vaporized material travels from the source to the substrate, it tends to move in straight lines due to its high kinetic energy. This directional motion allows for the deposition of thin films with good adhesion and uniformity. However, it also introduces a phenomenon known as the "shadow effect". This

occurs when the substrate is partially shielded by features on its surface, leading to variations in film thickness and potential gaps in coverage. One common approach is to rotate the substrate or the deposition source during the process, ensuring more uniform coverage and minimizing the impact of shadowing. Additionally, the use of multiple deposition sources or a collimated vapor source can enhance deposition uniformity.

The high purity and control over film thickness make TVD suitable for many applications, including semiconductor manufacturing, optical coatings, protective layers, and electronic device fabrication. It offers advantages in terms of cost-effectiveness, scalability, and compatibility with different substrates. By adjusting the deposition parameters such as temperature, pressure, and deposition rate, precise control over the film thickness can be achieved. This versatility allows for the deposition of diverse materials, enabling the fabrication of functional films for various applications.

In this thesis, we use a high current source to heat ceramic-coated Tungsten boats to evaporate materials of interest in a vacuum chamber. A quartz sensor is connected with a feedback loop that interfaces with a PID controller. This configuration allows us to set and maintain the desired deposition rate according to our specific requirements

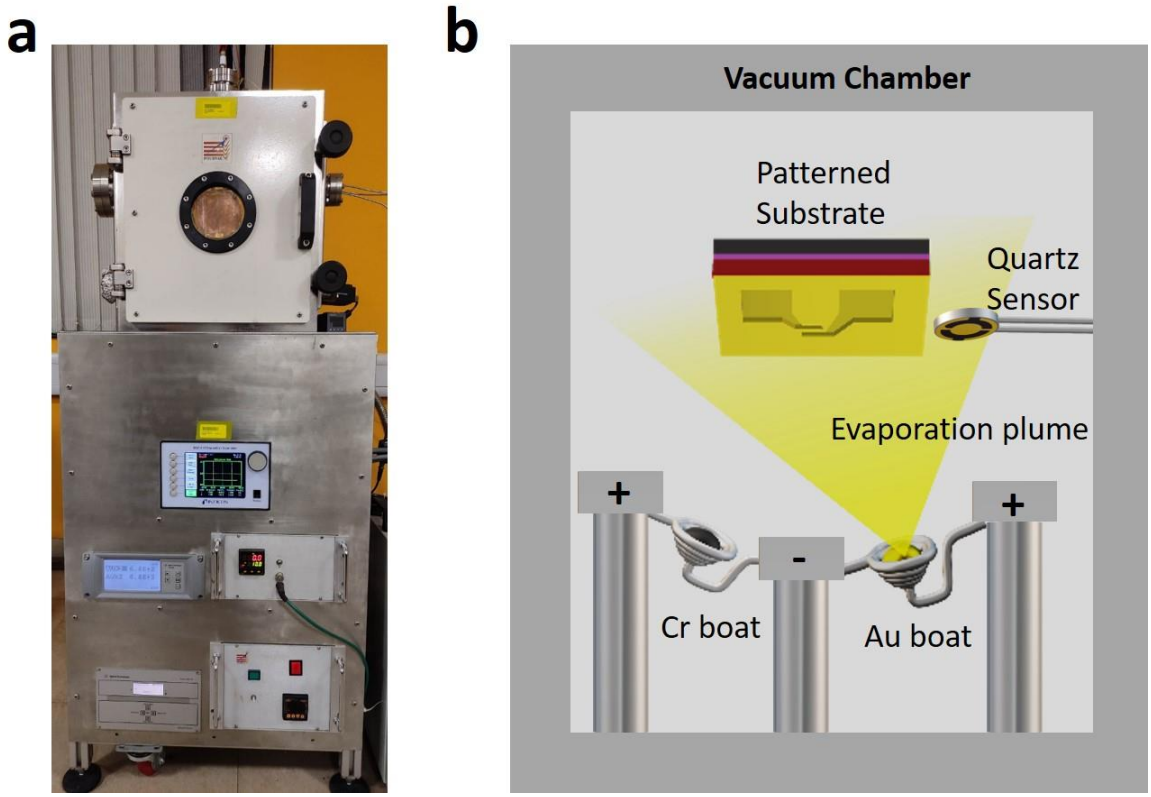


Figure 2.6: (a) Thermal vapor deposition setup we used. (b) a schematic of TVD setup in operation.

Magnetron sputtering has gained significant traction in industrial applications, particularly in the fields of semiconductor manufacturing, and vacuum deposition. As a highly versatile and continuously evolving technology, magnetron sputtering offers numerous advantages over other sputtering techniques. These advantages include the ability to deposit any material by sputtering them using a plasma.[32,33]

In the experiments discussed in this thesis we have used DC and RF sputtering techniques to deposit hard-to-evaporate materials like Indium doped Tin Oxide (ITO), $Si_3N_4$, Platinum etc. We used the Moorfield minilab magnetron sputter coating system for this. A picture of the setup is given in Fig. 2.7. DC sputtering was used to sputter metals and RF sputtering was primarly used to sputter non-metals like ITO and $Si_3N_4$. The sputter system also uses a Quartz crystal for monitoring and a PID controller to controlling the deposition rate.

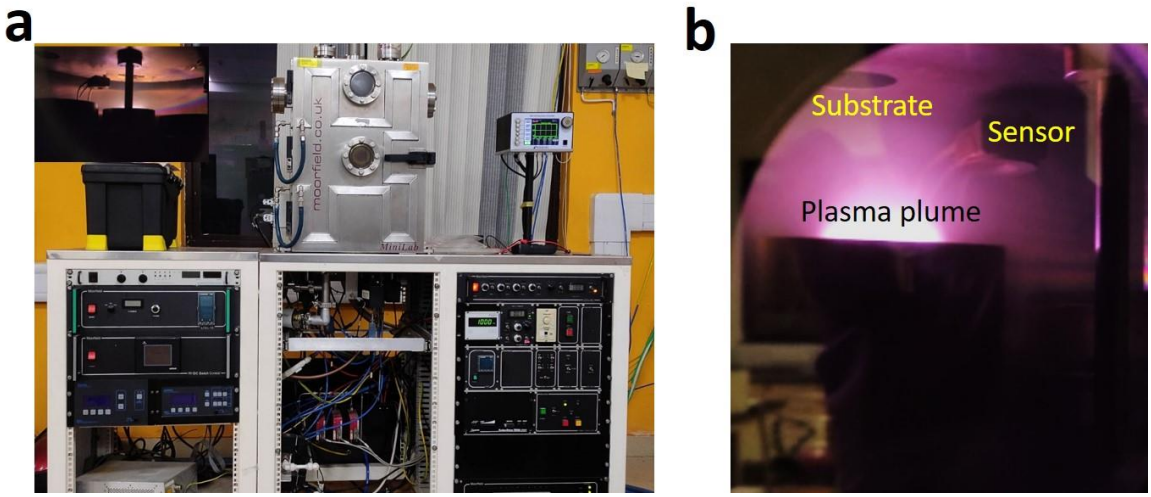


Figure 2.7: (a) Photograph of Moorfield MINILAB magnetron sputter coating system used. (b) a photograph of the sputtering in operation.

### 2.3.3 Wire Bonding

Wire bonding is a widely employed reliable packaging technology in the semiconductor and microelectronics industries.[34–36] It plays a crucial role in connecting integrated circuit (IC) chips to power sources and facilitating signal distribution among IC chips and microelectronic devices.

In this thesis, wire bonding is employed as a crucial technique to establish electrical connections between our micro devices, which are fabricated using lithography and deposition techniques, to a Printed Circuit Board (PCB). These PCBs facilitate the mounting of the samples on holders for low temperature measurements. The use of Au-Au bonding ensures excellent contact between the devices and the boards.

For our wire bonding processes, we utilize ultrasonic bonding, which harnesses ultrasonic energy to enable the cold-welding of metals. This technique ensures reliable and robust wire bonding. Notably, the bonding temperature is maintained at relatively low levels, typically between 60-100 °C, thanks to the utilization of ultrasonic bonding. Fig. 2.8a depicts a photograph of the Hybond model 626 wire bonder that was utilized in our study. Additionally, Fig. 2.8b, c, and d showcase photographs of the wire bonder needle, a device with bonded Au wires, and a micro device connected to the PCB using the Au wire bonding technique, respectively. Fig. 2.8e depicts the schematic of a typical wire bonding process.

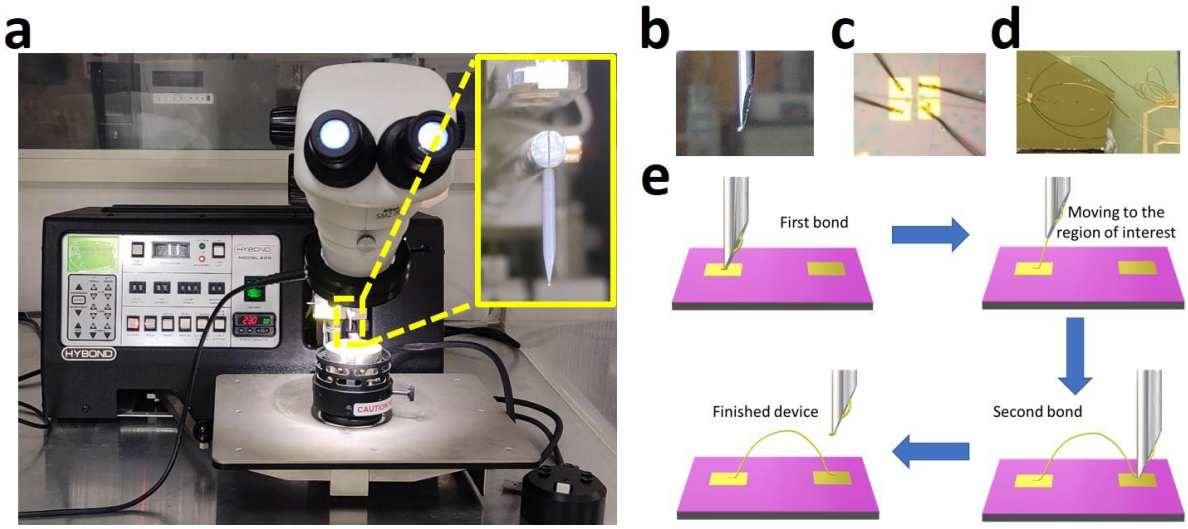


Figure 2.8: (a) photograph of the Hybond model 626 wire bonder. (b) photograph of the wire bonder needle with Au wire sticking out of its tip. (c) A microdevice with the Au pads connected with the Au wires. (d) A photograph of a microdevice connected to a PCB. (e) A schematic showing the wire bonding process

## 2.4 Summary

The chapter focuses on the characterization techniques and device fabrication methods employed in the research work related to TMDs and perovskites. Various characterization techniques, including XPS, XRD, PL, Raman Spectroscopy, SHG, FESEM, and HRTEM, are discussed. The chapter also covers the fabrication techniques employed for device fabrication, including photolithography, TVD, sputtering, and wire bonding. Photolithography is a crucial technique for creating patterns and defining the device's geometry. TVD and sputtering are used for depositing thin films to fabricate functional devices. Wire bonding is a crucial step in connecting fabricated devices to external components, ensuring proper electrical connections and functionality. The chapter highlights the importance of these characterization techniques and fabrication methods in investigating the properties of TMDs and perovskites.

**Bibliography**

[1] Apelian D 2012 Materials science and engineering's pivotal role in sustainable development for the 21st century *MRS Bull.* **37** 318–23

[2] Wood J 2008 The top ten advances in materials science *Mater. Today* **11** 40–5

[3] Ciarrocchi A, Tagarelli F, Avsar A and Kis A 2022 Excitonic devices with van der Waals heterostructures: valleytronics meets twistronics *Nat. Rev. Mater.* **7** 449–64

[4] Stein H S and Gregoire J M 2019 Progress and prospects for accelerating materials science with automated and autonomous workflows *Chem. Sci.* **10** 9640–9

[5] Bisri S Z, Piliego C, Gao J and Loi M A 2014 Outlook and Emerging Semiconducting Materials for Ambipolar Transistors *Adv. Mater.* **26** 1176–99

[6] Ouyang Y, Zhang Z, Li D, Chen J and Zhang G 2019 Emerging Theory, Materials, and Screening Methods: New Opportunities for Promoting Thermoelectric Performance *Ann. Phys.* **531** 1800437

[7] Glavin N R, Rao R, Varshney V, Bianco E, Apte A, Roy A, Ringe E and Ajayan P M 2020 Emerging Applications of Elemental 2D Materials *Adv. Mater.* **32** 1904302

[8] Wei S, Liao X, Wang C, Li J, Zhang H, Zeng Y-J, Linghu J, Jin H and Wei Y 2021 Emerging intrinsic magnetism in two-dimensional materials: theory and applications *2D Mater.* **8** 012005

[9] Bragg W L 2014 The Diffraction of X-rays by Crystals *Zeitschrift für Phys. Chemie* **228** 957–68

[10] B.D.Cullity 1978 *Elements of X-Ray Diffraction* (Addison-Wesley Longman, Inc.)

[11] Waseda Y, Matsubara E and Shinoda K 2011 *X-Ray Diffraction Crystallography* (Berlin, Heidelberg: Springer Berlin Heidelberg)

[12] Stevie F A and Donley C L 2020 Introduction to x-ray photoelectron spectroscopy *J. Vac. Sci. Technol. A* **38** 063204

[13] RAMAN C V. and KRISHNAN K S 1928 A New Type of Secondary Radiation *Nature* **121** 501–2

[14] Valeur B and Berberan-Santos M N 2011 A Brief History of Fluorescence and Phosphorescence before the Emergence of Quantum Theory *J. Chem. Educ.* **88** 731–8

[15] Franken P A, Hill A E, Peters C W and Weinreich G 1961 Generation of Optical Harmonics *Phys. Rev. Lett.* **7** 118–9

[16] Boyd R W, Gaeta A L and Giese E 2023 Nonlinear Optics pp 1097–110

[17] Vaquero D, Clericò V, Salvador-Sánchez J, Martín-Ramos A, Díaz E, Domínguez-Adame F, Meziani Y M, Diez E and Quereda J 2020 Excitons, trions and Rydberg states in monolayer

MoS2 revealed by low-temperature photocurrent spectroscopy *Commun. Phys.* **3** 194

[18] Velický M, Rodriguez A, Bouša M, Krayev A V., Vondráček M, Honolka J, Ahmadi M, Donnelly G E, Huang F, Abrunã H D, Novoselov K S and Frank O 2020 Strain and Charge Doping Fingerprints of the Strong Interaction between Monolayer MoS2and Gold *J. Phys. Chem. Lett.* **11** 6112–8

[19] Binnig G, Quate C F and Gerber C 1986 Atomic Force Microscope ed R Splinter *Phys. Rev. Lett.* **56** 930–3

[20] Huey B D, Ramanujan C, Bobji M, Blendell J, White G, Szoszkiewicz R and Kulik A 2004 The Importance of Distributed Loading and Cantilever Angle in Piezo-Force Microscopy *J. Electroceramics* **13** 287–91

[21] Melitz W, Shen J, Kummel A C and Lee S 2011 Kelvin probe force microscopy and its application *Surf. Sci. Rep.* **66** 1–27

[22] Alexeev A, Loos J and Koetse M M 2006 Nanoscale electrical characterization of semiconducting polymer blends by conductive atomic force microscopy (C-AFM) *Ultramicroscopy* **106** 191–9

[23] Raşa M, Kuipers B W M and Philipse A P 2002 Atomic Force Microscopy and Magnetic Force Microscopy Study of Model Colloids *J. Colloid Interface Sci.* **250** 303–15

[24] Ghosh T, Samanta M, Vasdev A, Dolui K, Ghatak J, Das T, Sheet G and Biswas K 2019 Ultrathin Free-Standing Nanosheets of Bi 2 O 2 Se: Room Temperature Ferroelectricity in Self-Assembled Charged Layered Heterostructure *Nano Lett.* **19** 5703–9

[25] Egerton R F 2005 *Physical Principles of Electron Microscopy* (Boston, MA: Springer US)

[26] Lambert L and Mulvey T 1996 Ernst Ruska (1906–1988), Designer Extraordinaire of the Electron Microscope: A Memoir *Advances in Imaging and Electron Physics* vol 95 pp 2–62

[27] Humphreys F J 2001 Grain and subgrain characterisation by electron backscatter diffraction *J. Mater. Sci.* **36** 3833–54

[28] Seiler H 1983 Secondary electron emission in the scanning electron microscope *J. Appl. Phys.* **54** R1–18

[29] Leuschner R and Pawlowski G 2000 Photolithography *Handbook of Semiconductor Technology* (Weinheim, Germany: Wiley-VCH Verlag GmbH) pp 177–263

[30] Srikanth S, Dudala S, Raut S, Dubey S K, Ishii I, Javed A and Goel S 2020 Optimization and

characterization of direct UV laser writing system for microscale applications *J. Micromechanics Microengineering* **30** 095003

[31] Wasa K, Kitabatake M and Adachi H 2004 Thin Film Processes *Thin Film Materials Technology* (Elsevier) pp 17–69

[32] Xiang Y, Chengbiao W, Yang L, Deyang Y and Tingyan X 2006 Recent Developments in Magnetron Sputtering *Plasma Sci. Technol.* **8** 337–43

[33] Kelly P . and Arnell R . 2000 Magnetron sputtering: a review of recent developments and applications *Vacuum* **56** 159–72

[34] Zulkifli M N, Abdullah S, Othman N K and Jalar A 2012 Some thoughts on bondability and strength of gold wire bonding *Gold Bull.* **45** 115–25

[35] Harman G and Albers J 1977 The Ultrasonic Welding Mechanism as Applied to Aluminum- and Gold-Wire Bonding in Microelectronics *IEEE Trans. Parts, Hybrids, Packag.* **13** 406–12

[36] Neppiras E A 1965 Ultrasonic welding of metals *Ultrasonics* **3** 128–35

# Chapter 3

# Instrumentation

This chapter discusses some of the experimental and characterization techniques built by us, that are used for material characterization and device fabrication in this thesis.

## 3.1 Introduction

Setting up an experimental lab is an uphill battle, requiring proposal writing, fund securing, and equipment procurement. However, even after a sufficient budget, equipment procurement could put the researcher in a dilemma. As an experimental researcher, one might often have to use multiple instruments. It's often challenging to acquire all the necessary instruments, especially some seemingly small yet crucial equipment that can greatly impact experimental outcomes. These seemingly simple tools have the potential to enhance repeatability and streamline experiments.

To overcome these limitations, and to procure most of what one needs to set up their dream lab, one cost-effective approach is to build the instruments yourself, expanding your collection at a fraction of the cost of ready-made setups. This do-it-yourself approach offers the added advantage of tailoring the instruments to your specific needs and the freedom to tinker and modify them as desired. While building instruments component by component can be time-consuming and meticulous, it remains a more accessible and economical alternative to purchasing the setups directly from a company.

However, in some cases, it is easier to purchase ready-made largely available components and assemble them to setup the instruments. This method allows researchers to start their investigations sooner, as the assembly and interfacing of components are relatively faster and easier. Additionally, custom-designing parts or setups becomes feasible when specific requirements or unavailable parts are encountered. With the availability of modern workshops equipped with CNC machines, this customization process has become more accessible than ever before. In this chapter, we delve into the instruments we have set up in our lab, aiming to

maximize the value of our funding and broaden our experimental capabilities. Through a combination of resourcefulness, DIY spirit, and strategic use of funding, we have established a cost-effective and efficient laboratory setup that made our research endeavours much smoother.

## 3.2 Setting up Instruments from Scratch

During our research, we set up a lot of instruments from the ground up. Although we procured many components, there were instances where we took matters into our own hands, machining certain parts ourselves. Additionally, there were occasions when we relied on the expertise of professionals to construct custom parts tailored to our specific requirements. In this section, we delve into the process of assembling instruments by integrating various components, resulting in the creation of functional instruments that embody our unique instrumentation concepts and ideas.

### 3.2.1 Powell lens

Powell lens is a great optical component that could fan out the laser spot into a one-dimensional laser line with a uniform distribution of intensity.[1] Powell lens is a much better approach than using a cylindrical lens that would give a Gaussian beam with intensity falling rapidly toward the edges.[2][3]

In order to transform the parallel Gaussian laser beam into a laser line with consistent intensity, Powell introduced a lens component that consists of two surfaces, a primary, and two or more secondary surfaces. The primary surface is shaped like a linear conic with a short radius and a relatively high conic constant.[4] The conic surface can be described mathematically by the following two-dimensional equation:

$$y = \frac{cx^2}{1 + \sqrt{1 - (1 + Q)c^2y^2}}$$

Where $c$ is the radius of curvature and $Q$ is the conic constant of the surface. By varying the radius of curvature and theconic constant we can control the angular divergence of the lens.

We designed and built our Powell lens from a 1 cm diameter Quartz rod. We cut the road using a diamond-coated saw blade to create the basic shape as shown in Fig. 3.1a. Then the structure

was sanded down with waterproof sandpapers all the way from 80 grit to 3000 grit. The final polishing was done using cerium oxide and the resulting Powell lenses are shown in Fig. 3.1b. Our Powell lens was able to distribute the intensity much more evenly, as compared to a cylindrical lens, as can be seen in Fig. 3.1d. The slight haziness of the beam at some parts along the line suggests that the surface needs a bit more smoothening. But overall performance was still better than a cylindrical lens as the entire length of the laser has sufficient intensity for laser annealing in a controlled manner over a large area. This can be achieved by combining it with an appropriate laser.

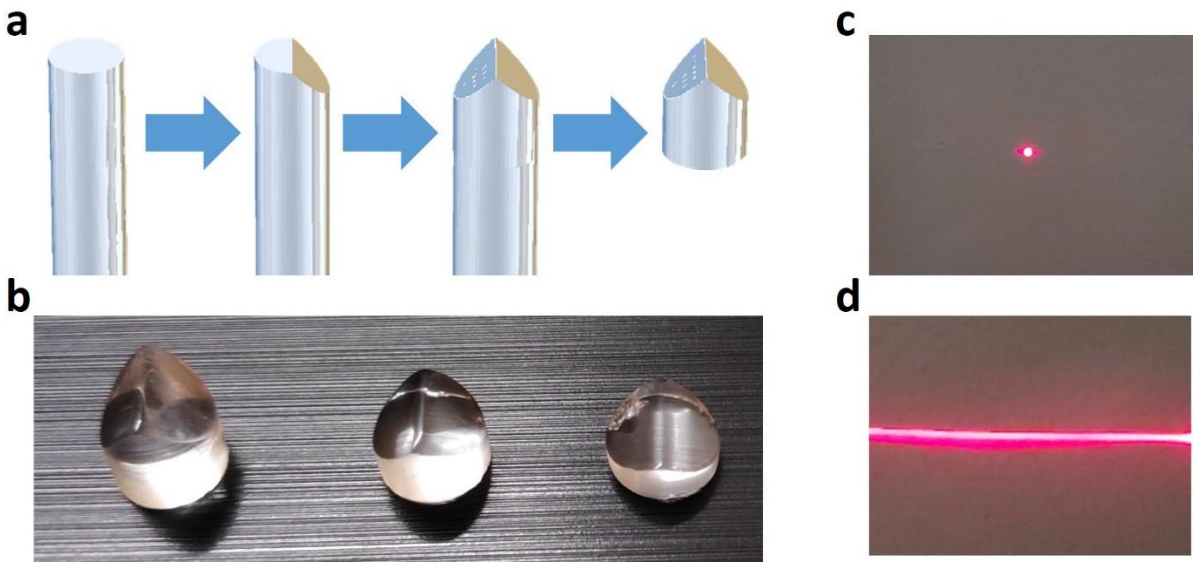


Figure 3.1: (a) Schematic illustration of the process for converting a quartz tube into a basic shape of Powell lens by cutting. (b) Photograph showcasing a collection of Powell lenses fabricated by cutting after polishing. (c) Projection of a laser spot from a diode laser onto a distant wall. (d) Altered laser spot resulting from the passage of laser light through the Powell lens.

### 3.2.2 Plasma cleaner

Plasma is a very effective tool for growing crystals, as well as modifying and cleaning surfaces. [5][6][7] Microwaves generated by a magnetron have been used to create plasma before.[5] Thus people have used a kitchen microwave oven to make a plasma source. [7][8] The fundamental process for creating a plasma with microwaves lies in the fact that, during high-frequency gas discharge breakdown, the primary gas ionization resulting from the motion of electrons is the sole production mechanism that governs the breakdown.[9] The discharge

breakdown occurs when the gain in electron density due to the ionization of the gas becomes greater than or equal to the loss of electrons by diffusion, attachment to neutral molecules, and recombination. Adding metal strips or mesh can help in the initial generation of electrons through discharge.[10] Microwave radiation provides the field needed for the acceleration of electrons. These accelerated electrons subsequently collide with gas molecules, leading to ionization when they possess sufficient energy to generate additional electrons and ions, thereby leading to the formation of plasma. The gas pressure plays as a critical factor in this process. If the pressure is excessively high, the frequency of average collisions increases and this may hinder the electrons from attaining sufficient energy for a given power level of radiation. Conversely, when the pressure is too low, the lack of collisions becomes a limiting factor, thereby impeding the formation of the plasma state due to the insufficient availability of gas molecules required for the continuous generation of new electrons and ions.[11] Thus the Pressure of the gas and the power of the radiation play important roles in the generation of microwave plasma.

In this section, we discuss the method we used to convert a microwave oven into a plasma cleaner. We commissioned the construction of a flat stainless steel plate with two stainless steel pipes, one for vacuum and one for gas flow, attached to one side of the SS plate. The microwave oven's bottom plate and motor were removed and a through hole was cut open for the easy accessibility of the gas inlet and vacuum port (see Fig. 3.2). The top surface of the SS plate is smooth, with no sharp edges. The gas inlet and vacuum attachments are located on the lower side and pass through the bottom hole of the microwave.

To elevate the plasma cleaning platform and facilitate gas flow and pumping, we placed a metal mesh stand above the gas inlet and vacuum ports. This metal mesh stand also aids in generating plasma by facilitating electron discharge. An O-ring larger than the stand is placed in the SS plate while ensuring the vacuum and gas inlets are within the O-ring's confines.

To create a sealed glass chamber, we placed a microwave-safe glass bowl with the same outer diameter as the O-ring on top. The rim of the bowl makes contact with the O-ring to establish a seal. The vacuum port is connected to a T-connect, with one end attached to a Pirani gauge for pressure monitoring. The other end of the T-connect is connected to a bellows sealed SS angle valve linked to the pump. By opening the valve, the pressure in the glass bowl decreases,

and the external atmospheric pressure helps seal the glass chamber tight. Once the pressure drops below 0.01 mbar, the desired gas is introduced into the chamber using a needle valve attached to the 6mm SS gas inlet tube, increasing the pressure to a range of 0.3 mbar to 0.1 mbar. It is advisable to wait for approximately 10 minutes to ensure that the chamber is filled majorly with the desired gas. After closing the microwave oven, we turn on the microwave to create plasma within the glass chamber. The plasma can be extinguished by turning off the microwave supply.

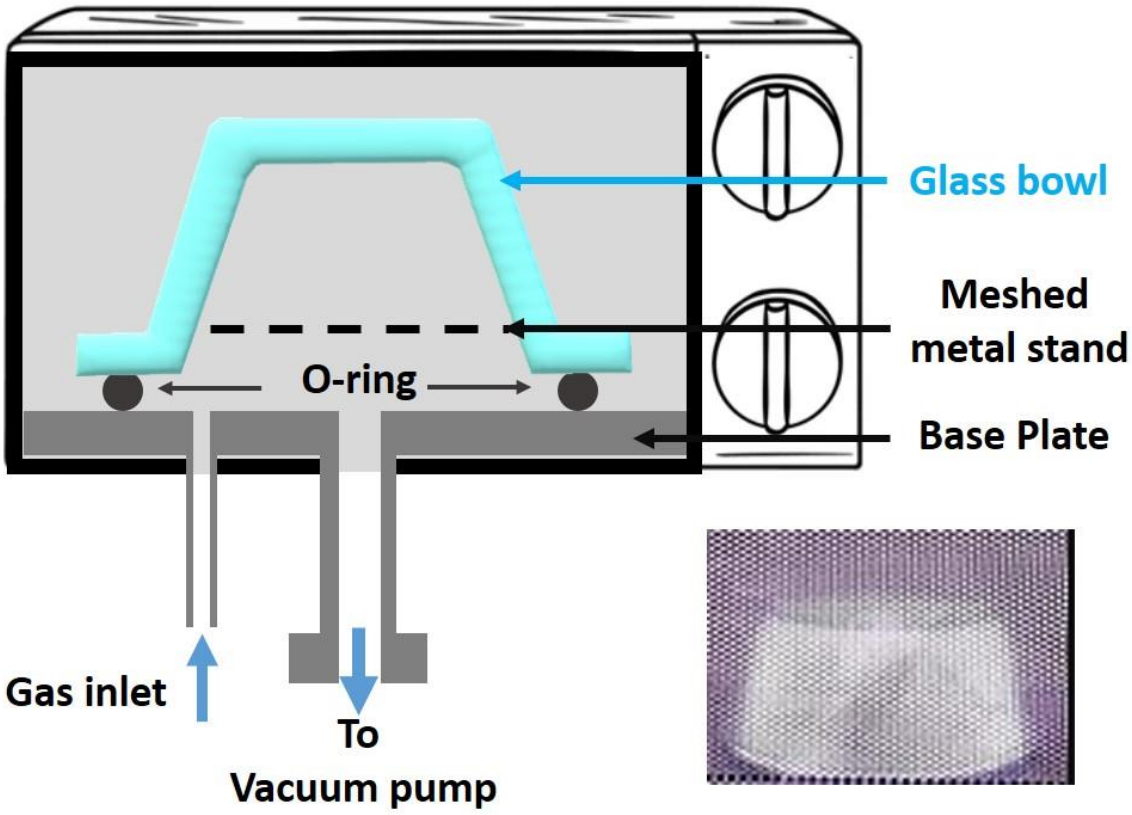


Figure 3.2: Schematic showing the Plasma cleaner made by modifying a microwave oven. The inset in the lower right-hand side provides a close-up view of the plasma generation occurring within the glass chamber of the microwave oven.

This setup is particularly useful when precise power control is not required. If necessary, metal grids can be placed near the waveguide path to reduce power. However, in our case, we primarily used the plasma asher to clean organic materials from substrate surfaces and enhance substrate wettability. Thus we did not opt to add a power-reducing arrangement.

### 3.2.3 UV lamp and intensity measurement system

In this section, we delve into the assembly and implementation of two systems: a UV curing setup and a handheld intensity measurement system. The UV setup comprises several components, including a power supply, a programmable timer relay, and a UV 365 LED with a 3W power output. The LED is attached to a heat sink, which is equipped with a focusing mirror. To ensure proper enclosure, all these components are housed within a metallic structure. Additionally, we employ a cylindrical flask lined with aluminium tape on its inner surface to effectively block the 365 nm light. The primary applications of this system involve exposing SU8 and other photoresists using a physical mask for lithography, as well as crosslinking specific polymers that respond to 365 nm wavelengths.

To optimise the intensity of the emitted light for these processes, we developed an intensity measurement system utilising the OPT101 sensor from Texas Instruments. This sensor has a detection range spanning from 300 nm to 1100 nm. The sensor was soldered onto a printed circuit board (PCB) according to the connection scheme depicted in Figure 21 of the sensor's datasheet. A 9V rechargeable battery serves as the power source and is connected through a toggle switch. The toggle switch allows for three distinct states: the first state enables light intensity measurement by connecting the detector to a BNC connector and also connecting the battery to the detector. The second state disconnects both the battery and detector from the system's BNC port, while the third state directly connects the BNC to the battery, primarily for charging purposes.

The entire intensity measurement system is housed in a compact aluminium box that features a quartz window mounted on a 3D-printed holder. Fig. 3.3 provides photographs of both the UV curing setup and the light intensity measurement setup. The approach of utilising the output voltage and time to determine the dosage simplifies the usage of arbitrary sources, such as halogen lamps used in our projection lithography set up, where the entire spectrum is being measured. For precise intensity measurement, we employ a Thorlabs PM 100A power meter with a PM120VA sensor.

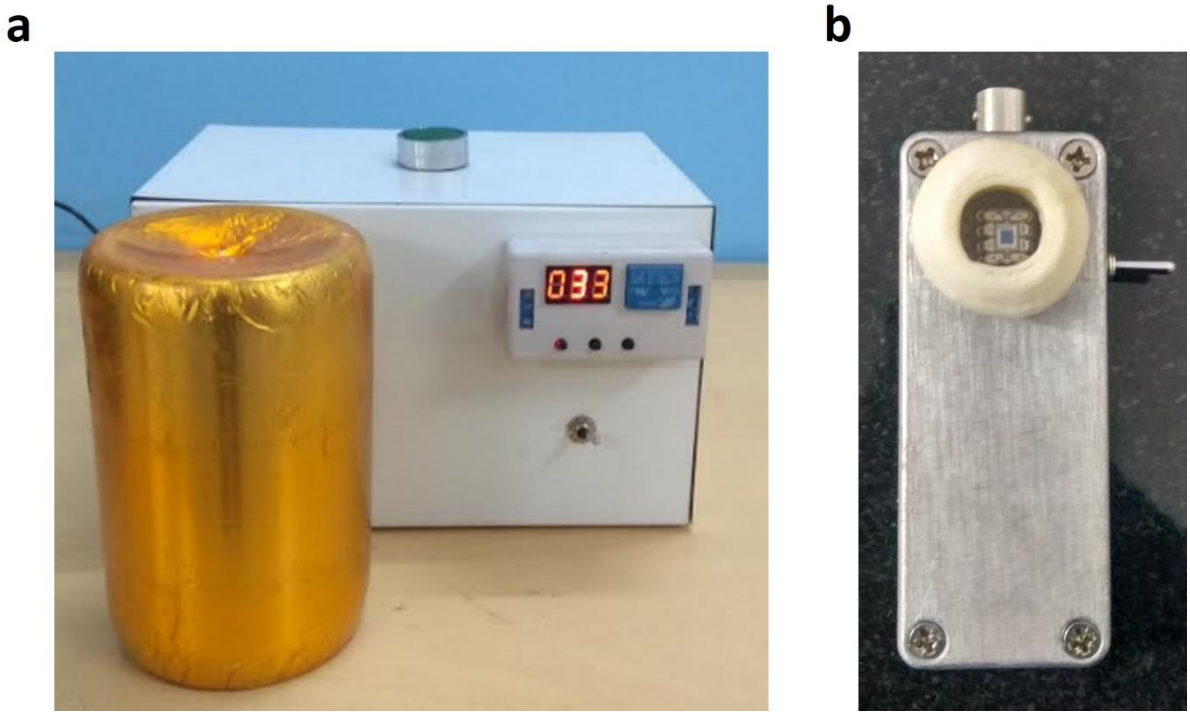


Figure 3.3: (a) Photograph of the UV lamp. (b) the photograph of the handheld light intensity measurement unit

### 3.2.4 Transient photocurrent/voltage measurement system

Transient photocurrent/voltage measurement provides valuable insights into the dynamics of charge carriers generated by incident photons and their recombination processes. By measuring the current/voltage response as a function of time, following light excitation, transient photocurrent measurements are great techniques to grasp the fundamental properties and performance of various optoelectronic systems, including solar cells, photodetectors, photodiodes, and other light-sensitive devices.[12][13] The decay and rise of the photocurrent as a function of time give valuable information on carrier lifetimes and charge extraction efficiencies.

The image of our custom-built Setup is depicted in Fig. 3.4a, with the three inset images at the top showing the operation of the setup using 3 distinct wavelengths. The LED holder was specifically designed to accommodate three different wavelengths of LEDs. In order to cover most of the visible range, one can choose 405 nm, 535 nm, and 660 nm. The holder features a one-inch through hole, surrounded by a total of nine LEDs. These LEDs are arranged in groups

of three for each wavelength, with an angular spacing of 120 degrees between LEDs of the same wavelength, as depicted in Figure 3.4b. To facilitate easy operation, the LEDs are connected to a BNC output connector via toggle switches. Each wavelength has its own set of toggle switches for independent control. The LEDs are securely connected to the holder using female socket wires, allowing for easy replacement when necessary. The inclination of the LEDs is carefully adjusted to ensure that when illuminated, they form a uniformly lit one-inch diameter circle at a distance of 5 cm from the holder. Furthermore, the LED holder can be raised or lowered using a screw arrangement, providing flexibility in positioning.

For testing the devices, a fixed sample holder is utilized, which features phosphor bronze slide-in connectors. These connectors establish a reliable connection with the sample under test. The connections from the phosphor bronze connectors are conveniently taken out using BNC connectors, enabling straightforward integration with measurement equipment. The entire arrangement is placed in an Aluminum box with an optical quartz window at the top.

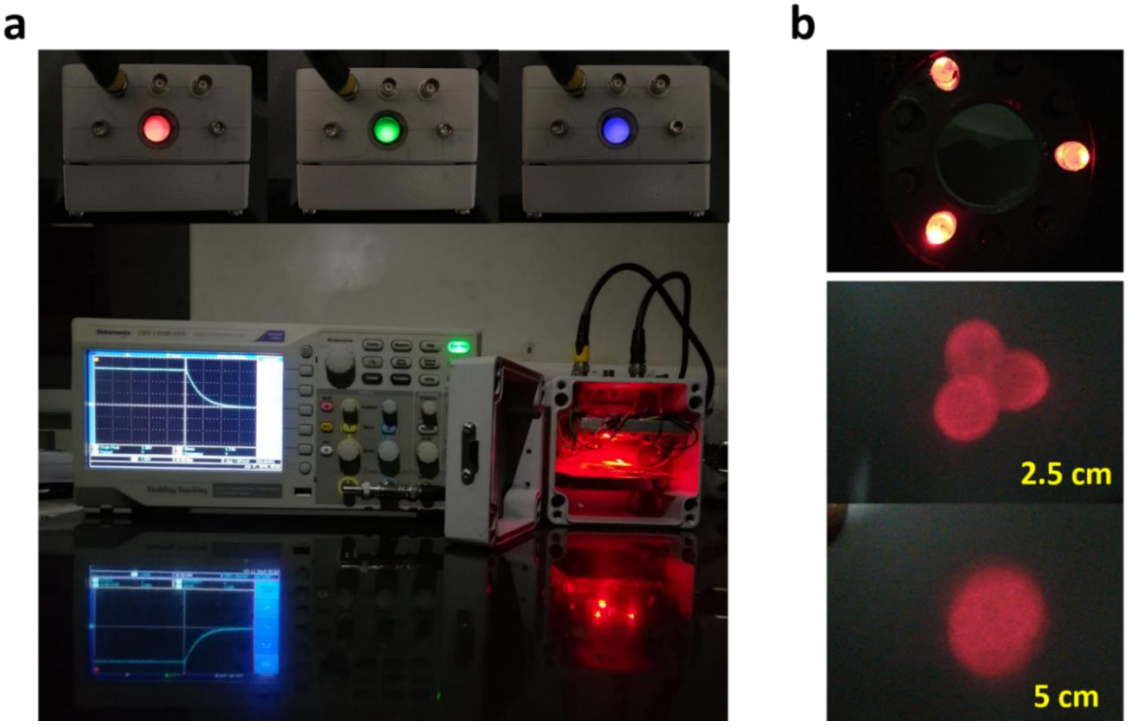


Figure 3.4: (a) Schematic of the setup for measuring the decay curve of a silicon solar cell. The top portion of the figure showcases the system with different LEDs activated. (b) Photographs demonstrating the illumination profiles produced by the three LEDs. The first image is the image of the holder with 660 nm turned on. The second and third images depict the focused light on the surface of a paper positioned at different distances. At a distance of approximately 5 cm, the light uniformly illuminates the paper, creating a circular region with a diameter of 1 inch.

### 3.2.5 Environment control box

This section aims to present a box design for environmental testing, specifically targeting the evaluation of electronic devices and materials in the presence of various gases, temperature, 254 nm light, and ozone. Such a chamber has many applications in the testing of electronic devices and materials.[14][15] Since elevated conditions of moisture, temperature, and/or UV can all accelerate the ageing of devices, the system's capabilities extend beyond material testing and encompass accelerated ageing tests as well.[16][17] The chamber offers a practical, cost-effective, and efficient approach to evaluating device performance and reliability in diverse environmental conditions.

The box is constructed using Aluminum material and features an O-ring positioned along the rim to create an airtight seal when the box is closed. Inside the box, an Aluminum block is placed on top of an SS Platform, which is attached to the walls of the box. The purpose of this floating SS platform is to minimise heat loss from the Aluminum block, which can be heated using two cartridge heaters embedded within it. To measure the temperature of the block, a k-type thermocouple is used. The connections for the heater and temperature sensor are taken out of the box using BNC connectors.

Adjacent to the Aluminum block, a Slide-in PCB holder is installed to ensure proper contact between the PCB and the block while maintaining isolation. The PCB holder accommodates ten connections from the PCB, and an additional four connections from an IC mount are available for a humidity sensor. To protect all the connections, individual Teflon protective tubing is utilized, ensuring their durability and resilience in harsh conditions. The ends of the protective tubes are secured with a generous amount of silicone sealant.

Positioned 3cm above the Aluminum block, a 254 nm UV lamp is mounted and powered by an AC source connected in series with a toggle switch and a capacitor. The capacitor serves to minimize the overall voltage drop across the bulb while the switch controls the lamp's activation. Two 6 mm push-fit connectors are integrated into the box at two opposite ends, serving as gas inlet and outlet. The 254 nm light emitted by the lamp can generate ozone when exposed to oxygen. As a result, atmospheric air, oxygen mixtures, or pure oxygen can be used to produce ozone within the system.

To ensure a leak-proof setup, the entire box undergoes pressurisation and is checked for any

potential leaks. Any detected leakages are permanently sealed using araldite adhesive. For clarity, a schematic of the box without the connecting wires and capacitor is depicted in Fig. 3.5a and b, while a photograph of the box is presented in Fig. 3.5c.

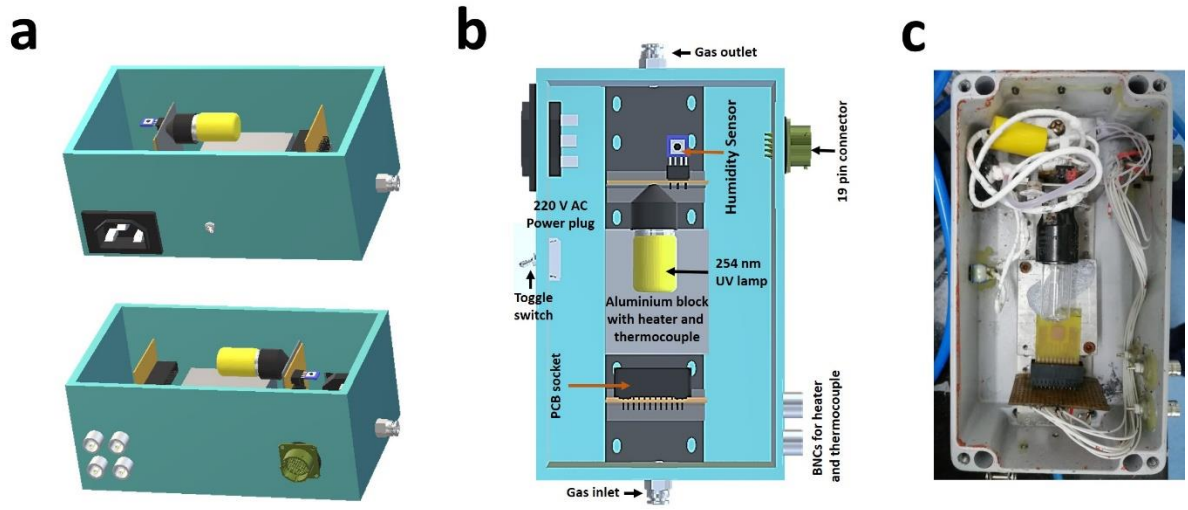


Figure 3.5: (a) and (b) are the schematic diagram of the box layout showing the components and connections (excluding wires and capacitor for better clarity). (c) Photograph of the constructed box showcasing the overall design and appearance

### 3.2.6 Noise spectroscopy

Noise spectroscopy, particularly the study of 1/f noise, provides valuable insights into the characteristics and behaviour of physical systems. Intrinsic electronic noise, including 1/f noise, arises from various sources which can be intrinsic or extrinsic to the system of interest. Understanding its origins and properties is crucial for minimising its impact and harnessing its potential applications. 1/f noise is a universal phenomenon observed in many systems, characterised by a frequency spectral density inversely proportional to frequency. By analyzing 1/f noise and its relationship to charge carrier number fluctuation, mobility fluctuation, defect migration or similar effects, valuable information on the system such as defects, interface quality, material conditions, etc can be obtained. [18][19]

In this thesis, we have tried to look into defect migration using Noise spectroscopy. The understanding of 1/f noise is grounded in the notion that defects within a system influence the initial velocity of conduction electrons following lattice collisions, leading to the generation of 1/f noise. The migration of defects and their interaction with conduction electrons affect the

characteristics of 1/f noise.

To minimize external sources of noise, we employed a 9V battery connected to a potentiometer as our power source. This approach effectively eliminates the influence of external electrical noise, which would have been challenging to mitigate if a digital source was used to bias our device. The device, along with a low noise current preamplifier (SR 570), was connected in series, as illustrated in Figure 3.6a. The output of the SR 570 was connected to the NI BNC 21110 board via a BNC cable. Subsequently, a 192061-02 cable was employed to transfer the data to a data acquisition card, PCIe-6321, which was then connected to a computer. The data acquisition and transfer process was facilitated by LabVIEW. A schematic depicting the setup is provided in Figure 3.6b.

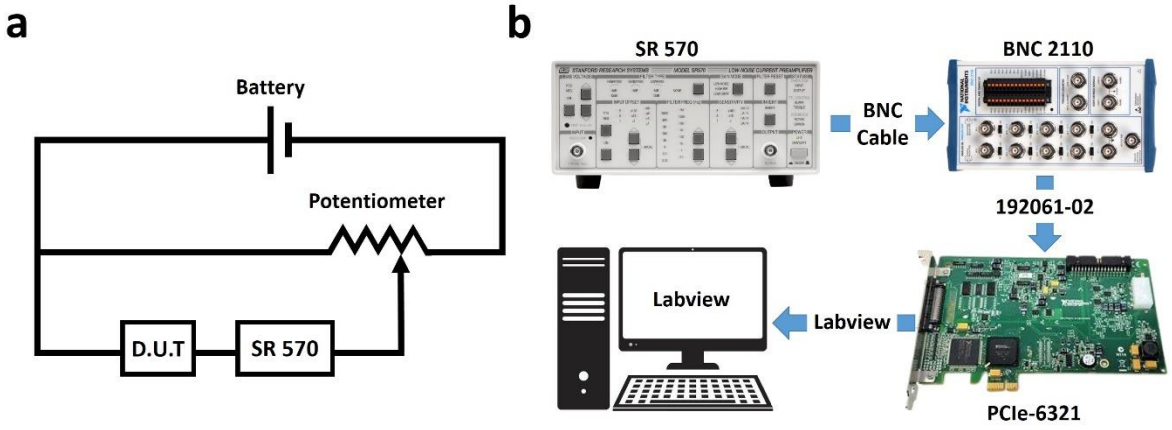


Figure 3.6: (a) Schematic diagram illustrating the setup for connecting the Device Under Test (D.U.T) with the voltage source and the low noise current preamplifier (SR 570). (b) Schematic diagram showcasing the connections from the SR 570 to the computer, including the intermediate connectors and Digital-to-Analog Converters (DACs) employed in the signal acquisition process.

### 3.2.7 Probe station

Probe stations are effective tools for establishing temporary connections on microscopic devices.[20][21] They utilise sharp tungsten tips attached to a Micropositioner, enabling the measurement of device properties. This method serves to assess individual device functionality and select specific devices for further measurements by wire-bonding them onto a PCB. A schematic of our custom-built probe station is given in Fig 3.7a. This setup has played a vital role in a vast majority of the electrical measurements done in our lab.

The probe station in our custom-built setup also has an Aluminum block mounted on an XYZ stage. This block was meticulously cut and drilled with holes to accommodate the insertion of thermocouples, heaters, and a small 1mm hole for vacuum at the centre of the block as depicted in Fig 3.7b. These components were mounted on the Aluminum block using a Teflon spacer. The small hole at the centre of the block allows the system to be connected to a vacuum pump, ensuring secure sample placement. The Teflon insulating block effectively isolated the Aluminum block from the XYZ stage, allowing our custom build probe station to measure temperatures ranging from room temperature up to 200 °C. It is important to note that Teflon begins to degrade above 250 °C, hence the temperature limitation. To control the heater, we utilised a UCT 421-P PID controller powered by a 24V DC source. As for the sensor, a K-type thermocouple was employed. While the near-room temperature readings were not highly accurate as the voltage developed is minimal for the Cromel-Alumel thermocouple.[22] But above 40 °C, the accuracy remained within 1 °C. We verified this by using a Pt 100 sensor. Directly connecting a Pt 100 can improve the accuracy near room temperature. However, since the heating measurements were primarily conducted above 40 °C, the compact K-type thermocouple proved to be sufficiently adequate.

For the Micropositioner, we utilized magnetic-based ones from Everbeing. The top plate of the probe station was made from a magnetic stainless steel plate, facilitating easy attachment of the Micropositioner. This design allowed us to effortlessly slide the manipulator to the desired position. The I-shaped pillars and the breadboard were constructed using non-magnetic stainless steel. The breadboard was specifically designed with holes for fixing M6-threaded stainless steel Allen screws, enabling the convenient addition of multiple components. The BNC output from the probe station was used to connect it to measuring systems of interest.

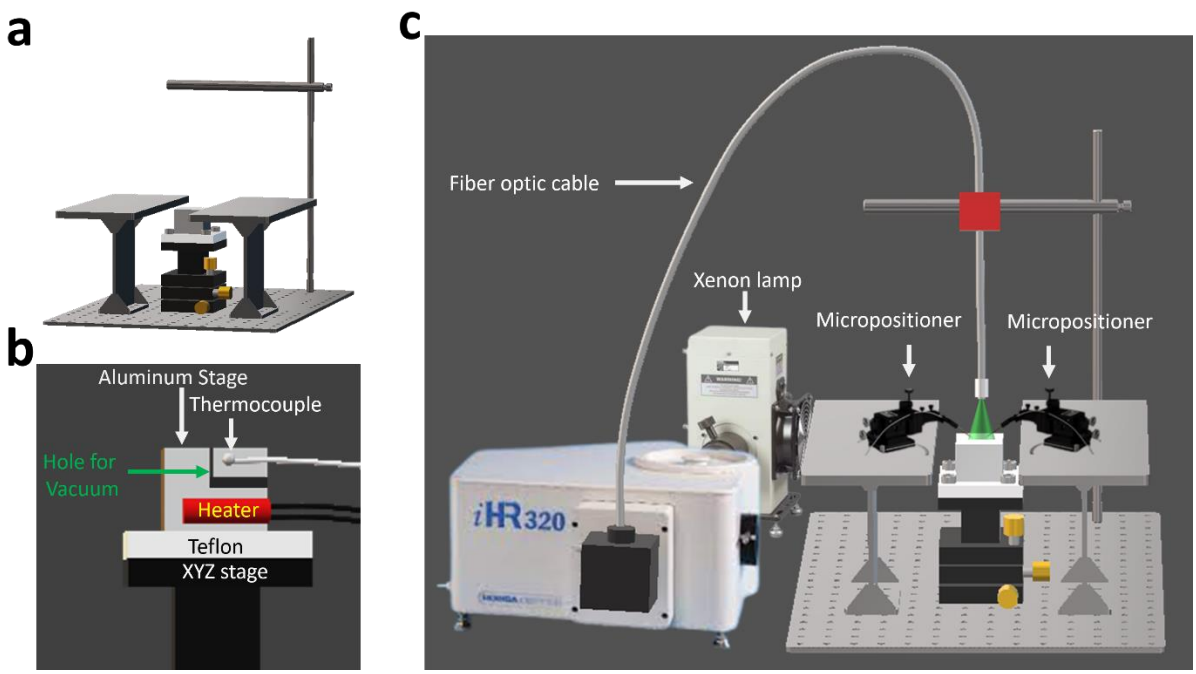


Figure 3.7: (a) Schematic representation of the custom-designed probe station featuring an XYZ stage, Teflon insulating block, and heater block. (b) Detailed cross-sectional view of the heater block, with the central hole for vacuum, a heater, and a thermocouple, secured to the XYZ stage using a Teflon spacer. (c) Implementation of the probe station in conjunction with a monochromator and xenon lamp for photocurrent measurements.

For performing optoelectric measurements such as responsivity, detectivity, and photocurrent measurements, it is important to use different wavelengths of known intensity. A continuous wavelength scan is important to comment on the bandgap of the material and to figure out the wavelength of light to which the device shows the best response. To achieve a continuous wavelength scan, we used a Xenon lamp as the light source and used a monochromator, which selects specific wavelengths by splitting the light using a grating, coupled with a fiber optic cable to direct light of the desired wavelength onto the D.U.T. A schematic of this setup is depicted in Fig. 3.7c.

To connect the probes to the microscopic device, we used a camera attached to a continuous zoom telescopic lens. An LED array around the bottom end of the telescope illuminates the entire device and the image is taken via the telescope and projected on the camera, which is connected to the computer allowing us to monitor the system in real-time. The telescopic arrangement provides ample working distance between the imaging system and the stage.

There is provision to move the telescopic lens in the vertical direction and the device is focused by moving the telescope up or down. The XYZ stage on which the device is mounted is moved to bring the device of interest to the centre of the camera image and the probes are moved towards the vicinity by sliding the Micropositioner by hand. Once in the vicinity of the device we move the probes towards the device of interest using the Micropositioners. The device is then zoomed to have better visual clarity and the probes are adjusted to the pads of interest and probes are lowered till contact is made with the device. The photograph of our Probe station with the camera and telescopic lens arrangement, without the fiber optic cable, is given in Fig. 3.8a. The inset shows 530 nm light coming from the optical fiber cable falling on a PCB with a large crystal connected using the probe station in the presence of light from the LEDs on the telescope. Fig. 3.8b shows the close-up image of the stage with the probes connected to a device and the optical fiber cable and an LED which are used for optical study in the vicinity of the probes. Fig. 3.8 c and d depict the 700 nm and 530 nm light falling on a sample through the optical fiber cable.

The LEDs attached to the probe station via a magnetic stand and controlled via an Arduino UNO (for on-off larger than 1 ms) or a function generator (for on-off smaller than 1 ms) are used to measure the transient response of D.U.Ts. A variable resistance box in series with the Arduino or function generator as the source is used to control the intensity of the LED. The intensity of the LED is measured using a Thorlabs PM 100A power meter with a PM120VA sensor.

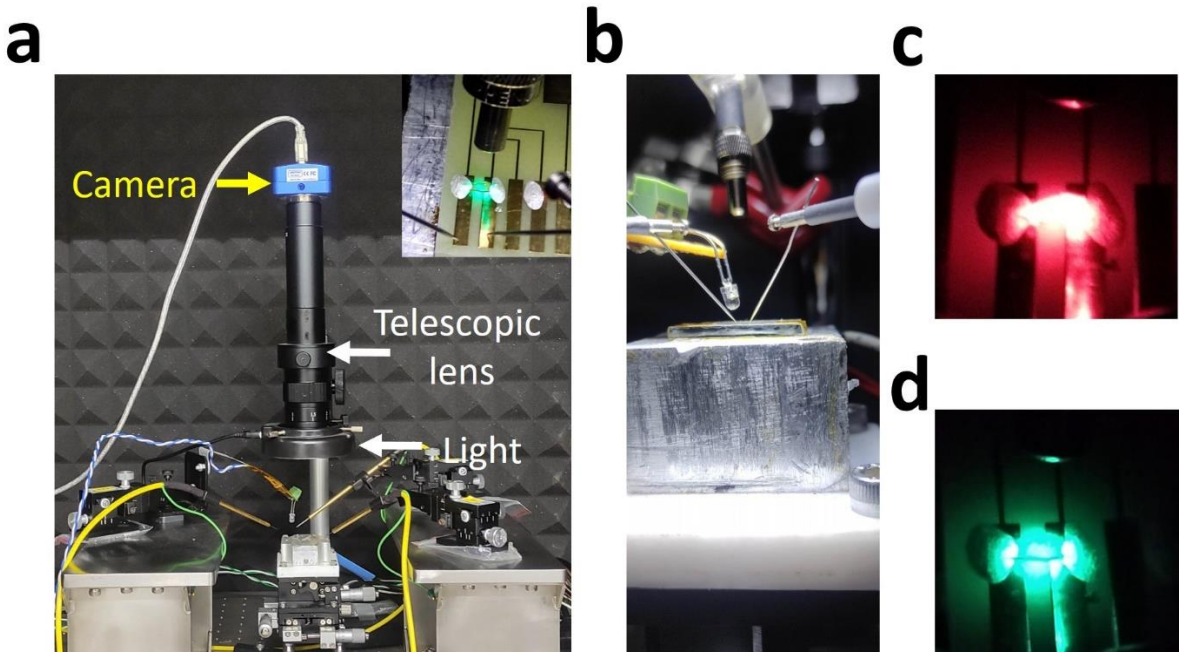


Figure 3.8: (a) Photograph of the probe station with the telescope with a camera and LED and three micropositioners and LED controlled using Arduino. The inset shows an optical fiber cable transmitting a 530 nm light. From the monochromator. (b) A close-up photo of the stage with probes, LED, Optical fiber, and probes. (c) and (d) are the images of 700 nm and 530 nm falling on a sample from the optical fiber cable.

### 3.2.8 Reactive ion etching

Micro/nanofabrication in silicon has become a widely employed technique for manufacturing micro/nano-mechanical structures essential for various sensors and actuators. One crucial aspect of this process is patterning the substrate, which relies on different etching processes. The development of etching techniques for micromachining requires achieving high etch rates, precise linewidth control, uniformity, and selectivity over both the mask and underlying layers. However, traditional wet etchants often fail to meet these requirements for several reasons. Firstly, wet etching involves pure chemical reactions, resulting in anisotropic etching profiles unless a crystal orientation-dependent etch is used, which puts a lot of restriction on the type of pattern and substrate used. Secondly, the poor adhesion of the photoresist to the substrate can cause the etchant to seep beneath the photoresist causing undesired etching. Thirdly, the surface tension of the liquid makes it challenging for the wet etchant to penetrate very small patterns in the resist and thus leaves the substrate unaffected. Lastly, the gas bubble formed

during wet etching locally could hinder the etching process, leading to poor uniformity.[23]

To address these challenges, dry etching techniques that can induce directionality in the etching process, such as reactive ion etching (RIE), have emerged as a viable alternative. RIE provides anisotropic etch profiles while offering reasonable selectivity under various conditions such as electrode geometry, radio frequency (RF) power, pressure, gas flow rate, and composition.[24] This makes techniques like RIE attractive for micro/nanofabrication. RIE differs from sputter etching as it involves a chemical reaction that enhances selectivity and improves the etching rates. In a typical RIE process, gases are introduced into the reaction chamber. RF ionises the gas and the ionised molecules are propelled toward the substrate surface, where they remove the top layer of material through a combination of mechanical and chemical reactions.

Fig. 3.9 shows the schematic of the RIE system we designed, along with a photograph of the system during operation. The chamber can be seen glowing with a pinkish hue. Our design of the RIE had a parallel plate configuration. The chamber was constructed using stainless steel (SS) and included a viewport with a quartz window to ensure plasma formation during operation. To introduce the gas into the chamber, a 6mm SS tube was used. The gas, after entering the chamber, passes through a showerhead from the top. The active electrode within the chamber was an SS plate, although, for longer runs, we also utilized an aluminum plate as the cathode to aid in thermal regulation. However, the use of Aluminum as the active cathode can lead to contamination while etching silicon.[24] This active electrode was connected to the RF power supply, specifically the Cesar RF power supply from Advanced Energy, via an impedance matching network called Navio, also from Advanced Energy. The connection was established through a single-pin n-type connector. To ensure electrical insulation and thermal conductivity, an Aluminum Nitride spacer was used to separate the active electrode from the grounded main body. Aluminum Nitride was used because of its good electrical insulation and high thermal conductivity.[25] The chamber base contained grooves beneath the insulating layer to facilitate the flow of gas from the chamber to the vacuum pump, while additional grooves underneath aided in maintaining water flow for cooling. Two KF16 ports, one at the top and another at the bottom, equipped with Pirani gauges, were utilized to monitor the pressure inside the chamber. To achieve an airtight seal, a Viton O-ring was positioned along the chamber's rim. Initially, the chamber was securely closed using two screws positioned in

front. For lowering the pressure in the chamber, a KF25 port served as the vacuum port and was connected to a bellows-sealed stainless steel angle valve, which was linked to the vacuum pump. The gas flow to the chamber was controlled by two Alicat mass flow controllers (MFC), which had a resolution of 0.1 sccm. These MFCs were connected to the active gases SF6 and O2, which we used in a process similar to previous reports.[26][27]

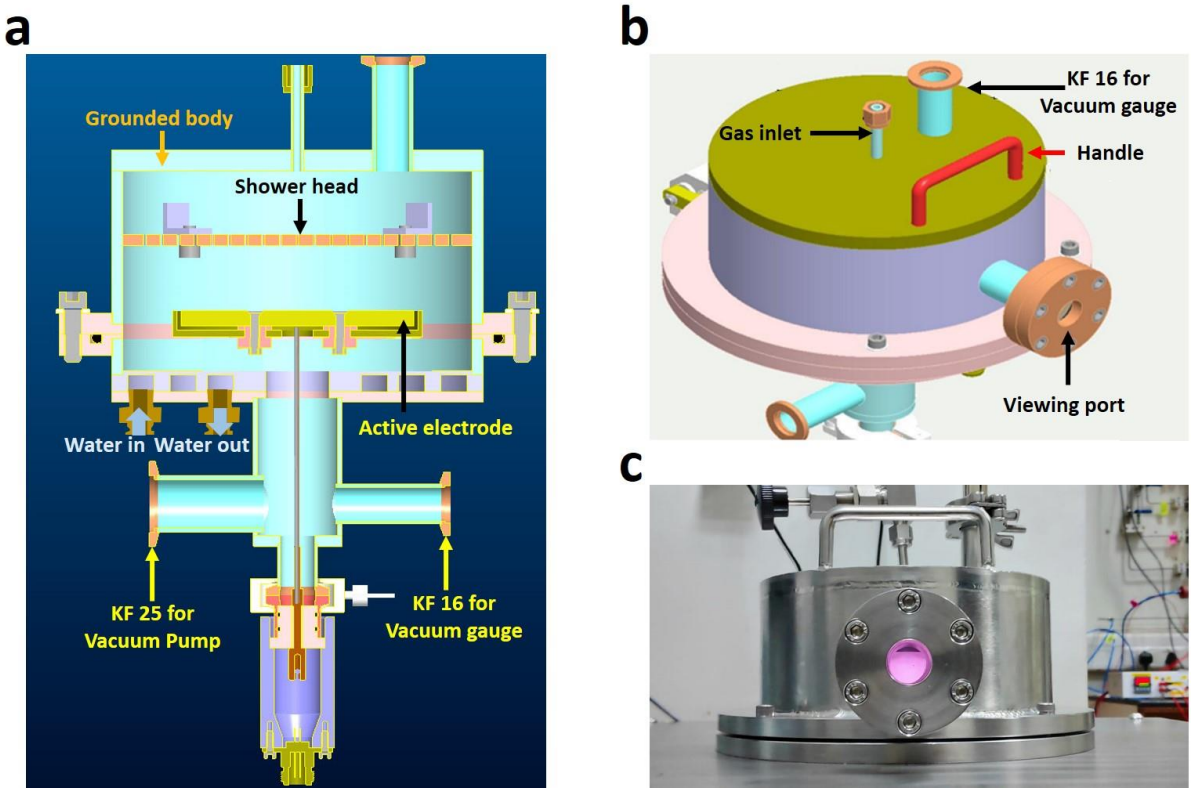


Figure 3.9 presents the schematics depicting the inner and outer design of the RIE chamber, denoted as (a) and (b) respectively. Additionally, (d) showcases a photograph of the RIE chamber during operation.

The plasma chamber is designed as a capacitively coupled Plasma RIE (CCPRIE).[28] In CCPRIE a self-bias voltage develops on the active electrode, due to the blocking capacitor (impedance matching network) in the RF power supply connection. The self-bias occurs due to the significant difference in mass between electrons and ions in a plasma discharge, which leads to electrons having more velocity than the ions. Consequently, electrodes exposed to the plasma encounter a difference in the arrival rate of electrons and ions. In the case of an insulated

electrode, the self-bias voltage is generated to balance the electron and ion currents. This self-bias DC voltage attracts positive ions toward the active electrode, resulting in their bombardment of the surface. Consequently, atoms from the substrate being etched are sputtered, and often chemically react with the etching gas, leading to the formation of gaseous by-products that are subsequently pumped out of the chamber.

The pressure in RIE is a critical factor. When the pressure is above 0.1 torr (0.133 mbar), the process loses its anisotropy, leading to under-etching.[29] In this case, it can be categorized as a regular plasma etch where directionality is reduced. On the other hand, when the pressure is below 1 mtorr (1.33 μbar), the material is removed from the substrate primarily through physical bombardment by high-energy ions. At these lower pressures, the role of chemical reactions becomes insignificant, and the kinetic energy of the ions becomes crucial. Therefore, it is highly important to maintain the pressure between 1 and 100 mtorr to ensure the process operates within the RIE regime.[29]

In our RIE we optimize the reaction at 0.09 mbar with a flow of $SF_6$ at 4 sccm and $O_2$ at 1sccm. The flow rate can be improved by connecting an appropriate vacuum pump. But for our needs a vacuum pump that can go to 0.001 mbar was sufficient. Using a pump with a higher pump rate can give additional control over the flow rate. The use of Aluminum electrode did not contaminate the $SiO_2$ etching which is optimized to get a 1 nm/s etch rate at 120 W power. But it does cause contamination in silicon substrates.

The photograph in Fig. 9.7 a and b shows the logo of IISER Pune, a 6 mm and a 50 $\mu$m logo, etched into the silicon substrate using our RIE. This demonstrates the scalability of the technique. Fig. 9.7d shows the etching done at a slightly higher pressure of 0.13 mbar. The pattern starts to become slightly isotropic. Fig. 9.7e shows a double step pattern created using the RIE at 0.09 mbar. This demonstrate that we can use multiple steps to get complex patterns with good anisotropy using RIE. Fig. 9.7d shows a pattern created using the RIE at 0.001 mbar by physical bombardment. Though the pattern was highly anisotropic the etch rate and selectivity was much lower compared to the regular process. These experiments demonstrate that the chamber pressure can be controlled to fabricate various patterns using our RIE.

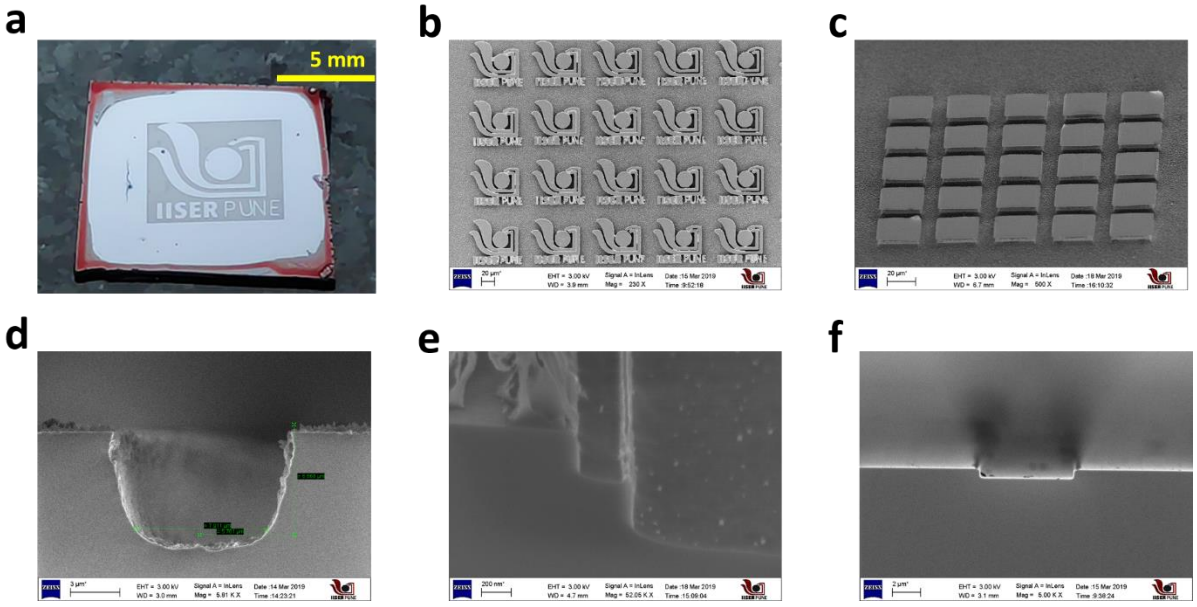


Figure 3.10: Patterns etched using a custom-built RIE system. (a) and (b) depict photographs of a large and small logo of IISER Pune etched on Silicon using RIE, with the large logo measuring 6mm in size and the small logos measuring approximately 50 µm in length. (c) showcases a FESEM image of an array of square patterned etchings. (d), (e), and (f) display FESEM images of samples etched at pressures of 0.18 mBar, 0.09 mBar, and 0.01 mBar, respectively.

## 3.3 Chemical vapor deposition system

Chemical vapor deposition (CVD) is a versatile technique widely employed in the synthesis of various two-dimensional (2D) materials, including TMDs, and is hailed as the most promising technique for industrial-scale production of large-area monolayers.[30] The CVD process involves the condensation of compounds from the gas phase onto a substrate, where reactions occur to produce solid deposits. It follows a nucleation and growth mechanism, where atoms adsorb and diffuse on the substrate surface before forming nucleation sites.[31]

In order to achieve successful material growth using CVD, it is essential to carefully consider the thermodynamics and kinetics of the deposition reaction. This involves evaluating the concentrations (partial pressures) of the reactants at chemical equilibrium in relation to their initial concentrations. It is also important to take into account the most stable valence state of reactants that possess multiple valence states. Ensuring the thermodynamic feasibility of the reaction is crucial. Additionally, factors such as deposit-substrate adherence, uniformity of deposition thickness, and composition need to be thoroughly addressed to attain the desired film

properties.[31]

In this thesis, the focus is on the growth of 2D TMD monolayers using CVD, and we will discuss shortly on the setup that was established for synthesizing these materials in this section. The CVD system utilized is an atmospheric pressure chemical vapor deposition (APCVD) system, incorporating a Nabertherm split zone furnace. The setup consists of a quartz tube, sealed with corks with 6 mm push-fit connectors for the gas inlet and outlet. Flow control was initially achieved using flow meters and later transitioned to more precise Alicat MFCs. To prevent backflow, an empty bubbler is placed in the gas flow path, followed by a silicone oil bubbler to minimize moisture contamination. Lastly, a $CaCO_3$-water bubbler neutralizes acidic byproducts before releasing gases into the chemical hood exhaust pipe.

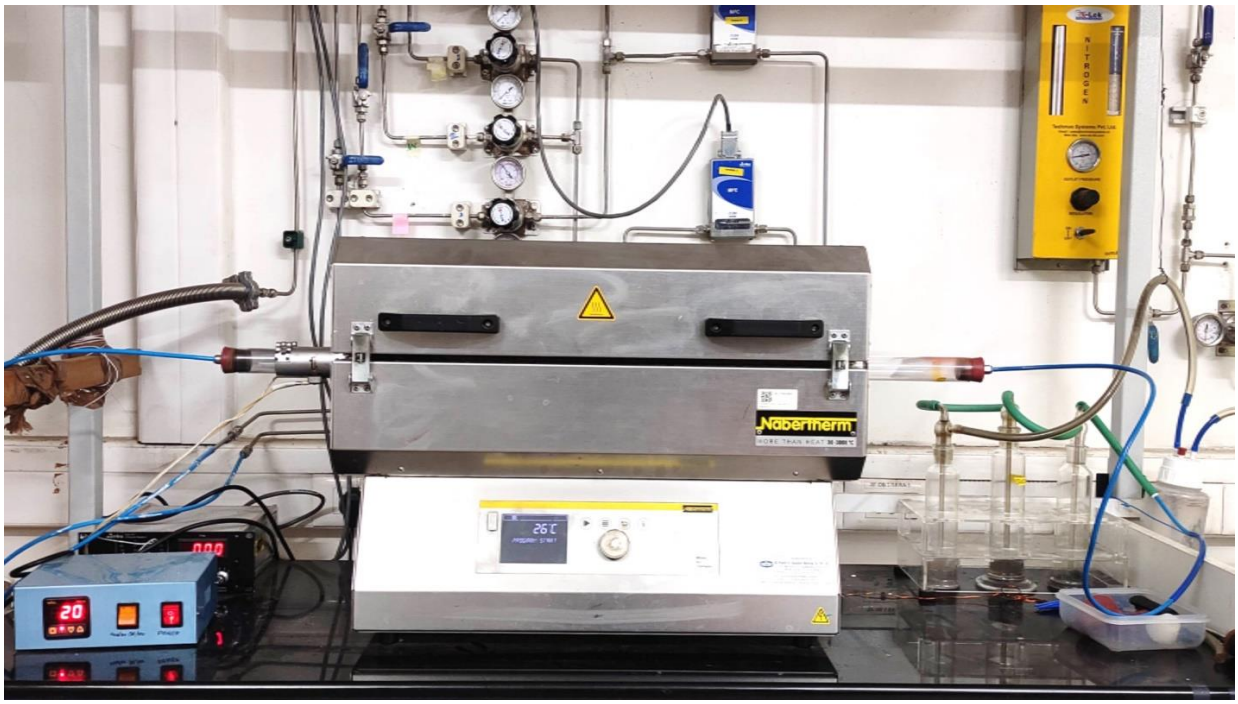


Figure 3.11: Photograph of our CVD setup used for synthesizing monolayer TMDs

## 3.4 Modification of CCR substrate holders

Access to low-temperatures and high magnetic fields is of paramount importance for exploring the underlying mechanisms and physics of materials through low-temperature high magnetic field transport measurements. These measurements offer significant advantages in investigating

a wide range of phenomena, including quantum oscillations, superconductivity, Hall effect, carrier properties, and magneto-resistance effects.[32][33][34] By subjecting materials to such extreme conditions, researchers can uncover valuable insights into materials' fundamental properties and behavior, leading to advancements in our understanding of quantum physics and the development of innovative materials and technologies.

This section focuses on the modification of the substrate holder of a commercial Sumitomo cold head for the purpose of conducting measurements on samples at low temperatures in the presence of a magnetic field. In order to achieve this, we made alterations to our 4K Closed Cycle Refrigerator (CCR) setup. The entire CCR was mounted on a sliding stage. The original sample holder at the cold head was replaced with an elongated one, allowing it to reach all the way down to the electromagnet. To facilitate easy sample insertion, a PCB mount was designed with male pins that can be inserted into the female connectors of the holder. The PCB mount was specifically crafted to ensure that the PCB with the sample rests securely on the cold copper surface of the modified sample holder. All necessary wire connections to the cold head were extended and joined using copper wires. A photograph illustrating the modified setup is provided in Figure 3.11. We also modified the outer jacket and the radiation shield to ensure minimal gain in temperature from the surroundings.

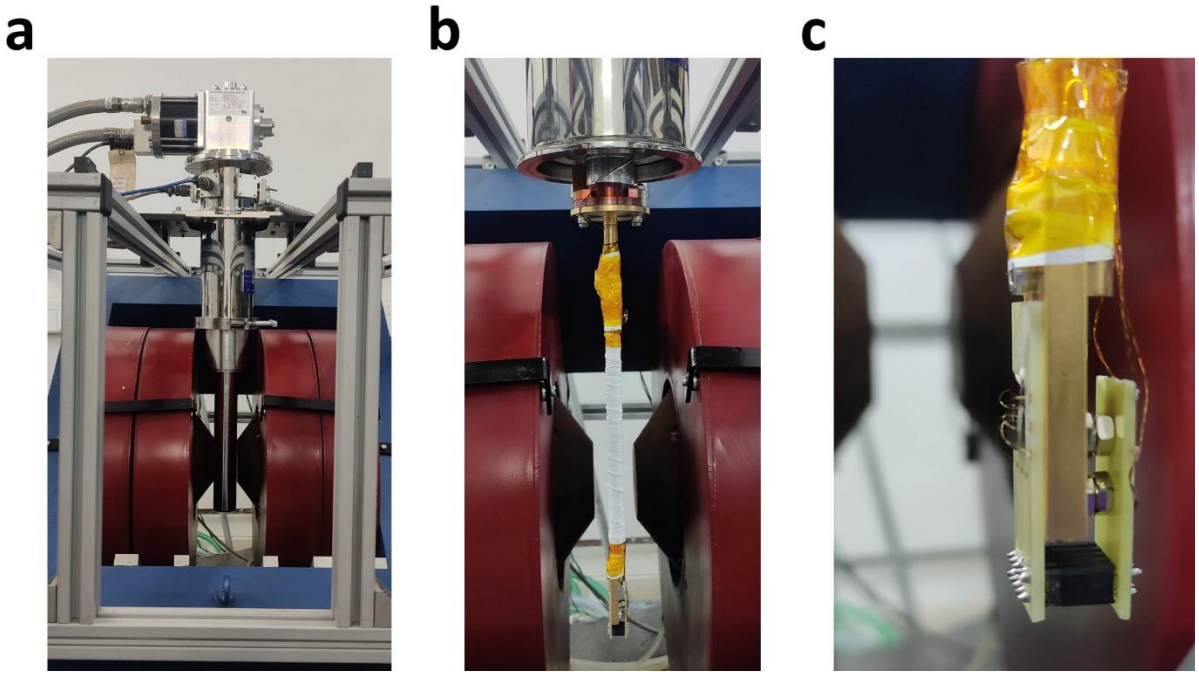


Figure 3.12: (a) photograph of the modified sample holder with the modified vacuum jacket near the electromagnet. (b) the photograph of the modified sample holder without the modified vacuum jacket and shield. (c) the close up image of a sample wire bonded on to a PCB attached to the modified sample holder for measurements.

## 3.5 Combining UV Microscope with a Spectrometer

PL microscopes that use a strong monochromatic light source and appropriate filters are great tools to image the photoluminescence of materials. The filter blocks the lower wavelength monochromatic light used to excite the material and passes the higher wavelength PL emission from the sample. The microscope optics project the magnified image of the material that is luminescing. By replacing the camera with a fiber optic cable, we can feed the PL light into a spectrometer. Our PL microscope was Drawell PL microscope that used a 465 nm LED as light source and a 505 nm long pass filter to filter out all wavelengths below 505 nm. We used the STS-VIS spectrometer from ocean optics to collect and analyze the spectrum from the microscope. The microscope iris diaphragm can be adjusted to select a very small area to do selective area PL analysis, which is beneficial for studying properties of individual crystals of interest, provided they cover an area of a few micrometers. The PL should be relatively strong as in the case of Perovskites or $WS_2$ both of which can be imaged using the PL microscope

thanks to their high PL intensity. Alternatively, we can use AvaSpec-ULS2048CL-EVO spectrometer from Avantes which, although much larger, has a better range and is more sensitive.

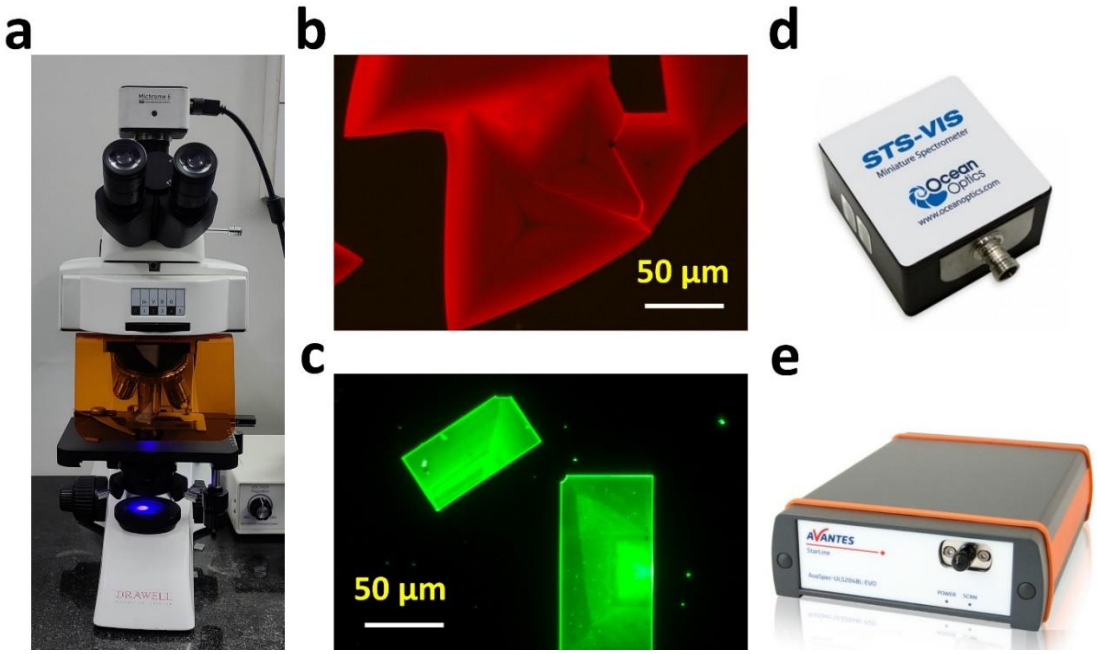


Figure 3.13: (a) photograph of the Drawell PL microscope used in this thesis for PL imaging. (b) and (c) are the PL images of $CsPbBr_3$ and $WS_2$ taken using the PL microscope. (d) and (e) are the spectrometers in our lab that we coupled with the PL microscope for spectral analysis.

## 3.6 Summary

To conclude, this chapter has presented a comprehensive overview of the instrumental setups successfully established in our lab at IISER Pune as part of my PhD. With dedicated efforts and expertise, I have played a pivotal role in developing and optimizing various essential instruments crucial to our research activities. The detailed discussion covers the successful establishment of several instrumental setups, including the RIE system, probe station, and modification of commercial setups. Through the process of designing, implementing, and optimizing these sophisticated instruments, we have experienced firsthand the tremendous advantages they bring to our research endeavors. The establishment of our lab, with its advanced instrumental infrastructure, has proven to be immensely beneficial. These advantages have significantly contributed to the progress and success of our research activities, enabling us to explore new

frontiers and make meaningful advancements in our field.

**Bibliography**

[1] Cai F, Tang R, Wang S and He S 2018 A compact line-detection spectrometer with a Powell lens *Optik (Stuttg).* **155** 267–72

[2] Bewsher A, Powell I and Boland W 1996 Design of single-element laser-beam shape projectors *Appl. Opt.* **35** 1654

[3] Christensen K A and Morris M D 1998 Hyperspectral Raman Microscopic Imaging Using Powell Lens Line Illumination *Appl. Spectrosc.* **52** 1145–7

[4] Powell I 1987 Design of a laser beam line expander *Appl. Opt.* **26** 3705

[5] Kamo M, Sato Y, Matsumoto S and Setaka N 1983 Diamond synthesis from gas phase in microwave plasma *J. Cryst. Growth* **62** 642–4

[6] Marchack N, Buzi L, Farmer D B, Miyazoe H, Papalia J M, Yan H, Totir G and Engelmann S U 2021 Plasma processing for advanced microelectronics beyond CMOS *J. Appl. Phys.* **130** 080901

[7] Barnes B K, Ouro-Koura H, Derickson J, Lebarty S, Omidokun J, Bane N, Suleiman O, Omagamre E, Fotouhi M J, Ogunmolasuyi A, Dominguez A, Gonick L and Das K S 2021 Plasma generation by household microwave oven for surface modification and other emerging applications *Am. J. Phys.* **89** 372–82

[8] Law V J and Dowling D P 2018 Converting a Microwave Oven into a Plasma Reactor: A Review *Int. J. Chem. Eng.* **2018** 1–12

[9] Gould L and Roberts L W 1956 Breakdown of Air at Microwave Frequencies *J. Appl. Phys.* **27** 1162–70

[10] Sun J, Wang W, Yue Q, Ma C, Zhang J, Zhao X and Song Z 2016 Review on microwave–metal discharges and their applications in energy and industrial processes *Appl. Energy* **175** 141–57

[11] Herlin M A and Brown S C 1948 Breakdown of a Gas at Microwave Frequencies *Phys. Rev.* **74** 291–6

[12] Le Formal F, Sivula K and Grätzel M 2012 The Transient Photocurrent and Photovoltage Behavior of a Hematite Photoanode under Working Conditions and the Influence of Surface

Treatments *J. Phys. Chem. C* **116** 26707–20

[13] Wheeler S, Bryant D, Troughton J, Kirchartz T, Watson T, Nelson J and Durrant J R 2017 Transient Optoelectronic Analysis of the Impact of Material Energetics and Recombination Kinetics on the Open-Circuit Voltage of Hybrid Perovskite Solar Cells *J. Phys. Chem. C* **121** 13496–506

[14] Sloat J D and Geiger R L 2008 An inexpensive microelectronic environmental test chamber *2008 IEEE International Conference on Electro/Information Technology* (IEEE) pp 168–70

[15] Hook M D and Mayer M 2017 Miniature environmental chambers for temperature humidity bias testing of microelectronics *Rev. Sci. Instrum.* **88** 034707

[16] Zhao X, Liu T, Burlingame Q C, Liu T, Holley R, Cheng G, Yao N, Gao F and Loo Y L 2022 Accelerated aging of all-inorganic, interface-stabilized perovskite solar cells *Science (80-. ).* **377** 307–10

[17] Patra D, Reza A K, Hassan M K, Katoozi M, Cannon E H, Roy K and Cao Y 2018 Adaptive accelerated aging for 28 nm HKMG technology *Microelectron. Reliab.* **80** 149–54

[18] Dutta P and Horn P M 1981 Low-frequency fluctuations in solids: 1/f noise *Rev. Mod. Phys.* **53** 497–516

[19] Stephany J F 2000 Frequency limits of 1/ f noise *J. Phys. Condens. Matter* **12** 2469–83

[20] Dantu R V., Dimopoulos N J, Patel R V. and Al-Khalili A J 1989 Micromanipulator Vision for Wafer Probing *IEEE Trans. Semicond. Manuf.* **2** 114–7

[21] Jiao L (Heidi) and Ray J 2006 Design And Implementation Of A Probe Station As Capstone Project *2006 Annual Conference & Exposition Proceedings* (ASEE Conferences) pp 11.397.1-11.397.12

[22] Roeser W F, Dahl A I and Gowens G J 1935 Standard tables for chromel-alumel thermocouples *J. Res. Natl. Bur. Stand. (1934).* **14** 239

[23] Li Y X, Wolffenbuttel M R, French P J, Laros M, Sarro P M and Wolffenbuttel R F 1994 Reactive ion etching (RIE) techniques for micromachining applications *Sensors Actuators A Phys.* **41** 317–23

[24] Pinto R, Babu R S and Bhattacharya P K 1986 Annealing of Si damage caused by reactive ion etching in SF6 gas mixtures *Appl. Phys. Lett.* **48** 1427–9

[25] Hoque M S Bin, Koh Y R, Braun J L, Mamun A, Liu Z, Huynh K, Liao M E, Hussain K,

Cheng Z, Hoglund E R, Olson D H, Tomko J A, Aryana K, Galib R, Gaskins J T, Elahi M M M, Leseman Z C, Howe J M, Luo T, Graham S, Goorsky M S, Khan A and Hopkins P E 2021 High In-Plane Thermal Conductivity of Aluminum Nitride Thin Films *ACS Nano* **15** 9588–99

[26] Pinto R, Ramanathan K V. and Babu R S 1987 Reactive Ion Etching in SF 6 Gas Mixtures *J. Electrochem. Soc.* **134** 165–75

[27] Wells T 1997 Low temperature reactive ion etching of silicon with SF[sub 6]/O[sub 2] plasmas *J. Vac. Sci. Technol. B Microelectron. Nanom. Struct.* **15** 434

[28] Park H M, Garvin C, Grimard D S and Grizzle J W 1998 Control of Ion Energy in a Capacitively Coupled Reactive Ion Etcher *J. Electrochem. Soc.* **145** 4247–52

[29] Huff M 2021 Recent Advances in Reactive Ion Etching and Applications of High-Aspect-Ratio Microfabrication *Micromachines* **12** 991

[30] Li H, Li Y, Aljarb A, Shi Y and Li L-J 2018 Epitaxial Growth of Two-Dimensional Layered Transition-Metal Dichalcogenides: Growth Mechanism, Controllability, and Scalability *Chem. Rev.* **118** 6134–50

[31] Bryant W A 1977 The fundamentals of chemical vapour deposition *J. Mater. Sci.* **12** 1285–306

[32] Gu H, Zhang X, Wei H, Huang Y, Wei S and Guo Z 2013 An overview of the magnetoresistance phenomenon in molecular systems *Chem. Soc. Rev.* **42** 5907

[33] Fickett F R 1985 Standards for measurement of the critical fields of superconductors *J. Res. Natl. Bur. Stand. (1934).* **90** 95

[34] Goel N, Babuta A, Kumar A and Ganguli S 2020 Hall effect instruments, evolution, implications, and future prospects *Rev. Sci. Instrum.* **91**

# Chapter 4

# Chemical Vapor Deposition for Monolayer 2D Materials: Fine-Tuning Flow

This chapter is an adaptation of the research article published in "*Nanotechnology* **31** 415706, 2020".

## 4.1 Introduction

Two-dimensional (2D) materials, particularly in their monolayer form, exhibit unique characteristics distinct from their bulk counterparts, making them promising candidates for new avenues of research, including spintronics, straintronics, twistronics, and valleytronics.[1–9] However, isolating a single monolayer of 2D materials remains a challenging task. The most popular and straightforward approach to achieving a monolayer is through the method of mechanical exfoliation, which was utilized in the discovery of graphene, for which the Nobel Prize was awarded.[10,11] This process involves splitting the crystal multiple times using a tape and transferring it onto a substrate. Typically, a $SiO_2$ on Si substrate with a thickness of 280-300 nm is used as it provides good contrast for optically identifying the monolayer film.

Despite yielding high-quality monolayers, the exfoliation technique has a low yield, and the chances of obtaining a monolayer among hundreds or thousands of exfoliated layers of various thicknesses are unpredictable. Fig. 4.1 displays images of two exfoliated monolayers of $MoS_2$ on a 285 nm $SiO_2$ on Si substrate, revealing that the exfoliation process produces monolayer $MoS_2$ of varying sizes along with mostly multilayer $MoS_2$. Typically, the entire substrate contains 1 or 2 monolayers, and there are instances where no monolayer is obtained through this approach. While acquiring a few micrometer-sized monolayer films suffices for fundamental

studies, it is insufficient for industrial-scale applications that aim to advance device technologies utilizing these materials.

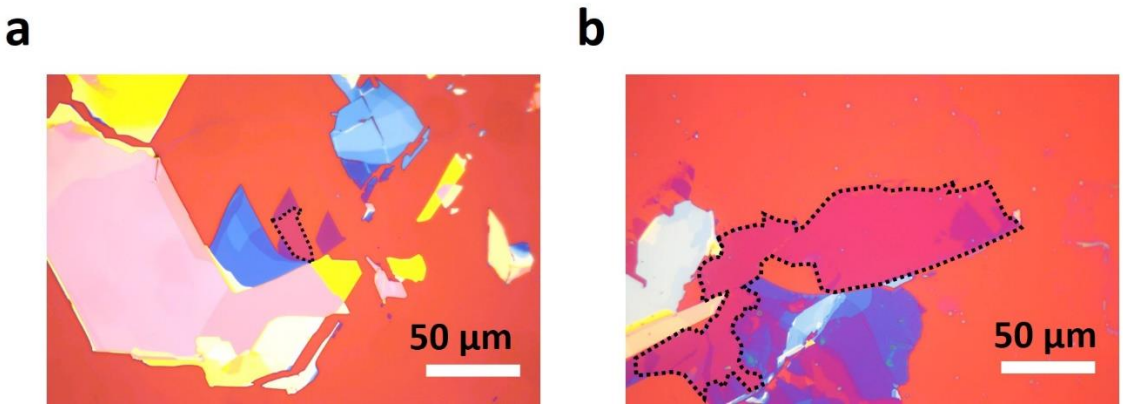


Figure 4.1: (a) a small monolayer $MoS_2$ (marked with a black dotted line) surrounded by layers of various thicknesses (b) A large area $MoS_2$ monolayer with little patches of the bilayer (a darker shade of purple) obtained via mechanical exfoliation (also marked with a black dotted line) surrounded by layers of various thicknesses.

To obtain large crystals of monolayer materials, researchers employ bottom-up techniques, such as PVD, CVD, atomic layer deposition (ALD), and pulsed laser deposition (PLD), to directly synthesize monolayers onto desired substrates in a controlled fashion. [12–15] CVD has emerged as one of the most promising techniques for producing high-quality, large-area monolayers of TMDs.[16–28] However, the growth of TMDs using CVD depends on several parameters such as the type of substrates, synthesis temperature, precursor-substrate positioning, carrier gas flow rate, growth promoters, precursor type and amount, and timing of precursor introduction.[29–38] In a previous study, we investigated the influence of various parameters and how we optimized them to synthesize monolayer $MoS_2$.[39]

This chapter highlights the significant impact that flow can have on the growth of monolayer TMDs using CVD. By developing a method that fine-tunes precursor flow on the substrate surface, we have demonstrated the formation of continuous monolayers under synthesis conditions suited for bulk growth. By utilizing this approach, a self-limiting growth process can be achieved, eliminating the need for precise control of multiple CVD parameters. This is possible because the growth conditions required for growing bulk crystals are less stringent. To complement our experimental results, we carried out computational studies using COMSOL,

which were consistent with our observations. The study is concluded by performing a thorough characterization of the resulting monolayers using various techniques such as optical microscopy, Raman and PL spectroscopy, and FET measurements to assess the quality of the as-grown monolayers.

## 4.2 Effect of flow on CVD growth of monolayer on flow

Various techniques have been attempted by researchers to grow high-quality $MoS_2$ films using CVD, including thermal vapor sulfurization, sulfur-vapor counter flow diffusion, a dual-tube configuration, and others.[40–46] In these methods, achieving the desired growth of monolayers involved precise control over the precursor amount or its accessibility to the substrate surface. Simulation work has been conducted to understand precursor flow in a CVD chamber by considering concentration gradient distribution, which aligns well with experimental results. To investigate the effect of subtle changes in flow on the growth of continuous $MoS_2$ monolayer, we fixed all the growth parameters including the carrier gas flow through the CVD tube. We changed the configuration and size of the substrates to modulate the flow around the substrate surface, which in turn affected the growth of monolayers.

### 4.2.1 Sensitivity of growth to subtle changes in flow

The substrates used to grow $MoS_2$ were 300 nm $SiO_2$ on Si substrate. To prepare the substrates, we initially cleaned them by subjecting them to ultrasonication in acetone and then in IPA, each for a duration of 10 minutes. After cleaning, the substrates were blow-dried. To enhance the substrate's wettability, we performed an additional cleaning step using an oxygen plasma asher at 40 W power for 10 minutes. The cleaned substrates were further treated by applying a few drops of a 0.001 Molar NaCl solution. Subsequently, the substrates were blow-dried to remove any residual liquid. We used a 3.2 cm inner diameter quartz tube to grow $MoS_2$. The alumina boat containing 60 mg of $MoO_3$ precursor was kept 16 cm from the boat that contained 600 mg of sulphur precursor and the boat containing the substrates was kept 2 cm from the $MoO_3$ boat. The $MoO_3$ and substrate boats are always within the region where the temperature of the furnace is read. The temperature of the furnace was set at 700 °C and the ramp rate was set at 300 °C/hr.

The sulphur boat was slightly outside the furnace and was pushed into the furnace by sliding the tube in when the furnace temperature reached 700 °C. Nitrogen gas was used as the carrier gas. The Nitrogen flow was set to 150 Standard Cubic Centimeters per Minute (sccm) initially and the flow was set to 27 sccm after 20 min. The flow rate of 27 sccm was maintained till the furnace cooled down to room temperature naturally. The arrangement of substrates in CVD during our first study is depicted in Fig. 4.2. Configuration 1 employed 4 substrates of 1 cm ×1 cm dimension, with the first one positioned 3 cm away from the end of the substrate boat. The remaining three were placed approximately 1-2 mm from the adjacent substrate, as shown in Fig 4.2a (configuration 1). The substrates were labeled A, B, C, and D along the flow direction (schematically shown in Fig. 4.2a)). Optical images were captured from four different regions of each sample (Fig. 4.2b) to demonstrate the size and coverage of the monolayers. Our observations revealed that the edges had scattered small monolayers while the layer coverage and size were significantly more toward the center of the substrate. This seemingly periodic change in growth, as we move from substrate A-D, hints that there is something that disrupts the growth near the edges of the substrate.

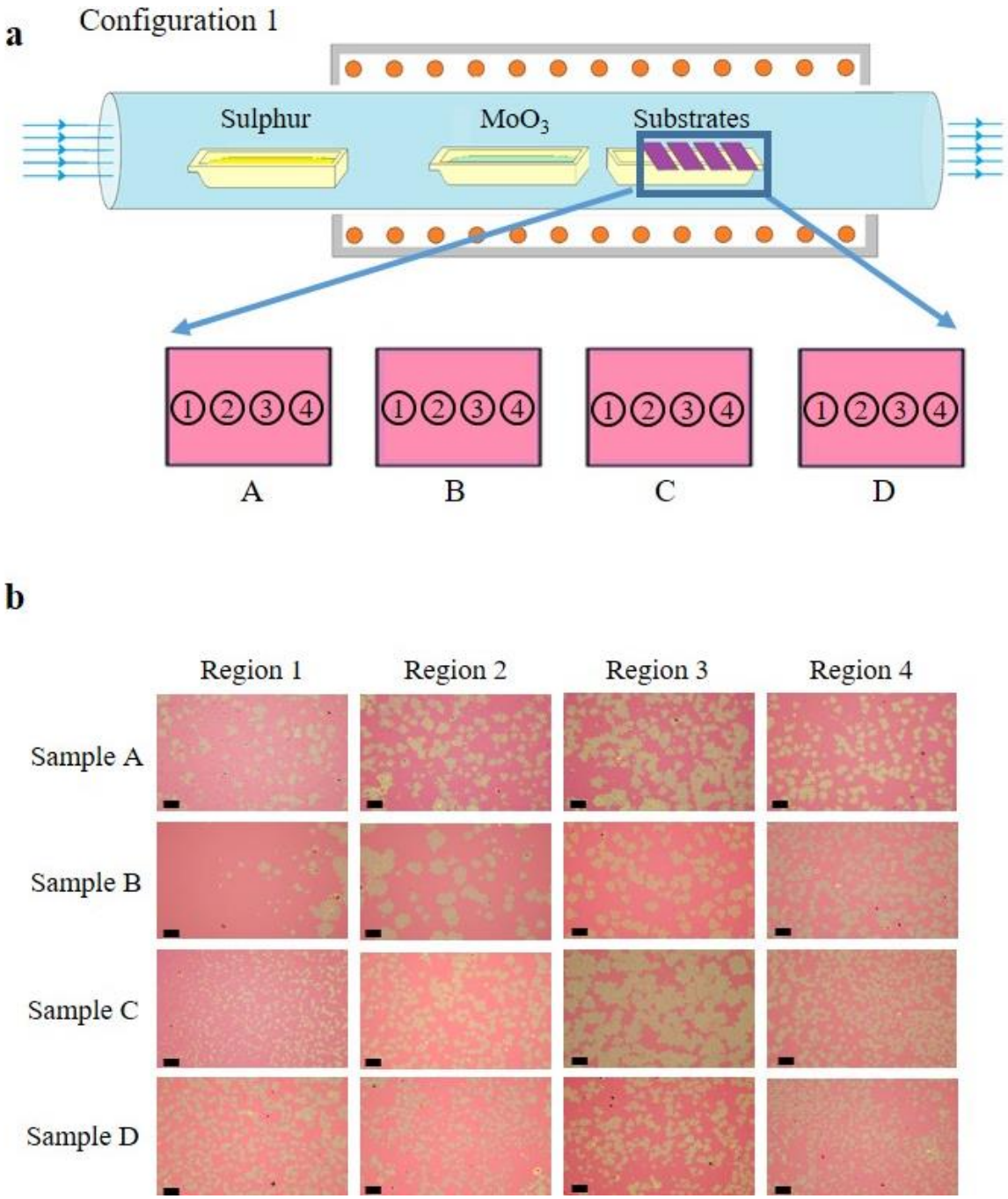


Figure 4.2: (a) Schematic showing the arrangement for growing $MoS_2$ on four substrates, sample A-D in CVD and the schematic of four regions on each substrate where the optical images were taken. (b) Corresponding 10x optical images from the regions of interest (scale bar 200**μ**m).

These exact conditions produced continuous monolayers with little pinholes in our previous study.[47] The only difference then was that we had a single substrate instead of four substrate.

So we hypothesized that for this peculiar distribution of monolayers during growth must be attributed to the flow disruption near the substrate edges, as illustrated in Fig. 4.3a. The gaps between the substrates could have caused disturbances in the flow, leading to scattered monolayer growth at the edges. The disturbances caused by this disturbance of flow near the edges will have a minimal effect on the central region of the substrate, resulting in larger area coverage of monolayers. To resolve this issue, we suggest using a continuous, single-long substrate instead of four separate substrates. Fig. 4.3b shows a schematic of how this change could mitigate flow disruptions and that should result in a more uniform monolayer growth. To test this hypothesis, we replaced the four substrate with a 9 cm long single substrate while keeping all the other parameters same as the previous growth. A schematic of the growth configuration used is shown in Fig. 4.3c. The substrate was kept on the second boat as shown in the schematic. In this case, we got a continuous monolayer throughout the substrate, with little discontinuity at the end facing the flow. This proved that the conditions in configuration 1 were good for the growth of a continuous monolayer but did not happen because of the disturbance in flow created by the way they were arranged.

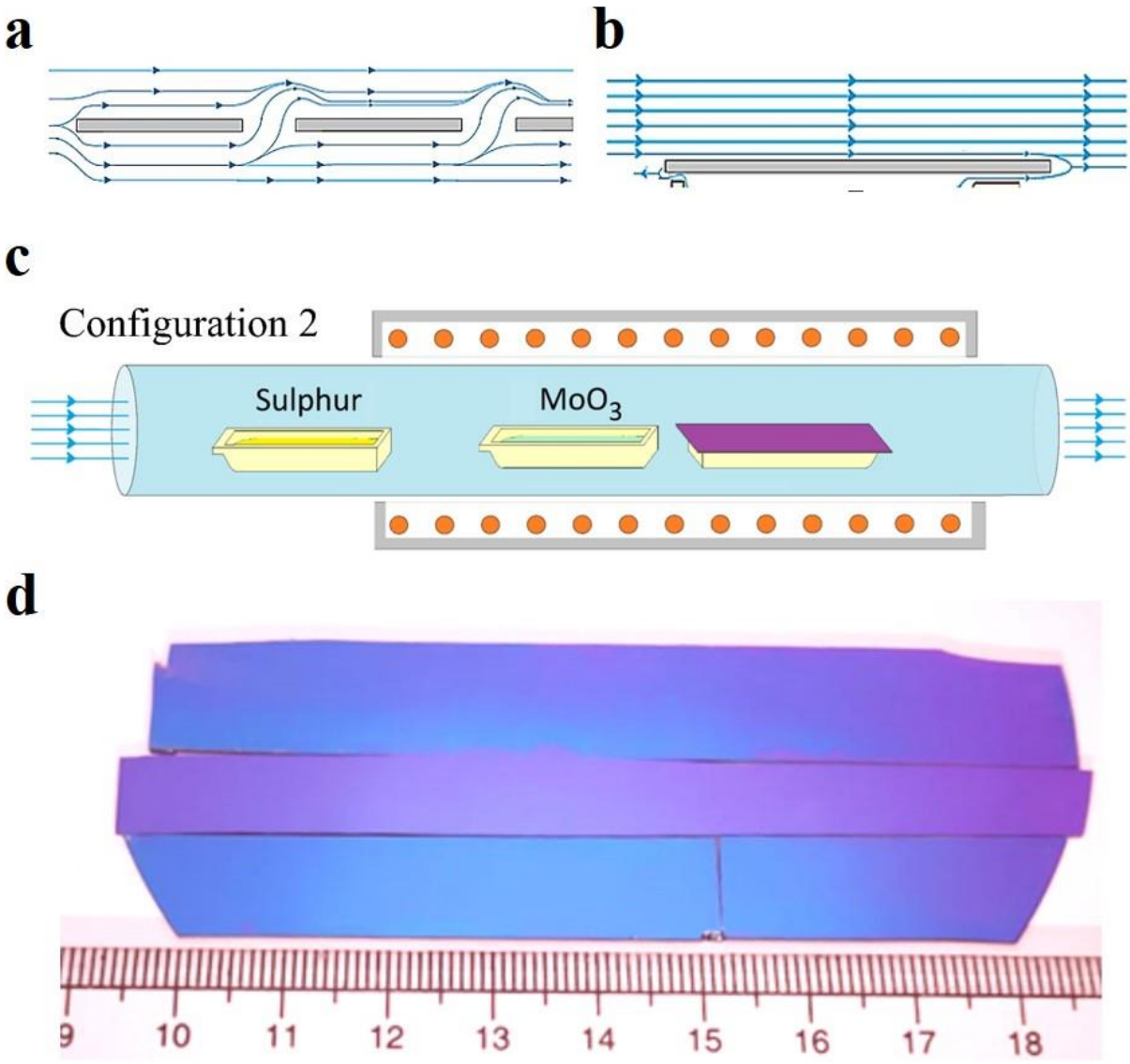


Figure 4.3: (a) Speculative model of how the flow might be affected locally near the substrates in configuration 1. (b) The flow remains steady or uniform after replacing the 4 substrates with a single long one. (c) Schematic of configuration 2 used to eliminate the changes in flow. (d)The image of a bare $SiO_2$/Si substrate (middle) with 2 long strips of continuous monolayer $MoS_2$ coated $SiO_2$/Si substrates on its two sides (a cm unit scale is kept for reference).

The monolayer is continuous in configuration 2 because the disturbance in flow was eliminated. The experiment was repeated thrice and we got reproducible results. An image of two 9 cm long continuous $MoS_2$ on $SiO_2$ coated Si substrate along with a regular 300 nm $SiO_2$ on Si substrate is shown in Fig. 4.3d. The 5x images from different regions of one of the 9 cm long $MoS_2$ are given in Fig. 4.4a. From the images, it is clear that in the region where the gas flow encounters

the substrate, we got scattered triangles and as we continued to move along the direction of flow, starting from region 2, the layers merged together to give a continuous monolayer of $MoS_2$ till the very end of the strip with very few pinholes.

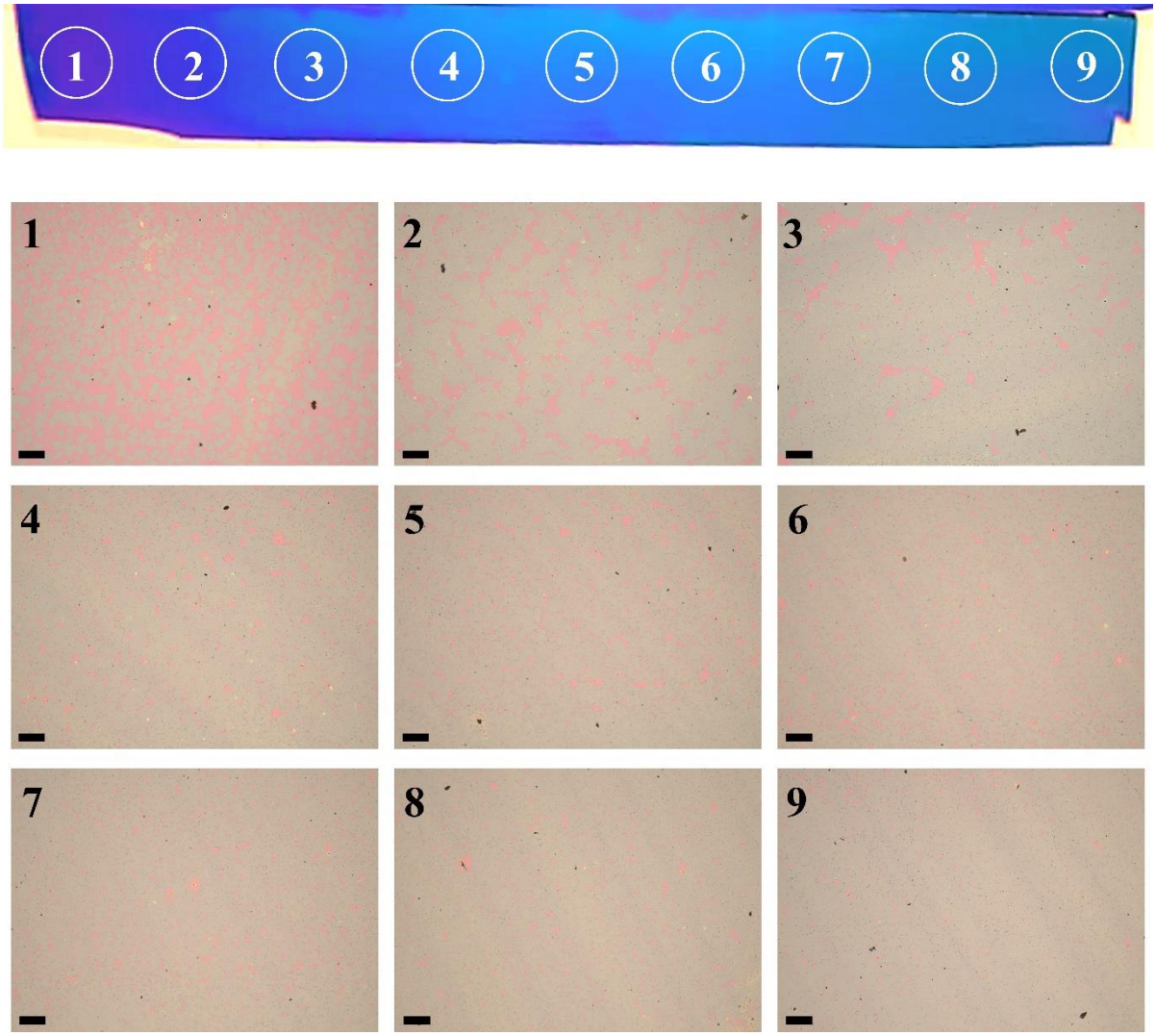


Figure 4.4: (a) Optical images taken at 5x magnification at different positions (as marked in the substrate as shown at the top of the image) of the $MoS_2$ film grown on the long substrate (scale bar 400$\mu$m).

## 4.3 Modulating flow near the substrate surface

The drastic change in the monolayer coverage with minute changes in flow demonstrates the extensive optimization required to achieve a monolayer.[39] The conditions suitable for bulk $MoS_2$ growth on the other hand are not as stringent as the monolayer growth as the layer number

can be arbitrary. So we thought of a way to grow monolayer $MoS_2$ utilizing subtle variations in substrate surface flow under conditions suited for bulk growth. In this context, "bulk" refers to a thickness sufficient to reflect the most visible part of the light, resulting in a coloration resembling that of bulk $MoS_2$. This occurs at a layer thickness of 9-10 layers or more, reflecting over 30% of light in the 500-600 nm range.[48] Our halogen vapor lamp emits yellowish light, aligning with the desired peak range. Since growing bulk $MoS_2$ requires less parameter optimization than monolayer growth, this method is less sensitive to intricate growth condition details. To obtain a monolayer in this scenario, we create a concentration gradient of precursors or restrict precursor accessibility to the substrate surface. Achieving this involves placing small silicon pieces, acting as blockades, on the substrate where $MoS_2$ growth is desired. The size, shape, and arrangement of these blockades affect the precursor flow on the substrate surface. The result is a decrease in the flow or quantity of material reaching the substrate as we approach the blockades. We refer to this phenomenon as "the blockade effect."

### 4.3.1 Blockades

In order to test our hypothesis, we utilized a quartz tube with a 4 cm inner diameter for the growth of $MoS_2$. It was crucial to creating favorable conditions for the bulk $MoS_2$ growth, so we adjusted the concentration of the growth promoter and $MoO_3$. Specifically, we increased the concentration of the growth promoter and used 600 mg of $MoO_3$ precursor in an alumina boat placed 16 cm away from another boat containing 600 mg of sulfur precursor. The substrates, cleaned as previously mentioned, were positioned on top of the $MoO_3$ boat after being treated with a few drops of a 0.01 Molar NaCl solution, and followed by blow-drying. The remaining growth conditions remained the same as in our previous experiments, with the exception of setting the Nitrogen flow to 50 sccm during the growth process and allowing the furnace to naturally cool down to room temperature. The schematic diagram of our second study can be observed in Fig. 4.5a, which illustrates the configuration of two substrates arranged in a cross-like pattern (Fig. 4.5b).

After the growth process, the substrate exhibited monolayers in proximity to the region where the blockade was located. Moving away from this region, the amount of bulk $MoS_2$ increased as expected. The monolayer itself had a width of approximately 100 micrometers and extended

continuously from one end of the substrate to the other, with its length limited by the size of the substrate used (1 cm in this case).

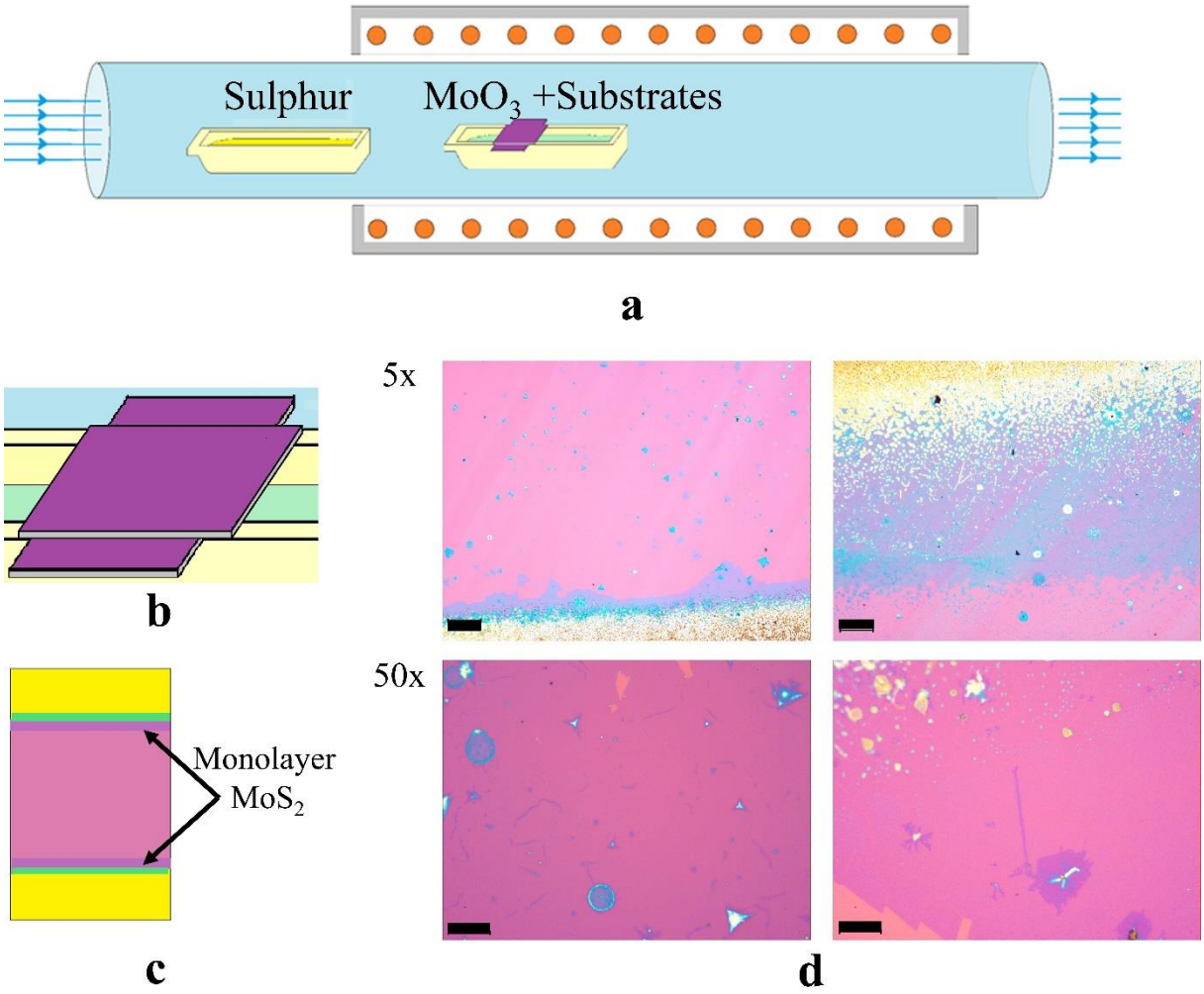


Figure 4.5: (a) Schematics showing the arrangement of the boats and substrate for the second study.(b) Shows how the substrates were kept on the $MoO_3$ boat.(c) Schematic of the substrate after the growth, the violet colored region on the pink substrate is the monolayer $MoS_2$ and the yellow and green colors are for bulk $MoS_2$.(d) The optical images of the two $MoS_2$ strips depicted in figure (c The left panel displays the bottom strip, while the right panel shows the top strip, both captured at magnifications of 5x and 50x. The scale bars in the 5x and 50x images correspond to 400 **µ**m and 50 **µ**m, respectively.

This technique demonstrates scalability, allowing for the production of large, continuous strips of monolayers. The only limitations are the length of the substrate and the presence of any blockades, assuming that the entire growth region is suitable for the growth of bulk $MoS_2$. In

Fig. 4.5b, the substrate and blockade configuration is depicted, while Fig. 4.5c provides a schematic representation of the substrate after $MoS_2$ growth. Additionally, Fig. 4.5d displays optical images captured under 5x (top row) and 50x (bottom row) magnification.

### 4.3.2 Calculating the Flow rate

We estimated the velocity of $N_2$ gas in the reaction zone by calculating the flow of gas in the tube and also taking the thermal expansion of the gas into consideration. The gas will expand in the reaction zone due to its high temperature, and the change in volume is related to temperature by the ideal gas equation.

$$V_2 = \frac{T_2}{T_1} V_1$$

Where, $V_1$ is the initial volume, $V_2$ is the volume of the expanded gas in the chamber, $T_1$ is room temperature and $T_2$ is the temperature of the furnace. This increase in volume will increase the flow by $\frac{T_2}{T_1}$. The gas entering the chamber is equal to the velocity of the gas multiplied by the cross-sectional area of the tube. Thus we get

$$F_i = v_i A$$

$$v_i = \frac{F_i}{A}$$

Where, $v_i$ is the velocity of gas inside the tube at room temperature, $A$ is the cross-sectional area of the tube and $F_i$ is the flow rate of the gas. Accounting for the expansion of gases we end up with

$$v_r = \frac{T_2}{T_1} v_i$$

$$v_r = \frac{F_i}{A} \times \frac{T_2}{T_1}$$

Here, $v_r$ is the velocity of carrier gas inside the furnace at $T_2$. The room temperature was always 298 K and the furnace temperature was 973 K.

In the first study, we used a flow rate of 27 sccm and a diameter of 3.2 cm. Thus we get

$$v_1 = \frac{27}{\Pi(1.6)^2} \times \frac{973}{298}\ cm/min$$

$$v_1 = 11\ cm.min^{-1} = 0.0018\ m.s^{-1} \sim 0.002\ m/s$$

Similarly, for the second study we used a tube with a diameter of 4 cm and a flow rate of 50 sccm we get

$$v_2 = 13\ cm.min^{-1} = 0.0022\ m.s^{-1} \sim 0.002\ m/s$$

The flow was kept nearly same for both tubes. This flow is however an underestimation as the real system would have evaporated sulphur and $MoO_3$. The flow of these two precursors is what determines the growth of monolayer. But for simplicity we assume that their flow rate is same as that of carrier gas. Using the simulation, we are trying to show that the blockade gradually reduces the flow rate in its vicinity.

### 4.3.3 Computing flow using COMSOL

We used COMSOL to simulate the flow. In COMSOL we manually adjusted the meshing to increase the resolution of the simulation. The physics interface solves the Navier-Stokes equations, for incompressible and Newtonian gas without the time-dependent part, which is given by

$$\rho(u.\nabla)u = \nabla.[-pI + \mu(\nabla u + (\nabla u)^T)] + F$$

$$\rho\nabla.u = 0$$

Also, $$S = \frac{1}{2}(\nabla u + (\nabla u)^T)$$

Where, $\rho$ is the density (kg/m$^3$), $u$ is the velocity vector (m/s), $p$ is pressure (Pa), $F$ is the volume force vector (N/m$^3$), $T$ is the absolute temperature (K), μ is the dynamic viscosity of the gas and $S$ is the strain-rate tensor.

For the boundary condition, the default boundary treatment is the automatic wall treatment and we did not alter it. The automatic wall treatment assumes that there is a small gap, δw$= \frac{h_w}{2}$, between the computational domain and the physical wall. Here, $h_w$ is the height of the mesh cell adjacent to the wall and here the velocity $u$ is taken as zero for the no-slip condition used in the simulation.

We made 3-D models of the substrate with the blockades as shown in Fig 4.6a and b which were used to simulate the flow. The meshing was adjusted manually to minimize computation time, keeping sufficient resolution, depending on the model. As the actual reaction includes more complex interaction, we only consider the decrease in flow and hence the decrease in the precursor vapor concentration locally near the substrate surface.

The exact solution is dependent on the dynamic viscosity and the density of the gas. The problem lies with the fact that sulphur vapor at temperatures of between 200 and 1000 °C consists of molecules with 2–10 atoms, some of which exist as two or more isomers.[49] This coupled with the fact that we can only give a very rough estimate of the amount of sulphur and $MoO_3$ vapors with not much idea of the exact viscosity or density of the gas mixture makes an exact simulation of flow very difficult. But the blockade effect will show a similar trend no matter what the gas used is.

The simulation provides a clear depiction of how the presence of a blockade on top of the substrate affects the flow dynamics. The expansion of gas as it enters the furnace was considered during the calculation of the flow rate. The simulated figures in Fig. 4.6a (for a single blockade) and 4.6b (for multiple blockades) illustrate the flow patterns and 3D representations of the objects for which the flow was simulated.

The simulation reveals that the flow is constrained in the vicinity of the blockade. As we move away from the blockade, the flow gradually returns to its normal value. This observation aligns well with the experimental findings presented in Fig. 4.5, where the region closest to the blockade exhibited monolayers, while the layers became thicker as we moved farther away. The precise gradient or extent to which the flow is affected depends on the properties of the gas mixture, but it is expected to follow a similar trend.

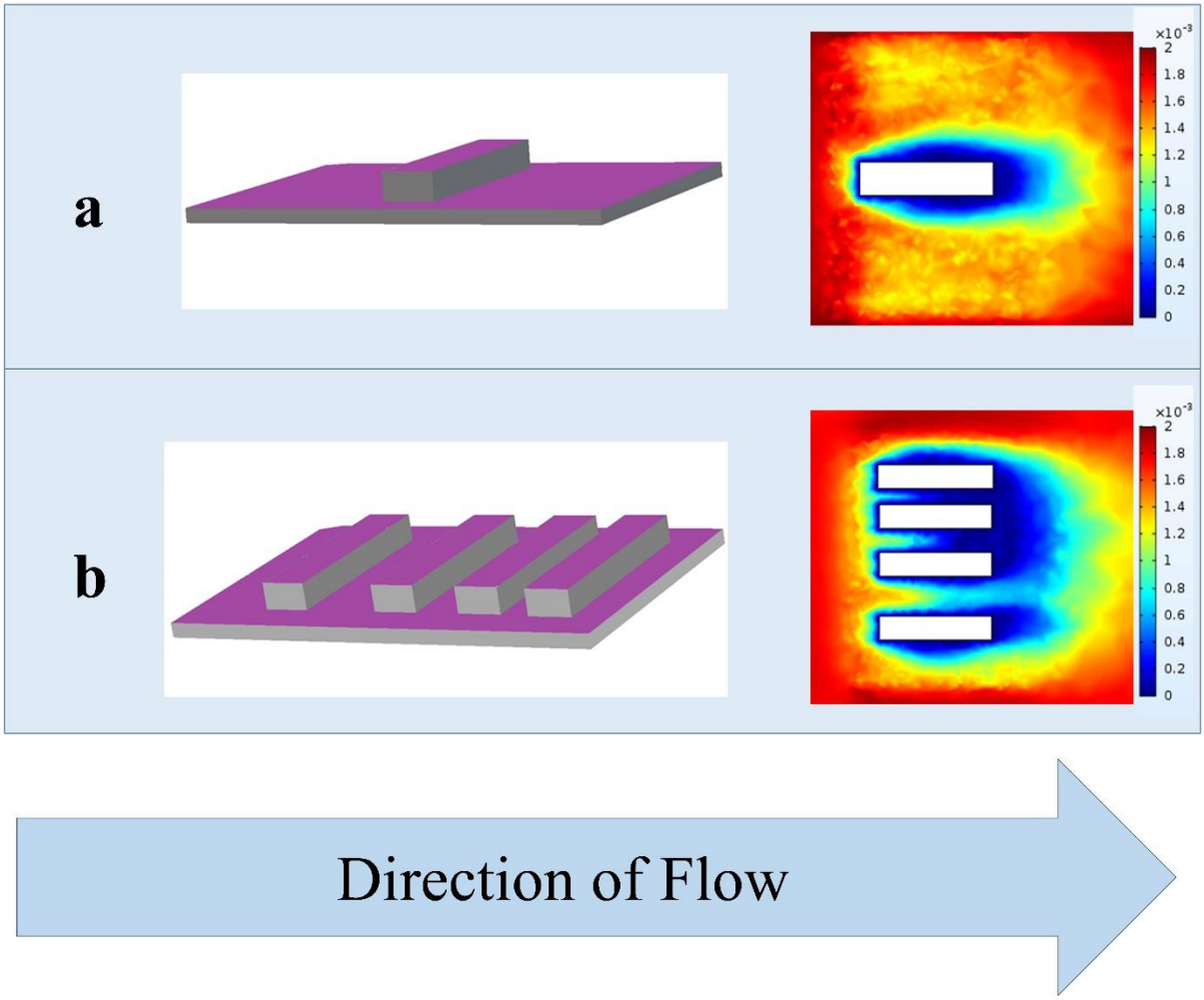


Figure 4.6: The schematic displays the 3D models used for simulation, presented at an angled view to emphasize their structural aspects. The left panel illustrates the 3D models used, while the right panel demonstrates the simulated flow patterns surrounding the blockades. The color bar indicates the velocity of the flow in m/s. Figure (a) illustrates the impact on flow dynamics with a single blockade, while Figure (b) showcases the simulated flow behavior in the presence of multiple blockades with varying spacing between them.

We tried to use different gases for simulation, like Helium, water vapor, Nitrogen, carbon dioxide and $SiF_4$, the properties of these gases are inbuilt to COMSOL and thus are easy to use, to simulate the flow. All gases showed the blockade effect. Out of these gases, the effect was more pronounced in $SiF_4$. We have used $SiF_4$ for our simulation. There is a rationale behind using this gas; $SiF_4$ has a molar mass of 104 u, which might be closer to the average density of the gas mixture. This is because the concentration of $S_4$ is maximum at 900 K and the molar mass is 128 u, that of $MoO_3$ is 143 u and Nitrogen gas is 28 u.[49] We vaporize 600 g of sulphur during growth, which means that the amount of sulphur vapor is much more than the others. A

comparison of simulations with different gases is shown in Fig. 4.7; inbuilt extremely fine meshing was used for this. It is clear that the flow of all gases decreases in a similar fashion. In $SiF_4$, the flow decreases less drastically and we can easily see the large variation in the region of interest.

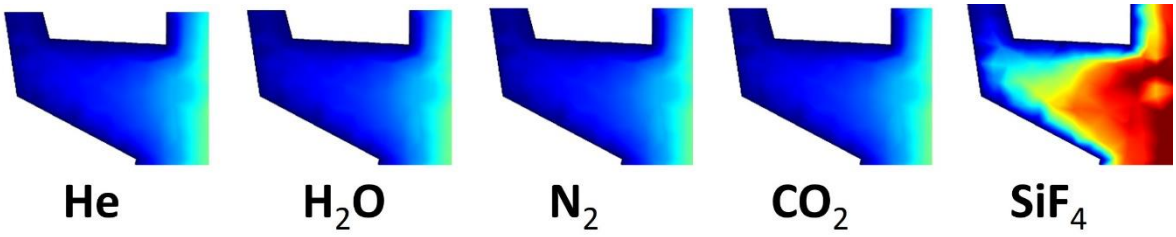


Figure 4.7: Simulation results using different gases from the lightest to the heaviest.

### 4.3.4 Fine tuning the flow using blockades

As the idea of blockade effect revolves around limiting the gas flow to self-optimize the conditions required for growing monolayer near the blockade, it is thus possible to use multiple blockade to limit flow to favor monolayer growth. From Fig. 4.6b it is clear that if two blockades are kept side by side, the flow is altered differently and is dependent on the distance between the adjacent blockades, given that their height and length remain the same. At the optimum separation between them, we can get a strip of clean monolayer of $MoS_2$. If the gap is too big, then bulk growth starts between the layers. If it is too short, then the continuous monolayers might form at the entrance and as we move in the direction of flow, scattered monolayers are observed. To show further how subtle change in flow on the substrate surface can affect the growth of monolayer, we kept the blockades of different shapes at various configurations and compared our experimental findings with simulated results. Fig. 4.8a shows the 3D model of blockades on $SiO_2$ that were kept for the growth. Simulated images in Fig. 4.8b correspond to the arrangements depicted in Fig. 4.8a. Additionally, Fig. 4.8c and d display optical images of the substrate after growth for four distinct blockade configurations at magnifications of 5x and 50x, respectively. The images demonstrate a strong correlation between the simulated and experimental outcomes.

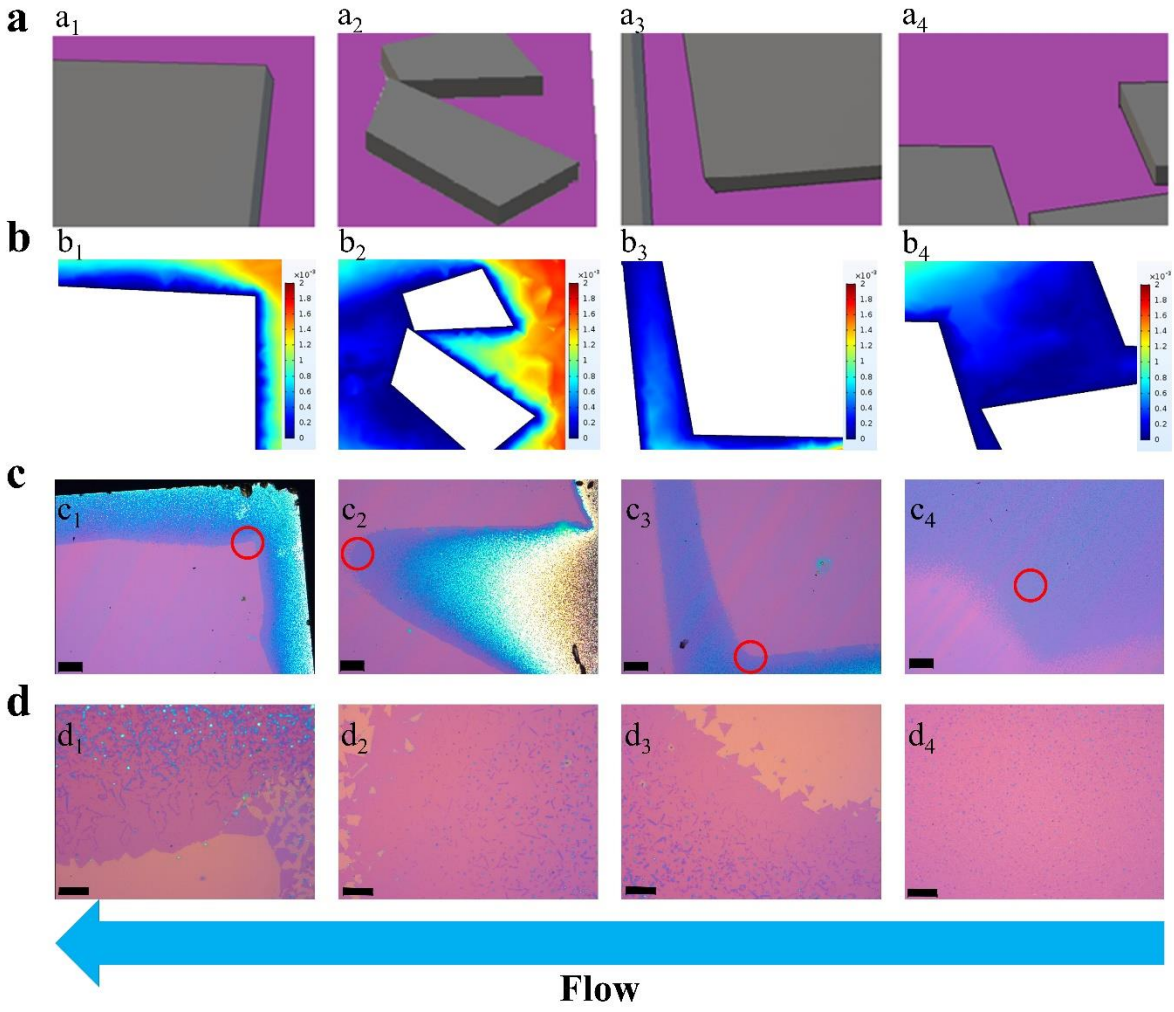


Figure 4.8: **(**a) Model of blockades on the substrate surface used for simulation using COMSOL. (b) Results of the simulation for the respective models. (c) Corresponding experimental results of the $MoS_2$ growth (scale bar 400**μ**m) show an excellent match between the experiment and simulation. Magnified images of regions marked in red circles are shown in (d). The scale bar is 50 **μ**m.

In Fig. 8b (b2), the second blockade configuration illustrates how the precursor flow decreases when entering the blockade, forming an angled path. As the flow reaches the corner within the blockade, it diminishes, resulting in a significant reduction in the number of $MoS_2$ layers in the corner region. Eventually, a continuous monolayer region of $MoS_2$ is obtained, with a few scattered $MoS_2$ flakes observed between the corner and the monolayer region. The experimental findings in Fig. 8b (b3) for the third blockade configuration are particularly intriguing, as they suggest the possibility of achieving patterned growth of $MoS_2$ monolayers using the blockade

effect. By precisely adjusting the distance and geometric shapes of the blockades, desired patterned MoS2 monolayers can be grown. In terms of area coverage, the fourth blockade configuration (Fig. 8b (b4)) yields a larger monolayer coverage. However, upon closer examination of the images, numerous thin cracks are visible in the film, indicating that it is not electrically continuous. These results clearly demonstrate that blockades offer a self-limiting control over the growth of monolayers in their proximity.

## 4.4 Characterization of $MoS_2$ films

It is of paramount importance to thoroughly assess whether the scalable synthesis techniques preserve the desirable properties of the materials or if the resulting products exhibit diminished quality. In the case of $MoS_2$, which possesses intriguing optical and electrical properties, we had to verify the optical and electrical quality of the samples. To ascertain the electrical quality of the synthesized monolayers, active field-effect transistor (FET) devices were fabricated and examined. Additionally, PL and Raman spectroscopy techniques were employed not only to serve as indicators of sample quality but also to confirm the monolayer nature of the films. By comprehensively assessing the optical and electrical characteristics, valuable insights can be gained regarding the suitability and viability of the fabrication technique for large-scale production.

### 4.4.1 Optical Characteristics

The optical properties of the samples were characterized through Raman spectroscopy and PL measurements at room temperature, utilizing a 532nm laser. Raman spectroscopy serves as a reliable method for determining the number of layers in layered materials. The difference in Raman shift between the in-plane vibrational mode ($E^1_{2g}$) and the out-of-plane vibrational mode ($A_{1g}$), provides insight into the layer number of $MoS_2$, particularly up to four layers.[50] In accordance with Fig. 4.9a, a Raman shift of 19 $cm^{-1}$ was observed, consistent with the value expected for a monolayer of $MoS_2$. [51]

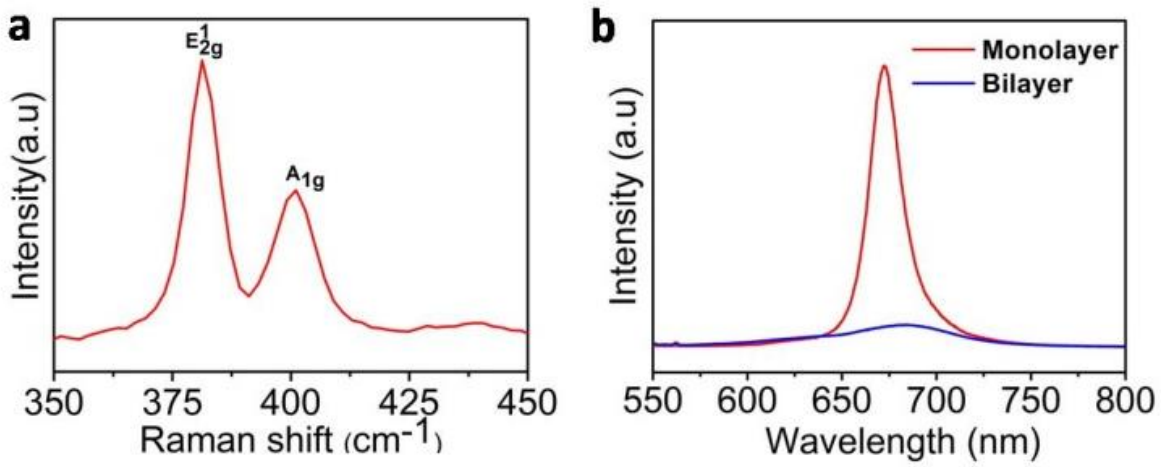


Figure 4.9: (a) Raman and (b) PL spectra demonstrating the monolayer characteristic of as-grown $MoS_2$. A PL spectrum from a bilayer is provided for reference, presented on the same scale. The monolayer exhibits a remarkably strong photoluminescence intensity owing to its direct band gap.

The photoluminescence spectra, as illustrated in Fig. 4.9b, exhibited two prominent peaks at 674 nm (1.84 eV) and 626 nm (1.98 eV), corresponding to the two direct excitonic transitions at the Brillouin zone K point, denoted as A and B excitons.[52] The full width at half maximum (FWHM) of the A excitonic peak, when fitted with a Lorentzian function, was determined to be 53 meV. This value closely resembles that of a freely suspended monolayer of exfoliated $MoS_2$, but additional analysis is required to further comment on the quality of monolayer in detail.[53] Another indicator of the optical sample quality is the very low ratio of the B- and A-exciton intensities as it reflects the density of non-radiative defects.[54] Our samples had a very low B/A exciton ratio which indicated a lack of defects that could cause non-radiative decays. However, these approaches are not dependable means of assessing the defect density of the sample, as the defects responsible for p-doping the sample play a role in suppressing non-radiative trionic decay in n-type $MoS_2$, thereby enhancing the PL intensity.[55] Kim *et al* studied the role of defects generated through processes like vacuum annealing or chemical doping, including the use of substances like $AuCl_3$, which caused a reduction in valley polarization.[55] This decline in valley polarization was primarily attributed to the presence of defects or impurities, leading to the alteration of the valley-contrasting optical selection rule. This finding underscores the

potential for conducting detailed investigations into these defects, thereby providing a more comprehensive and accurate understanding of defects. [55][56]

As the presence of P-type defects/impurities could explain the narrow FWHM and the low B/A exciton ratio it is important to explore the presence of these defects/impurities to comment on sample quality. Though we were unable to carry out valley polarization studies, exploring the electrical mobility of monolayers could confirm the presence of these defects/impurities. The charged defects or impurities responsible for p-doping in the n-type monolayer are expected to increase scattering, causing the mobility of the monolayer to decrease drastically.

### 4.4.2 Transfer Characteristics

The electrical properties of the monolayer $MoS_2$ were investigated through the fabrication of devices using photolithography. The $SiO_2$ on the Si substrate on which the monolayers were grown was used without further treatments. The devices were made using standard photolithography using S1813 photoresist and MF319 developer. This was followed by thermal vapor deposition of 5 nm chromium and 65 nm of gold. The liftoff was done in acetone and was washed in IPA and blow-dried before the measurements.

Fig. 4.10a presents an optical microscope image of a representative device. All electrical characterizations were conducted under ambient conditions in an open environment using our homebuilt probe station. Fig. 4.10b displays the I-V characteristics of the $MoS_2$ device in both dark and under illumination using a white LED. The consistent linear response of the device in both dark and light conditions indicates that the contact exhibits Ohmic behavior.

To evaluate the performance of the devices as field-effect transistors (FETs), a source-drain voltage ($V_{sd}$) was applied across a 4 μm channel, which was defined by etching the monolayer. The back gate insulator consisted of a 300 nm $SiO_2$ layer. Fig. 4.10b depicts the characteristics of a typical n-type channel FET device, demonstrating the relationship between gate voltage ($V_g$) and source-drain current ($I_{sd}$). [57] The gate scan of the FET from -50V to +50V demonstrated an $I_{on}/I_{off}$ ratio exceeding $10^4$ for the fabricated devices. The field-effect mobility was determined by analyzing the $I_{sd}$-$V_g$ curve, utilizing the following formula:

[57]

$$\mu = \frac{dI_{sd}}{dV_g}\frac{L}{WC_gV_{sd}}$$

where, $L$ is the channel length, $W$ is the channel width, $C_g$ is the gate capacitance per unit area

$$C_g = \frac{\varepsilon_0\varepsilon_r}{d}$$

where, $\varepsilon_0$ = 8.854×10$^{-12}$ Fm$^{-1}$, $\varepsilon_r$ for $SiO_2$ is 3.9, and $d$ is the thickness of $SiO_2$, here it is 300 nm. The device exhibited a carrier mobility of 0.85 cm$^2$/ Vs.

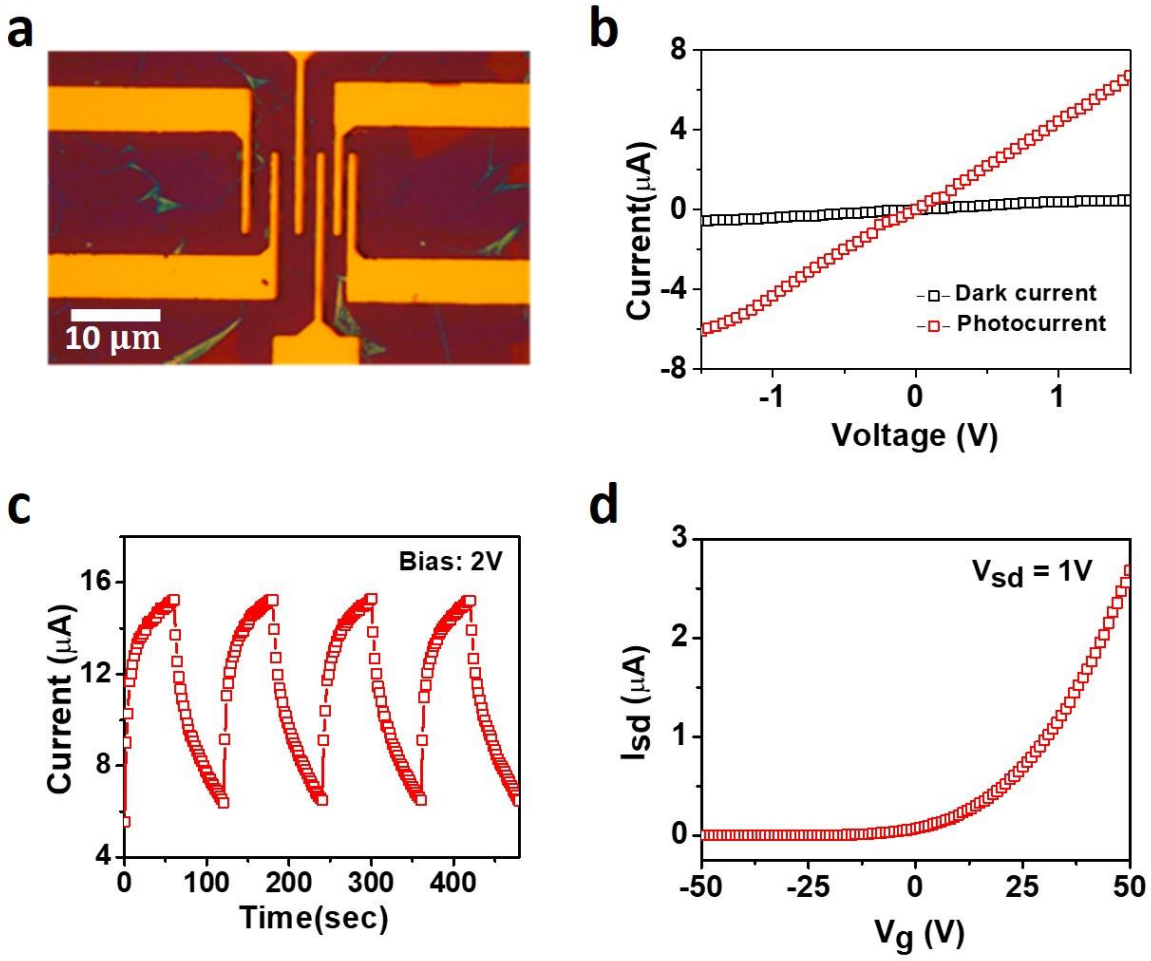


Figure 4.10: (a) Representative device captured in an optical microscope image. (b) The I-V plot of the device under dark and when illuminated using a white LED. (c) Transient photoresponse of the monolayer $MoS_2$ device. (d) Plot illustrating the relationship between source-drain current ($I_{sd}$) and gate voltage ($V_g$), indicating n-type behavior.

The values of mobility obtained were comparable to the values obtained in our previous study.[39] This implied that the approach of growing monolayers by modulating the flow does not affect the quality of the monolayers synthesized and is similar to the ones grown without the use of blockades.

## 4.5 Summary

In this chapter, we focused on the sensitivity of CVD growth of monolayer TMDs to subtle variations in flow dynamics. NaCl was used as a growth promoter at a temperature of 700 °C for this study. Through our experiments, we demonstrated that the flow can be selectively restricted by implementing obstacles referred to as "blockades." By employing these blockades, we successfully modulated the flow, thereby facilitating the growth of monolayers under conditions that are suitable for bulk growth. Further investigations revealed that the electric and optoelectronic properties of the synthesized monolayers were comparable to those synthesized without the use of blockades. The Field effect mobility of the as-synthesized monolayers is comparable to the ones grown without the blockade, but they were lacking when compared to exfoliated layers. The lower electrical quality of the monolayer is attributed to the growth promoter rather than inherent issues with the techniques employed. Overall, our findings highlight the significance of flow modulation using blockades in CVD growth, showcasing the potential to achieve monolayer growth under conditions that are suited for bulk growth, while maintaining comparable electrical and optical properties. Further exploration of growth promoters or synthesis conditions is needed to address the limitations in the quality of monolayers.

**Bibliography**

[1] Xu X, Yao W, Xiao D and Heinz T F 2014 Spin and pseudospins in layered transition metal dichalcogenides *Nat. Phys.* **10** 343–50

[2] Mak K F, He K, Shan J and Heinz T F 2012 Control of valley polarization in monolayer MoS2 by optical helicity *Nat. Nanotechnol.* **7** 494–8

[3] Zeng H, Dai J, Yao W, Xiao D and Cui X 2012 Valley polarization in MoS 2 monolayers by optical pumping *Nat. Nanotechnol.* **7** 490–3

[4] Xiao D, Liu G Bin, Feng W, Xu X and Yao W 2012 Coupled spin and valley physics in monolayers of MoS 2 and other group-VI dichalcogenides *Phys. Rev. Lett.* **108**

[5] Carr S, Massatt D, Fang S, Cazeaux P, Luskin M and Kaxiras E 2017 Twistronics: Manipulating the electronic properties of two-dimensional layered structures through their twist angle *Phys. Rev. B* **95**

[6] Bhattacharyya S, Pandey T and Singh A K 2014 Effect of strain on electronic and thermoelectric properties of few layers to bulk MoS 2 *Nanotechnology* **25** 465701

[7] Singh E, Singh P, Kim K S, Yeom G Y and Nalwa H S 2019 Flexible Molybdenum Disulfide (MoS 2 ) Atomic Layers for Wearable Electronics and Optoelectronics *ACS Appl. Mater. Interfaces* **11** 11061–105

[8] Wang H, Yuan H, Sae Hong S, Li Y and Cui Y 2015 Physical and chemical tuning of two-dimensional transition metal dichalcogenides *Chem. Soc. Rev.* **44** 2664–80

[9] Splendiani A, Sun L, Zhang Y, Li T, Kim J, Chim C-Y, Galli G and Wang F 2010 Emerging Photoluminescence in Monolayer MoS 2 *Nano Lett.* **10** 1271–5

[10] Lee C, Yan H, Brus L E, Heinz T F, Hone J and Ryu S 2010 Anomalous lattice vibrations of single- and few-layer MoS2 *ACS Nano* **4** 2695–700

[11] Zheng J, Zhang H, Dong S, Liu Y, Tai Nai C, Suk Shin H, Young Jeong H, Liu B and Ping Loh K 2014 High yield exfoliation of two-dimensional chalcogenides using sodium naphthalenide *Nat. Commun.* **5** 1–7

[12] Wu S, Huang C, Aivazian G, Ross J S, Cobden D H and Xu X 2013 Vapor-solid growth of high optical quality MoS2 monolayers with near-unity valley polarization *ACS Nano* **7** 2768–72

[13] Zhang W, Huang J K, Chen C H, Chang Y H, Cheng Y J and Li L J 2013 High-gain phototransistors based on a CVD MoS2 monolayer *Adv. Mater.* **25** 3456–61

[14] Tan L K, Liu B, Teng J H, Guo S, Low H Y and Loh K P 2014 Atomic layer deposition of a MoS2 film *Nanoscale* **6** 10584–8

[15] Late D J, Shaikh P A, Khare R, Kashid R V., Chaudhary M, More M A and Ogale S B 2014 Pulsed laser-deposited MoS2 thin films on W and Si: Field emission and photoresponse studies *ACS Appl. Mater. Interfaces* **6** 15881–8

[16] Liu H F, Wong S L and Chi D Z 2015 CVD Growth of MoS2-based Two-dimensional Materials *Chem. Vap. Depos.* **21** 241–59

[17] Li L, Long R and Prezhdo O V. 2018 Why Chemical Vapor Deposition Grown MoS2 Samples Outperform Physical Vapor Deposition Samples: Time-Domain ab Initio Analysis *Nano Lett.* **18** 4008–14

[18] Baek S H, Choi Y and Choi W 2015 Large-Area Growth of Uniform Single-Layer MoS2 Thin Films by Chemical Vapor Deposition *Nanoscale Res. Lett.* **10** 388

[19] Yang P, Zou X, Zhang Z, Hong M, Shi J, Chen S, Shu J, Zhao L, Jiang S, Zhou X, Huan Y, Xie C, Gao P, Chen Q, Zhang Q, Liu Z and Zhang Y 2018 Batch production of 6-inch uniform monolayer molybdenum disulfide catalyzed by sodium in glass *Nat. Commun.* **9** 1–10

[20] Smithe K K H, Suryavanshi S V., Muñoz Rojo M, Tedjarati A D and Pop E 2017 Low Variability in Synthetic Monolayer MoS 2 Devices *ACS Nano* **11** 8456–63

[21] Lee Y-H, Zhang X-Q, Zhang W, Chang M-T, Lin C-T, Chang K-D, Yu Y-C, Wang J T-W, Chang C-S, Li L-J and Lin T-W 2012 Synthesis of Large-Area MoS 2 Atomic Layers with Chemical Vapor Deposition *Adv. Mater.* **24** 2320–5

[22] Zhan Y, Liu Z, Najmaei S, Ajayan P M and Lou J 2012 Large-area vapor-phase growth and characterization of MoS 2 atomic layers on a SiO 2 substrate *Small* **8** 966–71

[23] Liu K K, Zhang W, Lee Y H, Lin Y C, Chang M T, Su C Y, Chang C S, Li H, Shi Y, Zhang H, Lai C S and Li L J 2012 Growth of large-area and highly crystalline MoS 2 thin layers on insulating substrates *Nano Lett.*

[24] Shi Y, Zhou W, Lu A-Y, Fang W, Lee Y-H, Hsu A L, Kim S M, Kim K K, Yang H Y, Li L-J, Idrobo J-C and Kong J 2012 van der Waals Epitaxy of MoS 2 Layers Using Graphene As Growth Templates *Nano Lett.* **12** 2784–91

[25] Jeon J, Jang S K, Jeon S M, Yoo G, Jang Y H, Park J H and Lee S 2015 Layer-controlled CVD growth of large-area two-dimensional MoS2 films *Nanoscale* **7** 1688–95

[26] Liu H F, Wong S L and Chi D Z 2015 CVD Growth of MoS 2 -based Two-dimensional Materials *Chem. Vap. Depos.* **21** 241–59

[27] Lim Y R, Song W, Han J K, Lee Y B, Kim S J, Myung S, Lee S S, An K-S, Choi C-J and Lim J 2016 Wafer-Scale, Homogeneous MoS 2 Layers on Plastic Substrates for Flexible Visible-Light Photodetectors *Adv. Mater.* **28** 5025–30

[28] Lim Y R, Han J K, Kim S K, Lee Y B, Yoon Y, Kim S J, Min B K, Kim Y, Jeon C, Won S, Kim J-H, Song W, Myung S, Lee S S, An K-S and Lim J 2018 Roll-to-Roll Production of Layer-Controlled Molybdenum Disulfide: A Platform for 2D Semiconductor-Based Industrial Applications *Adv. Mater.* **30** 1705270

[29] Govind Rajan A, Warner J H, Blankschtein D and Strano M S 2016 Generalized Mechanistic Model for the Chemical Vapor Deposition of 2D Transition Metal Dichalcogenide Monolayers *ACS Nano* **10** 4330–44

[30] Perea-López N, Lin Z, Pradhan N R, Iñiguez-Rábago A, Laura Elías A, McCreary A, Lou J, Ajayan P M, Terrones H, Balicas L and Terrones M 2014 CVD-grown monolayered MoS 2 as an effective photosensor operating at low-voltage *2D Mater.* **1** 011004

[31] Lin Z, Zhao Y, Zhou C, Zhong R, Wang X, Tsang Y H and Chai Y 2016 Controllable Growth of Large–Size Crystalline MoS2 and Resist-Free Transfer Assisted with a Cu Thin Film *Sci. Rep.* **5** 18596

[32] Yu Y, Li C, Liu Y, Su L, Zhang Y and Cao L 2013 Controlled scalable synthesis of uniform, high-quality monolayer and few-layer MoS2 films *Sci. Rep.* **3** 1–6

[33] Ozden A, Ay F, Sevik C and Perkgöz N K 2017 CVD growth of monolayer MoS2: Role of growth zone configuration and precursors ratio *Jpn. J. Appl. Phys.* **56**

[34] Wang S, Pacios M, Bhaskaran H and Warner J H 2016 Substrate control for large area continuous films of monolayer MoS 2 by atmospheric pressure chemical vapor deposition *Nanotechnology* **27** 085604

[35] Zhang T and Fu L 2018 Controllable Chemical Vapor Deposition Growth of Two-Dimensional Heterostructures *Chem* **4** 671–89

[36] Yang P, Yang A-G, Chen L, Chen J, Zhang Y, Wang H, Hu L, Zhang R-J, Liu R, Qu X-P, Qiu Z-J and Cong C 2019 Influence of seeding promoters on the properties of CVD grown monolayer molybdenum disulfide *Nano Res.* **12** 823–7

[37] Laskar M R, Ma L, Kannappan S, Sung Park P, Krishnamoorthy S, Nath D N, Lu W, Wu Y and Rajan S 2013 Large area single crystal (0001) oriented MoS 2 *Appl. Phys. Lett.* **102** 252108

[38] Zhu D, Shu H, Jiang F, Lv D, Asokan V, Omar O, Yuan J, Zhang Z and Jin C 2017 Capture the growth kinetics of CVD growth of two-dimensional MoS2 *npj 2D Mater. Appl.* **1** 8

[39] Narayanan V, M A G and Rahman A 2019 How to "train" your CVD to grow large-area 2D materials *Mater. Res. Express* **6** 125002

[40] Robertson J, Liu X, Yue C, Escarra M and Wei J 2017 Wafer-scale synthesis of monolayer and few-layer MoS2 via thermal vapor sulfurization *2D Mater.* **4**

[41] Chen B, Yu Q, Yang Q, Bao P, Zhang W, Lou L, Zhu W and Wang G 2016 Large-area high quality MoS2 monolayers grown by sulfur vapor counter flow diffusion *RSC Adv.* **6** 50306–14

[42] Xie S, Xu M, Liang T, Huang G, Wang S, Xue G, Meng N, Xu Y, Chen H, Ma X and Yang D 2016 A high-quality round-shaped monolayer MoS2 domain and its transformation *Nanoscale* **8** 219–25

[43] Mohapatra P K, Deb S, Singh B P, Vasa P and Dhar S 2016 Strictly monolayer large continuous MoS2 films on diverse substrates and their luminescence properties *Appl. Phys. Lett.* **108**

[44] Yang Y, Pu H, Lin T, Li L, Zhang S and Sun G 2017 Growth of monolayer MoS2 films in a quasi-closed crucible encapsulated substrates by chemical vapor deposition *Chem. Phys. Lett.* **679** 181–4

[45] Liu H and Chi D 2015 Dispersive growth and laser-induced rippling of large-Area singlelayer MoS 2 nanosheets by CVD on c-plane sapphire substrate *Sci. Rep.* **5** 1–8

[46] Zhang X, Nan H, Xiao S, Wan X, Ni Z, Gu X and Ostrikov K 2017 Shape-Uniform, High-Quality Monolayered MoS2 Crystals for Gate-Tunable Photoluminescence *ACS Appl. Mater. Interfaces* **9** 42121–30

[47] Narayanan V, M A G and Rahman A 2019 How to "train" your CVD to grow large-area 2D materials *Mater. Res. Express* **6**

[48] Li X, Shi Y, Li S, Shi W, Han W, Zhou C, Zhao X and Liang B 2018 Layer-number dependent reflection spectra of MoS 2 flakes on SiO 2 /Si substrate *Opt. Mater. Express* **8** 3082

[49] Steudel R, Steudel Y and Wong M W 2012 Speciation and Thermodynamics of Sulfur Vapor 117–34

[50] Li H, Zhang Q, Yap C C R, Tay B K, Edwin T H T, Olivier A and Baillargeat D 2012 From bulk to monolayer MoS 2: Evolution of Raman scattering *Adv. Funct. Mater.* **22** 1385–90

[51] Liang L and Meunier V 2014 First-principles Raman spectra of MoS2, WS2 and their heterostructures *Nanoscale* **6** 5394–401

[52] Splendiani A, Sun L, Zhang Y, Li T, Kim J, Chim C Y, Galli G and Wang F 2010 Emerging photoluminescence in monolayer MoS2 *Nano Lett.* **10** 1271–5

[53] Van Der Zande A M, Huang P Y, Chenet D A, Berkelbach T C, You Y, Lee G H, Heinz T F, Reichman D R, Muller D A and Hone J C 2013 Grains and grain boundaries in highly crystalline monolayer molybdenum disulphide *Nat. Mater.* **12** 554–61

[54] McCreary K M, Hanbicki A T, Sivaram S V. and Jonker B T 2018 A- and B-exciton photoluminescence intensity ratio as a measure of sample quality for transition metal

dichalcogenide monolayers *APL Mater.* **6**

[55] Kim D H and Lim D 2015 Effects of defects and impurities on the optical properties and the valley polarization in monolayer MoS2 *J. Korean Phys. Soc.* **66** 1564–8

[56] Mujeeb F, Chakrabarti P, Mahamiya V, Shukla A and Dhar S 2023 Influence of defects on the valley polarization properties of monolayer MoS 2 grown by chemical vapor deposition *Phys. Rev. B* **107** 115429

[57] Radisavljevic B, Radenovic A, Brivio J, Giacometti V and Kis A 2011 Single-layer MoS2 transistors. *Nat. Nanotechnol.* **6** 147–50

# Chapter 5

# Sodium silicate as growth promoter for TMD growth

## 5.1 Introduction

Growth promoters play a crucial role in enhancing the growth of monolayer TMDs in CVD by increasing the tolerance to variations in growth parameters. They enable the synthesis of monolayers over a significantly wider range of parameters, ensuring improved control and reproducibility in the growth process.[1,2] Various growth promoters containing alkali metals or aromatic organic molecules are widely used for growing monolayer TMDs as they help in seeding and growth.[1,3,4] Alkali metal compounds are the most commonly available and easy to use among them. It is reported that TMD monolayers of high quality can be grown at a fast rate by using alkali ions in glass.[5–7] Despite the significant improvement in the growth of monolayer TMDs achieved by commonly available growth promoters like NaCl, they remain highly sensitive to variations in growth parameters.[8] Furthermore, the unavailability of aromatic compounds, known for their superior coverage capabilities, poses an additional constraint. Substrates such as alkali metal-containing glass exhibit limited versatility, as they can only support the growth of monolayers on themselves and necessitate transfer techniques to achieve monolayers on substrates of interest.

To enable the widespread and large-scale implementation of monolayer TMDs, there is a need for an effective growth promoter that can reliably grow high-quality monolayers over large areas, while remaining resilient to subtle fluctuations in growth conditions and readily available. The development of such a growth promoter, which excels in terms of availability, ease of use, and effectiveness, is crucial for the advancement of monolayer TMD-based technologies. In this chapter, we present a readily available, easy-to-use, and effective growth promoter, sodium

silicate, commonly known as water glass (WG), for the growth of high-quality TMD monolayers. Our approach enables the conformal coating of monolayer TMDs onto nanotextured substrates, overcoming previous limitations. The WG growth promoter offers a broad range of applicability, exhibiting excellent performance across various CVD parameters, including temperature, precursor quantity, carrier gas flow, and substrate characteristics. Moreover, it requires minimal fine-tuning to achieve high-quality monolayers over large areas for different TMDs.

## 5.2 Sodium silicate as a growth promoter

While looking for an effective growth promoter we came across works on TMD monolayers synthesized on alkali ions containing glass.[5–7] We realized that the effectiveness of alkali ion-containing glass substrate for growing TMDs could be related to the fact that the bonds of the Na with O break as temperature increases, and the $Na^+$ ions are generated, which are highly mobile.[9] This mechanism of bond breaking in alkali metal-containing glass and has been exploited for anodic bonding[10,11] of glass and was also used to exfoliate monolayers of various 2D materials[12]. Thus we hypothesized that these highly mobile $Na^+$ ions will react more readily with $MoO_3$ than NaCl and form an intermediate of $Na_2Mo_2O_7$.[13]

With this realization, it became apparent that the efficient growth of TMDs could be achieved by applying a thin layer of heavily alkali metal-ion-doped glass. The presence of a glass matrix allows for a controlled and gradual supply of Na+ ions, with only the surface ions readily reacting with $MoO_3$ to form $Na_2Mo_2O_7$ Thus improving our control over the growth. In order to achieve coating a thin layer of alkali metal doped glass we decided to use sodium silicate solution. Sodium silicate is a chemical compound composed of sodium oxide ($Na_2O$) and silica ($SiO_2$). It is typically available in liquid or solid form and is highly soluble in water. WG is commonly used in various industrial applications, and thus is easily available and very affordable. By diluting WG in water, it becomes feasible to apply an extremely thin layer of WG onto any desired substrate using spin coating techniques.

To appraise the effectiveness of WG in growing TMDs, the growth using WG was compared to the ones using NaCl under similar conditions. For this NaCl (0.001 Molar) coated substrates were placed alternatively between WG (0.5%) coated substrates.[14] A schematic of the

arrangement used for the comparison of $MoS_2$ growth on WG-coated and NaCl-coated substrates is depicted in Fig. 5.1a. This arrangement ensured that the growth conditions and amount of vapor reaching the substrates are comparable. The CVD growth was carried out in a quartz tube of 3.5 cm diameter, in a single zone furnace. There is a separate heater just outside the furnace attached to the tube to heat the sulphur separately. Argon gas is used as a carrier gas. The alumina boat containing the sulphur is placed just outside the furnace where we have attached a separate heater and the boat containing the 10 mg of $MoO_3$ precursor is kept 15 cm away, downstream, from the boat containing the sulphur as shown. The substrates were kept facing up on a separate boat 2 cm from the boat containing the $MoO_3$ precursor. Initially, the tubes were flushed with Argon gas at 500 sccm for 5 min, and then the flow was brought down to 30 sccm and maintained at a constant value throughout the reaction. The furnace was ramped up at a rate of 5 °C/min till the reaction temperature of 700 °C is attained and maintained for 5 min to. The heater for sulphur was set at 200 °C and was turned on 5 min before the target temperature is attained and turned off after the reaction. The entire set-up is allowed to cool down naturally and the samples are taken out after it cools down to room temperature. Very good coverage of monolayer $MoS_2$ was achieved on WG-coated substrates and little to no growth was observed on the NaCl-coated substrate (Fig. 5.1a and 5.1b). By increasing the MoO3 precursor to 30 mg and the reaction time to 20 min we were able to grow continuous monolayers over a one-inch quartz slide. The photograph of the quartz slide with the continuous monolayer is kept along with an uncoated quartz slide is given in Fig. 5.1d. This demonstrated the superior performance of WG over NaCl in its efficacy to grow TMDs.

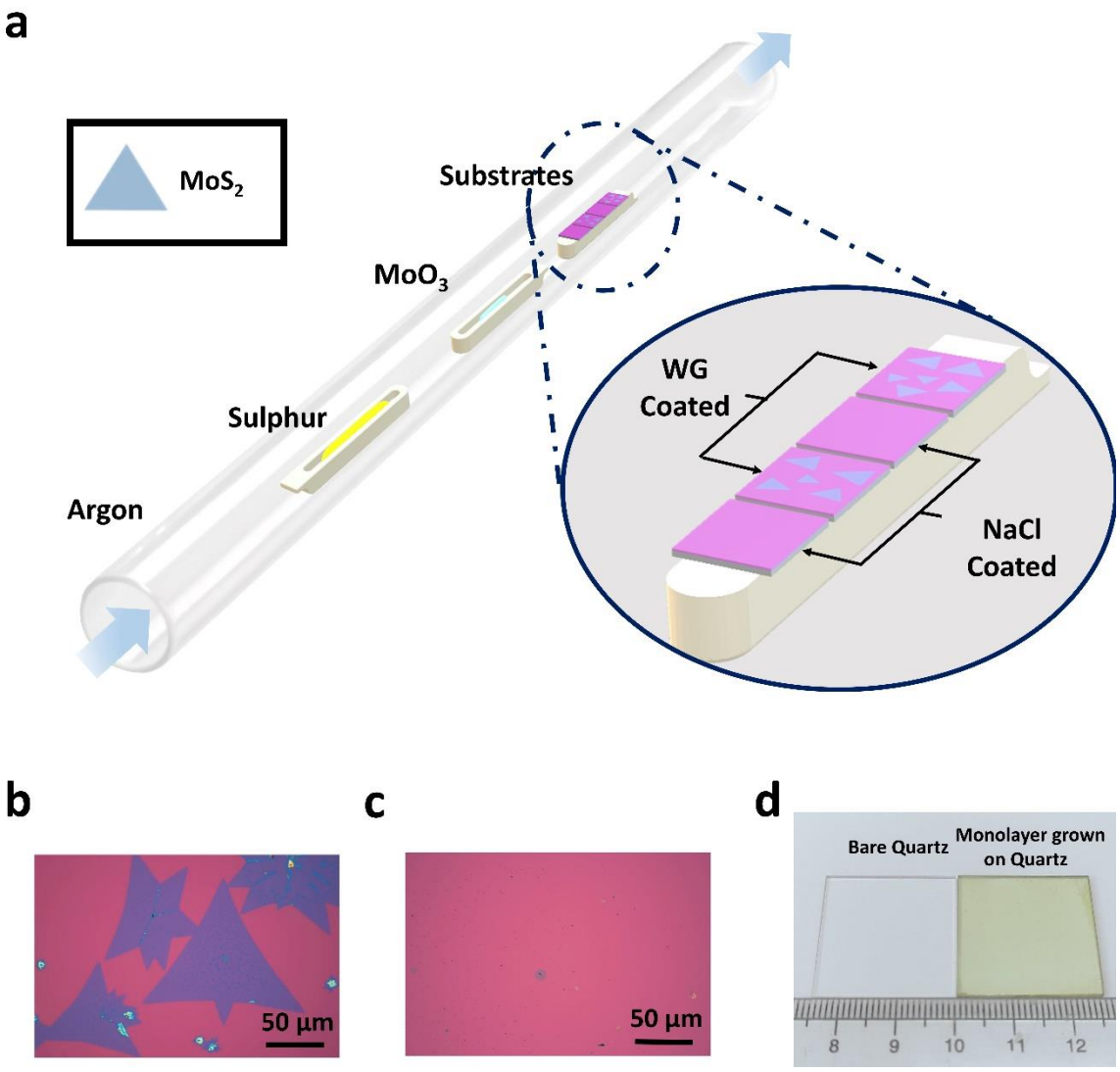


Figure 5.1: Improving the growth of monolayer TMDs using sodium silicate (WG). (a) schematic of the arrangement used to compare the effectiveness of WG and NaCl. The substrates coated with WG exhibited excellent growth whereas, the one coated with NaCl showcased poor growth under similar growth conditions. (b) and (c) are the optical microscope image of MoS2 synthesized using WG and NaCl respectively, as depicted in (a). (d) the images of a transparent fused quartz substrate, in which a continuous MoS2 monolayer is grown, (right) and an uncoated fused quartz substrate (left) were kept close for comparison.

## 5.3 Reaction mechanism

To gain further insights into the growth mechanism of $MoS_2$ with the help of WG, we need to have a better understanding of the reaction. For this, we choose to analyze the mixtures using thermo gravimetric analysis (TGA), a technique that tracks the weight change of a sample as it is heated at a constant rate. we dried WG at 400 °C for half an hour and ground it into a fine powder, and heated it again at 400 °C for another half an hour. It is crucial to heat WG at 400 °C to remove the water content completely as any leftover water could result in a slight mass loss.[15] 122 mg of this WG powder was mixed with 288 mg of $MoO_3$ in a mortar and 10 mg of the mix was used for TGA and the rest was annealed in the furnace at 27 sccm $N_2$ flow at 700 °C for half an hour for analyzing the XRD of the reacted mixture. The TGA of the WG mixture was compared to that of a mixture of 11.7 mg of NaCl mixed with 43.2 mg of $MoO_3$. 10 mg of which was used for TGA. The TGA shown in Fig. 5.2a clearly shows that the WG reacts with $MoO_3$ at a much lower temperature and the reaction is slow. The increase around 800 °C is because $MoO_3$ loses its weight significantly around this temperature. The TGA analysis of the WG mixture revealed a gradual decrease in mass even at temperatures as low as 100 °C, whereas the mass of the NaCl mixture remained constant until 380 °C. It can be inferred from the TGA results that the formation of $Na_2Mo_2O_7$ in the reaction mixture of WG+$MoO_3$ occurs at significantly lower temperatures when compared to the NaCl+$MoO_3$ mixture. These results support the hypothesis that WG powder would easily react with $MoO_3$ to form $Na_2Mo_2O_7$. The mass loss increased significantly beyond 750 °C for the WG+$MoO_3$ mixture. The low mass loss at lower temperatures might be because Na+ ions are within the glass matrix and thus only the Na+ ions at the surface react to form $Na_2Mo_2O_7$ which sublimes slowly. The XRD of the product is plotted in Fig. 5.2b and is that of $Na_2Mo_2O_7$ with some peaks from intermediate and unreacted compounds.

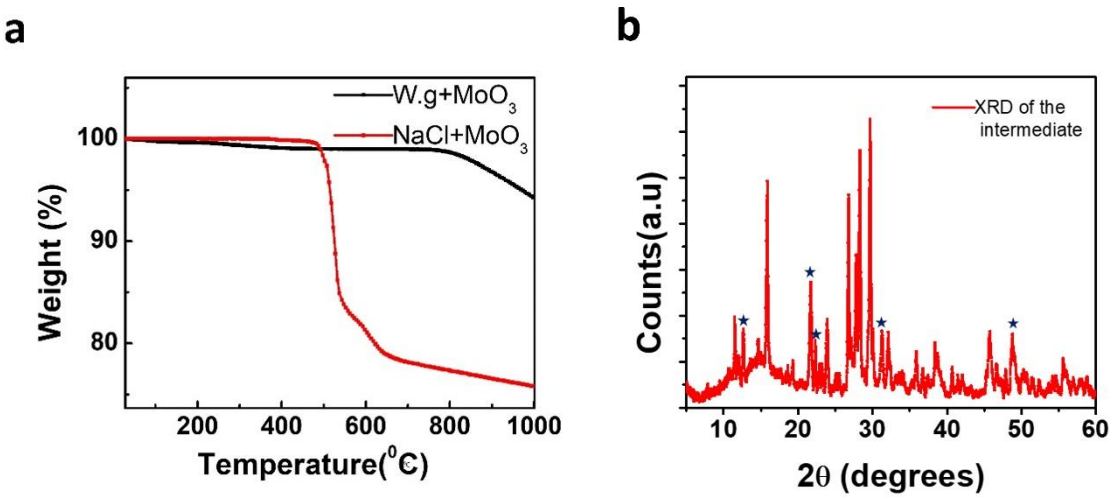


Figure 5.2: (a) TGA of the two mixtures from room temperature to 1000 °C. (b) XRD of the mixture after annealing at 700 °C. The XRD shows peaks of Na2Mo2O7 along with peaks of by-products (indicated by a star mark).

The intermediate compounds formed during the reaction were also analyzed using XPS, and Energy Dispersive X-ray spectroscopy (EDAX) Fig. 5.3. The intermediate was synthesized by repeating the synthesis process in the absence of sulfur. Initially, we spin-coated three $SiO_2$/Si substrates with 0.5% of WG in water. We heated one of the substrates inside the furnace, using a fresh tube to avoid contamination, by keeping the $N_2$ gas flow at 30 sccm at 700 °C. No visible changes were observed on the substrate. The other two substrates were heated under the same condition but in the presence of $MoO_3$ kept in a separate boat upstream of flow, 2 cm away from the substrate. Some small spheres were formed on the substrates as intermediate. One of these substrates was sulfurized at 700 °C for 10 min and the spheres acted as a nucleation point for the growth of $MoS_2$.

XPS was used to examine the bonding states in the intermediate and the $MoS_2$. The XPS data with optical images of the corresponding sample in the inset of the corresponding graphs are shown in Fig. 5.3 a, b and c. The XPS of $MoS_2$ showed $Mo^{4+}$ $3d_{5/2}$ and $3d_{3/2}$ doublet peaks at ~230 and ~232.78 eV respectively.[16] The sulfur peaks for S $2p_{3/2}$ and $2p_{1/2}$ were 162.48 and 163.68 eV, respectively and the peak emerged at 226.78 eV from 2s of sulfur (Fig. 5.3c.[17] The peaks of $Mo^{4+}$ and sulfur are in agreement with the reported values of $MoS_2$. [17] The XPS

of the intermediate showed peaks at 233.26 and ~236.18 eV corresponding to the $Mo^{6+}$ $3d_{5/2}$ and $3d_{3/2}$ doublets of $MoO_x$.[18]

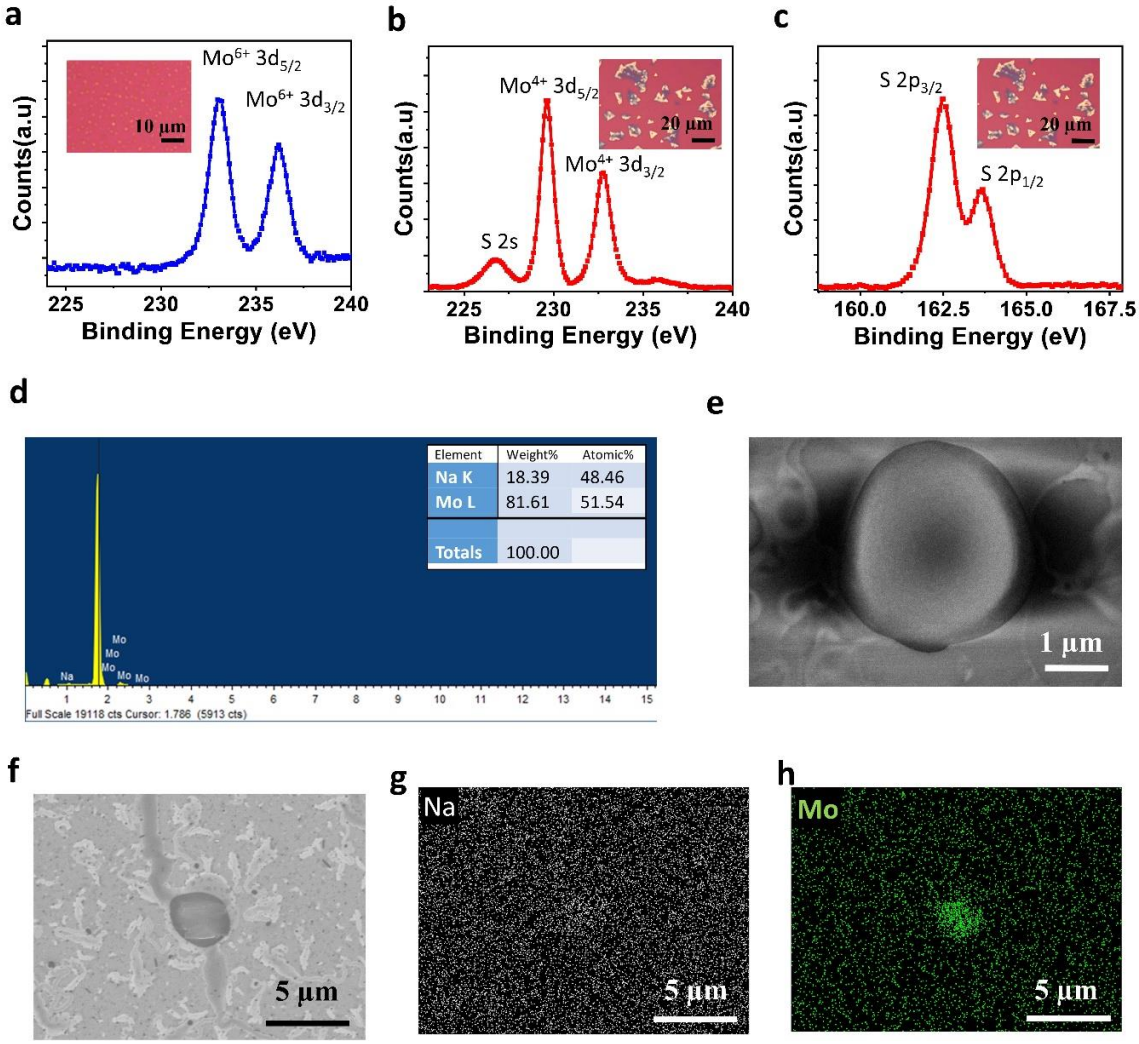


Figure 5.3: (a) The XPS spectra of the Mo 3d region of the intermediate. (b), and (c) are the XPS spectra of Mo 3d and S of the $MoS_2$ formed after annealing the intermediate in presence of sulfur gas. The inset shows the optical images of the respective samples in (a), (b), and (c). The scale bars in (a) is 10 µm and (b) and (c) are both 20 µm. (d) EDAX spectra confirming the ratio of Na: Mo to be 1:1. (e) FESEM image of the intermediate sodium molybdenum compound formed. (f) FESEM image of the area containing an intermediate that is chosen for elemental mapping. (g), and (h) is the EDS elemental maps showing Na (white) and Mo (green) of the sample shown in the SEM image in (f).

The XPS analysis revealed that Molybdenum is in the $Mo^{6+}$ oxidation state in the intermediate compound and EDAX of the intermediate showed a Mo: Na ratio of 1:1. These results indicate

that the intermediate compound formed is $Na_2Mo_2O_7$.[13] We believe that a small amount of $MoO_3$ sublimated at 700 °C and it reacted with Na ions in the WG to form $Na_2Mo_2O_7$ which were the small spheres that were formed as the intermediate for the growth of $MoS_2$. The spheres were formed because of the aggregation of $Na_2Mo_2O_7$ as the reaction proceeded. This happened due to the low melting point of the eutectic intermediate. The EDS elemental mapping shows the uniform distribution of Na and the relatively high concentration of Mo in the region where $Na_2Mo_2O_7$ is present (Fig. 5.3 g and h). All the results point to the formation of $Na_2Mo_2O_7$ as the intermediate which is the same as that formed with NaCl.[13]

## 5.4 Computing the reaction energy

From the experiments it is evident the intermediate product, i.e., $Na_2Mo_2O_7$ is the same for both WG and NaCl, we hypothesize that the differences observed in the production of $MoS_2$ for the two cases are primarily due to the differences in the efficiency with which $Na_2Mo_2O_7$ is produced. To understand this, our collaborator, Dr. Prasenjit Ghosh, have computed the reaction energies for the two reactions. Since WG exists in several forms, here we have studied the two most commonly occurring forms, sodium metasilicate ($Na_2SiO_3$) and sodium orthosilicate ($Na_4SiO_4$). We considered the following reactions for the formation of the intermediate $Na_2Mo_2O_7$:

(a) from NaCl: $2\ NaCl + 3\ MoO_3 = Na_2Mo_2O_7 + MoO_2Cl_2$

(b) from $Na_2SiO_3$: $Na_2SiO_3 + 2\ MoO_3 = Na_2Mo_2O_7 + SiO_2$

(c) from $Na_4SiO_4$: $Na_4SiO_4 + 4\ MoO_3 = 2\ Na_2Mo_2O_7 + SiO_2$

While reaction (a) has been proposed by S. Li *et al*,[13] reactions (b) and (c) have been proposed by us based on the experimental evidence that, similar to NaCl, with WG, $Na_2Mo_2O_7$ is the reaction intermediate. The structures considered for the reactants and products are shown in supplementary (Fig. 5.4). The reaction energy ($E_{rxn}$ ) is computed as the difference in total energies of products and reactants and provides the thermodynamic driving force for the reaction to happen. More negative is the value of $E_{rxn}$, larger is the driving force. Our calculations show

that while for reaction (a) $E_{rxn}$ = 0.49 eV, for (b) and (c) $E_{rxn}$ is -1.48 eV and -4.04 eV. This shows that the reaction of WG with $MoO_3$ is highly exothermic while that between NaCl and $MoO_3$ is endothermic. Typically, exothermic reactions have lower barriers than endothermic reactions.[19] Based on these calculations, we anticipate that the enormously large thermodynamic driving force is responsible for the reaction to proceed with reasonable ease in (b) and (c) compared to (a). Such a large exothermicity observed can be due to the formation of a stable product ($SiO_2$) in (b) and (c). Fig. 5.4 shows the structures of the reactants (top row) and products (bottom row) that were considered for the calculation of reaction energies.

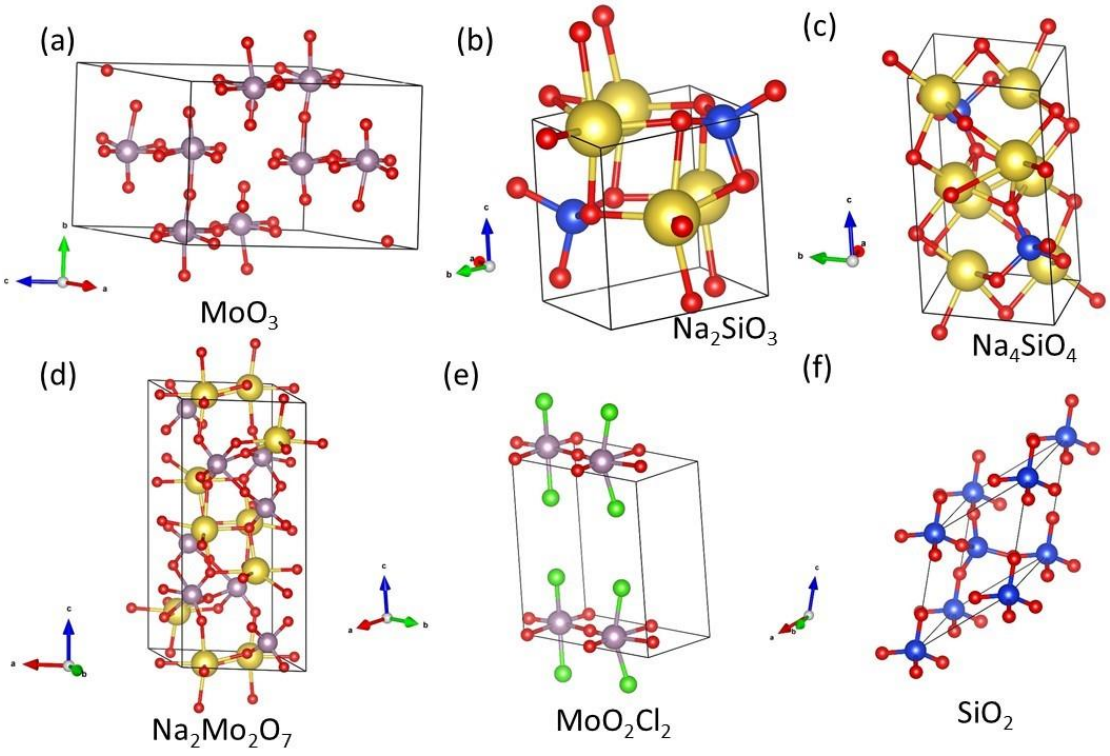


Figure 5.4: Structures of the reactants (top row) and products (bottom row) were considered for the calculation of reaction energies.

The k-grids used for the different systems are given in Table 1 below. The starting configurations were taken from the Materials Project website.

Table 5.1: k-grid used for different systems

| System | k-grid |
|---|---|
| NaCl | 6×6×6 (shifted) |
| $Na_2SiO_3$ | 5×5×7 (unshifted) |
| $Na_4SiO_4$ | 7×7×5 (unshifted) |
| $MoO_3$ | 7×7×5 (unshifted) |
| $MoO_2Cl_2$ | 8×4×4 (shifted) |
| $Na_2Mo_2O_7$ | 7×7×5 (unshifted) |
| $SiO_2$ | 6×6×6 (shifted) |

Table 5.2: Computed lattice parameters of the reactants and products.

| System | Computed lattice parameters (lengths are in Å and angles are in °) |
|---|---|
| NaCl | 5.69 (fcc) |
| $Na_2SiO_3$ | a=b=6.15, c=4.88 (hex) |
| $Na_4SiO_4$ | a=5.64 b=5.65 c=8.53<br>α=98.95, β=81.05, γ=112.40 |
| $MoO_3$ | a=7.38, b=7.74, c=10.83<br>α =90, β =132.95, γ =90 |
| $MoO_2Cl_2$ | a=3.94, b=7.76, c=8.15, orthorhombic |
| $Na_2Mo_2O_7$ | a=b=7.006, c=14.992, γ =117.931, α = β = 90 |
| $SiO_2$ | a=b=c=5.16, α=β=γ=60 |

## 5.5 Properties of the synthesized monolayers

### 5.5.1 Field effect mobility and optical characterization

To study the quality of the as-synthesized monolayers, they were grown on flat $SiO_2$/Si substrates for comparison with the literature. The electrical transport properties of TMDs were investigated by fabricating devices on monolayer $MoS_2$ synthesized using WG. The field-effect mobility of the devices was calculated from the linear region of the transfer curve using the

equation[20]

$$\mu = \frac{dI_{ds}}{dV_{bg}} \frac{L}{WC_g V_{ds}}$$

where, $L$ is the channel length, $W$ is the channel width, $C_g$ is the gate capacitance per unit area $C_g = \frac{\varepsilon_0 \varepsilon_r}{d}$, $\varepsilon_0$ = 8.854×10$^{-12}$ Fm$^{-1}$, $\varepsilon_r$ for $SiO_2$ is 3.9, and d is the thickness of $SiO_2$, here it is 300 nm.

Representative data from one of the devices is shown in Fig. 5.5a. The devices exhibited mobility 15 to 35 cm$^2$ V$^{-1}$s$^{-1}$ with an $I_{on}$/ $I_{off}$ ratio of $10^5$ to $10^6$. For comparison, devices were also fabricated on $MoS_2$ synthesized with NaCl (salt). The performance of the samples synthesized using WG was superior to that of the ones grown using NaCl. Typical mobility values of devices with salt were in the range of 0.1 to 1 cm$^2$ V$^{-1}$s$^{-1}$, which is more than one order magnitude less as compared to the WG devices. The mobility statistics of devices with NaCl and WG are shown in Fig. 5.5 (b and c) respectively for comparison. Mobility values of our WG samples are comparable to or higher than the reported values of exfoliated $MoS_2$ and the best-reported CVD-grown monolayer $MoS_2$.[21][22] The high quality of the samples synthesized using WG is evident from the electrical transport measurements.

Our collaborators in France analyzed the optical properties of the sample. The PL spectrum of $MoS_2$ synthesized at 800 °C is given in Fig. 5.5 d. The spectrum is mainly composed of an A exciton peak at 1.83 eV (678 nm) with an FWHM of 0.05 eV. There was no significant contribution to the signal from the B exciton, which indicates a very low B/A exciton ratio is indicative of good sample quality.[23][24]

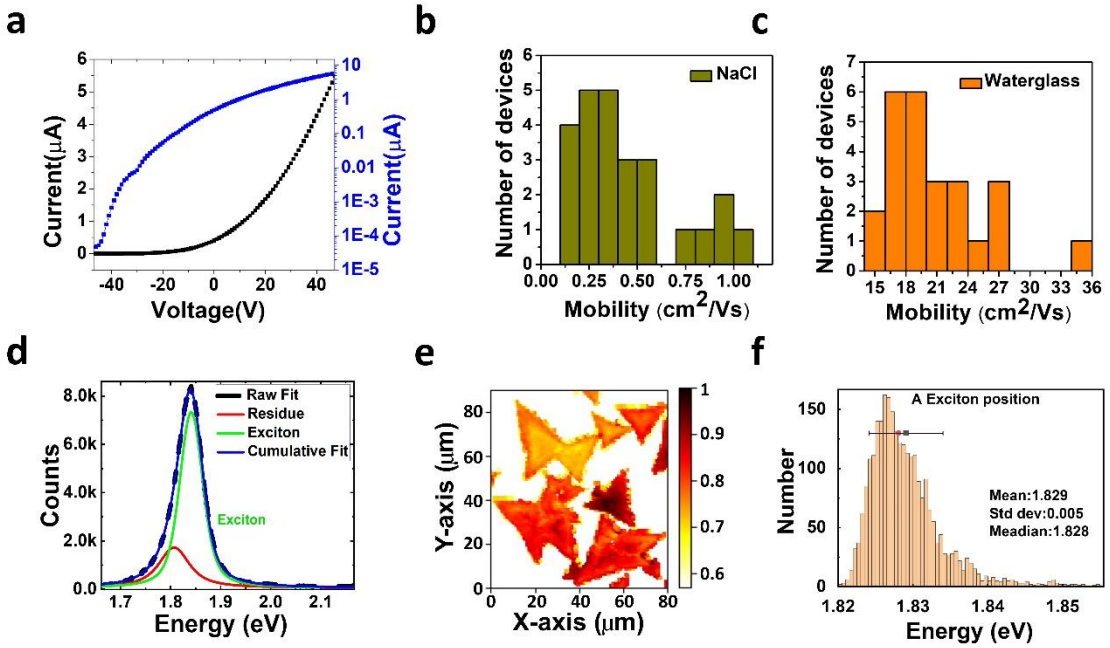


Figure 5.5: Electrical and optical properties of $MoS_2$ monolayers. (a) Source-drain current versus back gate voltage sweep of a field-effect transistor (FET) fabricated out of $MoS_2$ synthesized using WG on a plain 300 nm $SiO_2$ on Si substrate to eliminate the effects of strain. (b) and (c) are the mobility statistics of devices fabricated on monolayer $MoS_2$ synthesized with NaCl and WG respectively. (d) PL spectra of $MoS_2$ monolayer synthesized using WG at 800 °C. (e) PL mapping over a large area shows the uniformity of the sample PL (in log scale) over a large area for individual flakes synthesized using WG. (f) The statistics of the PL spectra from the mapped region.

### 5.5.2 HRTEM of $MoS_2$

The crystalline nature of the $MoS_2$ and its lattice structure was verified using HRTEM. The $MoS_2$ was transferred onto the carbon-coated TEM grid using a wet transfer technique.[25] A 10 % polystyrene solution in toluene (by weight) was spin-coated onto the substrate with $MoS_2$, which was then baked at 120°C. The sample was then immersed in water, allowing the $MoS_2$ to float on the water with the polystyrene acting as a support film. The film was scooped onto the TEM grid and was heated to 120 °C again. The polystyrene was subsequently removed using toluene, followed by sample cleaning using acetone and IPA. The TEM grid was then kept in a vacuum for 24 hrs. The lattice image was further processed using ImageJ software to resolve the Mo and S atoms. The Mo atoms are the brighter big spheres seen in the processed TEM image in Fig. 5.6 b whereas the smaller dim spheres are the Sulphur atoms. The selected area

electron diffraction (SAED) pattern in Fig. 5.6 c confirms the crystalline nature of the $MoS_2$ monolayers.

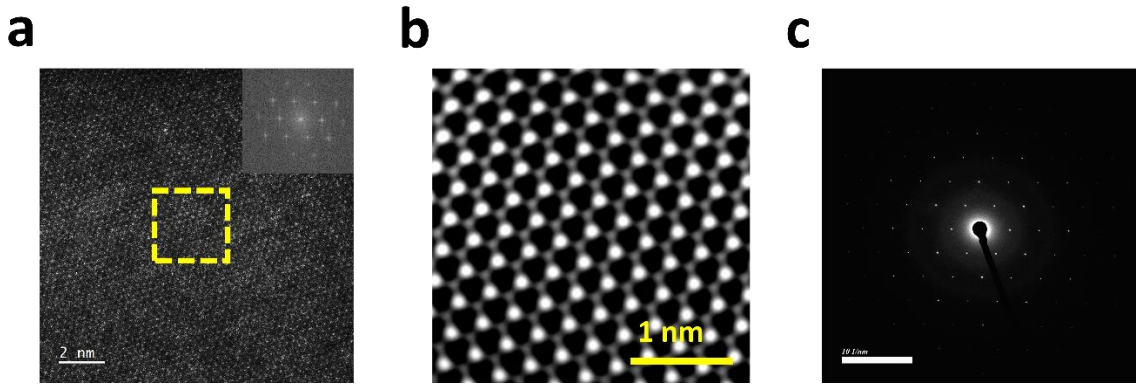


Figure 5.6: (a) The HAADF-STEM image of $MoS_2$ taken at Brookhaven National Laboratory with the inset showing the FFT image of the lattice produced using ImageJ software. (b) the inverse FFT image of the FFT pattern in (a). (c) is the SAED pattern that shows the existence of a single domain and the highly crystalline nature of the monolayer.

## 5.6 Expanding the Scope of Synthesizing monolayers

In order to show the versatility of WG as a growth promoter for monolayer TMDs. We synthesized different monolayers such as $WS_2$, $MoSe_2$, and $WSe_2$ using WG. The CVD growth was again carried out using a similar arrangement as the one used for $MoS_2$ growth. Argon gas is used as a carrier gas for the synthesis of $WS_2$. Argon hydrogen mixture (10% $H_2$) was used to synthesize $WSe_2$ and $MoSe_2$. The precursor for $MoSe_2$ was 30 mg of $MoO_3$ and 300 mg of selenium. The precursors for $WSe_2$ and $WS_2$ were 500 mg of $WO_3$ and 300 mg of selenium and sulphur respectively. The arrangement is shown in Fig. 5.7. For synthesizing $WS_2$ and $WSe_2$ (both synthesized at 850°C) the substrate was kept with WG coated smooth side facing down and for $MoSe_2$ synthesized at 700 °C the substrate was kept similar to $MoS_2$ synthesis. Initially, the tubes were flushed with Argon gas at 500 sccm for 5 min, and then the flow was brought down and maintained at a constant value throughout the reaction. The flow rate for $MoSe_2$ and $WS_2$ was 30 sccm and for $WSe_2$ was 200 sccm. The heater for chalcogens was set at 200 °C for sulfur and 300 °C for selenium. This heater was turned on 5 min before the target temperature is attained and turned off after the reaction. The entire set-up is allowed to cool down naturally and the samples are taken out after it cools down to room temperature.

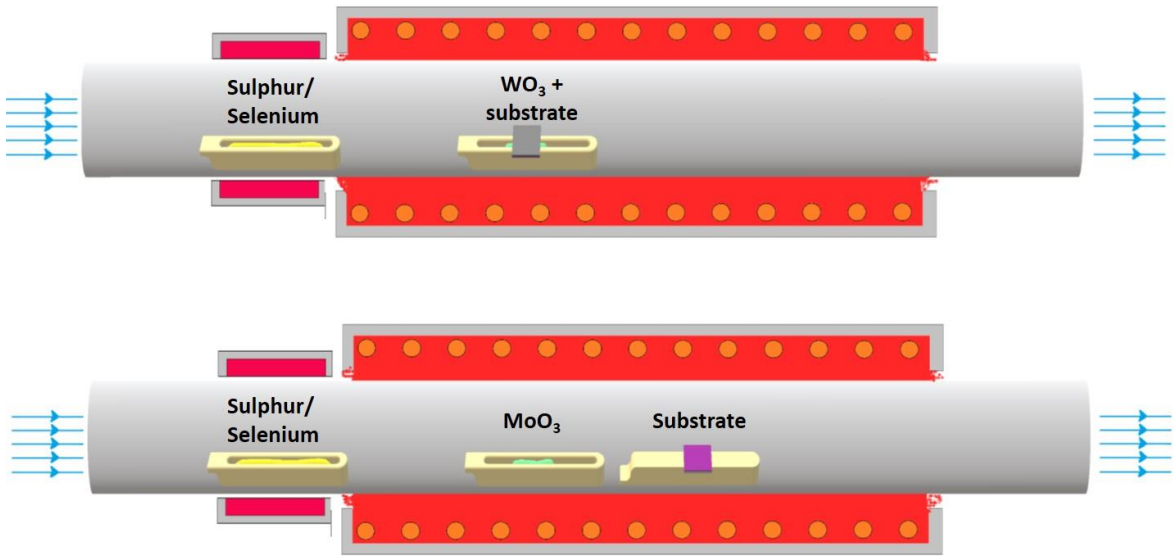


Figure 5.8: A schematic showing the two arrangement used to grow TMDs in CVD.

### 5.6.1 Characterization of the Monolayers

The properties of the samples were characterized through PL and TEM measurements. As these materials, in their monolayer limit, are direct bandgap, they exhibit good PL. The $WS_2$ monolayer spectrum showed strong PL emission (Fig. 5.8a) and it has an excitonic peak at 1.97 eV (629.4 nm) and an FWHM of 0.04 eV which is similar to earlier reports.[26,27] The $WSe_2$ PL spectrum is given in Fig. 5.8b and it has an excitonic peak at 1.61 eV (769.5 nm) with an FWHM of 0.06 eV, which is similar to earlier report.[28] The $MoSe_2$ PL spectrum is given in Fig. 5.8c and it has an excitonic peak at 1.54 eV (804.4 nm) with an FWHM of 0.04 eV, which is also similar to earlier report.[29][30]

A high-angle annular dark-field scanning transmission electron microscope (HAADF-STEM) image of the $WS_2$ having a high PL is shown in Fig. 5.8d and it shows a lattice with little to no defects. When the amount of WO3 precursor used in synthesis was reduced, from 500 mg to 100 mg, the PL was considerably weaker and was not visible to the naked eye using the same PL microscope. HAADF-STEM study revealed that there was a considerable increase in tungsten vacancy in the monolayers, Fig. 5.8e, which explained the low PL. The HAADF-STEM image of the $WSe_2$ monolayer is given in Fig. 5.8f which shows a defect-free lattice. This result showed that with WG it is possible to synthesize monolayers even when conditions are

suboptimal, and at optimal conditions the synthesized film quality is high.

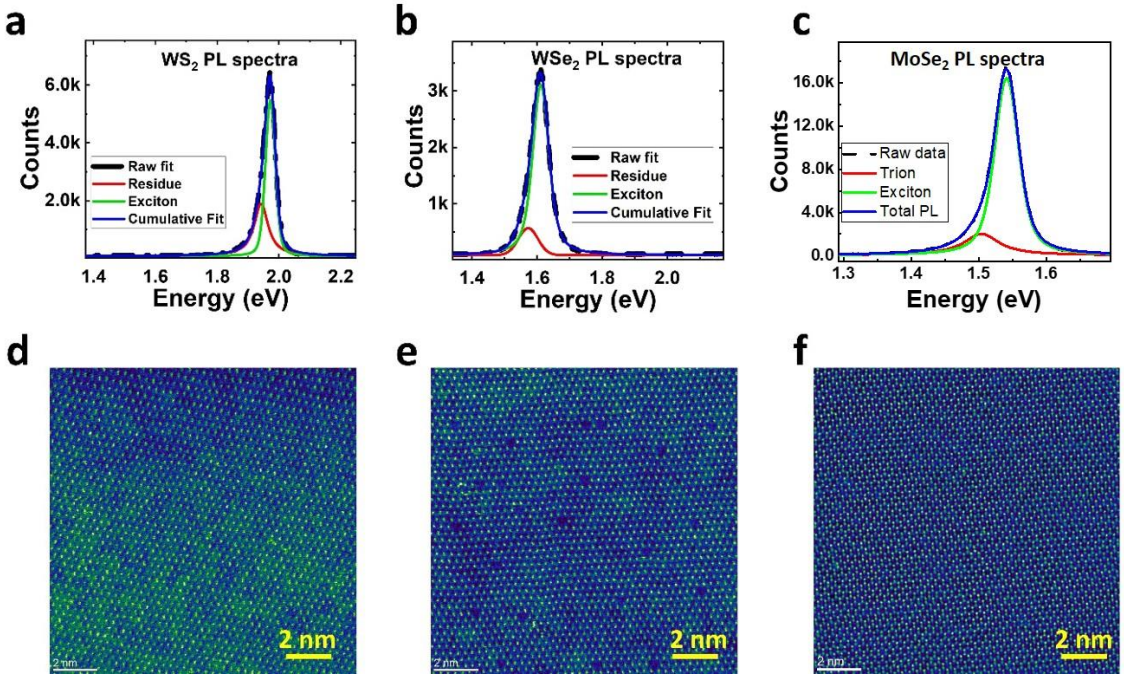


Figure 5.8: (a), (b) and (c) are the PL spectra of $WS_2$, $WSe_2$, and $MoSe_2$ monolayers respectively. The PL is sharp and narrow indicating high film quality. (d) HAADF-STEM image of $WS_2$ with high PL showing little to no defects. (e) The HAADF-STEM image of $WS_2$ with low PL (synthesized by reducing the amount of $WO_3$ by five times). The lattice image shows a considerable increase in the Tungsten vacancies in the monolayer crystals. (f) HAADF-STEM image of $WSe_2$

## 5.7 Summary

In this chapter, we explored the effectiveness of sodium silicate as a novel growth promoter. The growth of TMD monolayers demonstrated enhanced tolerance to variations in CVD parameters, owing to the lower energy of formation required for the reaction. Through a comparison with NaCl as a growth promoter, we established the superior performance of WG in promoting the growth of TMD monolayers. Notably, the electrical mobility of the monolayers grown using WG surpassed those grown with NaCl under similar conditions by more than an order of magnitude, and exhibited comparability to findings reported in other studies. Furthermore, we successfully demonstrated the synthesis of diverse TMD monolayers utilizing WG as an effective growth promoter.

**Bibliography**

[1] Wang P, Lei J, Qu J, Cao S, Jiang H, He M, Shi H, Sun X, Gao B and Liu W 2019 Mechanism of Alkali Metal Compound-Promoted Growth of Monolayer MoS 2 : Eutectic Intermediates *Chem. Mater.* **31** 873–80

[2] Lee Y H, Zhang X Q, Zhang W, Chang M T, Lin C Te, Chang K Di, Yu Y C, Wang J T W, Chang C S, Li L J and Lin T W 2012 Synthesis of large-area MoS2atomic layers with chemical vapor deposition *Adv. Mater.* **24** 2320–5

[3] Ling X, Lee Y-H, Lin Y, Fang W, Yu L, Dresselhaus M S and Kong J 2014 Role of the Seeding Promoter in MoS 2 Growth by Chemical Vapor Deposition *Nano Lett.* **14** 464–72

[4] Yang P, Yang A-G, Chen L, Chen J, Zhang Y, Wang H, Hu L, Zhang R-J, Liu R, Qu X-P, Qiu Z-J and Cong C 2019 Influence of seeding promoters on the properties of CVD grown monolayer molybdenum disulfide *Nano Res.* **12** 823–7

[5] Chen J, Zhao X, Tan S J R, Xu H, Wu B, Liu B, Fu D, Fu W, Geng D, Liu Y, Liu W, Tang W, Li L, Zhou W, Sum T C and Loh K P 2017 Chemical Vapor Deposition of Large-Size Monolayer MoSe 2 Crystals on Molten Glass *J. Am. Chem. Soc.* **139** 1073–6

[6] Chen J, Zhao X, Grinblat G, Chen Z, Tan S J R, Fu W, Ding Z, Abdelwahab I, Li Y, Geng D, Liu Y, Leng K, Liu B, Liu W, Tang W, Maier S A, Pennycook S J and Loh K P 2018 Homoepitaxial Growth of Large-Scale Highly Organized Transition Metal Dichalcogenide Patterns *Adv. Mater.* **30** 1–9

[7] Yang P, Zou X, Zhang Z, Hong M, Shi J, Chen S, Shu J, Zhao L, Jiang S, Zhou X, Huan Y, Xie C, Gao P, Chen Q, Zhang Q, Liu Z and Zhang Y 2018 Batch production of 6-inch uniform monolayer molybdenum disulfide catalyzed by sodium in glass *Nat. Commun.* **9** 1–10

[8] Narayanan V, M A G and Rahman A 2019 How to 'train' your CVD to grow large-area 2D materials *Mater. Res. Express* **6** 125002

[9] Schmidt B, Nitzsche P, Lange K, Grigull S, Kreissig U, Thomas B and Herzog K 1998 In situ investigation of ion drift processes in glass during anodic bonding *Sensors Actuators A Phys.* **67** 191–8

[10] Wallis G and Pomerantz D I 1969 Field Assisted Glass-Metal Sealing *J. Appl. Phys.* **40** 3946–9

[11] Knowles K M and van Helvoort A T J 2006 Anodic bonding *Int. Mater. Rev.* **51** 273–311

[12] Gacem K, Boukhicha M, Chen Z and Shukla A 2012 High quality 2D crystals made by anodic bonding: a general technique for layered materials *Nanotechnology* **23** 505709

[13] Li S, Lin Y-C, Zhao W, Wu J, Wang Z, Hu Z, Shen Y, Tang D-M, Wang J, Zhang Q, Zhu H, Chu L, Zhao W, Liu C, Sun Z, Taniguchi T, Osada M, Chen W, Xu Q-H, Wee A T S, Suenaga K, Ding F and Eda G 2018 Vapour–liquid–solid growth of monolayer MoS2 nanoribbons *Nat. Mater.* **17** 535–42

[14] Gokul M A, Narayanan V and Rahman A 2020 Modulating flow near substrate surface to grow clean and large-area monolayer MoS2 *Nanotechnology* **31** 415706

[15] Mohsin H, Maron S, Maurin I, Burov E, Tricot G, Devys L, Gouillart E and Gacoin T 2021 Thermal behavior of waterglass: foaming and xerogel-to-glass evolution *J. Non. Cryst. Solids* **566** 120872

[16] Kim I S, Sangwan V K, Jariwala D, Wood J D, Park S, Chen K S, Shi F, Ruiz-Zepeda F, Ponce A, Jose-Yacaman M, Dravid V P, Marks T J, Hersam M C and Lauhon L J 2014 Influence of stoichiometry on the optical and electrical properties of chemical vapor deposition derived MoS2 *ACS Nano* **8** 10551–8

[17] Wang X, Feng H, Wu Y and Jiao L 2013 Controlled synthesis of highly crystalline MoS2 flakes by chemical vapor deposition *J. Am. Chem. Soc.* **135** 5304–7

[18] Anwar M, Hogarth C A and Bulpett R 1989 Effect of substrate temperature and film thickness on the surface structure of some thin amorphous films of MoO3 studied by X-ray photoelectron spectroscopy (ESCA) *J. Mater. Sci.* **24** 3087–90

[19] Zumdahl S S and Zumdahl S A 2007 *Chemistry* ed R Stratton, R Schwartz and C Brooks (Boston, New York: Houghton Mifflin Company)

[20] Radisavljevic B, Radenovic A, Brivio J, Giacometti V and Kis A 2011 Single-layer MoS2 transistors *Nat. Nanotechnol.* **6** 147–50

[21] Li H, Yin Z, He Q, Li H, Huang X, Lu G, Fam D W H, Tok A I Y, Zhang Q and Zhang H 2012 Layered Nanomaterials: Fabrication of Single- and Multilayer MoS2 Film-Based Field-Effect Transistors for Sensing NO at Room Temperature (Small 1/2012) *Small* **8** 2–2

[22] Schmidt H, Wang S, Chu L, Toh M, Kumar R, Zhao W, Castro Neto A H, Martin J, Adam S, Özyilmaz B and Eda G 2014 Transport properties of monolayer MoS2 grown by chemical vapor deposition *Nano Lett.* **14** 1909–13

[23] Wang G, Chernikov A, Glazov M M, Heinz T F, Marie X, Amand T and Urbaszek B 2018 Colloquium: Excitons in atomically thin transition metal dichalcogenides *Rev. Mod. Phys.* **90** 021001

[24] McCreary K M, Hanbicki A T, Sivaram S V. and Jonker B T 2018 A- and B-exciton photoluminescence intensity ratio as a measure of sample quality for transition metal dichalcogenide monolayers *APL Mater.* **6**

[25] Xu Z-Q, Xia X and Bao Q 2015 Synthesis and Transfer of Large-Area Monolayer WS2 Crystals: Toward the Recyclable Use of Sapphire Substrates *Light, Energy and the Environment 2015* (Washington, D.C.: OSA) p DTu3D.2

[26] Plechinger G, Nagler P, Kraus J, Paradiso N, Strunk C, Schüller C and Korn T 2015 Identification of excitons, trions and biexcitons in single-layer WS 2 *Phys. status solidi - Rapid Res. Lett.* **9** 457–61

[27] McCreary K M, Hanbicki A T, Jernigan G G, Culbertson J C and Jonker B T 2016 Synthesis of Large-Area WS2 monolayers with Exceptional Photoluminescence *Sci. Rep.* **6** 19159

[28] Zeng H, Liu G-B, Dai J, Yan Y, Zhu B, He R, Xie L, Xu S, Chen X, Yao W and Cui X 2013 Optical signature of symmetry variations and spin-valley coupling in atomically thin tungsten dichalcogenides *Sci. Rep.* **3** 1608

[29] Le C T, Clark D J, Ullah F, Senthilkumar V, Jang J I, Sim Y, Seong M-J, Chung K-H, Park H and Kim Y S 2016 Nonlinear optical characteristics of monolayer MoSe 2 *Ann. Phys.* **528** 551–9

[30] Li D, Trovatello C, Dal Conte S, Nuß M, Soavi G, Wang G, Ferrari A C, Cerullo G and Brixner T 2021 Exciton–phonon coupling strength in single-layer MoSe2 at room temperature *Nat. Commun.* **12** 954

# Chapter 6

# Straining MoS2 monolayer – Effect of uniform and non-uniform strain

## 6.1 Introduction

Monolayers of transition metal dichalcogenides (TMDs) possess exceptional mechanical strength, allowing them to withstand numerous bending cycles while maintaining their structural integrity.[1]Strain engineering has emerged as a powerful technique for tuning the optoelectronic properties of materials, and monolayer TMDs, in particular, present an outstanding candidate for strain studies due to their ability to endure high strains without damage. Among the TMDs, molybdenum disulfide ($MoS_2$) has garnered significant attention as applied strain can effectively modulate its electrical and optical properties. Remarkably, $MoS_2$ monolayers can tolerate strains up to 11% without experiencing any detrimental effects.[2]

Uniformly straining the monolayer improves electron mobility and helps modulate its optoelectric properties. The easiest method of applying uniform uniaxial strain is to transfer it onto a flexible substrate and bend it. The superior mechanical stability of $MoS_2$ and its tunable optical and electrical properties with strain positions it as a viable material for flexible device applications such as photodetectors, strain sensors, solar cells, light-emitting diodes, and transistors.[3–6]

Interestingly the properties of monolayer TMDs, including their electronic structure, dipole moment, band gap, mobility, carrier density, and local charge distribution, depend on their morphology, which can be finely tuned through stretching, twisting, bending, or wrinkling [7–11] Precise control over the morphology of two-dimensional (2D) materials unlocks new possibilities for engineering material properties, enabling unconventional light-matter interactions in optical metasurfaces achieved through subwavelength-scale morphological

control of TMDs.[12,13]

Current methods for controlling monolayer morphology, such as transferring 2D materials onto textured substrates, suffer from limitations in achieving conformal coating on complex geometries, lack of precise control, and film cracking.[14,15] Consequently, alternative techniques such as ALD, CVD, or a combination of conformal deposition of transition metal precursors and sulphurization have been employed to create conformal coatings.[16–19] However, while these methods have shown promise in producing anisotropic properties, they often yield highly polycrystalline films (nanosheets) rather than continuous monolayers.[18] A very strong growth promoter can help in the conformal growth of monolayer TMDs.[20]

In this chapter, we explore strain studies on $MoS_2$ monolayers, capitalizing on their exceptional mechanical stability and strain-tunable optoelectronic properties. By subjecting $MoS_2$ monolayers to controlled strains, we investigate the influence of strain on their electronic and optical characteristics. Additionally, we also explored alternative techniques to achieve conformal growth and precise control over monolayer morphology, addressing the limitations of current methods. Through these efforts, we aim to advance the understanding of strain engineering in $MoS_2$ monolayers and pave the way for their application in flexible and high-performance devices.

## 6.2 Uniformly straining $MoS_2$ monolayers uniaxially

A very easy way to apply uniaxial strain to $MoS_2$ is by placing it on a flexible substrate and bending it.[21–24] In order to conduct our study we choose to transfer monolayer $MoS_2$ onto a silicon nitride ($Si_3N_4$) deposited fluorine-doped tin oxide-coated polyethylene terephthalate (FTO/PET) substrate. The growth and transfer techniques used for $MoS_2$ are the same as the ones used in chapter 5. Fig. 6.1a-d shows the optical image of monolayer $MoS_2$ triangles transferred on a $Si_3N_4$/FTO/PET substrate of different thickness. It has been reported that $Si_3N_4$ has good optical visibility for 2D materials in the thickness regime of 50-100 nm on silicon substrate[25]. But for better optical visibility of $MoS_2$ on the FTO/PET substrate, we optimized the $Si_3N_4$ layer thickness to be 150 nm. Fig. 6.1e shows the photograph of $Si_3N_4$ sputtered FTO/PET substrates of different thicknesses. The substrate with the pinkish color at the center

which had a $Si_3N_4$ coating of 150 nm exhibited the best contrast.

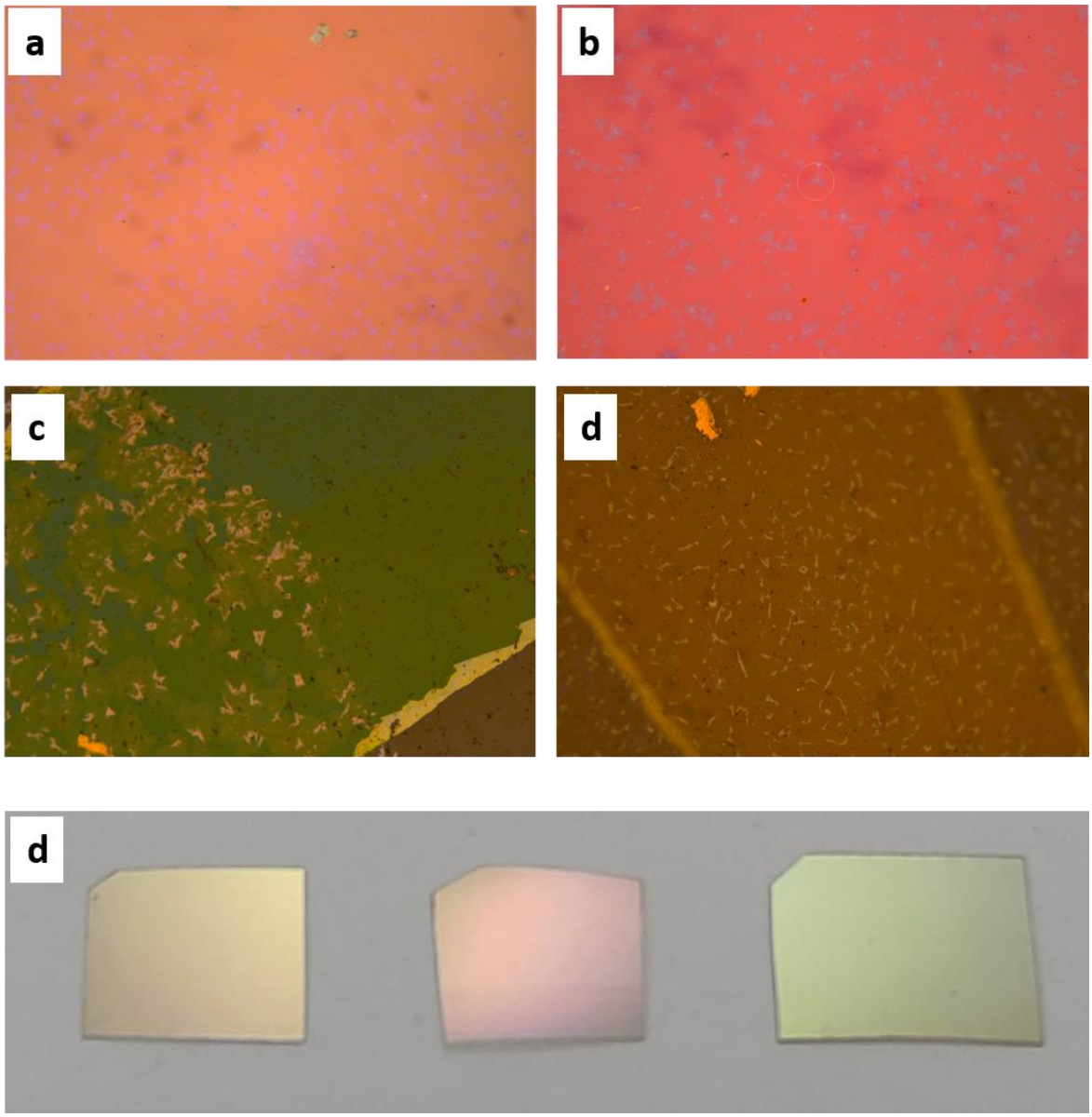


Figure 6.1: (a) – (d) images of $MoS_2$ on the $Si_3N_4$ of different thickness. 145 nm, 150 nm, 160 nm and 280 nm respectively. (e) The photographs of 145 nm, 150 nm, and 160 nm of $Si_3N_4$ on FTO/PET substrate.

Thus we choose 150 nm $Si_3N_4$ coated substrate for all our study. Fig. 6.2a shows the optical microscope image and Fig. 6.2b shows the FESEM image of the flexible device fabricated using chromium-gold (Cr (5 nm)-Au (65 nm)) van der Pauw contacts. A schematic of the fabricated flexible device is shown in Fig. 6.2c. The PL spectra of monolayer $MoS_2$ exhibit (Fig. 6.2d) two

peaks at ~678 nm (1.83 eV) (with an FWHM of ~110 meV) and ~624 nm (1.98 eV) corresponding to the two direct excitonic transitions at the Brillouin zone K point. The PL spectra confirm that the monolayer $MoS_2$ has inherent defects due to the appearance of a shoulder peak at 624 nm [26]. We found a B exciton to A exciton PL intensity ratio of around 0.22. We intentionally chose such a sample to study the effect of strain on the native defects. As the formation energy of defects is the least for sulphur vacancies, the defects should predominantly be sulphur vacancies.[27][28][29]

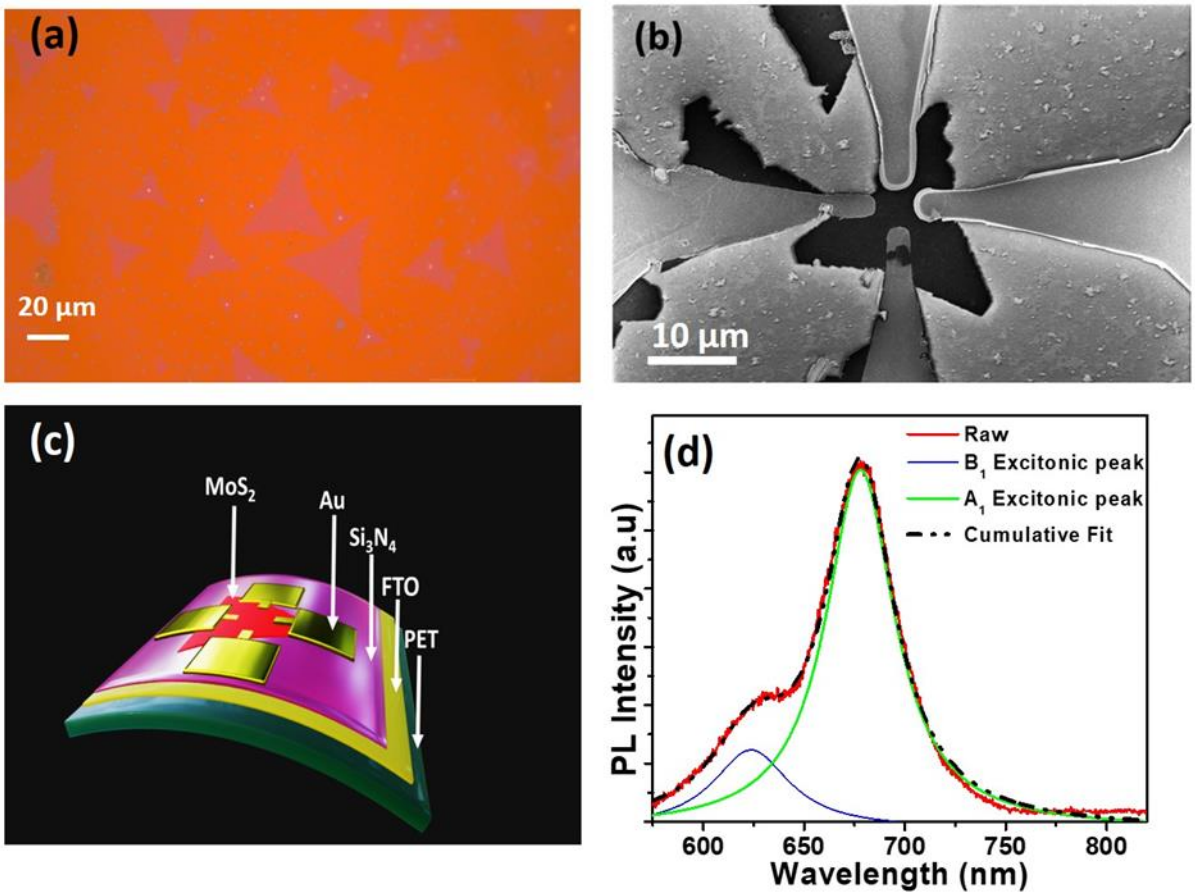


Figure 6.2: (a) Optical image of $MoS_2$ transferred to a $Si_3N_4$/ITO/PET substrate, (b) FESEM image of the device fabricated on monolayer $MoS_2$ (c) Schematic representation of flexible $MoS_2$ device, and (d) Photoluminescence spectra of monolayer $MoS_2$ shows the characteristic monolayer $MoS_2$ peak (A exciton) and a shoulder peak corresponds to B exciton and the relatively high B exciton to A exciton PL emission ratio suggests the presence of intrinsic defects in the sample.

### 6.2.1 Optical studies on flexible devices

Bending studies were performed on the flexible monolayer $MoS_2$ devices to study the effect of strain on the intrinsic defects. The applied strain was approximately calculated using the formula,[21]

$$s = t/2R$$

where *s* is the strain applied, *t* is the thickness of FTO/PET substrate (*t* is measured as 0.02 cm) and *R* is the radius of curvature of the curved surfaces which is used here for applying strain (Fig.6.3a shows a representative photograph of a flexible substrate with devices, placed on a curved surface). Raman and PL measurements were used to substantiate the presence of strain in the strained sample (Fig.6.3 b and c). Raman measurement showed a decrease in the $E_{2g}$ peak value and the corresponding PL spectra from samples showed a red shift with an increase in strain.[30] This confirmed that the monolayer was being subjected to strain without any slippage. This slippage is absent because of the low value of applied strain.[31]

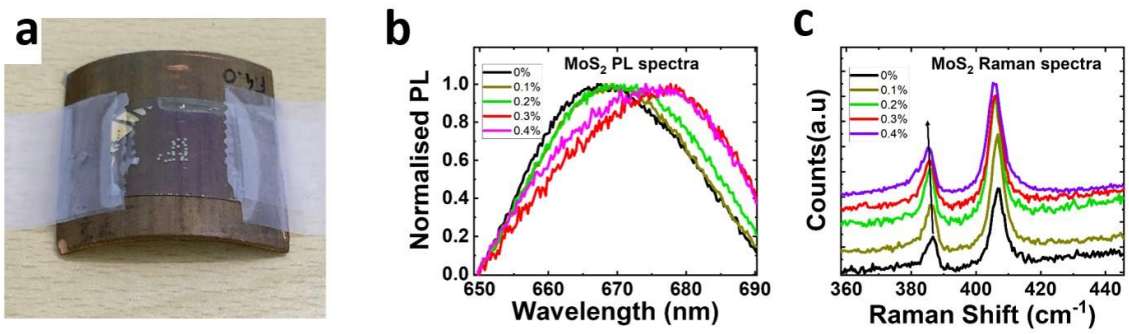


Figure 6.3: (a) Image of a flexible device positioned on a curved surface with a radius of 5.4 cm, exhibiting a strain of 0.4%. (b) Photoluminescence (PL) spectra of $MoS_2$ on a flexible substrate under varying levels of strain. The PL demonstrates a redshift as strain increases. (c) Raman spectra of monolayer $MoS_2$ at different levels of strain. The $E_{2g}$ mode exhibits a downward shift in Raman shift value with increasing uniaxial strain.

### 6.2.2 Electrical studies on flexible devices

The photoresponse measurements were performed on flexible monolayer $MoS_2$ devices by applying a maximum of 3 V bias voltage for I-V studies and 1V steady dc bias for I-t studies.

More than two orders increase in the current was observed under light illumination (405 nm, 20 $mW/cm^2$) compared to the dark current. The current under light illumination was 19 nA compared to 0.16 nA measured at dark. Fig. 6.4a shows current vs. voltage (*I-V*) plots under light illumination for a flexible monolayer $MoS_2$ device by varying the tensile strain from 0 to 0.4%. When we increased the tensile strain from 0 to 0.2%, the photocurrent initially decreased from 19 nA (at 0%) to 12 nA (at 0.2%), and at 0.3% strain, we observed an enhancement in the photocurrent (14 nA). Interestingly, under light illumination, photocurrent was taking more time to saturate at particular values of strain, which was not observed at other strains. This can be attributed to the activation of metastable defects at that particular strain. When the applied strain is higher than the activation point (here it is 0.4%), the current decreases to 11 nA which confirms that a higher strain had detrimental effects on the photocurrent. Fig. 6.4b shows the change in photocurrent and photoresponsivity to the applied strain and clearly illustrates an increase in photocurrent and responsivity[32]

$$I_{photo} = I_{light} - I_{dark} \quad \text{and} \quad R = (I_{light} - I_{dark})/(P \times A)$$

at 0.3% strain corresponding to the defect activation. Interestingly, we observed the same phenomena in different devices at different strains, which confirms that as the defect density varies from sample to sample, the defect activation point also varies from device to device.

Table 6.1. Rise time (Ƈr) and decay time (Ƈd) for different strain

| Strain | $Ƈ_r$(S) | $Ƈ_d$(S) |
|---|---|---|
| 0 % | 9.8 | 37.1 |
| 0.1 % | 15.4 | 47.2 |
| 0.2 % | 13.5 | 42.4 |
| 0.3 % | 21.4 | 48.4 |
| 0.4 % | 19.8 | 55.2 |

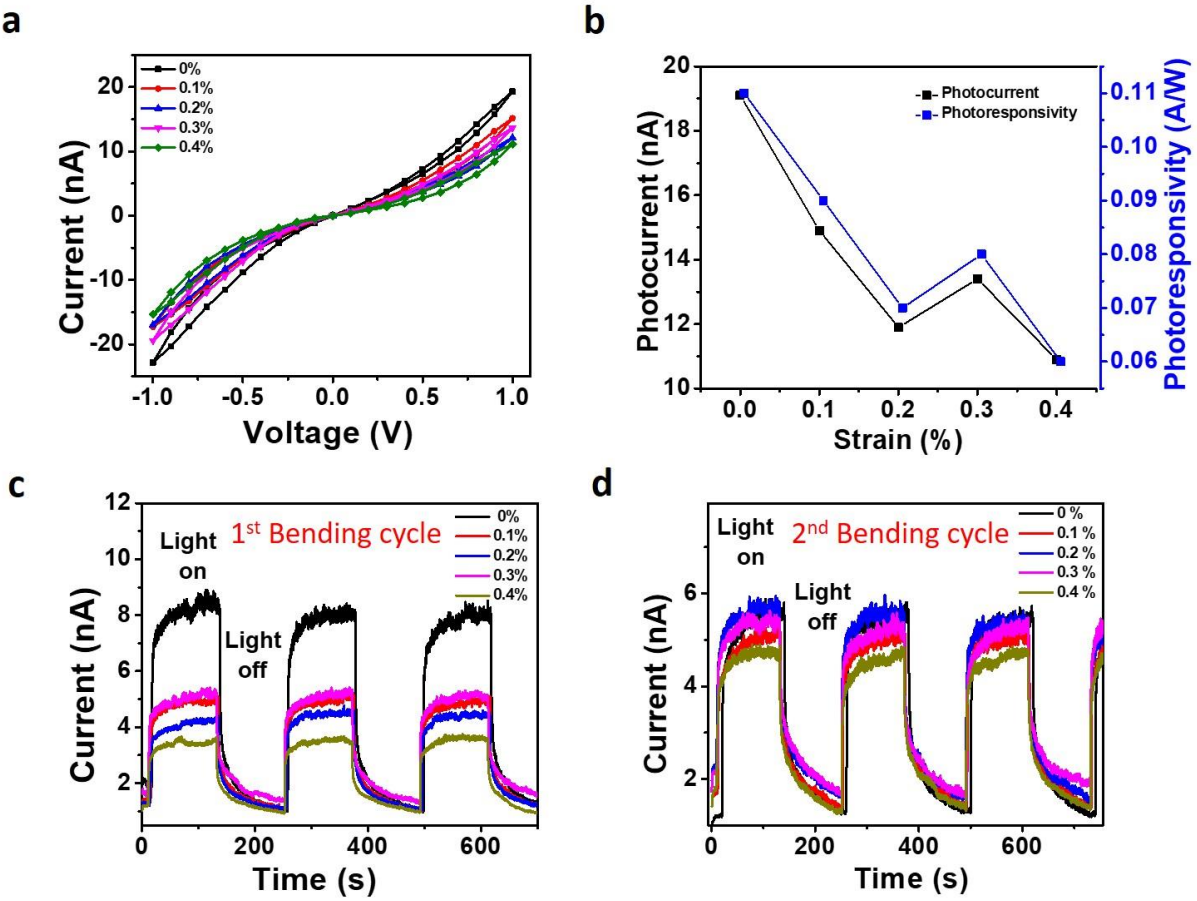


Figure 6.4: (a) I-V curves of monolayer $MoS_2$ in the presence of light by applying strain shows a decrease in photocurrent with the increase in strain under 1V bias voltage. (b) Photocurrent and photoresponsivity vs. strain, showing initially a decrease in current by increasing strain, but an increase in photocurrent at 0.3% strain reveals the defect activation at a particular strain. (c) I-t plot of monolayer $MoS_2$ under different strains in first bending cycle under 0.5 V bias voltage shows a gradual decrease in photocurrent with an increase in strain but shows an enhancement in current at 0.3% strain. (d) I-t plot of monolayer $MoS_2$ after defect activation (second bending cycle) depicts at 0.3% strain current increases as time progresses

Interestingly it is the I-t that gives a noticeable response to the effect of the strain. Once the defects in the devices got activated it was taking more time for the photocurrent to saturate and showed persistent photoconductivity. It has been reported that in TMDs small external activation energy can activate the metastable defects. The activation and deactivation of these defects can be reversible depending on the type of defects [33]. Our study suggests that even

low strain can activate these metastable defects, which can be deactivated by applying a higher strain. Since these defects are optically active, the effect of defect tuning will be more pronounced in the photoresponse measurements. Also, the defect level tuning under applied strain due to the trapping of charge carriers in mid-gap states alters the photoresponse characteristics [34]

Repeated IV measurements showed reproducible data and the I-V was more or less symmetric. However, after the prolonged I-t measurements, the device started exhibiting diodic behavior. We applied prolonged biasing of 1 V for half an hour and then measured I-V at different strains. In Fig. 6.4a, I-V curve is initially symmetric at 0% strain (black curve). When we applied strain from high to low (0.4% to 0%), at 0.3 % strain under prolonged light illumination and applied bias, a slight enhancement of the photocurrent was observed and the I-V characteristics remained symmetric. But the photocurrent was not saturating at this strain value and it was increasing with time, suggesting that some deep-level traps were getting activated at this particular value of strain. As we gradually reduced the strain from 0.3% to 0%, the I-V curve became asymmetric, and the asymmetry persisted even after relaxing to 0% strain (0%-R).

To explain this asymmetric behavior, we looked for signs of some of the reported effects. Since most 2D materials lack inversion centrosymmetry [1] when they have an odd number of layers, strain can induce piezoelectric and piezoresistive effects [35,36]. In the piezoelectric effect, the strain-induced polarization modifies the charge distribution within the material and thereby changes the electric properties. Whereas in the piezoresistive effect strain alters the band structure of the semiconductor, which modifies the electric transport properties. However, even after multiple cycles of I-V measurement, for all values of strain, the I-V graph remained nearly symmetric. This meant that prolonged biasing is crucial to transform the symmetric I-V into an asymmetric I-V (Fig. 6.5).

A possible explanation is that the asymmetric I-V characteristics due to the accumulation of defects at one of the contacts. [37] At specific values of strain, the diffusion barrier energy needed for the migration of defects reduces, this makes the defects highly mobile at lower bias. The  This argument goes well with some reported computational results in $MoS_2$ and other materials where the energy barriers for migration changed as a function of strain [38–40]. We believe that this happened because at 0.2% and 0.1% strain, the migration energy barrier

decreases and the defects becomes highly mobile. This causes the defects to migrate with ease under the applied bias. However, the asymmetry disappeared after some time suggesting that the defects diffused back to the $MoS_2$.

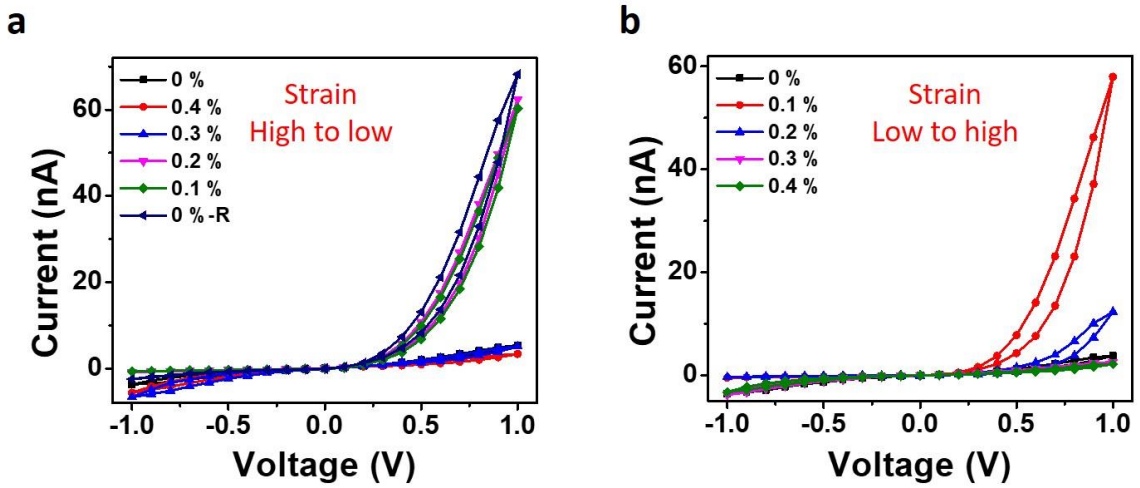


Figure 6.5: I-V characterization of the device after prolonged bias of 1 V under various strains. (a) I-V characteristics under light illumination shows a symmetric to asymmetric switching when strain is applied from high (0.4%) to low value (0%). The asymmetry started at 0.2% strain (b) I-V characteristics by varying strain value from low (0%) to high (0.4%). In this case the asymmetry started at 0.1% strain. These experiments suggest that the transition of I-V characteristics from symmetric to asymmetric happen only around strain values of 0.1% and 0.2%.

To further validate our observations on lowering of migration energy and defect activation, strain-dependent low-frequency noise measurements under different strains were investigated. Fig. 6.6a shows the normalized power spectral density ($PSD/I^2$) vs. frequency at different strains. The graph shows an initial decrease in $PSD/I^2$ under strain and a gradual increase afterward with the increase in the applied strain. We calculated the slope of the noise spectrum at lower frequencies (Fig 6.6b). The slope showed an increase at 0.1% strain as compared to 0% strain, then showed a decrease with a further increase in strain value. This observation can be attributed to the contribution of noise originating from slowly migrating defects.[41][42] From the prolonged measurements on the $MoS_2$ monolayer device under strain, it is clear that the defect migration happens at 0.1% and 0.2% as these are the values of strain that have given rise to a diodic behavior. The diodic nature was more pronounced at 0.1% as compared to 0.2%

suggesting a lower value of migration energy at 0.1%. Thus the slope at 0.1% is higher as defects are now slowly migrating. At strain value of 0.2 % the migration energy increases slightly and this is reflected in the slope of the noise. As the migration of defects are much less than at 0.1% the slope decreases. Upon increasing to 0.3 % the migration energy has increased further but the slope remains comparable to 0.2% strain. This might be due to the fact that defects are getting activated at 0.3 % (defect activation point), as evidenced by our photoresponse study. Further increasing the strain value decreases the slope again (at 0.4 %) because the activation of defects or lowering of migration energy are missing at 0.4% strain and thus giving a slope comparable to the unstrained device

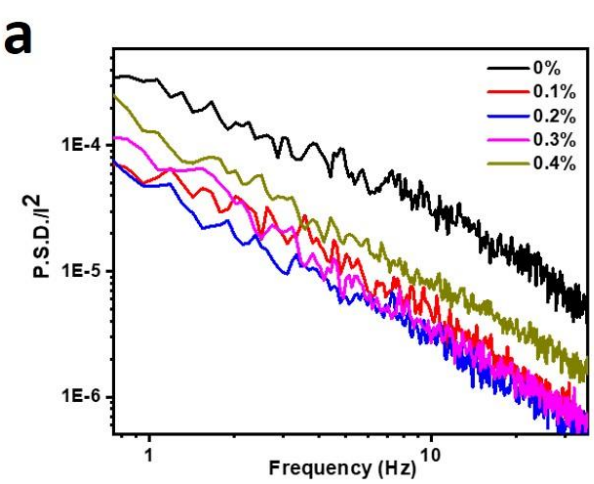


b

| Strain | Slope |
|---|---|
| 0 % | 1.28±0.02 |
| 0.1 % | 1.49±0.01 |
| 0.2 % | 1.33±0.01 |
| 0.3 % | 1.34±0.01 |
| 0.4 % | 1.25±0.01 |

Figure 6.6: (a) Low noise measurement under tensile strain is shown. The normalized power spectral density vs. frequency characteristics are shown when strain varied from 0 % to 0.4 %. (b) The table listing the slopes corresponding to different values of strain.

We also studied the effect of strain on electronic mobility. Fig. 6.7a shows the transfer characteristics of flexible single-layer $MoS_2$ devices under different strains, for that gate voltage varied from -3V to 3V. The field-effect mobility is calculated from the slope of Fig. 6.7a using the equation,[43]

$$\mu = \frac{dI_{ds}}{dV_{bg}} \frac{L}{W C_g V_{ds}}$$

where, $L$ is the channel length, $W$ is the channel width, $C_g$ is the gate capacitance per unit area

$C_g = \frac{\varepsilon_0 \varepsilon_r}{d}$, $\varepsilon_0$ = 8.854×10$^{-12}$ Fm$^{-1}$, $\varepsilon_r$ for $Si_3N_4$ is 7.5, and d is the thickness of $Si_3N_4$, here it is 150 nm.

We observed an increase in the field-effect mobility by increasing the uniaxial tensile strain from 0% to 0.4%. The mobility increased from 26.24 cm$^2$/V.s at 0% strain to 38.79 cm$^2$/V.s at 0.4% and the threshold voltage also showed an increase with increasing strain (mobility and threshold voltage at different strains are listed in Table 2). Fig. 6.7b clearly illustrates a sharp increase in mobility at 0.1% strain and further reaches a plateau above 0.3% strain. Our findings indicate that electronic band gap tuning as well as defect level tuning due to the applied strain, effects the mobility of the device. We have also done the gate hysteresis and pulse measurements at lower strains.

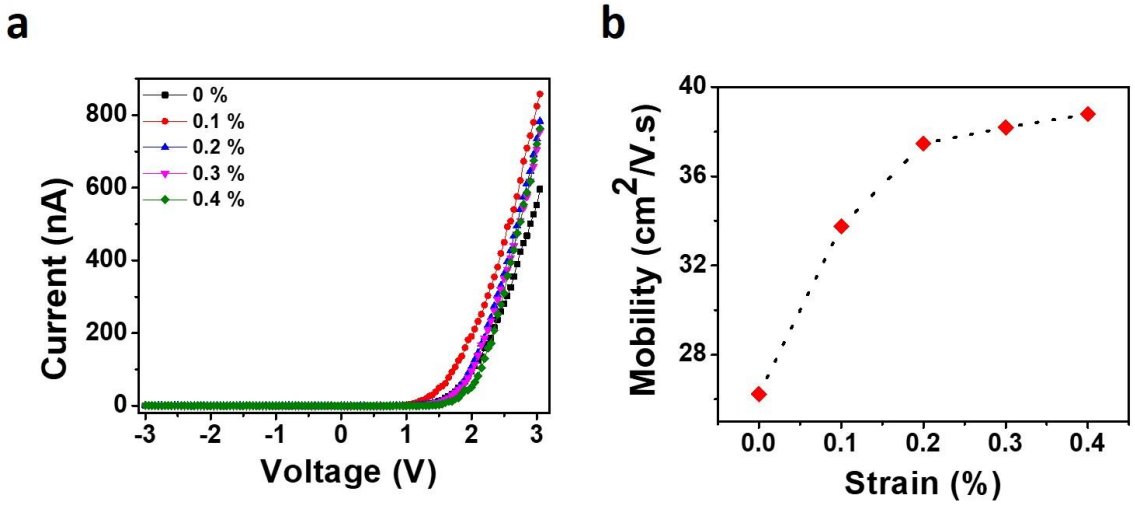


Figure 6.7: (a) Source-drain current versus gate voltage when drain-source voltage is 1V. (b) Mobility variation with an increase in strain.

Table 6.2: Mobility and thresh hold voltage at different strains

| Applied strain | Mobility ($cm^2$/V. s) | Threshold Voltage (V) |
|---|---|---|
| 0% | 26.24 | 2.0 |
| 0.1% | 33.76 | 1.9 |
| 0.2% | 37.47 | 2.1 |
| 0.3% | 38.19 | 2.2 |
| 0.4% | 38.79 | 2.2 |

## 6.3 Conformal growth of monolayer $MoS_2$

WG is an efficient growth promoter as demonstrated in chapter 5. This makes it possible for the growth of MoS2 monolayers conformally on to the textured substrate and textured substrates could help attain controlled strain as per previous reports.[20]

### 6.3.1 Preparation of textured substrates

In order to test the conformal growth of $MoS_2$ we prepared various textured substrate. Fig. 6.8a shows the schematic of making a 300 nm $SiO_2$ on a Si substrate with trenches of various widths. The Si substrate was spin-coated with S1813 photoresist and trenches of various sizes were drawn using a laser writer. The pattern was developed using the MF319 developer. Using a home build RIE trenches were etched onto Si wafer as photoresist acted as a mask, protecting the unexposed parts of Si. The reaction mixture contained 4 sccm of $SF_6$ and 1 sccm of $O_2$ gas. The presume was 0.06 mBar and the RF generator was at a power of 120 W. After 1 min in RIE the trenches were etched and the sample was taken out. The photoresist was washed off in acetone followed by cleaning in IPA and finally blow-drying. The substrate was again cleaned in a plasma asher at 40 W for 5 min in $O_2$ plasma. The substrate was kept in the CVD furnace

with a fresh tube and was taken to 1100 °C and was maintained at this temperature for 5 hrs under the flow of dry $O_2$ to grow 285 nm of $SiO_2$. The furnace was allowed to cool naturally and the substrate was taken out and coated with 0.5% WG solution at 4000 rpm after cleaning again in a plasma asher. The substrate was then used as mentioned in chapter 5 to grow $MoS_2$ in the CVD to get scattered triangles.

A textured substrate, with hemispheres of around 24 nm diameter in a honeycomb lattice, was made by growing 80 nm $SiO_2$ on a nanopatterned Si substrate that was fabricated using a block-co-polymer technique as reported previously.[44,45]

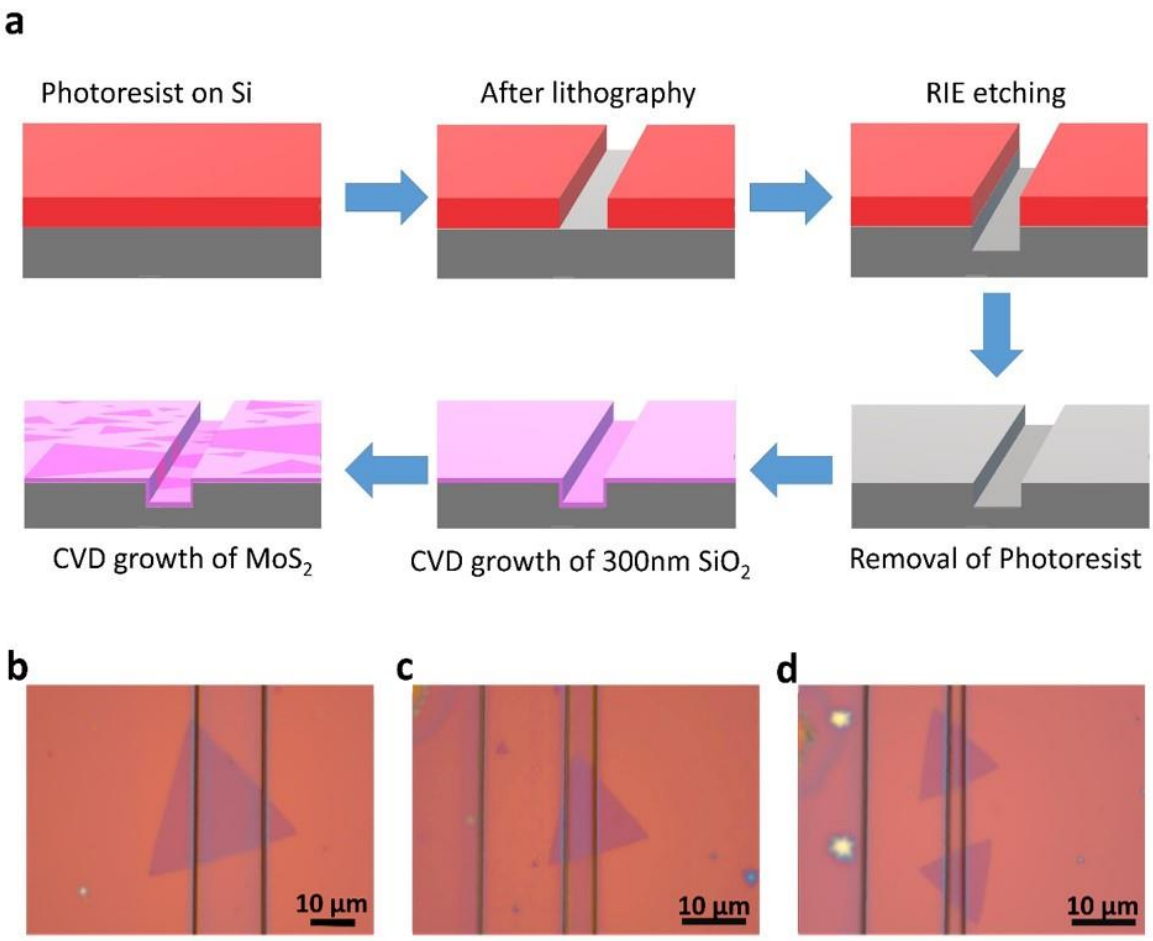


Figure 6.8: (a) schematic of patterning trenches onto Si substrate followed by the growth of the oxide layer and $MoS_2$. (b), (c) and (d) are OM images of monolayer $MoS_2$ grown on trenches of different widths.

To fabricate the slanted roof-like nanostructure, shown in Fig. 6.9, photolithography and a series of wet etching methods were implemented. Initially, lines of various thicknesses were drawn on $SiO_2$-coated Si using photolithography and after developing we used a photoresist as a mask to etch $SiO_2$ in Buffered oxide etchant (H.F, 10:1). The etching was carried out for 5 min. The substrate was then washed in D.I. water, followed by acetone and IPA. This was followed by lift-off in acetone and cleaning in IPA followed by $O_2$ plasma cleaning. Then it was immersed in 5M KOH in water with 5% IPA at 60 °C for an hour with stirring at 800 rpm in a beaker to have a smoothly etched surface[46]. The undercutting from both etching processes combined with selectivity helps us get the desired structure. The $SiO_2$ will also be slightly etched changing the color as thickness reduces by a few nm. The depth of KOH etching was shallower than expected, maybe because a very thin oxide layer was left after HF etching. Fig. 6.9a depicts the schematic of the entire process of fabricating this structure. Fig. 6.9 b-d shows images of $MoS_2$ conformally coated onto these patterned substrates. The image shows some monolayers hanging from the edges and is marked by a yellow circle.

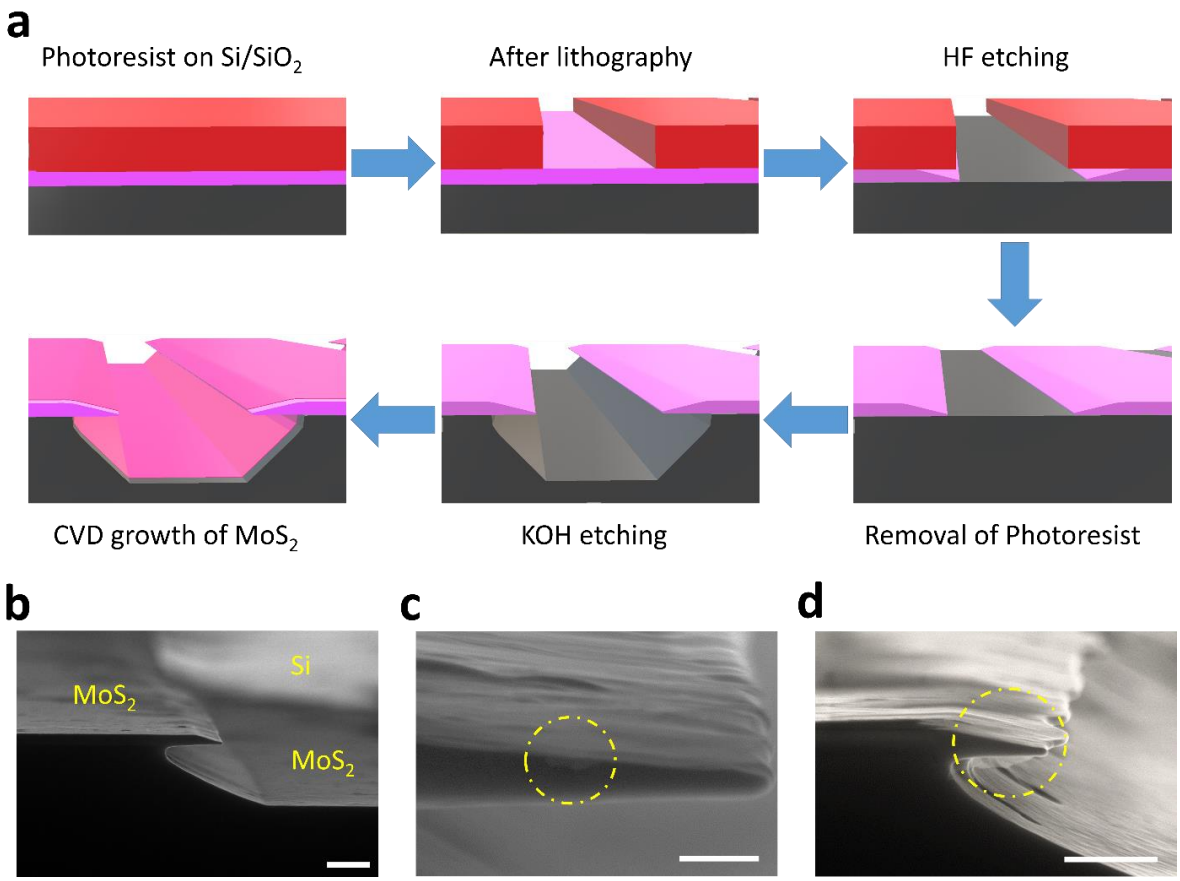


Figure 6.9: (a) is the schematic of making a structure with sharp edges and curves for the conformal growth of $MoS_2$. (b) is a continuous coating of $MoS_2$ on one of the patterned structures with the top right side of the image which is of a lighter shade is an uncoated region of Si. Contrast is adjusted to enhance the difference. The scale bar is 1 µm. (c) A small piece of monolayer $MoS_2$ can be seen hanging out. The scale bar is 200 nm. (d) Shows another structure where a bigger piece of $MoS_2$ monolayer is hanging out as it got cut while cleaving. The scale bar is 1 µm

The FESEM images comparing all the different textured substrates is shown in Fig. 6.10.

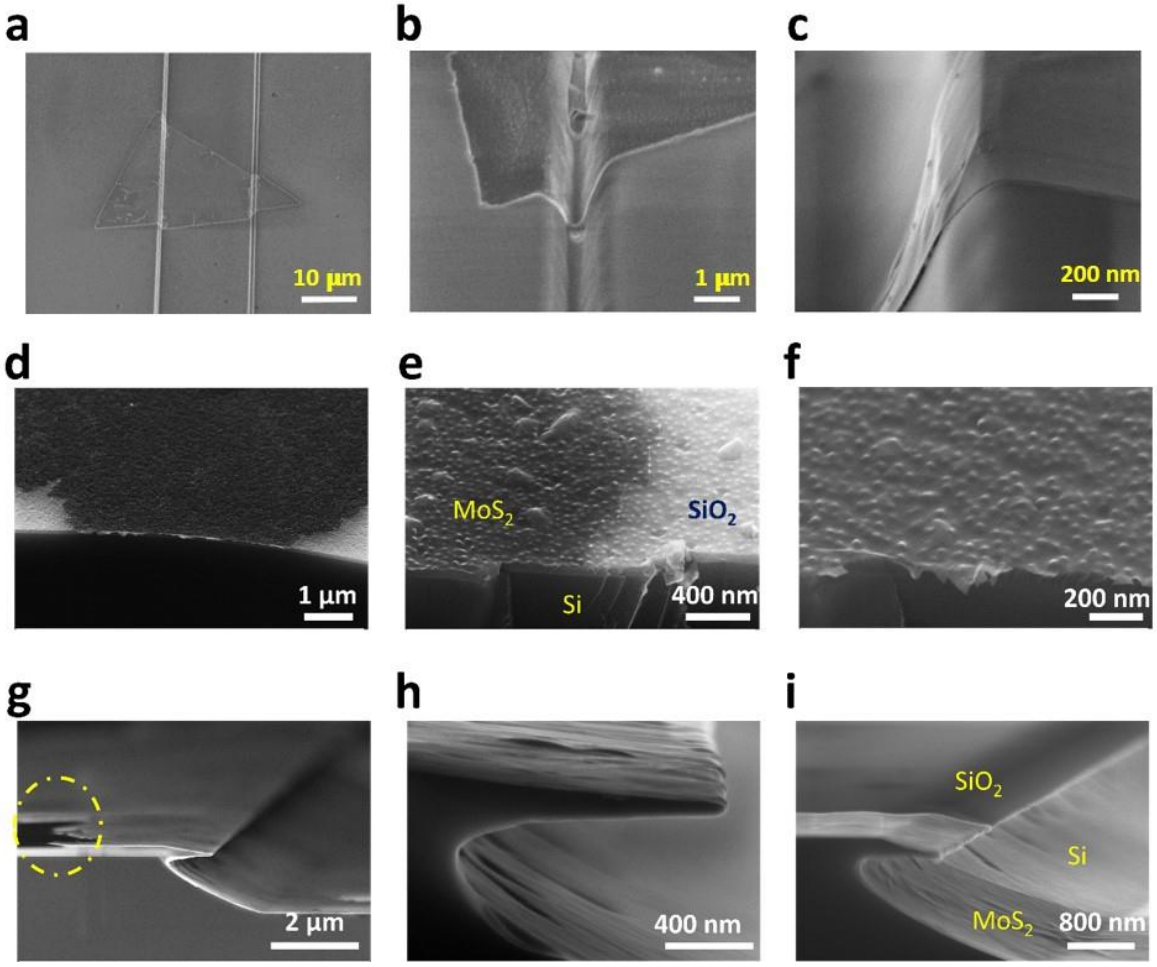


Figure 6.10: (a)-(c) are the FESEM images of the substrate with trenches. (d)-(f) are the FESEM images of the substrate with nano-hemispheres in a honeycomb lattice. (g)-(i) are the FESEM images of the substrate with the slanted roof-like geometry.

### 6.3.2 Optical properties of conformally grown $MoS_2$

We were interested in the formation of a nonuniformly strained structure. Thus we used the single shot PL technique to observe an enhancement at particular regions. Fig. 6.11 shows the schematic of the setup used for the single shot PL. To ensure large area uniform illumination of the substrate, we directed laser light onto the back focal plane of a 100X microscope objective, resulting in a quasi-parallel beam measuring 90 µm in diameter. To capture the PL images, an electron-multiplying charge-coupled device (EMCCD) camera was utilized, as illustrated in Fig.

6.11a. Due to the small structures, it is impossible to observe any localized enhancement on the hemisphere lattice.

Analysis of the single-shot PL revealed that only the roof-like structure exhibited distinct characteristics compared to other nanostructures. While the other nanostructures displayed relatively uniform PL, the roof-like structure demonstrated a notable increase in PL intensity in the localized regions adjacent to the nanostructure, as can be seen in Fig. 6.11b. This enhancement was predominantly observed in regions where $MoS_2$ was conformally grown, particularly in areas where the roof-like structure was slanted and in very rare cases in regions where the transition from a plane to a slanted structure was happening. The sharp edges of the nanostructure, as can be seen in Fig. 6.11c, exhibited a considerable quenching of PL. This change in PL intensity can be attributed to local variations in morphology, resulting in different strain gradients across different regions of the nanostructure.

Normally, strain leads to the quenching of PL in monolayers. However, the presence of a strain gradient can induce effects such as funneling or exciton-to-Trion conversion, resulting in a localized enhancement of PL intensity within the strained regions. We focused our attention on a region that showed enhancement and did further analysis. Fig. 6.12a displays an optical image of a monolayer $MoS_2$ grown conformally onto the slanted roof-like region of the substrate. In Fig. 6.12b, a corresponding single-shot PL image is presented, where false color is utilized to represent the signal intensity. An increase in the PL intensity was observed in the slanted region of the nanostructures. The PL spectra obtained from various regions were graphically represented in Fig. 6.12c. Our observations revealed a significant enhancement in the PL intensity, accompanied by modulations in the PL peak position and nature of the spectra within the slanted region.

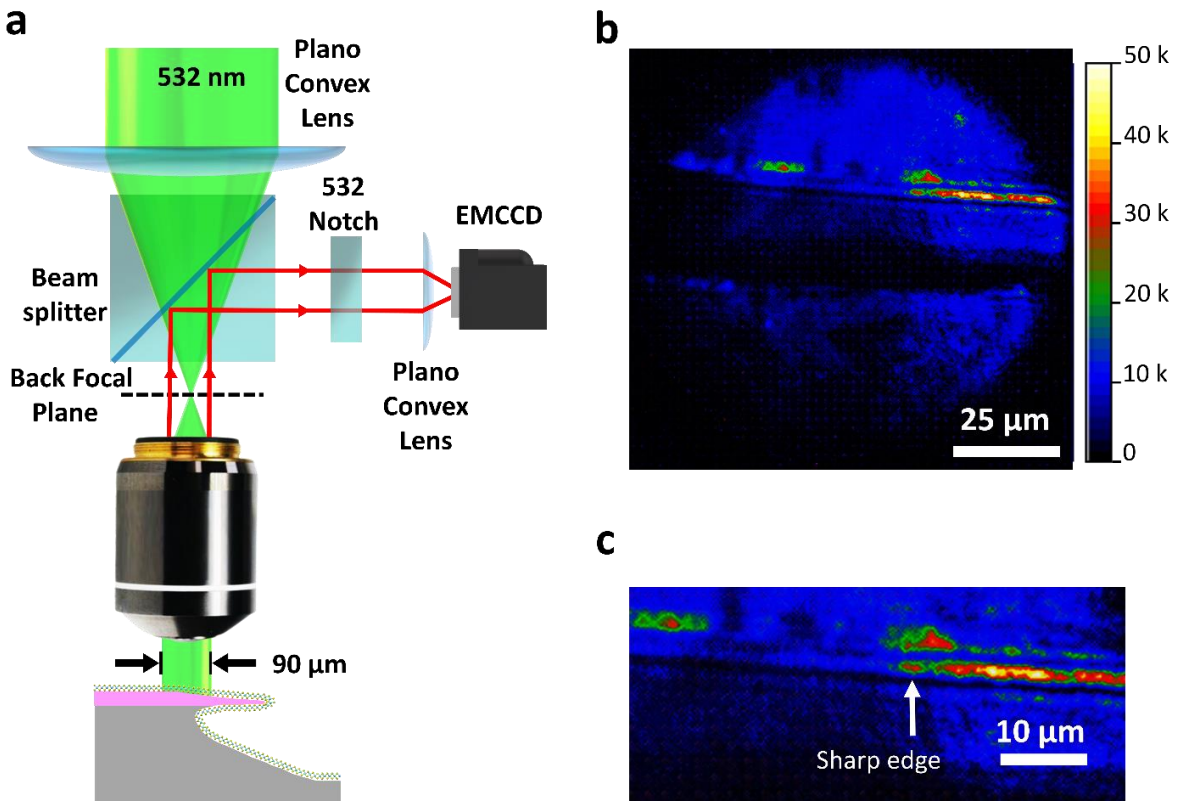


Figure 6.11: (a) A schematic is presented, illustrating the utilization of a convex lens to focus the 532 nm laser onto the back focal plane of the objective (not to scale). This configuration enables the generation of a quasi-parallel beam with a diameter of 90µm. (b) The PL intensity is depicted in a false color image captured by an EMCCD. (c) The zoomed image of (b) reveals that minimal intensity is observed at the sharp edge of the slanted roof-like structure. This observation suggests that the high strain present at the edge of the $MoS_2$ may be the reason behind this quenching. Conversely, the conformally coated $MoS_2$ in the slanted region exhibits high PL intensity. Additionally, some regions where the structure transitions from a plane to a slanted configuration, corresponding to region 1, also exhibit enhancement in PL

The modulation in the peak spectra can be attributed to strain and the increase in PL intensity suggest that the monolayer is non-uniformly strained.[9,47] The monolayer in the region that exhibiting this peculiar behavior could have a gradual change in strain in the slanted roof like region. The region can be identified under optical microscope easily as there is a continuous change in the coloration of the substrate, caused by the variation in the thickness of $SiO_2$ in this region. In the region marked as region 3, the PL signal was enhanced significantly and the PL peak position was modulated by the emergence of additional peak that appears to be a red-shifted peak. The PL intensity of regions other than region 4 were significantly lower than that of region 3. An FESEM image of the slanted roof like nanostructure with conformally grown

MoS2 was taken after the optical measurements Fig. 6.12d and a schematic of the same is given Fig. 6.12e. To facilitate visualization, the schematic in Figure 4e also illustrates the regions within the sample from which the spectra were collected.

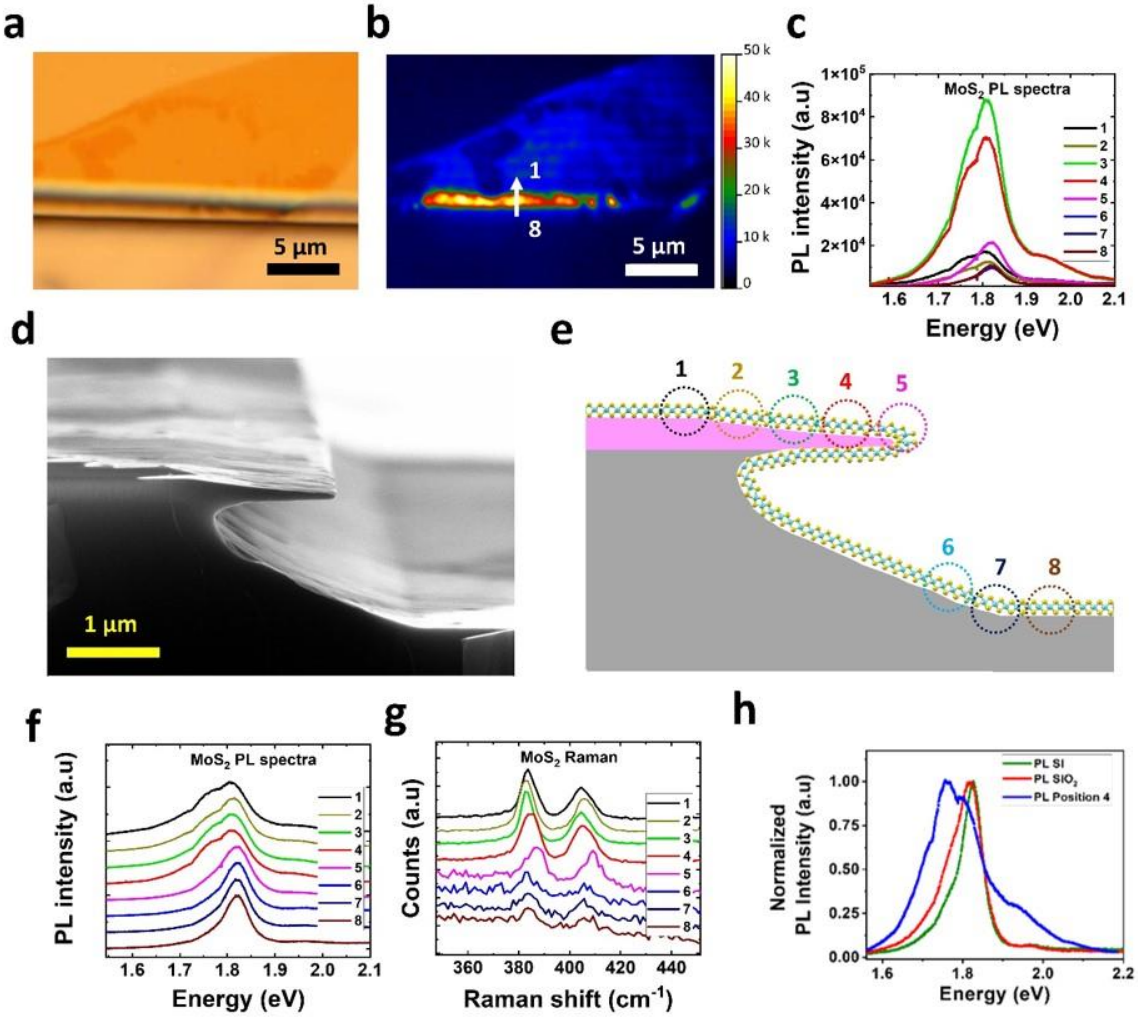


Figure 6.12: (a) Optical microscopic images of $MoS_2$ grown on the slanted roof-like nanostructure. (b) Single shot PL image of the region shown in (a). The labeled line in the (b), marked from 8 to 1, indicates the region from which eight spots that were selected for obtaining Raman and PL spectra. (c) PL intensity was collected from the 8 spots. The enhancement in the PL in regions 3 and 4 is more than four times the PL in region 1. (d) FESEM image of the slanted roof-like nanostructure with conformally grown $MoS_2$ that exhibited an increase in PL spectral weightage. (e) a schematic of the nanostructure with $MoS_2$ indicating regions 1 to 8. (f) and (g) are the normalized PL and Raman spectra from regions 1 to 8 plotted in a cascade fashion. The change in the nature of the spectra is visible in the PL and a slight shift in Raman modes is also observed. (h) Normalized PL spectra obtained from region 4 of a similar nanostructure, monolayer of $MoS_2$ on Si and $SiO_2$ regions far away from the nanostructure.

## 6.4 Summary

In this chapter, we focused on the influence strain has on the properties of monolayer $MoS_2$. A shift in optical characterization and an enhancement in mobility with strain were observed. More importantly, our results revealed that very small values of strain can lower the migration energy for the defects and this result could have profound implications on memristor and flexible device application. An approach to induce non-uniform strain by conformal coating was also explored and we found the technique to be effective in modulating the properties of MoS2 locally. The main challenge to this however is the precise design of textured substrate while considering other parameters like thermal expansion coefficient slippage etc. Nonetheless, the conformal growth of monolayers also holds immense potential in fine-tuning the device properties both optically and electrically.

**Bibliography**

[1] Frisenda R, Drüppel M, Schmidt R, Vasconcellos S M De, Lara D P De, Bratschitsch R, Rohl M and Castellanos-gomez A 2017 Biaxial strain tuning of the optical properties of single-layer transition metal dichalcogenides *npj 2D Mater. Appl.* **10** 1–7

[2] Bertolazzi S, Brivio J and Kis A 2011 Stretching and breaking of ultrathin MoS 2 *ACS Nano* **5** 9703–9

[3] Park M, Park Y J, Chen X, Park Y and Kim M 2016 MoS 2 -Based Tactile Sensor for Electronic Skin Applications *Adv. Mater.* **28** 2556–62

[4] Salvatore G A, Mu N, Petti L, Zysset C, Bu L, Ensslin K and Troster G 2013 Fabrication and Transfer of Flexible Few-Layers MoS 2 Thin Film Transistors to Any Arbitrary Substrate *ACS Nano* **7** 8809–15

[5] Cheng R, Jiang S, Chen Y, Liu Y, Weiss N, Cheng H, Wu H, Huang Y and Duan X 2014 Few-layer molybdneum disulfide transistors and circuits for high-speed flexible electronics *Nat. Commun.* 1–9

[6] Lee G, Yu Y, Cui X, Petrone N, Lee C, Choi S, Lee D, Lee C, Yoo W J, Watanabe K, Taniguchi T, Nuckolls C, Kim P, Hone J and Al L E E E T 2013 Flexible and Transparent MoS2 Field-Effect Transistors on Hexagonal Boron *ACS Catal.* **7** 7931–6

[7] Zhang R, Lai Y, Chen W, Teng C, Sun Y, Yang L, Wang J, Liu B and Cheng H-M 2022 Carrier Trapping in Wrinkled 2D Monolayer MoS 2 for Ultrathin Memory *ACS Nano* **16** 6309–16

[8] Liu T, Liu S, Tu K-H, Schmidt H, Chu L, Xiang D, Martin J, Eda G, Ross C A and Garaj S 2019 Crested two-dimensional transistors *Nat. Nanotechnol.* **14** 223–6

[9] Castellanos-Gomez A, Roldán R, Cappelluti E, Buscema M, Guinea F, van der Zant H S J and Steele G A 2013 Local Strain Engineering in Atomically Thin MoS 2 *Nano Lett.* **13** 5361–6

[10] Yang S, Wang C, Sahin H, Chen H, Li Y, Li S-S, Suslu A, Peeters F M, Liu Q, Li J and Tongay S 2015 Tuning the Optical, Magnetic, and Electrical Properties of ReSe 2 by Nanoscale Strain Engineering *Nano Lett.* **15** 1660–6

[11] Deng S, Che S, Debbarma R and Berry V 2019 Strain in a single wrinkle on an MoS 2 flake for in-plane realignment of band structure for enhanced photo-response *Nanoscale* **11** 504–11

[12] Martella C, Mennucci C, Lamperti A, Cappelluti E, de Mongeot F B and Molle A 2018 Designer Shape Anisotropy on Transition-Metal-Dichalcogenide Nanosheets *Adv. Mater.* **30** 1705615

[13] Camellini A, Mennucci C, Cinquanta E, Martella C, Mazzanti A, Lamperti A, Molle A, de Mongeot F B, Della Valle G and Zavelani-Rossi M 2018 Ultrafast Anisotropic Exciton Dynamics in Nanopatterned MoS 2 Sheets *ACS Photonics* **5** 3363–71

[14] Suk J W, Kitt A, Magnuson C W, Hao Y, Ahmed S, An J, Swan A K, Goldberg B B and Ruoff R S 2011 Transfer of CVD-Grown Monolayer Graphene onto Arbitrary Substrates *ACS Nano* **5** 6916–24

[15] Watson A J, Lu W, Guimarães M H D and Stöhr M 2021 Transfer of large-scale two-dimensional semiconductors: challenges and developments *2D Mater.* **8** 032001

[16] Chen C T, Pedrini J, Gaulding E A, Kastl C, Calafiore G, Dhuey S, Kuykendall T R, Cabrini S, Toma F M, Aloni S and Schwartzberg A M 2019 Very High Refractive Index Transition Metal

Dichalcogenide Photonic Conformal Coatings by Conversion of ALD Metal Oxides *Sci. Rep.* **9** 1–9

[17] Martella C, Mennucci C, Cinquanta E, Lamperti A, Cappelluti E, Buatier de Mongeot F and Molle A 2017 Anisotropic MoS 2 Nanosheets Grown on Self-Organized Nanopatterned Substrates *Adv. Mater.* **29** 1605785

[18] Martella C, Ortolani L, Cianci E, Lamperti A, Morandi V and Molle A 2019 Large-area patterning of substrate-conformal MoS2 nano-trenches *Nano Res.* **12** 1851–4

[19] Camellini A, Mennucci C, Cinquanta E, Martella C, Mazzanti A, Lamperti A, Molle A, de Mongeot F B, Della Valle G and Zavelani-Rossi M 2018 Ultrafast Anisotropic Exciton Dynamics in Nanopatterned MoS 2 Sheets *ACS Photonics* **5** 3363–71

[20] Wang K, Puretzky A A, Hu Z, Srijanto B R, Li X, Gupta N, Yu H, Tian M, Mahjouri-Samani M, Gao X, Oyedele A, Rouleau C M, Eres G, Yakobson B I, Yoon M, Xiao K and Geohegan D B 2019 Strain tolerance of two-dimensional crystal growth on curved surfaces *Sci. Adv.* **5** 1–11

[21] Li Z, Lv Y, Ren L, Li J, Kong L, Zeng Y, Tao Q, Wu R, Ma H, Zhao B, Wang D, Dang W, Chen K, Liao L, Duan X, Duan X and Liu Y 2020 Efficient strain modulation of 2D materials via polymer encapsulation *Nat. Commun.* **11** 1151

[22] Sun Y, Wang R and Liu K 2017 Substrate induced changes in atomically thin 2-dimensional semiconductors: Fundamentals, engineering, and applications *Appl. Phys. Rev.* **4** 011301

[23] Zhu C R, Wang G, Liu B L, Marie X, Qiao X F, Zhang X, Wu X X, Fan H, Tan P H, Amand T and Urbaszek B 2013 Strain tuning of optical emission energy and polarization in monolayer and bilayer MoS2 *Phys. Rev. B* **88** 121301

[24] Yang S, Chen Y and Jiang C 2021 Strain engineering of two-dimensional materials: Methods, properties, and applications *InfoMat* **3** 397–420

[25] Rubio-Bollinger G, Guerrero R, de Lara D P, Quereda J, Vaquero-Garzon L, Agraït N, Bratschitsch R and Castellanos-Gomez A 2015 Enhanced visibility of MoS2, MoSe2, WSe2 and black-phosphorus: Making optical identification of 2D semiconductors easier *Electron.* **4** 847–56

[26] McCreary K M, Hanbicki A T, Sivaram S V. and Jonker B T 2018 A- and B-exciton photoluminescence intensity ratio as a measure of sample quality for transition metal dichalcogenide monolayers *APL Mater.* **6**

[27] Ci P, Tian X, Kang J, Salazar A, Eriguchi K, Warkander S, Tang K, Liu J, Chen Y, Tongay S, Walukiewicz W, Miao J, Dubon O and Wu J 2020 Chemical trends of deep levels in van der Waals semiconductors *Nat. Commun.* **11** 5373

[28] Komsa H-P and Krasheninnikov A V. 2015 Native defects in bulk and monolayer MoS2 from first principles *Phys. Rev. B* **91** 125304

[29] Zhou W, Zou X, Najmaei S, Liu Z, Shi Y, Kong J, Lou J, Ajayan P M, Yakobson B I and Idrobo J-C 2013 Intrinsic Structural Defects in Monolayer Molybdenum Disulfide *Nano Lett.* **13** 2615–22

[30] Conley H J, Wang B, Ziegler J I, Haglund R F, Pantelides S T and Bolotin K I 2013 Bandgap Engineering of Strained Monolayer and Bilayer MoS 2 *Nano Lett.* **13** 3626–30

[31] He K, Poole C, Mak K F and Shan J 2013 Experimental Demonstration of Continuous Electronic Structure Tuning via Strain in Atomically Thin MoS 2 *Nano Lett.* **13** 2931–6

[32] De Fazio D, Goykhman I, Yoon D, Bruna M, Eiden A, Milana S, Sassi U, Barbone M, Dumcenco D, Marinov K, Kis A and Ferrari A C 2016 High Responsivity, Large-Area Graphene/MoS 2 Flexible Photodetectors *ACS Nano* **10** 8252–62

[33] Precner M, Polaković T, Qiao Q, Trainer D J, Putilov A V., Di Giorgio C, Cone I, Zhu Y, Xi X X, Iavarone M and Karapetrov G 2018 Evolution of Metastable Defects and Its Effect on the Electronic Properties of MoS2 Films *Sci. Rep.* **8** 1–10

[34] Bahmani M, Faghihnasiri M, Lorke M, Kuc A-B and Frauenheim T 2020 Electronic Properties of Defective MoS 2 Monolayers Subject to Mechanical Deformations: A First-Principles Approach *Phys. status solidi* **257** 1900541

[35] Lin P, Zhu L, Li D, Xu L, Pan C and Wang Z 2018 Piezo-Phototronic Effect for Enhanced Flexible MoS2/WSe2 van der Waals Photodiodes *Adv. Funct. Mater.* **28** 1–8

[36] Gant P, Huang P, Lara D P De, Guo D, Frisenda R and Castellanos-gomez A 2019 A strain tunable single-layer MoS 2 photodetector *Mater. Today* **27** 8–13

[37] Wu W, Wang L, Yu R, Liu Y, Wei S H, Hone J and Wang Z L 2016 Piezophototronic Effect in Single-Atomic-Layer MoS2for Strain-Gated Flexible Optoelectronics *Adv. Mater.* **28** 8463–8

[38] Sensoy M G, Vinichenko D, Chen W, Friend C M and Kaxiras E 2017 Strain effects on the behavior of isolated and paired sulfur vacancy defects in monolayer MoS2 *Phys. Rev. B* **95** 014106

[39] Kushima A and Yildiz B 2009 Role of Lattice Strain and Defect Chemistry on the Oxygen Vacancy Migration at the (8.3% Y 2 O 3 -ZrO 2 ) / SrTiO 3 Hetero-Interface: A First Principles Study *ECS Trans.* **25** 1599–609

[40] Yang Q, Cao J X, Ma Y, Zhou Y C, Jiang L M and Zhong X L 2013 Strain effects on formation and migration energies of oxygen vacancy in perovskite ferroelectrics: A first-principles study *J. Appl. Phys.* **113** 184110

[41] Dutta P and Horn P M 1981 Low-frequency fluctuations in solids: 1/f noise *Rev. Mod. Phys.* **53** 497–516

[42] Stephany J F 2000 Frequency limits of 1/ f noise *J. Phys. Condens. Matter* **12** 2469–83

[43] Radisavljevic B, Radenovic A, Brivio J, Giacometti V and Kis A 2011 Single-layer MoS2 transistors *Nat. Nanotechnol.* **6** 147–50

[44] Checco A, Rahman A and Black C T 2014 Robust Superhydrophobicity in Large-Area Nanostructured Surfaces Defined by Block-Copolymer Self Assembly *Adv. Mater.* **26** 886–91

[45] Rahman A, Ashraf A, Xin H, Tong X, Sutter P, Eisaman M D and Black C T 2015 Sub-50-nm self-assembled nanotextures for enhanced broadband antireflection in silicon solar cells *Nat. Commun.* **6** 1–6

[46] Zubel I and Kramkowska M 2001 The effect of isopropyl alcohol on etching rate and roughness of (1 0 0) Si surface etched in KOH and TMAH solutions *Sensors Actuators A Phys.* **93** 138–47

[47] Li H, Contryman A W, Qian X, Ardakani S M, Gong Y, Wang X, Weisse J M J M, Lee C H, Zhao J, Ajayan P M, Li J, Manoharan H C and Zheng X 2015 Optoelectronic crystal of artificial atoms in strain-textured molybdenum disulphide *Nat. Commun.* **6** 7381

# Chapter 7

# Unveiling the Phase Evolution of All-Inorganic Perovskite Nanowires

This chapter is an adaptation of the research article published in "*Nanotechnology* **33** 085706, 2021"

## 7.1 Introduction

The remarkable properties of lead halide perovskites have positioned them as the rising stars among optoelectric materials, offering advantages such as high absorption coefficients, long carrier diffusion lengths, and cost-effective fabrication. However, challenges related to stability, especially in the case of organic-inorganic hybrid perovskites, have impeded their widespread use. In contrast, all inorganic perovskites exhibit excellent thermal stability and demonstrate promising optoelectric characteristics. Notably, nanowires have gained significant interest due to their potential applications in optics and optoelectronics.[1–8] Among these $CsPbI_3$, which exhibits a bandgap of 1.73 eV in its α-phase is of particular interest. However, this phase is metastable at room temperature and spontaneously transforms into the δ-phase, characterized by a higher bandgap of ~2.82 eV.[9,10] The stability of the cubic phase is surpassed by the thermodynamically more stable δ-phase, leading to the degradation of the former into the latter.[11] Various factors, such as size, temperature, light, surfactants, and solvents, have been found to influence phase transitions in $CsPbI_3$ nanowires.[11–15] Among the different methods employed to obtain α-phase $CsPbI_3$ nanowires, hot injection (HI) has gained prominence due to its simplicity, precise control, and high yield. The $CsPbX_3$ (X=Cl, Br, I) nanocrystals (NCs) were first synthesized using the HI method by Protesescu et al.[16] Subsequent research expanded the synthesis to achieve nanowires with different morphologies, including nanospheres, nanoplatelets, and nanorods. [17–22]. In this study, we present a modified HI method for the growth of $CsPbBr_3$ and $CsPbI_3$ perovskites, with a particular focus on the

evolution of crystals from Quantum dots (QDs) to nanowires. Through comprehensive analyses, we establish the presence of photoactive perovskite phases in the NCs of both materials and observe the successful growth of $CsPbBr_3$ nanowires in the perovskite phase. However, $CsPbI_3$ nanowires primarily grow in the non-perovskite δ-phase. Moreover, we provide in situ evidence for the crystal growth of $CsPbI_3$ nanowires, supporting the notion that they inherently grow in the δ-phase rather than undergoing a phase transition. We also found that during the HI synthesis, the presence of QDs or nanocrystals (NCs) alongside the nanowires poses challenges in characterizing the nanowire's true phase. The signals from NCs can obscure signals from the non-perovskite δ-phase, and this is true for both bulk photoluminescence (PL) and X-ray diffraction (XRD) measurements, making it difficult to discern the nanowire's phase. This research significantly contributes to our understanding of the growth of all inorganic perovskite nanowires and also points out the importance of microscopic techniques to discern between different phases of perovskite.

## 7.2 Synthesizing QDs

The $CsPbBr_3$/$CsPbI_3$ QDs were prepared using the hot injection method. Freshly prepared Cesium oleate was synthesized by adding 0.2 g of $Cs_2CO_3$ to 8 ml of Octadecene (ODE) along with 0.6 ml of Oleic acid (OA). The mixture was kept in the vacuum at a temperature of 120 °C till all the $Cs_2CO_3$ dissolved. Then dry nitrogen was flushed and the temperature was cranked up to 150 °C which is kept on standby. Simultaneously we take 0.1 g of $PbBr_2$/$PbI_2$, 8 ml of ODE, 1 ml of Oleylamine (OLA), and 0.2 ml of Octylamine (OctA) in a separate 3-necked flask and heated to 90 °C in the vacuum till $PbI_2$ dissolves. We then pass dry $N_2$ and crank the temperature to 120 °C and inject the freshly prepared Cesium oleate, about 0.6 ml into this. The color of the solution immediately turns reddish-brown and is kept at 120 °C for 1 min and is quenched in an ice bath. The Raw solution can either be diluted using Toluene or ODE and can be stored at -40 °C for long-term storage.

## 7.3 Modifying the HI process

Previous studies have revealed that the crystal growth process in the hot injection (HI) technique consists of two stages: nucleation, followed by a rapid crystal formation lasting a few tens of seconds, and subsequent Oswald ripening, where smaller crystals dissolve and feed the growth of larger crystals.[23][24] Building on this knowledge, we hypothesized that we can resume the reaction after quenching once the first stage is complete. We anticipated that by heating the quenched solution of QDs at a later stage, we could resume the growth process and obtain different crystal morphologies according to the temperature and/or surfactants used.

To test our hypothesis, we quenched the HI reaction within one minute after injecting freshly prepared Cesium oleate at 120°C. At this point, all the formed nanocrystals were in the form of quantum dots, exhibiting photoactive perovskite properties. Comprehensive characterizations of these QDs were performed using photoluminescence (PL), UV-Vis absorption, and time-resolved PL measurements (Fig. 7.1a-c). The PL peak at 680 nm corresponded to an energy of 1.82 eV, with a full width at half maximum (FWHM) of 36 nm. The observed peak shift from the material's energy of 1.73 eV was attributed to the quantum confinement effects of the QDs, wherein smaller QDs exhibited a more significant blue shift. [25][26]

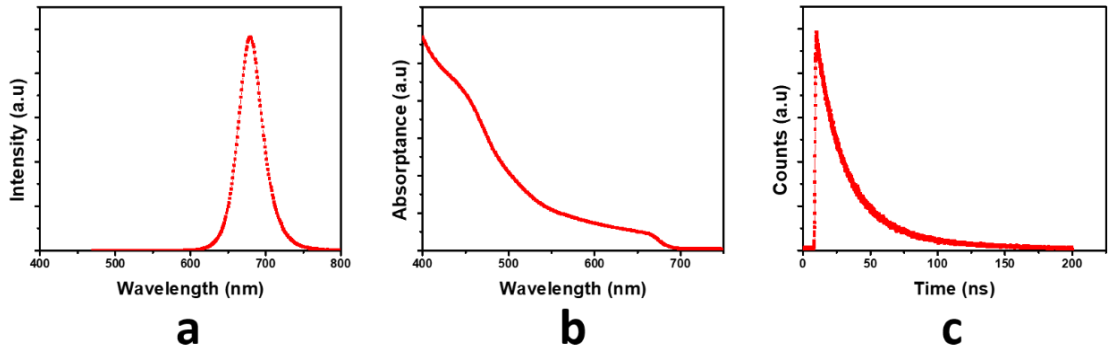


Figure 7.1: (a) PL spectra of $CsPbI_3$ QDs which peaks at 680 nm, (b) UV−vis absorption of the QDs. (c) Time-resolved PL decay curves of the QDs showing a decay lifetime of 23 ns.

To verify the size of the crystals we used High-resolution transmission electron microscopy (HRTEM) images (Fig. 7.2 a). The HRTEM analysis revealed an average particle size estimation of approximately 9 nm, and a corresponding size histogram is presented in Fig. 7.2b. The analysis was done using ImageJ software. The UV-Vis absorption curve and the PL decay curve, indicating a lifetime of 23 ns, aligned with previous reports on α-$CsPbI_3$ QDs synthesized using oleic acid (OA).[27]These findings confirmed that the initial solution contained photoactive QDs in a perovskite state with an average size of 9 nm.

Subsequently, a drop of the original QD solution was placed on a microscope coverslip and heated under inert conditions at 200°C for approximately 10 minutes. Remarkably, the clear solution observed under the microscope transformed into a dense cluster of nanowires upon heating, proving that nanowire growth could be resumed from the QDs by heating the solution at a later stage. The same procedure was successfully applied to $CsPbBr_3$ as well. The PL images confirmed the growth of nanowires from the solution, with $CsPbI_3$ nanowires displaying a faint yellowish emission, attributed to the presence of the δ-phase.[28] The bright green PL of $CsPbBr_3$ nanowires demonstrated that our method was capable of producing perovskite nanowires as effectively as conventional HI or other solution-based approaches.

To ensure the comparability of our approach to the conventional HI method in terms of nanowire quality, we initially validated our technique using $CsPbBr_3$ as a model system. The measured interatomic distance of the wires, determined to be 0.56 nm, aligned with reported values for orthorhombic $CsPbBr_3$ grown using the HI method.[28] These results affirm that our method of interrupting and resuming the reaction can rapidly produce high-quality nanowires on demand.

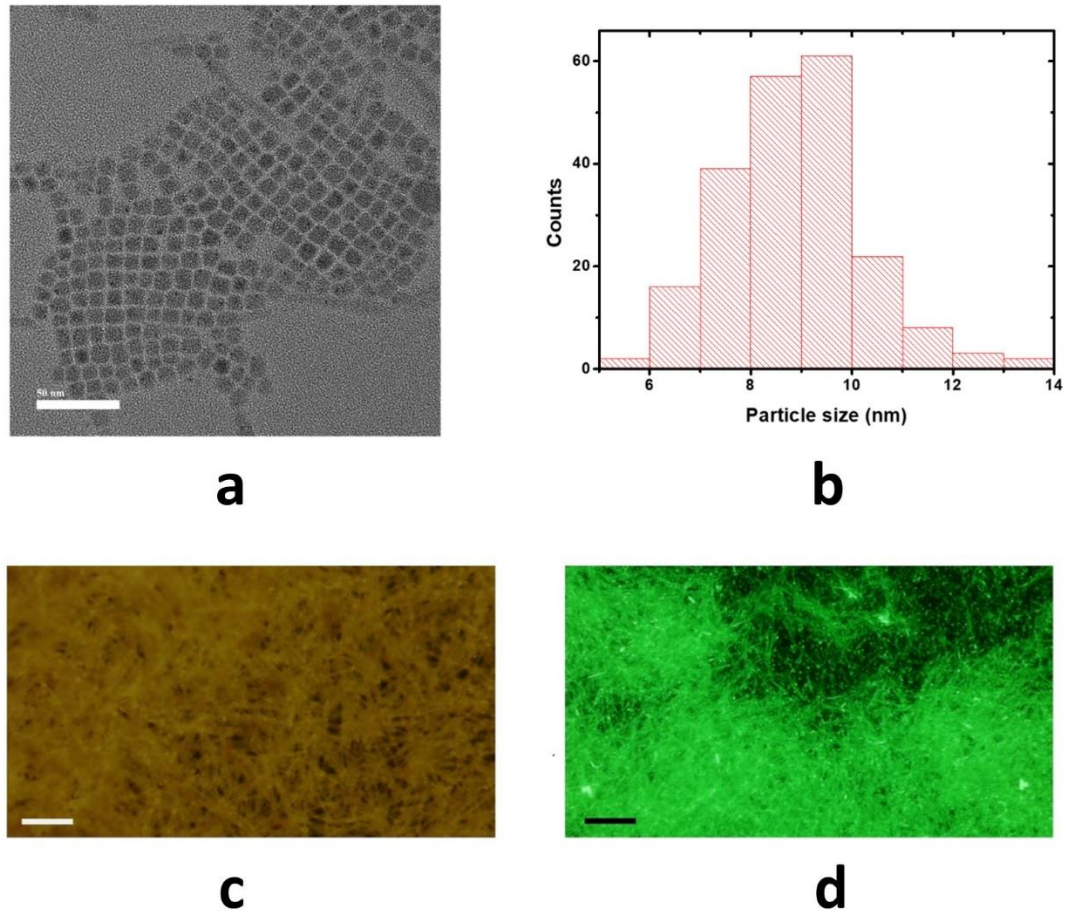


Figure 7.2: (a) HRTEM images of the $CsPbI_3$ QDs (scale bar is 50 nm). (b) Histogram showing the size distribution of the QDs. (c) and (d)) are PL images of nanowires formed by heating the QD raw solutions of $CsPbI_3$ and $CsPbBr_3$, respectively (scale bar 30 µm).

### 7.3.1 XRD of nanowires

During the growth of $CsPbI_3$, we made observed that the color of the raw solution changes as it was heated. Initially, the solution turns black and subsequently transitions to a yellow color. If we rapidly heat the solution to 220°C, it will turn black by the time it reaches the target temperature. If we do not immediately quench the heating process, the solution will gradually change to a yellow color within a few tens of seconds. Additionally, there is a slight evaporation of the organic solvent (ODE), which increases the solution's concentration.

To halt the reaction, we quenched the heating process by introducing cold water into the stage as soon as the solution turned black. XRD of the black solution, as well as on the dense clusters

of nanowires were taken. The XRD data from both samples were plotted and compared with the ICSD data of alpha(α) and delta (δ)-phase of $CsPbI_3$ (Fig. 7.3 a and b). The black solution primarily consisted of the photoactive phase, referred to as the α-phase, which is represented by the red plot. In contrast, the nanowires were in the δ-phase, indicated by the yellow plot. The XRD pattern displayed similarities to that of the cubic phase, with two additional peaks and a double peak near 30 degrees, which could be attributed to the presence of mixed phases. The prominent peak near 10 degrees is likely from the δ-phase, as it aligns with its characteristic peak. The presence of the twin peaks may arise from a combination of the cubic phase and a strained phase, which also exists in the photoactive perovskite phase, such as the gamma (γ) or beta (β) phases of $CsPbI_3$.[29,30]

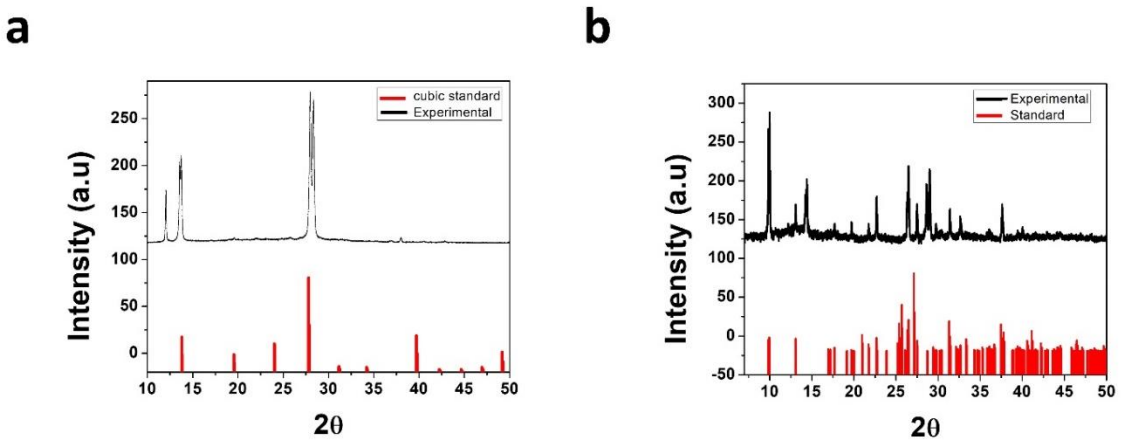


Figure 7.3: (a) shows the XRD of experimental cubic $CsPbI_3$ compared with standard XRD peak and (b) shows the XRD of experimental δ-$CsPbI_3$ with the standard XRD peak. ICSD ID are 161481 and 27979 respectively for cubic and δ-phases.

### 7.3.2 HRTEM of nanowires

To verify the presence of mixed states in the obtained crystals, we transferred the NCs onto a carbon-coated transmission electron microscopy (TEM) grid. This transfer was achieved by immersing the substrate in toluene and drop-casting the solution onto the TEM grid. Fig. 7.4a displays a low magnification high-resolution TEM (HRTEM) image, revealing the presence of long wires and numerous quantum dots, most of which appear as cubes with rounded edges as seen in Fig. 7.4b. The interatomic distance and the FFT pattern of the crystals confirm the crystals to be in the cubic phase. The particle size distribution histogram of 110 cubes is shown

in Fig. 7.4d indicating an average size of approximately 44 nm. The wires, on the other hand, exhibited diameters ranging from 25 to 30 nm with a length of a few micrometers. The discrepancy in diameter and length suggest that surfactants aid in the directional growth of the δ-phase but not in the cubic phase. This phenomenon explains why the cubes uniformly grew from 9 nm to 44 nm in all directions, while the wires, which have elongated several micrometers in a particular direction, only reached diameters of 25-30 nm. HRTEM images provide visual evidence of the existence of different forms of perovskite NCs. Moreover, analysis of the interatomic spacing and the FFT of the crystal structure of the wires (Fig. 7.4 e and f) and cubes confirms their distinct crystal structures. Energy-dispersive X-ray spectroscopy (EDX) analysis of the wires confirms that their composition corresponds to $CsPbI_3$.

The HRTEM data firmly establish the presence of multiple phases in the NCs. The measured nanowire with a diameter of approximately 25 nm is identified as being in the δ-phase, while the cube with a side length of 47 nm corresponds to the α-phase, as evident from their respective interatomic spacing (0.61 nm and 0.46 nm) and FFT analysis.[31] [28] The predominance of cubic particles aligns with the stronger peaks observed in the XRD data for the α-phase. However, due to the mixed nature of the system, utilizing bulk techniques to explore the phase of the wires can introduce experimental artifacts, as the properties of one phase may mask the other. Therefore, it is essential to employ microscopic techniques and characterize the wires individually to accurately determine their actual phase.

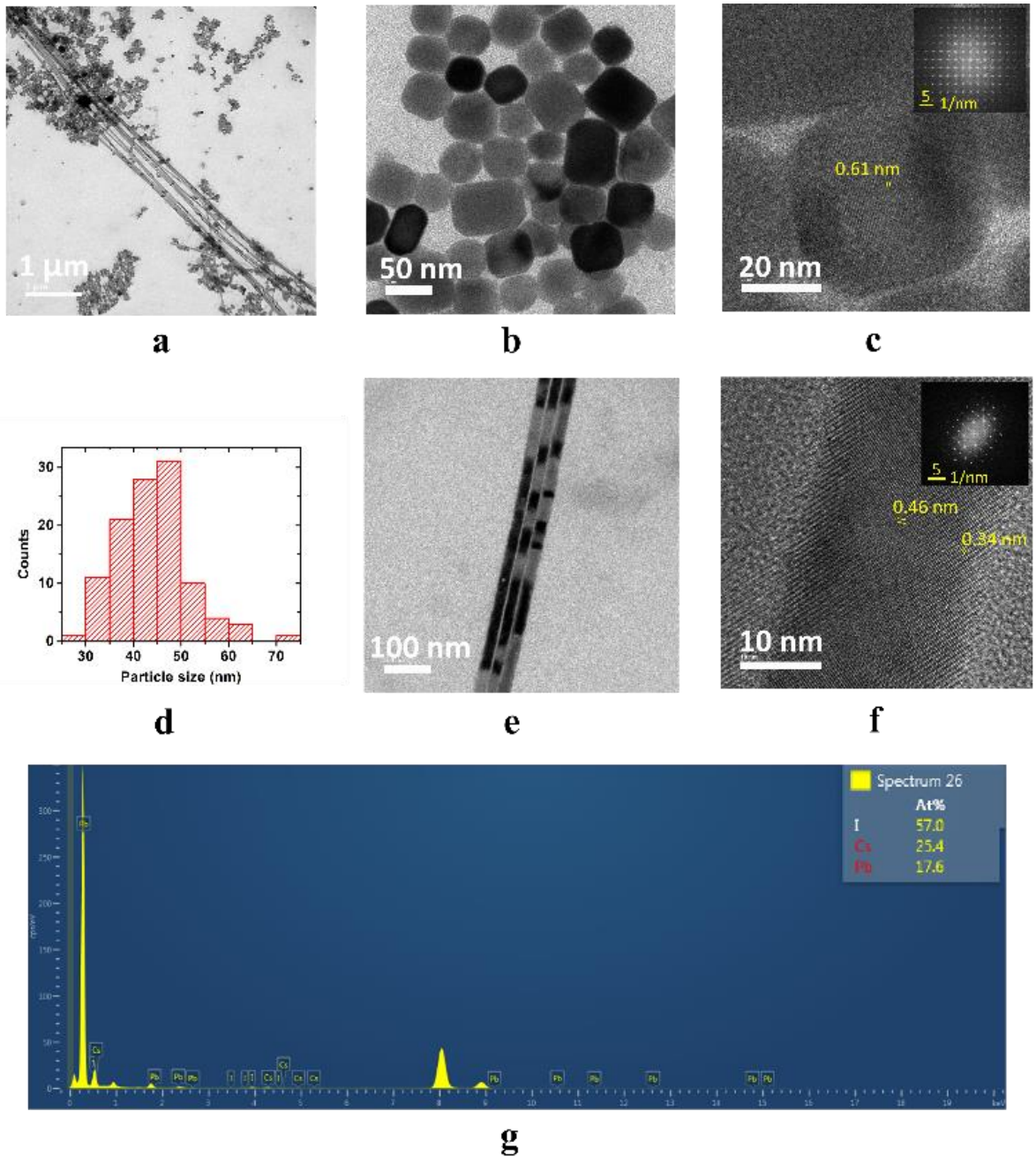


Figure 7.4: (a) Lower magnification HRTEM image of the NCs. (b) and (e) are high-resolution images of cubes and wires. (c) and (f) is the HRTEM images of the respective cubes and wires showing the interatomic spacing with FFT patterns of the corresponding lattice shown in the inset of each image. (d) Histogram of the size distribution of cubes (110 cubes) from a small cluster. (g) EDX spectrum showing the elemental composition of the nanowires

### 7.3.3 Electrical characterization of nanowires

The optoelectronic characteristics of the nanowire devices were assessed through a series of measurements. As the wires dissolved in water, it was impossible to do photolithography on the wires. Using shadow-masking was also not an option as we had to have a micro mask aligned perfectly with the nanowires. Thus, we choose to drop-cast the wires onto the interdigitated leads and subsequently dried them. To ensure that only the nanowires, which extend several micrometers in length, made contact between the two leads, the spacing between consecutive leads was maintained at 4 μm. The use of a dilute solution and large spacing ensures that no QDs make a complete connection and the electrical signal that we measure is purely from the nanowires. Optical microscopic images (Fig. 7.5 a and b clearly depict that the device had only a few nanowires forming connections between the leads, while no nanoparticle clusters were observed (as evident from the dark field image, Fig. 7.5b).

The device was measured under open environmental conditions using a home-built probe station and a Keithley 2450 source measure unit. Light-emitting diodes (LEDs) powered and controlled by Arduino were employed as the light sources. Upon illumination with a 9 $mW/cm^2$ 535 nm LED, the device exhibited no photo-response. However, when illuminated with a 405 nm LED at an intensity of 12 $mW/cm^2$, a significant photo-response was observed (Fig. 7.5c). The nanowire device displayed reproducible photo-response behavior under repeated ON/OFF cycles of the 405 nm LED, with no reduction in the peak photocurrent value as can be seen in Fig. 7.5d. Remarkably, the device performance remained stable over several months, even when exposed to an open environment.

The fact that the nanowires exclusively responded to the 405 nm LED and not the 535 nm LED can be attributed to the absorption characteristics of the δ-phase, which begins around 457 nm.[28] This result further corroborated the presence of nanowires in the δ-phase.

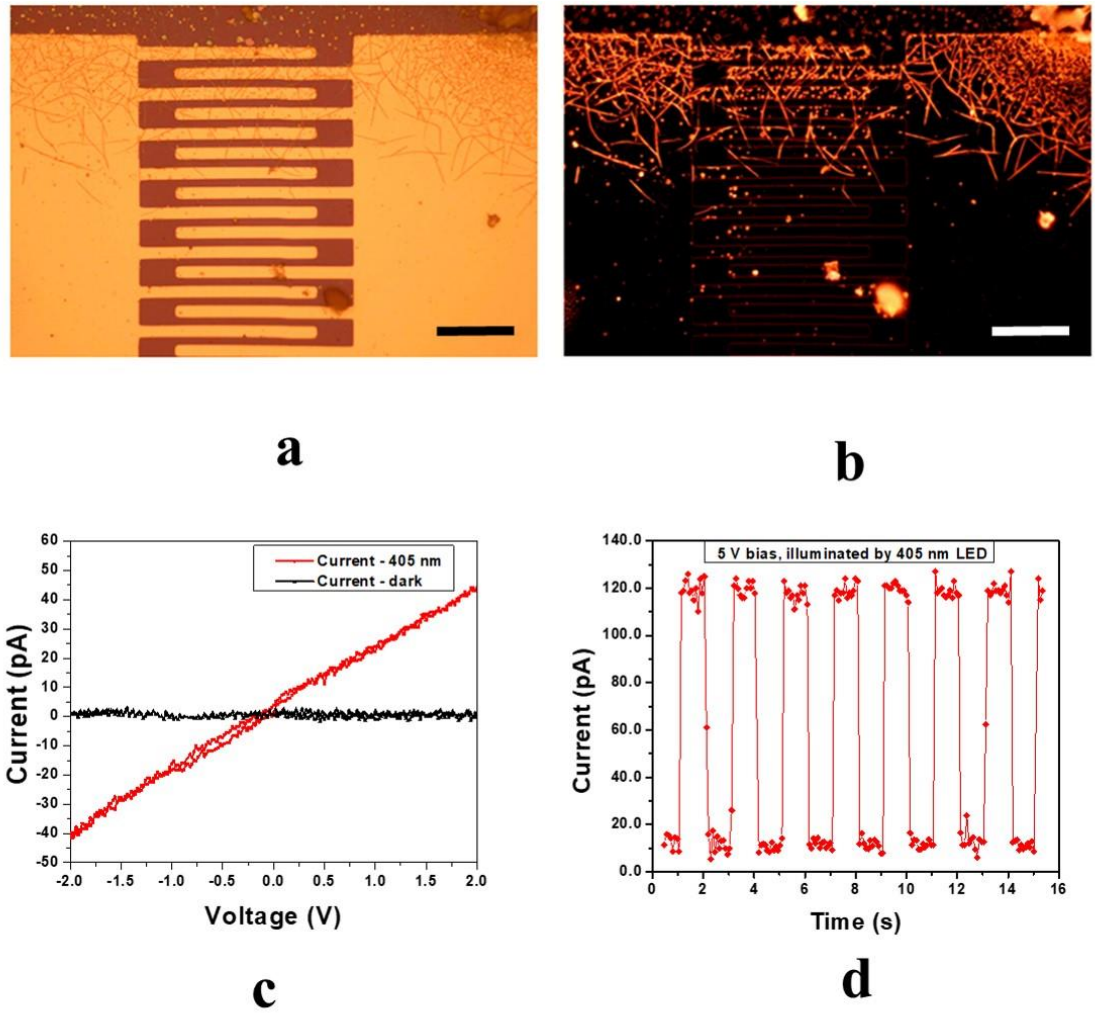


Figure 7.5: (a) The optical microscopic image of the device, (b) Dark-field image of the same clearly showing the presence of nanowires. (scale bars are 50 µm for both (a) and (b) ). (c) The I-V characteristics of the nanowire device with and without the 405nm LED (12 mW/cm2). (d) I-t response of the device was obtained by repeatedly turning on and off the 405 nm LED. 5V bias was applied to the nanowire device during the measurement.

## 7.4 In-situ observation of growth

$CsPbI_3$ nanowires synthesized using various techniques such as vapor phase growth, asymmetric wettability-topographical template, or solution dipping, have exhibited photoluminescence (PL) images or device responses, confirming that they are in the perovskite phase.[31] [5,32–34][35] Notably, some of these wires were reported to be 1 µm wide, indicating the potential for the nanowires to grow long and wide in their active perovskite state.[35] However, the nanowires

produced using the hot injection (HI) process, despite being thinner than the α-phase quantum dots (QDs), were found to be in the δ-phase. This disparity could be attributed to the distinct growth mechanism employed in the HI technique, which utilizes surfactants such as lead oleate, oleylammonium halide, oleic acid (OA), oleylamine (OLA), and octylamine (OctA) for the formation of perovskite nanocrystals (NCs).[36] Consequently, the suitability of the HI method for synthesizing nanowires of highly symmetric cubic phase perovskites may be limited. This notion gains further support from the fact that most of the NCs were larger in diameter than the wires observed in Fig. 7.4a. If the surfactants indeed confined the growth of α -phase QDs into wires through selective adsorption, the cubes would not have grown symmetrically to such sizes. The observed wires were a few micrometers in length with a diameter of around 25 nm, whereas the majority of QDs grew symmetrically in all directions, increasing their size by nearly five times, from approximately 9 nm to 44 nm (Fig.7.4a). The symmetrically growing QDs were in the cubic phase, whereas the nanowires were in the δ-phase, as indicated by their lattice spacing and fast Fourier transform (FFT) patterns. Therefore, the most plausible explanation is that preferential growth of NCs, facilitated by surfactants, leading to nanowire formation, occurs when the highly symmetric cubic phase transitions to beta (β), gamma (γ), or delta (δ) phases in the case of the HI technique. This notion is supported by recent work on $CsPbBr_3$, where QDs are grown into wires by utilizing light to selectively remove surfactants from one plane, promoting the self-assembled growth of cubic nanowires.[37] This indicates that the surfactants naturally cover all sides of the cubic crystal, and an external stimulus is necessary to eliminate these ligands. The selective adsorption of ligands onto crystal planes aids in nanowire growth in ligand-mediated processes.[38,39] Based on our observations, we propose that since crystals in the cubic phase grow isotropically while crystals in the δ-phase grow anisotropically, the selective adsorption occurs in the δ-phase rather than the cubic phase of $CsPbI_3$.

### 7.4.1 Design of the heater box and controller

This method of resuming the growth by heating the liquid makes it possible to view the nanowire growth under a microscope with an appropriate setup. For this, we designed a compact heater box with rapid heating and cooling capability. We used an Aluminum box with an O-ring positioned along the rim to ensure an airtight seal as the body of the heater box. Inside the box,

an Aluminum block is placed on top of a floating SS (stainless steel) platform, which is securely attached to the walls of the box. The floating platform ensures minimal heat loss from the Aluminum block to the box. Within the block, two Cartridge heaters of 30 W each as the heating element. To monitor the temperature of the block, a k-type thermocouple is employed. We used a Nickel-Alumel thermocouple as the temperature sensor and the accuracy of the designed temperature on the surface of the block, in the range 60-400 °C, was tested using a Pt-100 sensor. The temperature was found to be accurate up to 1°C. We also installed a water circulating system to quench the box fast. The box also has a glass/quartz window made with a microscope coverslip. The box can reach 250 °C within 2 min from the room temperature of around 25°C. The water circulation option rapidly quenches the temperature down to room temperature as we pump chilled water through it. The sample stage with the heating-cooling arrangement is placed very close to the window making it possible to observe the reaction under a microscope. The box was purged with nitrogen to create an inert environment during the reaction. A rough diagram of the box with its lid open is shown in Fig. 7.6 a and b. An actual photograph of the box and controller is given in Fig. 7.6c. The rapid heating and cooling capability of the box help to resume the reaction fast and also to quench the reaction immediately when needed.

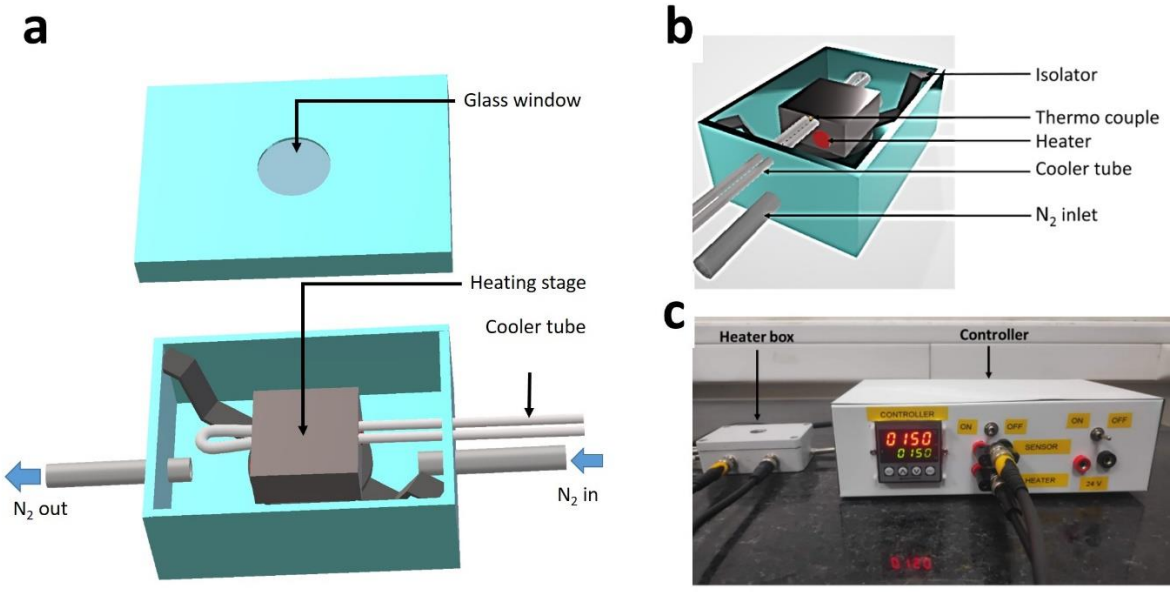


Figure 7.6: (a) and (b) are the diagrams of the home-built box used for the study, and (c) is the photograph of the home-built box and controller used for the experiment.

### 7.4.2 Growth inside the chamber

To further explore the growth mechanism, we tried to observe the growth of nanowires from the raw solution under a microscope. For this, we diluted the raw solution in ODE/toluene and heated the solution on a $SiO_2$/Si substrate. The dilution will reduce the concentration of compounds initially. But it will gradually increase as we heat the solution as some ODE or all of the toluene will vaporize. The vaporization rate would be higher due to the large surface-to-volume ratio. Solutions diluted with toluene will reach the desired concentration much faster and the time of the start of reaction is greatly reduced but makes it difficult to do high-temperature growth. Both methods, apart from the time taken for the reaction, gave us a similar result. After dilution, the solution was PL active for over a week and we did not observe much change in particle size or phase of $CsPbI_3$ within a day, similar to observations made by others on both $CsPbI_3$ and $Br_3$.[40,41] Another concern with this method is the concentration of surfactants. As is known from recent studies that excess amines like oleylamine could induce the decomposition of crystals and excess oleic acid can cause it to revert to a tetragonal structure gradually.[15] Here such cases did not arise as the samples were diluted and the end products were indeed confirmed to be $CsPbI_3$ in either cubic or δ-phase. There are other advantages to diluting the solution. The initial low concentration will give enough time to attain the temperature before the growth begins. It also reduces the density of particles allowing us to better visualize the growth. A schematic of the whole process is shown in Fig. 7.7. Depending on the composition of $PbI_2$ and $PbBr_2$ we can make QDs of desired composition. The solution is then diluted in toluene or ODE. A few drops of the solution are placed to a 1 cm X 1 cm $SiO_2$/Si substrate kept inside the heater box. The box is sealed and is purged with nitrogen gas to create an inert atmosphere. The entire setup is kept under the microscope and the stage is taken to the temperature of interest and the growth is observed as it happens.

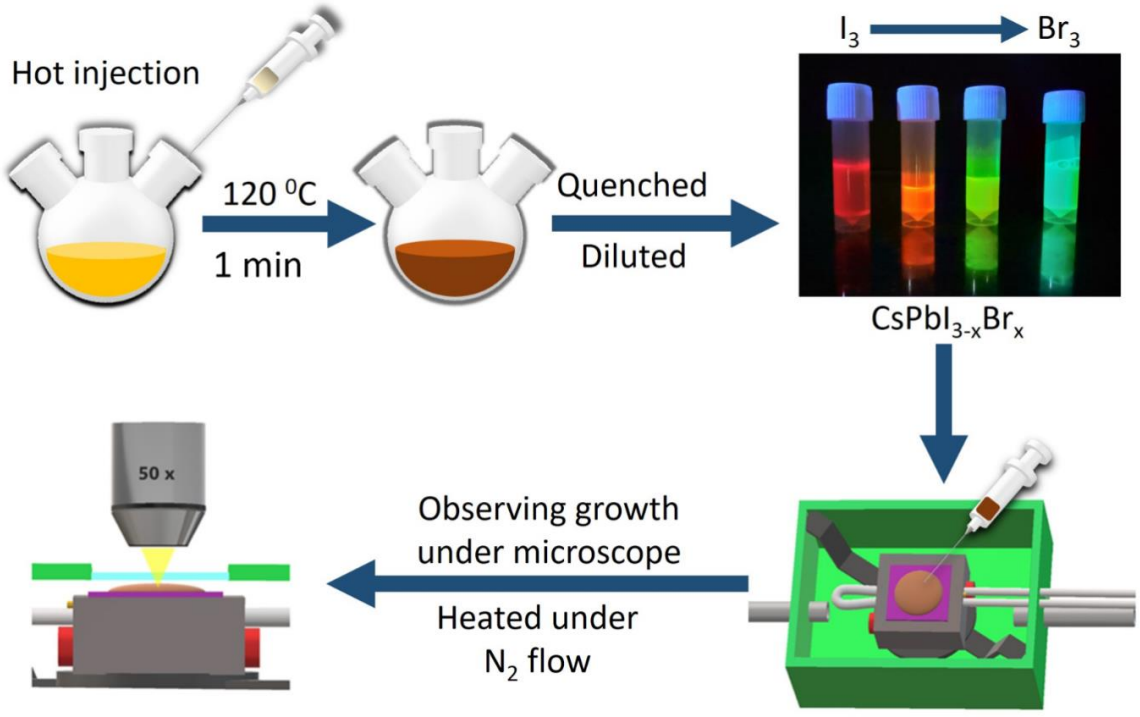


Figure 7.7: Various steps are involved in the in situ observation of the growth of nanowires under an optical microscope. By injecting freshly prepared Cesium oleate into the reaction mixture perovskite QDs are formed. Based on the composition of $PbI_2$/ $Br_2$ in the mixture we can get $CsPbI_{3-x}Br_x$. The varying composition of QDs gives different colors, as seen in the image above. The QD solution is then heated in an inert atmosphere under the microscope using the heater box, making it possible to observe the wires as they grow.

### 7.4.3 Observed growth

We used p++ $SiO_2$ on Si substrates as it ensures efficient transfer of heat and provides a clean background, which helps to observe the reaction. Nanowires of different diameters and different lengths were grown by varying the temperature of the growth. The reactions proceed for about 10-25 min before quenching it. We start observing the growth after 3-10 min of turning the heater on, the exact timing can vary depending on the temperature and concentration. The solution was diluted by adding one part of the raw solution with four parts of ODE/Toluene. This solution is left for a day so that the larger particles can settle down at the bottom. The supernatant solution, whose PL characteristics confirmed the presence of the photoactive perovskite phase, was taken for the nanowire growth. After the growth, we clean the substrate by dipping it in toluene followed by blow-drying. Nanowires of length up to 90 µm were grown

using this technique Fig. 7.8 a and b. The growth at lower temperatures is slow and forms shorter nanowires, Fig. 7.8d. At higher temperatures, the growth is faster and we obtain longer nanowires, Fig. 7.8 e and f.

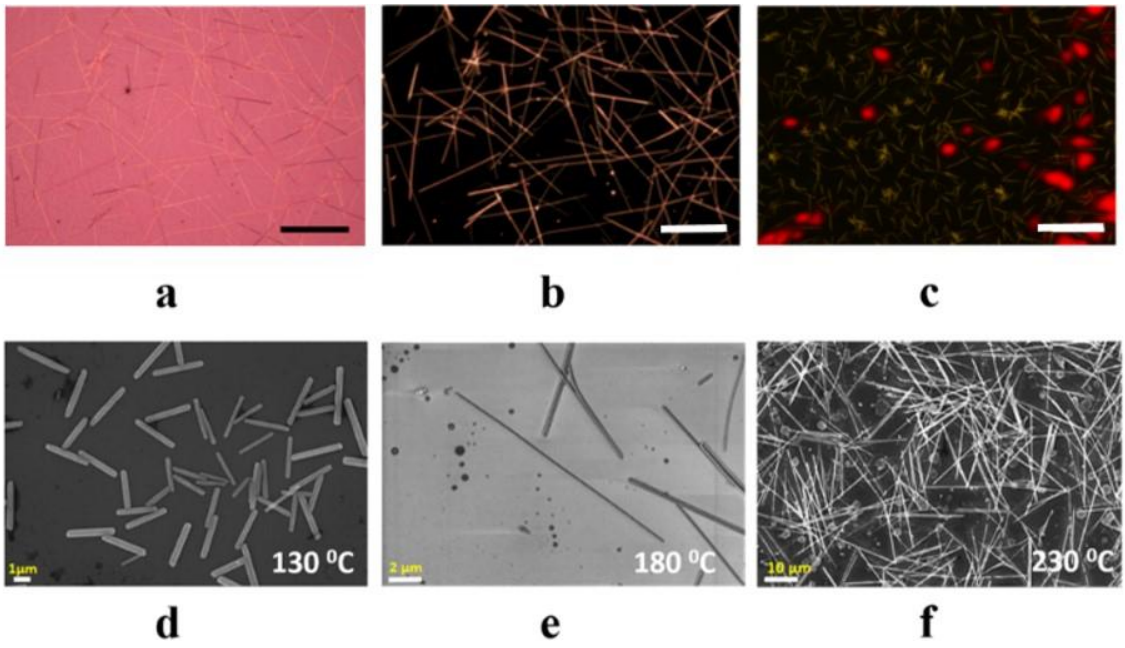


Figure 7.8: (a) Shows the optical microscopic image of nanowires synthesized at 230°C, (b) is the dark field image of the same, (c) shows the PL image of nanowire synthesized at 180°C, the excitation wavelength of the PL light source was 450 nm and a long pass filter of 505 nm was used to collect the light from the samples. The scale bars for all three are 50 µm. (d), (e) and (f) are FESEM images of $CsPbI_3$ nanowires synthesized at different temperatures.

Under the microscope, we often observed that at a particular temperature during growth, some particles started dissolving as nanowires grew nearby. The PL image QD solution before heating, shows a uniform red background (Fig. 7.9a and QD cluster and nanowires from the same region after the growth (Fig. 7.9 b and c respectively), it is clear that we do have QD clusters in their photoactive perovskite state, which are most likely in their cubic α phase, along with the δ- phase nanowires during the growth of wires. Fig. 7.9d shows the optical microscopic image of the liquid with no particles visible and as the solution was heated the QDs grew and started to form clusters (Fig. 7.9e) and after some time plenty of nanowires were observed (Fig. 7.9f). One such representative result observed at 200 °C has been shown in Fig. 7.9g. Here it is evident that the QDs are dissolving, eventually disappearing, as the reaction proceeds. Fig. 7.9g shows that these clusters began to dissolve while the wires grew as time progresses. After the

dissolution of the wires, we could see no red light-emitting QDs as can be seen in Fig. 7.2c. This shows that the QDs completely dissolved as the wires grew longer.

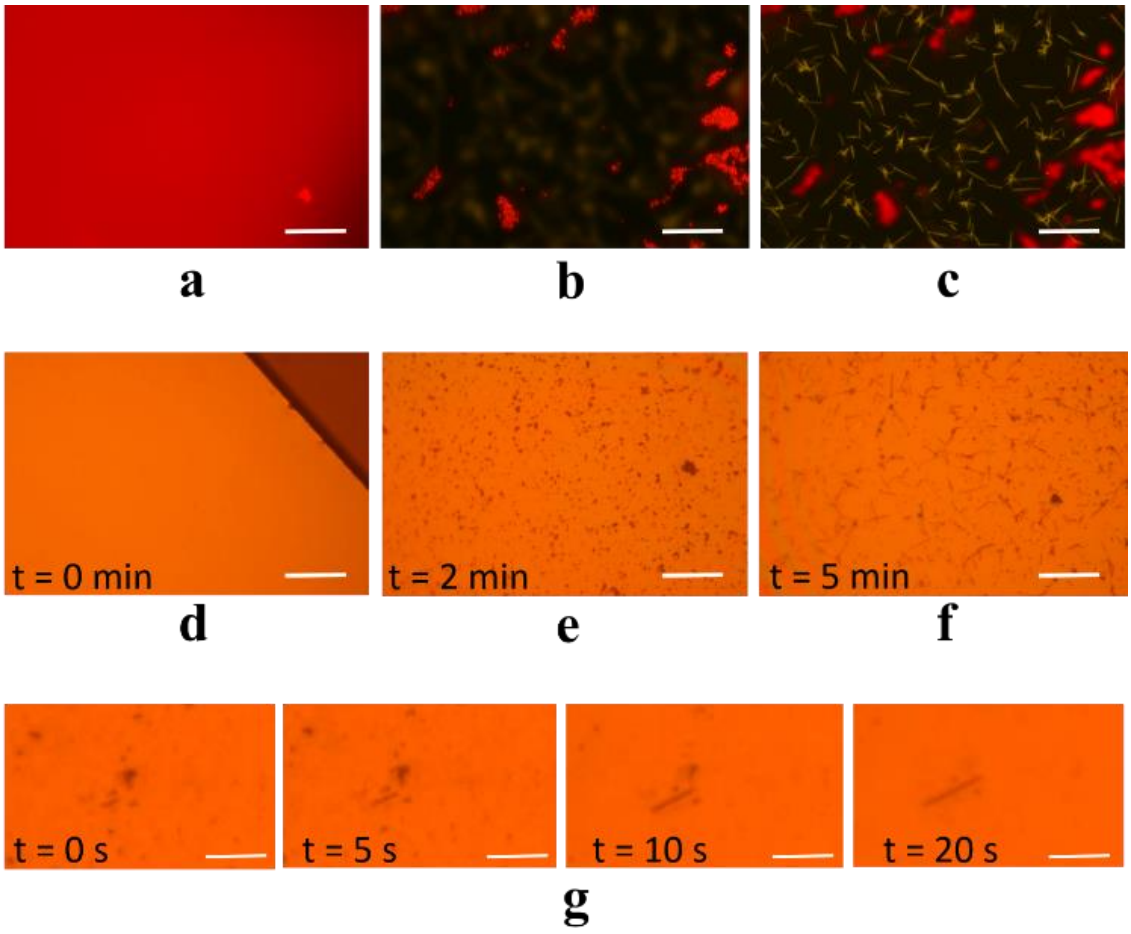


Figure 7.9: (a) is the PL image of the QD solution with almost no particles visible under the microscope, except for very few clusters of QDs (cluster emits a very bright red due to the density of QDs), before the starting of the growth of wires inside the heater box. The QDs are only a few nm in size and hence provide a uniform red background, they are not resolvable under a microscope unless they form a cluster as can be seen from the image. Images (b) and (c) are the PL images of the same region focused on nanowire and QDs respectively. These wires are grown from the solution and stopped before all the QDs melt. This shows that there are clusters of photoactive QDs in the vicinity of the wires during the growth. Image (d) is the regular microscopic image of the liquid before the growth, focused at the edge of the substrate as no visible particles were present. Image (e) and (f) are images taken from the same region with an interval of 3 min during the growth. The scale bar in all the images from (a)-(f) are 50 µm. (g) Shows the optical microscopic image of the growth of nanowires at different stages at 200°C. The left corner shows the time at which the image is taken. Here we set the time of the first image to be taken as 0 s. As the reaction proceeds, we observe that a few clusters of particles are dissolving with the growth of the wire. The scale bar is 10 µm

### 7.4.4 The growth mechanism

Recently the change of chemical potential energy concerning the particle size of α, γ, and δ phases of the $CsPbI_3$ crystal structure has been computed using DFT.[12] The results of the paper showed that till 2.6 nm α phase has the least potential energy but above 5.6 nm δ phase is the most stable. Though in our system, the values might differ due to the interaction of surfactants, the general trend should be the same. The PL image of nanowires (Fig. 7.9 b and c) shows that there were still photoactive perovskite quantum dots present after the growth. This indicated that both α and δ phases of the $CsPbI_3$ crystal coexist at this point of growth. But as the reaction proceeds the cubic phase QDs disappear leaving behind the δ phases nanowires.

We tried to explain our observation by using size-dependent chemical potential and the general relation for crystal growth from a solution. The crystal will grow when the condition for super-saturation is met. The super-saturation is equal to the difference in the chemical potential of the formation of the crystal and its chemical potential in the dissolved state. In short, the difference in chemical potential is

$$\Delta\mu = kT \ln\left(\frac{C}{C_0}\right)$$

Here, $C$ is the real concentration and $C_0$ is the equilibrium concentration.

Initially, when we inject Cesium oleate, α-phase $CsPbI_3$ is formed as it has a much lower chemical potential. As the crystals continue to grow at the expense of smaller crystals some crystals might get converted to δ-phase. The exact mechanism as to why only a few crystals undergo the phase transition is not clear. It could be because of inset of some random defects in the crystal as it grows beyond a certain size. It is also possible that during initial nucleation few crystals were formed in the δ-phase due to the system being in a state of supersaturation sufficient for some crystals to nucleate in the δ-phase. We believe that the growth of the crystal happens in two stages. First, the initial difference in chemical potential of the two crystal types is large and thus it is easier for the cubic phase to form over δ-phase. Second, the chemical potential for the two crystal types reverses as the crystals grow and so does the stability.[12] After the reversal of chemical potential, the chemical potential is lower for δ-phase particles than α-phase particles. This causes the α-phase QDs to melt and nourish the growing nanowires.

Initially, the orthorhombic phase grows directionally with the help of surfactants like oleylamine

into wires and the α-phase grows uniformly till the concentration of the solute drops below a critical point. At this point the crystals are large enough for their chemical potential to be reversed, that is it is now easier to form δ-phase. Once the Concentration of the solute drops below the equilibrium concentration of α-phase $CsPbI_3$ the α-phase $CsPbI_3$ will melt, this will help keep the concentration above the equilibrium concentration of δ-$CsPbI_3$ and the nanowires keep growing at the expense of the α-phase $CsPbI_3$. A schematic of the growth mechanism is given in Fig 7.10.

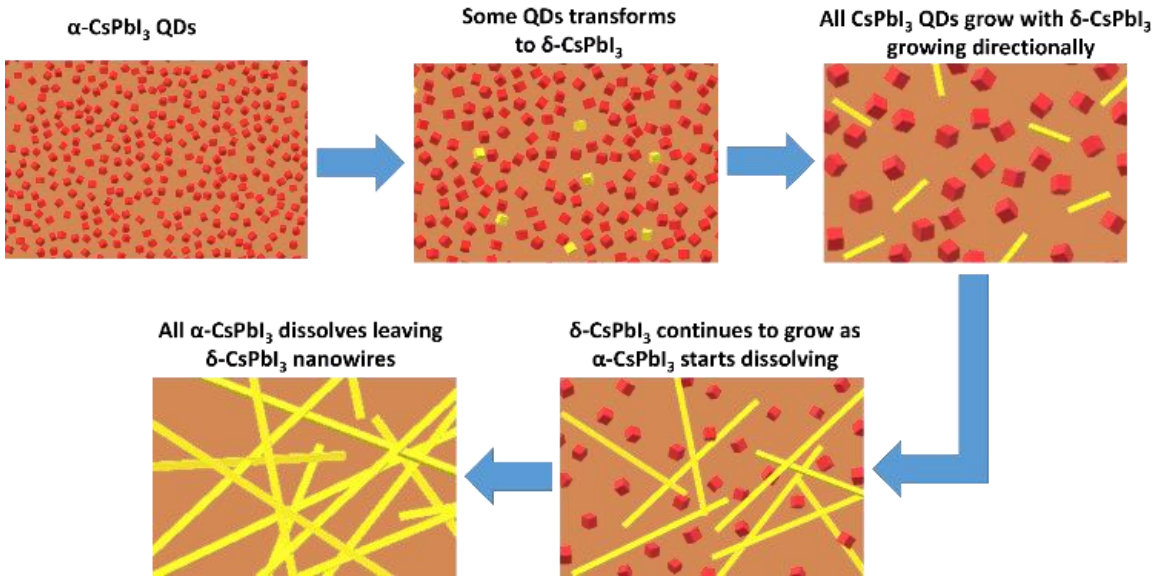


Figure 7.10: Fig. 8. Showing schematic of growth of δ-$CsPbI_3$ nanowires. At the time of hot injection, α-$CsPbI_3$ is formed, and as the reaction proceeds and the particles grow at the expense of smaller crystals some get converted to δ-$CsPbI_3$. Initially, all crystals grow in size with δ-$CsPbI_3$ growing directionally with the help of surfactants. As the reaction proceeds the concentration of solute in the solvent drops and α-$CsPbI_3$ start to dissolve maintaining the concentration needed for the growth of δ-$CsPbI_3$ which has a much lower chemical potential.

## 7.5 Summary

In this chapter, we successfully demonstrated that for an Oswald ripening mechanism of growth, it is possible to quench the reaction and resume it at a later time allowing us to check the growth under different temperatures efficiently. With this insight, we split the HI growth of $CsPbI_3$ and a series of thorough characterization and experiments came to the conclusion that the nanowires of $CsPbI_3$ inherently grow in the delta phase at the expense of cubic nanocrystals.

**Bibliography**

[1] Oksenberg E, Sanders E, Popovitz-Biro R, Houben L and Joselevich E 2018 Surface-Guided CsPbBr3 Perovskite Nanowires on Flat and Faceted Sapphire with Size-Dependent Photoluminescence and Fast Photoconductive Response *Nano Lett.* **18** 424–33

[2] Shoaib M, Wang X, Zhang X, Wang X, Zhou H, Xu T, Hu X, Liu H, Fan X, Zheng W, Yang T, Yang S, Zhang Q, Zhu X, Sun L and Pan A 2017 Directional Growth of Ultralong CsPbBr3 Perovskite Nanowires for High-Performance Photodetectors *J. Am. Chem. Soc.* **139** 15592–5

[3] Feng J, Yan X, Liu Y, Gao H, Wu Y, Su B and Jiang L 2017 Crystallographically Aligned Perovskite Structures for High-Performance Polarization-Sensitive Photodetectors *Adv. Mater.* **29** 1–8

[4] Eaton S W, Lai M, Gibson N A, Wong A B, Dou L, Ma J, Wang L W, Leone S R and Yang P 2016 Lasing in robust cesium lead halide perovskite nanowires *Proc. Natl. Acad. Sci. U. S. A.* **113** 1993–8

[5] Huang L, Gao Q, Sun L D, Dong H, Shi S, Cai T, Liao Q and Yan C H 2018 Composition-Graded Cesium Lead Halide Perovskite Nanowires with Tunable Dual-Color Lasing Performance *Adv. Mater.* **30** 1–6

[6] Zhou N, Bekenstein Y, Eisler C N, Zhang D, Schwartzberg A M, Yang P, Paul Alivisatos A and Lewis J A 2019 Perovskite nanowire–block copolymer composites with digitally programmable polarization anisotropy *Sci. Adv.* **5** 1–10

[7] Wang M, Tian W, Cao F, Wang M and Li L 2020 Flexible and Self-Powered Lateral Photodetector Based on Inorganic Perovskite CsPbI3–CsPbBr3 Heterojunction Nanowire Array *Adv. Funct. Mater.* **30** 1–7

[8] Bansode U, Rahman A and Ogale S 2019 Low-temperature processing of optimally polymer-wrapped α-CsPbI 3 for self-powered flexible photo-detector application *J. Mater. Chem. C* **7** 6986–96

[9] Wang C, Chesman A S R and Jasieniak J J 2017 Stabilizing the cubic perovskite phase of CsPbI3 nanocrystals by using an alkyl phosphinic acid *Chem. Commun.* **53** 232–5

[10] Stoumpos C C and Kanatzidis M G 2015 The Renaissance of Halide Perovskites and Their Evolution as Emerging Semiconductors *Acc. Chem. Res.* **48** 2791–802

[11] Eperon G E, Paternò G M, Sutton R J, Zampetti A, Haghighirad A A, Cacialli F and Snaith H J 2015 Inorganic caesium lead iodide perovskite solar cells *J. Mater. Chem. A* **3** 19688–95

[12] Yang R X and Tan L Z 2020 Understanding size dependence of phase stability and band gap in CsPbI3 perovskite nanocrystals *J. Chem. Phys.* **152**

[13] Liu L, Zhao R, Xiao C, Zhang F, Pevere F, Shi K, Huang H, Zhong H and Sychugov I 2019 Size-Dependent Phase Transition in Perovskite Nanocrystals *J. Phys. Chem. Lett.* **10** 5451–7

[14] Kirschner M S, Diroll B T, Guo P, Harvey S M, Helweh W, Flanders N C, Brumberg A, Watkins N E, Leonard A A, Evans A M, Wasielewski M R, Dichtel W R, Zhang X, Chen L X and Schaller R D 2019 Photoinduced, reversible phase transitions in all-inorganic perovskite nanocrystals *Nat. Commun.* **10** 504

[15] Ding H, Jiang H and Wang X 2020 How organic ligands affect the phase transition and fluorescent stability of perovskite nanocrystals *J. Mater. Chem. C* **8** 8999–9004

[16] Protesescu L, Yakunin S, Bodnarchuk M I, Krieg F, Caputo R, Hendon C H, Yang R X, Walsh A and Kovalenko M V 2015 Nanocrystals of Cesium Lead Halide Perovskites (CsPbX 3 , X = Cl, Br, and I): Novel Optoelectronic Materials Showing Bright Emission with Wide Color Gamut 1–5

[17] Hassan Y, Song Y, Pensack R D, Abdelrahman A I, Kobayashi Y, Winnik M A and Scholes G D 2016 Structure-Tuned Lead Halide Perovskite Nanocrystals *Adv. Mater.* **28** 566–73

[18] Bekenstein Y, Koscher B A, Eaton S W, Yang P and Alivisatos A P 2015 Highly Luminescent Colloidal Nanoplates of Perovskite Cesium Lead Halide and Their Oriented Assemblies *J. Am. Chem. Soc.* **137** 16008–11

[19] Shamsi J, Dang Z, Bianchini P, Canale C, Stasio F Di, Brescia R, Prato M and Manna L 2016 Colloidal Synthesis of Quantum Confined Single Crystal CsPbBr3 Nanosheets with Lateral Size Control up to the Micrometer Range *J. Am. Chem. Soc.* **138** 7240–3

[20] Zhang D, Yu Y, Bekenstein Y, Wong A B, Alivisatos A P and Yang P 2016 Ultrathin Colloidal Cesium Lead Halide Perovskite Nanowires *J. Am. Chem. Soc.* **138** 13155–8

[21] Tang X, Zu Z, Shao H, Hu W, Zhou M, Deng M, Chen W, Zang Z, Zhu T and Xue J 2016 All-inorganic perovskite CsPb(Br/I)3 nanorods for optoelectronic application *Nanoscale* **8** 15158–61

[22] Yang T, Zheng Y, Du Z, Liu W, Yang Z, Gao F, Wang L, Chou K C, Hou X and Yang W 2018 Superior Photodetectors Based on All-Inorganic Perovskite CsPbI3 Nanorods with Ultrafast Response and High Stability *ACS Nano* **12** 1611–7

[23] Koolyk M, Amgar D, Aharon S and Etgar L 2016 Kinetics of cesium lead halide perovskite nanoparticle growth; Focusing and de-focusing of size distribution *Nanoscale* **8** 6403–9

[24] Lignos I, Stavrakis S, Nedelcu G, Protesescu L, Demello A J and Kovalenko M V. 2016 Synthesis of Cesium Lead Halide Perovskite Nanocrystals in a Droplet-Based Microfluidic Platform: Fast Parametric Space Mapping *Nano Lett.* **16** 1869–77

[25] Zhao Q, Hazarika A, Schelhas L T, Liu J, Gaulding E A, Li G, Zhang M, Toney M F, Sercel P C and Luther J M 2020 (1) Zhao, Q.; Hazarika, A.; Schelhas, L. T.; Liu, J.; Gaulding, E. A.; Li, G.; Zhang, M.; Toney, M. F.; Sercel, P. C.; Luther, J. M. Size-Dependent Lattice Structure and Confinement Properties in CsPbI3 Perovskite Nanocrystals: Negative Surface Energy for *ACS Energy Lett.* **5** 238–47

[26] Imran M, Di Stasio F, Dang Z, Canale C, Khan A H, Shamsi J, Brescia R, Prato M and Manna L 2016 Colloidal Synthesis of Strongly Fluorescent CsPbBr 3 Nanowires with Width Tunable down to the Quantum Confinement Regime *Chem. Mater.* **28** 6450–4

[27] Liu F, Zhang Y, Ding C, Kobayashi S, Izuishi T, Nakazawa N, Toyoda T, Ohta T, Hayase S, Minemoto T, Yoshino K, Dai S and Shen Q 2017 Highly Luminescent Phase-Stable CsPbI3 Perovskite Quantum Dots Achieving Near 100% Absolute Photoluminescence Quantum Yield *ACS Nano* **11** 10373–83

[28] Zhang D, Eaton S W, Yu Y, Dou L and Yang P 2015 Solution-Phase Synthesis of Cesium Lead Halide Perovskite Nanowires *J. Am. Chem. Soc.* **137** 9230–3

[29] Zhao B, Jin S F, Huang S, Liu N, Ma J Y, Xue D J, Han Q, Ding J, Ge Q Q, Feng Y and Hu J S 2018 Thermodynamically Stable Orthorhombic γ-CsPbI3 Thin Films for High-Performance Photovoltaics *J. Am. Chem. Soc.* **140** 11716–25

[30] Steele J A, Jin H, Dovgaliuk I, Berger R F, Braeckevelt T, Yuan H, Martin C, Solano E, Lejaeghere K, Rogge S M J, Notebaert C, Vandezande W, Janssen K P F, Goderis B, Debroye E, Wang Y K, Dong Y, Ma D, Saidaminov M, Tan H, Lu Z, Dyadkin V, Chernyshov D, Van Speybroeck V, Sargent E H, Hofkens J and Roeffaers M B J 2019 Thermal unequilibrium of strained black CsPbI3 thin films *Science (80-. ).* **365** 679–84

[31] Swarnkar A, Marshall A R, Sanehira E M, Chernomordik B D, Moore D T, Christians J A, Chakrabarti T and Luther J M 2016 Quantum dot-induced phase stabilization of -CsPbI3 perovskite for high-efficiency photovoltaics *Science (80-. ).* **354** 92–5

[32] Wang X, Shoaib M, Wang X, Zhang X, He M, Luo Z, Zheng W, Li H, Yang T, Zhu X, Ma L and Pan A 2018 High-Quality In-Plane Aligned CsPbX3 Perovskite Nanowire Lasers with Composition-Dependent Strong Exciton-Photon Coupling *ACS Nano* **12** 6170–8

[33] Waleed A, Tavakoli M M, Gu L, Hussain S, Zhang D, Poddar S, Wang Z, Zhang R and Fan Z 2017 All inorganic cesium lead iodide perovskite nanowires with stabilized cubic phase at room temperature and nanowire array-based photodetectors *Nano Lett.* **17** 4951–7

[34] Meng Y, Lan C, Li F, Yip S, Wei R, Kang X, Bu X, Dong R, Zhang H and Ho J C 2019 Direct Vapor-Liquid-Solid Synthesis of All-Inorganic Perovskite Nanowires for High-Performance Electronics and Optoelectronics *ACS Nano* **13** 6060–70

[35] Chen G, Feng J, Gao H, Zhao Y, Pi Y, Jiang X, Wu Y and Jiang L 2019 Stable α-CsPbI 3 Perovskite Nanowire Arrays with Preferential Crystallographic Orientation for Highly Sensitive Photodetectors *Adv. Funct. Mater.* **29** 1–7

[36] De Roo J, Ibáñez M, Geiregat P, Nedelcu G, Walravens W, Maes J, Martins J C, Van Driessche I, Kovalenko M V. and Hens Z 2016 Highly Dynamic Ligand Binding and Light Absorption Coefficient of Cesium Lead Bromide Perovskite Nanocrystals *ACS Nano* **10** 2071–81

[37] Liu J, Song K, Shin Y, Liu X, Chen J, Yao K X, Pan J, Yang C, Yin J, Xu L, Yang H, El-Zohry

A M, Xin B, Mitra S, Hedhili M N, Roqan I S, Mohammed O F, Han Y and Bakr O M 2019 Light-Induced Self-Assembly of Cubic CsPbBr 3 Perovskite Nanocrystals into Nanowires *Chem. Mater.* **31** 6642–9

[38] Lee I and Zaera F 2010 Catalytic conversion of olefins on supported cubic platinum nanoparticles: Selectivity of (100) versus (111) surfaces *J. Catal.* **269** 359–66

[39] Bakshi M S 2016 How Surfactants Control Crystal Growth of Nanomaterials *Cryst. Growth Des.* **16** 1104–33

[40] Wen Z, Zhai W, Liu C, Lin J, Yu C, Huang Y, Zhang J and Tang C 2019 Controllable synthesis of CsPbI3 nanorods with tunable photoluminescence emission *RSC Adv.* **9** 24928–34

[41] Fanizza E, Cascella F, Altamura D, Giannini C, Panniello A, Triggiani L, Panzarea F, Depalo N, Grisorio R, Suranna G P, Agostiano A, Curri M L and Striccoli M 2019 Post-synthesis phase and shape evolution of CsPbBr 3 colloidal nanocrystals: The role of ligands *Nano Res.* **12** 1155–66

# Chapter 8

# Water-based Photolithography on water-soluble $CsPbBr_3$

This chapter is an adaptation of the research article published in "" *Adv. Mater. Interfaces* **10** 2201749, 2023"

## 8.1 Introduction

The semiconductor chip manufacturing industry heavily relies on photolithography, a versatile technique used for processes such as etching, doping, and material deposition. However, the extensive use of water in photolithography poses challenges when working with water-soluble materials. Finding a suitable substitute for water in photolithography is a monumental challenge due to the significant water consumption in the fabrication of devices.[1,2] However novel emerging materials like perovskite have way too much potential in optoelectronic applications, including ease of synthesis, low trap state density, high optical absorption coefficient, low exciton binding energies, narrow emission peaks, tunable bandgap, high charge carrier diffusion lengths, and long charge carrier lifetimes.[3–8] These properties of lead halide perovskites have made it possible to achieve high performance in photovoltaics, LEDs, and radiation detection.[9–12] The integration of MHPs into existing technology is hindered by the inability to fabricate high-performance devices using traditional water-dependent lithographic processes. While bulk perovskite single crystals are suitable for large-area devices, their performance in optoelectronic applications lags behind their polycrystalline thin-film counterparts.[13] Fabricating devices on perovskite thin films is relatively straightforward, as it allows for the deposition of large electrodes without complex lithography processes.

However, these films are often polycrystalline or composed of thin films of quantum dots with grain boundaries and defects that can affect their intrinsic properties and overall device performance compared to single-crystal films.[14,15]. Perovskite nanocrystals, with their direct bandgap, efficient light absorption, high defect tolerance, and high quantum efficiency, hold promise for nano/micro-device applications. Fabricating devices using single micro/nanocrystals is crucial for understanding their intrinsic charge transport properties at the nanoscale and achieving high-performance optoelectronic nanodevices. Traditional photolithography techniques dissolve perovskite materials due to their high solubility in water, leading researchers to explore alternative methods such as growth, spin coating, dry transferring, or drop-casting onto pre-patterned electrodes. [16–20] Depositing contacts onto the crystals using shadow masking or patterning using e-beam lithography. However, shadow masking faces challenges in precisely placing leads on a single micro/nanocrystal and lacks the flexibility of the photolithographic process. E-beam lithography has low throughput, is not cost-effective, and can damage hybrid perovskite materials.[21] Other approaches have used sacrificial layers etched by $O_2$ plasma to deposit contacts, but plasma power can significantly damage the perovskite surface.[22–24] As 2D perovskites are gaining traction a non-invasive method to make devices on them could make a great difference.[25] So a method that could enable photolithography without damaging the crystal, will be a big step toward studying exotic properties of perovskite crystals like ferroelectricity, spin-orbit interaction, and their potential application in detectors, FETs, LEDs memory devices, and spintronics.[26–30]

In this chapter, a technique that employed a sacrificial layer of polystyrene with suitable molecular weight to protect perovskite micro/nanocrystals is discussed. The hydrophobic nature of polystyrene effectively shields the samples from water. Additionally, it is easy to coat a thin layer onto the substrate and is readily soluble in organic solvents like toluene. This allows for the efficient removal of polystyrene while preserving the photolithography pattern. Leveraging these properties, we successfully fabricated high-performance devices using conventional photolithography techniques.

## 8.2 Drop casting vs deposition for device fabrication.

Device fabrication plays a crucial role in the development of various electronic and optoelectronic technologies. One important aspect of device fabrication involves the use of metal contact to make connections with the semiconductor material, which serve as essential components for interconnection that allows us to test, understand, and finally use the materials for device applications. In this section, we compare drop casting of semiconductors onto pre-existing metal pads and the deposition of metal pads directly onto the semiconductor substrate. We believe that the latter forms better contact as the deposition causes the metal to land on the entire surface as compared to drop casting, where a lot of things can hinder the semiconducting material from making good contact with the metal pads. Fig. 8.1a illustrates the reasons why drop casting is not a preferred method for making. The reasons are as follows: Firstly, there is no control over the crystal orientation, secondly as the solution dries it is more likely to leave behind some residue between the material and the pad. Lastly a good contact is only possible if both the surfaces are atomically flat. Deposition techniques overcome these limitation as we can control the orientation of pattern and as the deposition covers the entire material atom by atom it can overlook any debris or unevenness of the substrate as depicted in Fig. 8.1b.

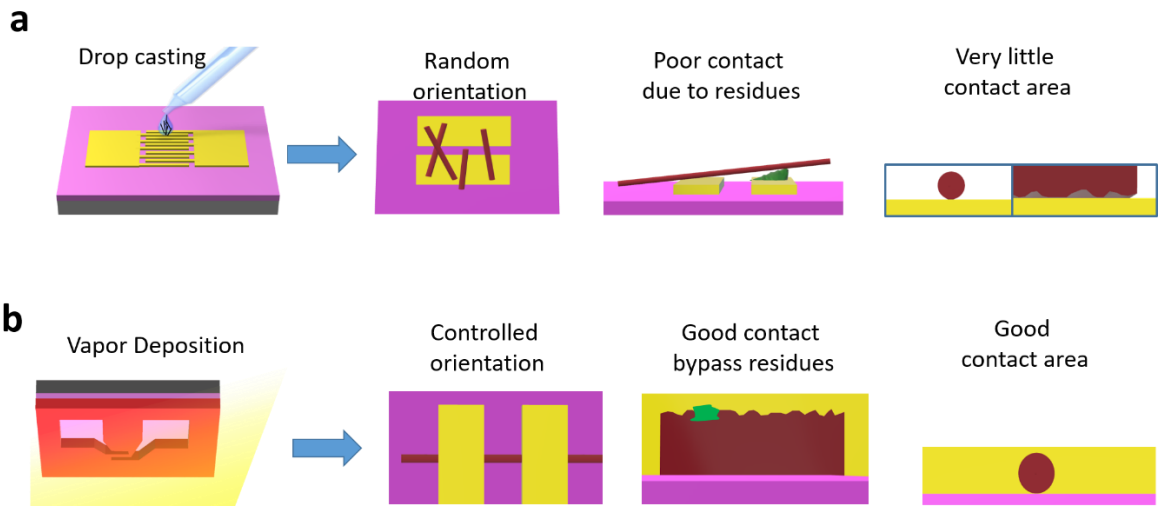


Figure 8.1: (a) schematic illustrating the limitations of drop casting for device fabrication. (b) schematic demonstrating how vapor deposition can overcome the challenges associated with drop casting.

## 8.3 Synthesis and characterization of $CsPbBr_3$

The $CsPbBr_3$ crystals were synthesized using a simple solution growth method. We use, 460 mg $PbI_2$ was dissolved in 1 mL anhydrous dimethylformamide and stirred at 70 °C overnight. The $PbI_2$ solution was spun onto a cleaned glass/Silicon substrate at 1,000 rpm for 120 s, then annealed at 100 °C for 15 min. The $PbI_2$ film was carefully submerged into a glass vial with 8 mg/mL CsBr (99.999%) solution in methanol (anhydrous, 99.8%), with the $PbI_2$ side facing up. The capped reaction vial was heated at 50 °C for 12 h, and the substrate was removed and washed in anhydrous isopropanol for 30 s followed by annealing at 50 °C as per the previous reports.[31] The supplementary figure, Fig. 8.2a, shows a FESEM image of the as-grown CsPbBr3 crystals. A variety of microcrystals of various morphologies, ranging from nanowires of various diameters and microcrystals of various dimensions, are formed. The XRD pattern of these crystals, (Fig. 8.2b), shows two peaks near 150 and 300 which shows the splitting of (020)/(101) and (040)/(202) peaks respectively in the spectrum which are characteristic of orthorhombic CsPbBr3 crystals.[32] To study the properties of a single crystal we scraped the crystals into toluene and this solution was drop cast onto a 300 nm $SiO_2$ coated on a degenerately doped p-type Si substrate. The solution can be diluted to get isolated crystals of CsPbBr3 as shown in Fig. 8.2c or can be concentrated to get denser coverage. Fig. 8.2d shows the PL spectra of the crystal, which is around 540 nm with an FWHM of ~92 meV. The inset shows a PL image of the microcrystal shown in Fig. 8.2c. The XRD and the large PL emission with a narrow FWHM indicate high-quality crystal formation. The FESEM images also show crystals of very smooth surfaces.

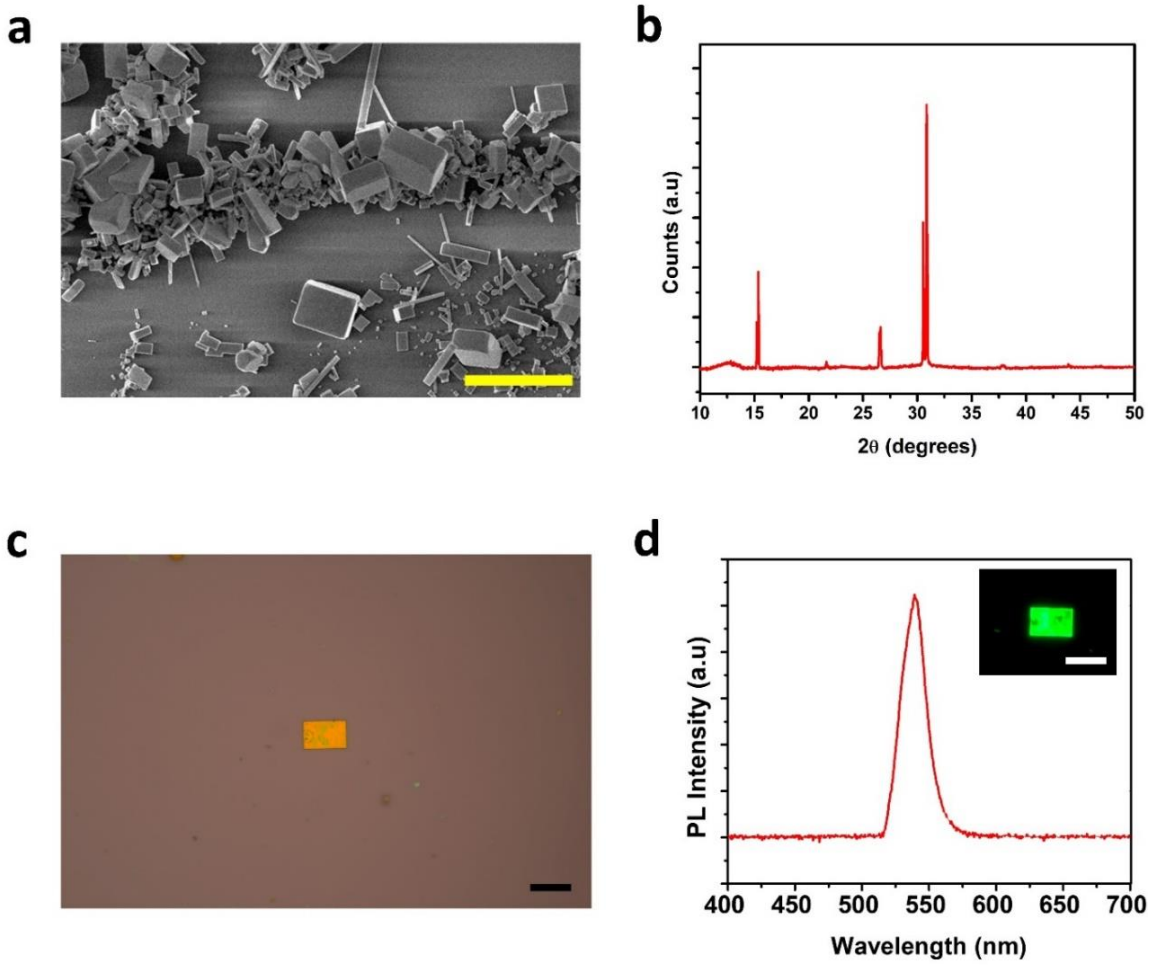


Figure 8.2: (a) Shows the FESEM images of the $CsPbBr_3$ crystals synthesized. The scale bar is 5 µm. (b), is the XRD pattern of the crystals. (c), is an optical microscopic image of a $CsPbBr_3$ after drop-casting it into a 300 nm $SiO_2$ on Si substrate. (d), is the PL spectra of the crystal and the inset image shows the PL image of the crystal in c. The scale bars in c and d are 20 µm.

## 8.4 Solubility of $CsPbBr_3$ and its effect on photolithography

Perovskites like $CsPbBr_3$ are extremely soluble in water, which makes it extremely hard to do photolithography on them. In Fig. 8.3a, conventional photolithography was performed using positive photoresists (see methods for details) on a drop-casted substrate with dense coverage of $CsPbBr_3$. We developed the sample for the minimum recommended time of 40 sec and immediately blow-dried the sample without washing it with water. This ensured that the crystals come in contact with the developer/water for the least possible time. Even then the crystals in

the exposed part get etched off completely, whereas the ones under the unexposed parts survived as they were protected by the photoresist. To demonstrate how fast the water could dissolve the perovskite crystals, we kept a microscope coverslip on top of the sample and put a 200 µl drop of water on one end. As the water seeped in, we observed the etching in real-time as shown in the optical and PL images in Fig. 8.3b.

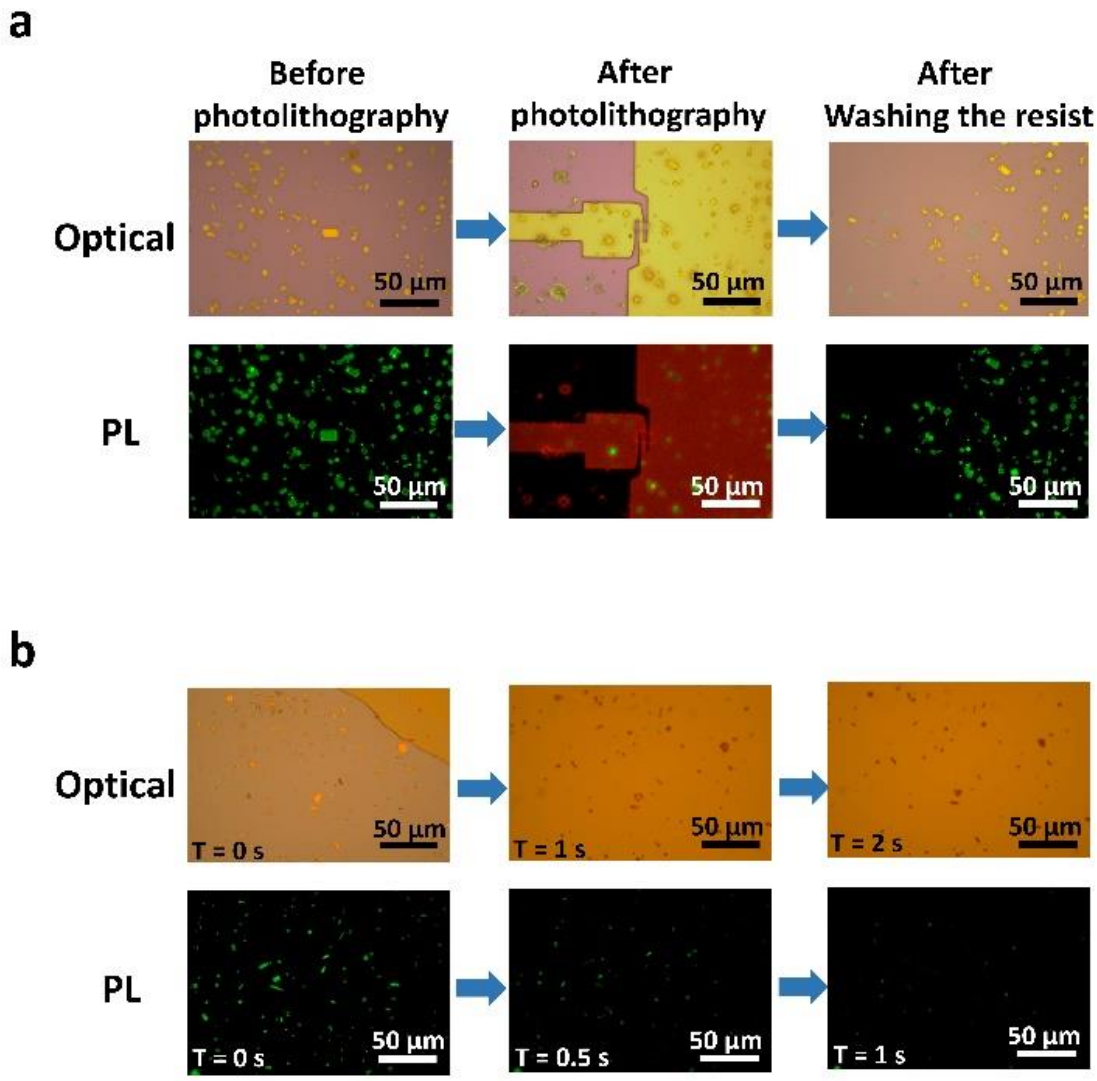


Figure 8.3: (a) Optical and PL images of the $CsPbBr_3$ crystals before and after conventional photolithography. The scale bar is 50 µm. (b) shows the optical and PL images of $CsPbBr_3$ crystals at various times as they come into contact with a very small amount of water.

An important factor is that the etching rate would depend on the concentration of $CsPbBr_3$ (solute) in the water (solvent). As the entire substrate contained $CsPbBr_3$ and a very little amount of water surged into the gap between the coverslip and substrate, the concentration of the dissolved ions would be higher as the water reaches the crystals. This could slow down the etching a bit and different trials could give slightly different results. Nonetheless, the etching was so fast that the crystals dissolved within 1 -3 sec every time. This indicates that the etching rate when we dip the sample in the developer would be much higher as the developer contains a huge amount of water with no dissolved perovskite in them. As most of the developers used in photolithography are water-based, all water-soluble thin films will get destroyed during the developing stage. This makes it nearly impossible to do conventional photolithography in these samples.

## 8.5 Sacrificial layer-assisted photolithography

To tackle this problem, we coated the substrate containing nano/microcrystals with polystyrene as a sacrificial layer before coating the photoresist. The layer of polystyrene will protect the perovskite crystals during photolithography and can later be washed off in toluene leaving the photoresist pattern intact. The advantage of polystyrene is that it is highly hydrophobic and can be removed with ease using toluene without leaving any significant residues behind, which made it an excellent choice for transferring 2D materials.[33] The device fabrication on perovskite crystals, which failed the conventional photolithographic process, succeeded when our approach was used. A schematic of the steps involved in the process is shown in Fig. 8.4a. Fig. 8.4b shows the optical and PL images of the $CsPbBr_3$ crystal of interest at various stages of lithography. The images of the intact crystal and the high PL from the crystal prove that the lithographic process did not do any damage to the crystal.

The thickness of the polystyrene film and its molecular weight along with the spin coating of the photoresist are crucial for the successful fabrication of the devices. The polystyrene is slightly soluble in the photoresist solution and can create pinholes if not done properly (Fig. 8.5a), which could adversely affect the lithographic process.

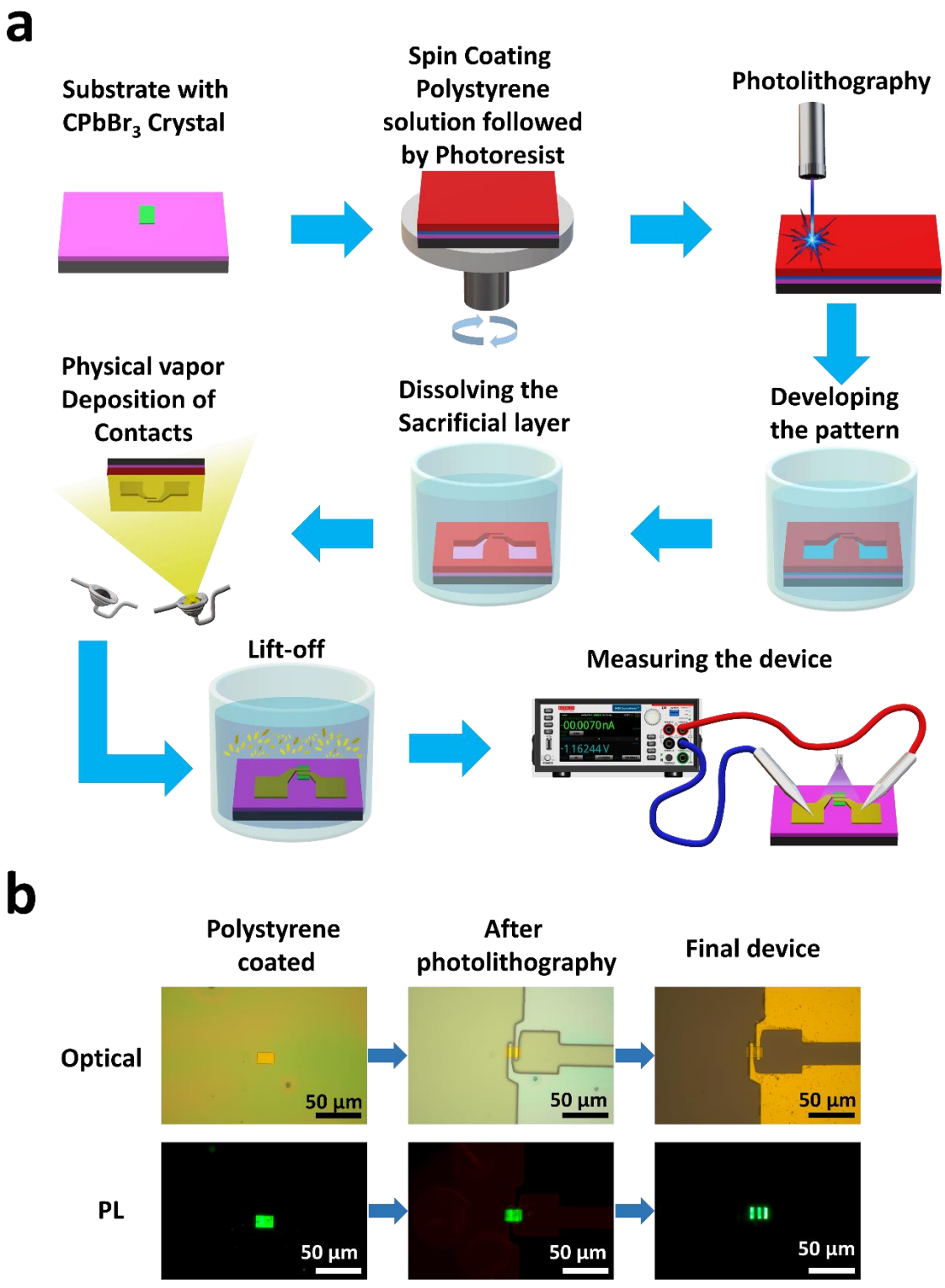


Figure 8.4: (a) shows a schematic of all the steps involved in our photolithography process. (b) is the optical and PL images of $CsPbBr_3$ crystals at various stages of device fabrication. The PL and optical images clearly show that the device fabrication was successful and did not damage the crystal.

Lower molecular weight polystyrene would inevitably cause pinholes to form in the protective coating while a higher molecular weight one will be harder to remove. The thickness of the film also determines its survivability during photoresist coating. A thicker film is more resistant to pinhole formation during lithography, whereas a thinner film is easy to remove in toluene after the lithography. We found out that for crystals with thickness less than 1 micrometer 2-4 % polystyrene in toluene by weight is sufficient to protect the crystal and thus used a 4% 35 K molecular weight polystyrene (4% is more reproducible) in the toluene solution for protecting the crystals. The solution was spin-coated at a rate of 3500 r.p.m and annealed for 5 min at 120 °C before the dynamic coating of the photoresist.

After the coating of polystyrene, the sample is ready for undergoing conventional photolithography. The coating we use is apt to protect crystals up to a few hundred-nanometer thicknesses, however, to protect thicker crystals of a few micrometers in thickness it is important to optimize the coating thickness of the polystyrene film. Dipping the substrate in water after coating a suitable thickness polystyrene layer will eliminate all the thicker crystals and it can be used as an easy and highly efficient method to select thin crystals from a collection of crystals of various thicknesses (in our case we are left with crystals less than a micrometer in thickness). The coating of the photoresist should be done fast or dynamically as pinholes can emerge in the polystyrene film if the exposure time to the photoresist solution is prolonged.

After the coating, we exposed the photoresist film and developed it. After developing the sacrificial layer of polystyrene is washed off in toluene by dipping the substrate in toluene for 30 sec and is blow-dried. We discovered that for a coating using 4% solution, 25 seconds is sufficient to remove the polystyrene layer. However, the precise duration varies slightly, and by extending the period to 30 seconds, we improved the repeatability of the procedure. The polystyrene film gets etched in the regions where it is not protected by the photoresist. The washing of polystyrene for a longer duration can cause significant under-etching which could lead to crack formation, due to stress while blow-drying (Fig. 8.5). We then deposited 5 nm chromium followed by 75 nm gold contacts by thermal vapor deposition. The lift-off was done by dipping the substrate in acetone for 20 sec to etch most of the photoresist and then we soak it in toluene for an hour followed by sonicating it gently. We then dip it in acetone for 5 sec followed by washing it in IPA. Acetone can etch the crystals and thus is used only to wash

toluene off before dipping in IPA.

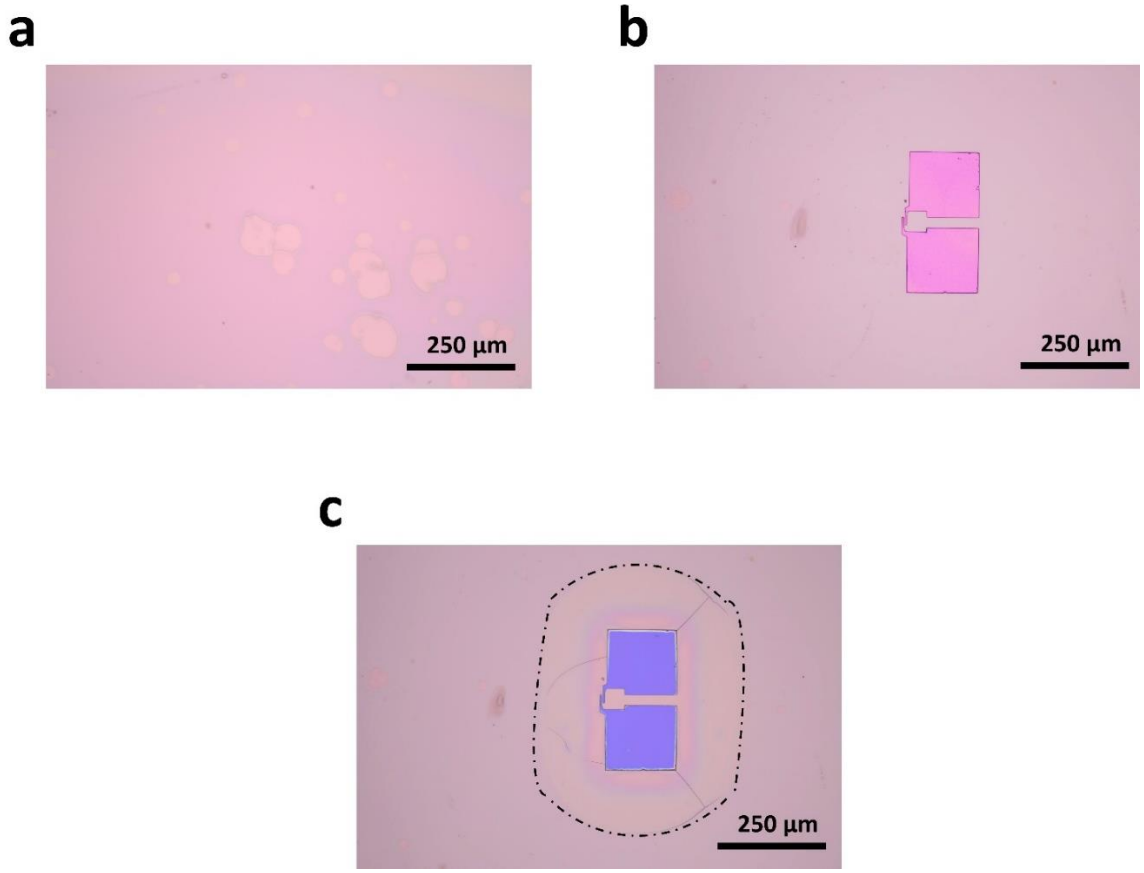


Figure 8.5: (a) is the optical microscopic image of 2% polystyrene coated substrate after photoresist coating. A few large pinholes can be seen in the film. (b), is the optical microscopic image of a 4% polystyrene-coated substrate after photoresist coating exposure and development. The film is intact with little to no pinholes. (c), is the optical microscopic image of the substrate shown in (b)**,** after polystyrene is washed off. Under etching can be seen by contrast and the under-etched part is marked by dotted lines. A few cracks also appeared on the film while blow drying as the supporting polystyrene layer was missing and gas pressure was a bit high.

## 8.6 Devices of $CsPbBr_3$ crystals

To explore the quality of the as-fabricated device we measured their electrical response without any further processing (such as rapid thermal annealing or vacuum annealing). As can be seen in Fig. 8.6a, the dark current was very low and is limited by the lower limit of the current-voltage (*I-V*) measurement instrument (Keithley 2450 SMU). When the device was illuminated with a 405 nm LED of 12 $mW/cm^2$ power we observed 3 orders of magnitude enhancement in the current. The on-off current ratio ($I_{on}/I_{off}$) and the responsivity (R) of the device can be found by the relations,

$$I_{on}/I_{off} = I_{light}/I_{dark}$$

and

$$R = (I_{light}-I_{dark})/(P \times A)$$

Respectively,[34] where, $I_{light}$ is the current under illumination and $I_{dark}$ is the dark current, P is the incident power intensity, and A the area of the device. This gives a current on/off ratio of 366.4, and a responsivity above 3 A/W at 0.5 V bias was obtained in the wavelength range between 400 nm – 480 nm. This value of responsivity is high for an applied voltage of 0.5 V and is comparable to that of thicker orthorhombic crystal-synthesized in other works[32,35] and is better than multigrain detectors of $CsPbBr_3$.[36] The non-Ohmic behavior of the device can be attributed to the Schottky barrier at the interface of Au and $CsPbBr_3$.

We can make devices on any substrate as demonstrated by fabricating one in a flexible polystyrene sheet. The metal deposition via photolithography will ensure good physical contact between the electrode and the crystal ensuring good device performance along with great control over the device geometry. Techniques like drop-casting, unfortunately, are a bit random and do not ensure great contact as debris or roughness of the surfaces could in turn affect the quality of the contact and hence the device performance. The excellent device performance indicates that our method of lithography on perovskite crystals or any other water-soluble microcrystals offers a reliable way of making high-quality nano/microdevices.

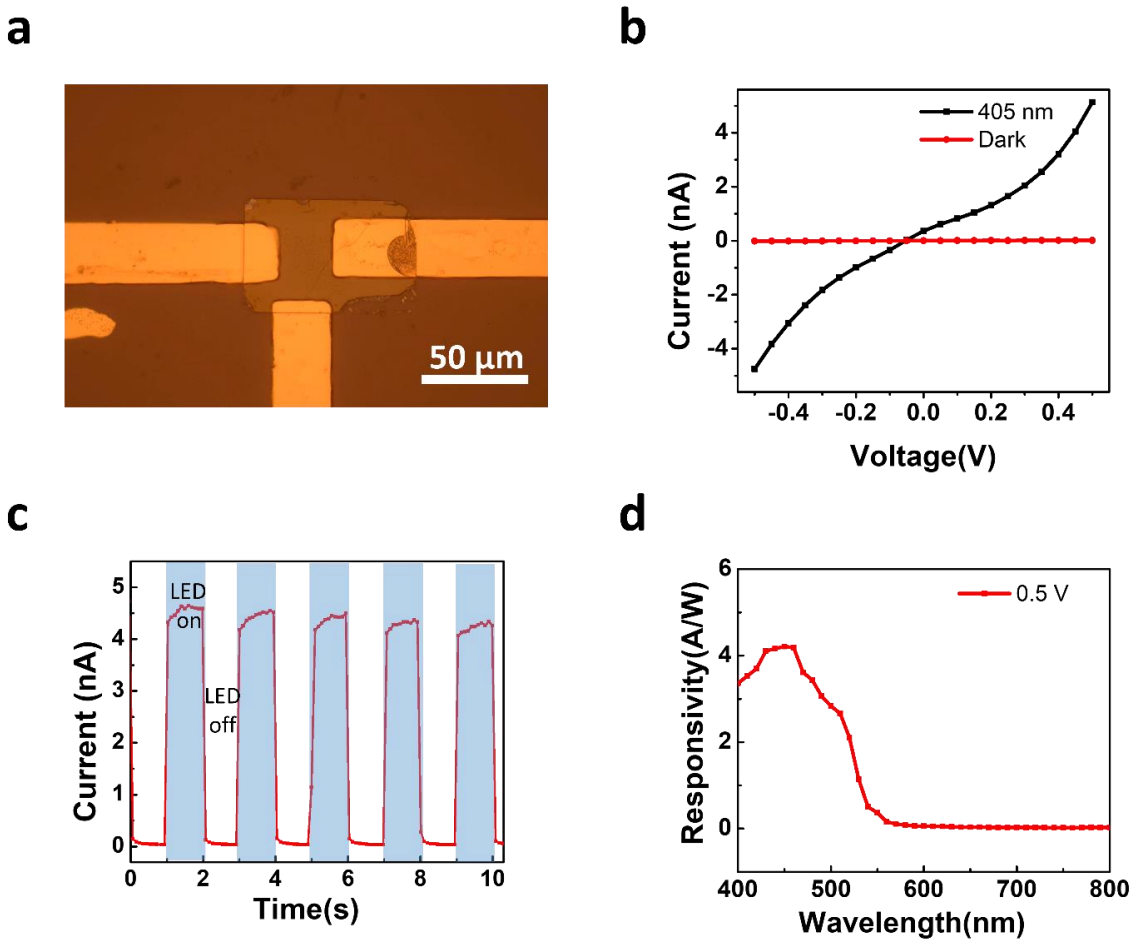


Figure 8.6: (a) is the optical microscope image of a device made on a flexible substrate. (b) is the I-V response of the device under dark conditions and illumination from a 405 nm LED of 12 mW/cm$^2$ output power. (c) is the time-resolved photoresponse of the device at 0.5 V bias. (d) is the Responsivity as a function of wavelength showing good photo-response for a wide range of wavelength.

### 8.6.1 Contact material

To explore the versatility of our technique for making other device architectures, we deposited asymmetric contact electrodes. Several applications required asymmetric contacts and it enhances the device performance.[37,38] Fabrication of asymmetric contacts generally requires two steps of photolithography and metal deposition. Though one can always place a crystal on top of prefabricated asymmetric leads, it is often difficult to transfer such crystals precisely, and until or unless both surfaces of the crystal and the contacts are atomically flat and are at the same level, it would be difficult to get good contacts by simply placing the crystal on top of

electrodes or vice-versa. Drop casting the samples are even worse as it is random and can also leave debris. The contact will be great only if the contact material is a 2D material or is done by any vacuum deposition which would ensure maximum contact area without leaving any gaps between the contact material and the crystal. Thus, to achieve a good asymmetric contact configuration on micro/nanocrystals it is imperative to use the lithographic technique. Thus we repeated our sacrificial layer-based photolithography technique and deposited gold and aluminum contact onto the crystal as shown in Fig. 8.7a.

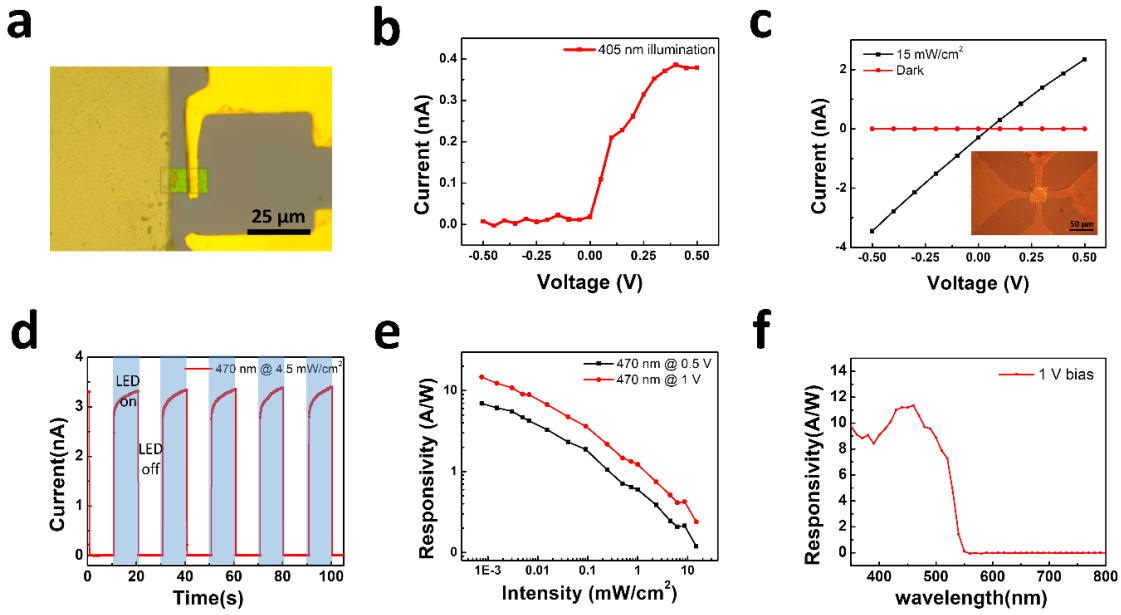


Figure 8.7: (a) is the optical microscope image of a device after two steps of lithography to deposit Gold and Aluminum contacts on it. (b) is the I-V response of the device under the illumination of a 405 nm LED light of 12 mW/cm$^2$ intensity. The device now shows strong diodic behavior. (c) is the dark and photocurrent (illuminated with 470 nm LED at 15 mW/cm$^2$ intensity) of the device made with ITO contact. The inset shows the optical image of the device. (d) shows the time-resolved photoresponse of the ITO device at 1 V bias and 4.5 mW/cm$^2$ intensity of 470 nm LED. (e) shows the responsivity of the ITO device as a function of intensity. (f) is the responsivity vs wavelength graph of the ITO device.

The asymmetric device had a very strong diodic behavior in the presence of light. The results clearly show that the method of photolithography can pave the way for contact engineering on perovskite and other water-soluble crystals. We also measured the electrical properties of the ITO fabricated device and found it was more or less ohmic and had excellent photoresponse and responsivity. The responsivity of the device was higher (14.7 A/W) at low intensity (0.75

$\mu W/cm^2$). The measured responsivity was found to be better with ITO contact than with gold and the contacts were Ohmic, suggesting ITO might be a better contact material for making high-efficiency perovskite optoelectronic devices.

## 8.7 Damage to the crystal

As the $CsPbBr_3$ crystals have great thermodynamic stability the as fabricated device should be stable.[39] We verified it by studying 2 devices that were prepared two-month prior for a longer time. The device area was smaller as the crystals were smaller but their performance were more or less stable for over 1000 seconds. The minor decline in one crystal's performance and a slight increase in the other crystal's response could be attributed to the quality of the crystal (Fig.8.8). The crystals mainly come in contact with toluene and IPA both of which will not damage the crystal, thus retaining its properties such as PL. We observed no observable change in PL of the crystal after our lithographic process which is in line with this argument. Some reports suggested that conventional vacuum-deposited metal contacts could seriously damage the underlying perovskite crystal and could affect the PL of the crystal.[40]

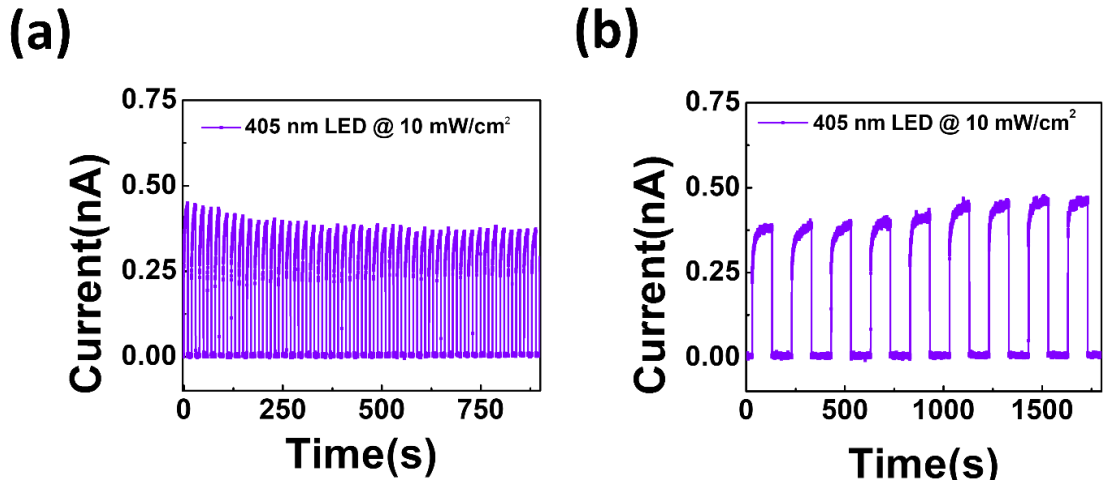


Figure 8.8: (a) and (b) Shows the photo-response of two similar devices with Au-Au contact measured after 4 months of fabrication. The nature of the devices varies slightly as we can see that the photocurrent in a slightly reduces with time whereas the photocurrent in (b) slightly increase with time, this shows that this nature of slight increment or decrement of photocurrent is sample dependent and is not due to the contacts.

To see if our approach had damaged the crystal, we sonicated the devices in IPA to peel the contact materials from the crystal. Fig. 8.9a, shows the image of a crystal on which first a gold

contact pad was deposited covering part of the crystal then it was removed by sonication. The process did lightly quench the PL of the crystal, but the change was not significant and might have happened during sonication rather than during the deposition of metal contacts. To confirm this, we repeated the process on another device (having narrow contact pads and thus requiring less sonication time/power to remove it) and this time it showed no change in PL (Fig. 8.9d). We also performed AFM to check the change in surface roughness after the process and found no considerable change. The line scan across both regions showed no significant difference in roughness.

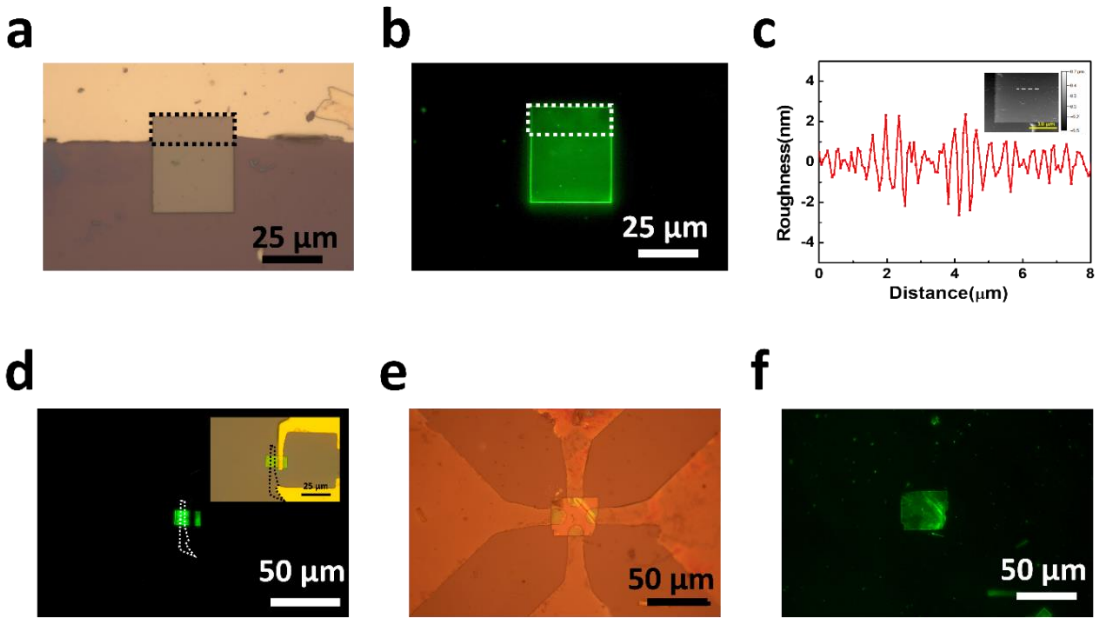


Figure 8.9: (a) is an optical microscopic image of a relatively large flake on which a large pattern was deposited and removed by sonication. b is the PL image of the crystal in a, there is a slight change in PL intensity in the region where the metal was deposited. c is the AFM line scan along the marked region, free of debris, which shows a relatively smooth surface on both the deposited region, after removal of lead, and the undeposited region. The inset in c is the AFM image of the sample. d, is the PL image of the device of another device, after removing one of the leads by sonicating it in IPA. The inset is the optical microscope image of the device. The PL from the region where the lead has been removed shows no change which suggests that the crystal sustained no damage during the lithographic process. e and f are the optical and PL images of a $CsPbBr_3$ device with transparent electrodes(ITO) deposited by sputtering. The PL image shows no change in intensity suggesting that sputter deposition also does not damage the crystal.

To examine if the sputter deposition of contact materials can cause damage to the crystals, we made transparent flexible devices by depositing ITO on CsPbBr3 nanocrystals placed on a

polystyrene substrate (Fig. 8.9e). The PL image of the device (Fig. 8.9f) exhibited no observable quenching of PL in the area covered by ITO contacts indicating little or no damage to the crystals[40]. These results showed that thermal deposition, sputtering or our device fabrication technique cause no damage to the crystals.

We also demonstrated the effectiveness of our method for fabricating active devices on nanowires by fabricating devices on $CsPbI_3$ nanowires. The nanowires of $CsPbI_3$ were synthesized using the route we reported earlier[41]. But as the wires were in the delta phase one or two were not enough to generate signals in the detectable range of Keithley 2450. But the wires that were soluble in water, just like $CsPbBr_3$, survived the lithography and thus demonstrates that our technique can also be used to make devices out of water-soluble nanowires. The FESEM images of the devices of $CsPbI_3$ are given in supplementary materials Fig. 8.10.

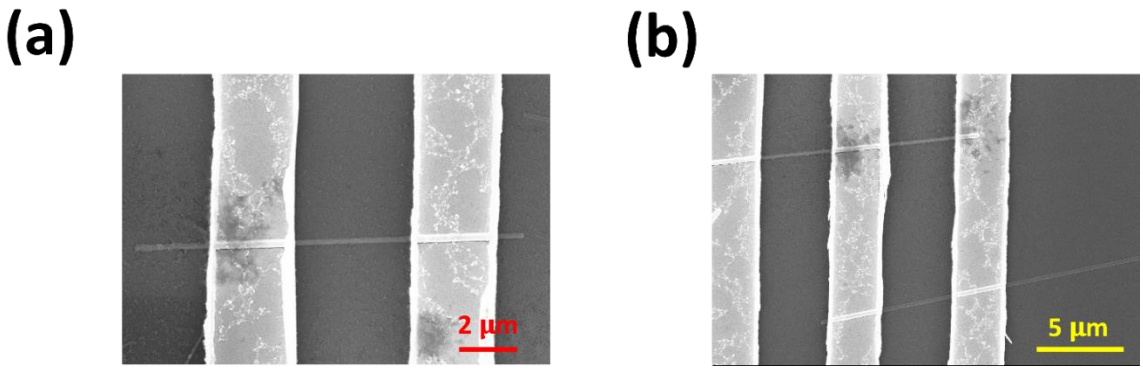


Figure 8.10: (a) and (b) are the FESEM images of devices made from CsPbI3 nanowires. This shows that the technique is applicable to nanowires too.

## 8.8 Summary

In this chapter, we have successfully developed a novel method for performing photolithography on water-soluble crystals, and we have applied this technique to fabricate electronic devices on $CsPbBr_3$ crystals. Overcoming the challenges associated with photolithography on perovskite crystals represents a significant milestone in device fabrication, enabling the exploration of their unique properties and their potential applications in various fields, including detectors, FETs, LEDs, memory devices, and spintronics. Moreover, our

method facilitates the fabrication of asymmetric contacts on these crystals, providing additional flexibility in device design. As research in 2D perovskites gains momentum, our technique holds great promise for device fabrication and the study of fundamental properties, while also enabling the integration of these crystals into existing semiconductor chip manufacturing processes for novel hybrid devices. Furthermore, by employing a suitable sacrificial layer, this method can be extended to other water-soluble crystals and polymers, offering a versatile approach for fabricating high-efficiency micro/nanodevices using such materials.

## Bibliography

[1] Frost K and Hua I 2019 "Quantifying spatiotemporal impacts of the interaction of water scarcity and water use by the global semiconductor manufacturing industry" *Water Resour. Ind.* **22** 100115

[2] Frost K and Hua I 2017 A spatially explicit assessment of water use by the global semiconductor industry *2017 IEEE Conference on Technologies for Sustainability (SusTech)* vol 2018-Janua (IEEE) pp 1–5

[3] Stranks S D, Eperon G E, Grancini G, Menelaou C, Alcocer M J P P, Leijtens T, Herz L M, Petrozza A and Snaith H J 2013 Electron-hole diffusion lengths exceeding 1 micrometer in an organometal trihalide perovskite absorber *Science (80-. ).* **342** 341–4

[4] Shi D, Adinolfi V, Comin R, Yuan M, Alarousu E, Buin A, Chen Y, Hoogland S, Rothenberger A, Katsiev K, Losovyj Y, Zhang X, Dowben P A, Mohammed O F, Sargent E H and Bakr O M 2015 3、SCIENCE sciencemag.org **347** 6221

[5] Liu D and Kelly T L 2014 Perovskite solar cells with a planar heterojunction structure prepared using room-temperature solution processing techniques *Nat. Photonics* **8** 133–8

[6] Protesescu L, Yakunin S, Bodnarchuk M I, Krieg F, Caputo R, Hendon C H, Yang R X, Walsh A and Kovalenko M V 2015 Nanocrystals of Cesium Lead Halide Perovskites (CsPbX 3 , X = Cl, Br, and I): Novel Optoelectronic Materials Showing Bright Emission with Wide Color Gamut 1–5

[7] Weidman M C, Seitz M, Stranks S D and Tisdale W A 2016 Highly Tunable Colloidal Perovskite Nanoplatelets through Variable Cation, Metal, and Halide Composition *ACS Nano* **10** 7830–9

[8] Gao P, Grätzel M and Nazeeruddin M K 2014 Organohalide lead perovskites for photovoltaic applications *Energy Environ. Sci.* **7** 2448–63

[9] Stranks S D and Snaith H J 2015 Metal-halide perovskites for photovoltaic and light-emitting devices *Nat. Nanotechnol.* **10** 391–402

[10] Yang W S, Noh J H, Jeon N J, Kim Y C, Ryu S, Seo J and Seok S Il 2015 High-performance photovoltaic perovskite layers fabricated through intramolecular exchange *Science (80-. ).* **348** 1234–7

[11] Tan Z-K K, Moghaddam R S, Lai M L, Docampo P, Higler R, Deschler F, Price M, Sadhanala A, Pazos L M, Credgington D, Hanusch F, Bein T, Snaith H J and Friend R H 2014 Bright light-emitting diodes based on organometal halide perovskite *Nat. Nanotechnol.* **9** 687–92

[12] Kim Y C, Kim K H, Son D-Y, Jeong D-N, Seo J-Y, Choi Y S, Han I T, Lee S Y and Park N-G 2017 Printable organometallic perovskite enables large-area, low-dose X-ray imaging *Nature* **550** 87–91

[13] Zhang Y, Lyu M, Qiu T, Han E, Kim I K, Jung M-C, Ng Y H, Yun J-H and Wang L 2020 Halide Perovskite Single Crystals: Optoelectronic Applications and Strategical Approaches *Energies* **13** 4250

[14] Chu Z, Yang M, Schulz P, Wu D, Ma X, Seifert E, Sun L, Li X, Zhu K and Lai K 2017 Impact of grain boundaries on efficiency and stability of organic-inorganic trihalide perovskites *Nat. Commun.* **8** 2230

[15] Trivedi S, Prochowicz D, Parikh N, Mahapatra A, Pandey M K, Kalam A, Tavakoli M M and Yadav P 2021 Recent Progress in Growth of Single-Crystal Perovskites for Photovoltaic Applications *ACS Omega* **6** 1030–42

[16] Hu X, Zhou H, Jiang Z, Wang X, Yuan S, Lan J, Fu Y, Zhang X, Zheng W, Wang X, Zhu X, Liao L, Xu G, Jin S and Pan A 2017 Direct Vapor Growth of Perovskite CsPbBr 3 Nanoplate Electroluminescence Devices *ACS Nano* **11** 9869–76

[17] Li D, Wang G, Cheng H-C, Chen C-Y, Wu H, Liu Y, Huang Y and Duan X 2016 Size-dependent phase transition in methylammonium lead iodide perovskite microplate crystals *Nat. Commun.* **7** 11330

[18] Gui P, Chen Z, Li B, Yao F, Zheng X, Lin Q and Fang G 2018 High-Performance Photodetectors Based on Single All-Inorganic CsPbBr3 Perovskite Microwire *ACS Photonics* **5** 2113–9

[19] Leng K, Abdelwahab I, Verzhbitskiy I, Telychko M, Chu L, Fu W, Chi X, Guo N, Chen Z, Chen Z, Zhang C, Xu Q-H, Lu J, Chhowalla M, Eda G and Loh K P 2018 Molecularly thin two-dimensional hybrid perovskites with tunable optoelectronic properties due to reversible surface relaxation *Nat. Mater.* **17** 908–14

[20] Liu X, Yu D, Cao F, Li X, Ji J, Chen J, Song X and Zeng H 2017 Low-Voltage Photodetectors with High Responsivity Based on Solution-Processed Micrometer-Scale All-Inorganic Perovskite Nanoplatelets *Small* **13** 1700364

[21] Xiao C, Li Z, Guthrey H, Moseley J, Yang Y, Wozny S, Moutinho H, To B, Berry J J, Gorman B, Yan Y, Zhu K and Al-Jassim M 2015 Mechanisms of Electron-Beam-Induced Damage in Perovskite Thin Films Revealed by Cathodoluminescence Spectroscopy *J. Phys. Chem. C* **119** 26904–11

[22] Zou C, Chang C, Sun D, Böhringer K F and Lin L Y 2020 Photolithographic Patterning of Perovskite Thin Films for Multicolor Display Applications *Nano Lett.* **20** 3710–7

[23] Cheng C, Zhu C, Huang B, Zhang H, Zhang H, Chen R, Pei W, Chen Q and Chen H 2019 Processing Halide Perovskite Materials with Semiconductor Technology *Adv. Mater. Technol.* **4** 1–8

[24] Lien S-Y, Wang C-W, Chen W-R, Liu C-H, Kang C-C and Huang C-J 2021 The Influence of Oxygen Plasma on Methylammonium Lead Iodide (MAPbI3) Film Doped with Lead Cesium Triiodide (CsPbI3) *Molecules* **26** 5133

[25] Tsai H, Nie W, Blancon J-C, Stoumpos C C, Asadpour R, Harutyunyan B, Neukirch A J, Verduzco R, Crochet J J, Tretiak S, Pedesseau L, Even J, Alam M A, Gupta G, Lou J, Ajayan P M, Bedzyk M J, Kanatzidis M G and Mohite A D 2016 High-efficiency two-dimensional Ruddlesden–Popper perovskite solar cells *Nature* **536** 312–6

[26] Li X, Chen S, Liu P-F, Zhang Y, Chen Y, Wang H-L, Yuan H and Feng S 2020 Evidence for Ferroelectricity of All-Inorganic Perovskite CsPbBr 3 Quantum Dots *J. Am. Chem. Soc.* **142** 3316–20

[27] Niesner D, Wilhelm M, Levchuk I, Osvet A, Shrestha S, Batentschuk M, Brabec C and Fauster T 2016 Giant Rashba Splitting in CH3NH3PbBr3 Organic-Inorganic Perovskite *Phys. Rev. Lett.* **117** 126401

[28] Yen M-C, Lee C-J, Liu K-H, Peng Y, Leng J, Chang T-H, Chang C-C, Tamada K and Lee Y-J 2021 All-inorganic perovskite quantum dot light-emitting memories *Nat. Commun.* **12** 4460

[29] Yu W, Li F, Yu L, Niazi M R, Zou Y, Corzo D, Basu A, Ma C, Dey S, Tietze M L, Buttner U, Wang X, Wang Z, Hedhili M N, Guo C, Wu T and Amassian A 2018 Single crystal hybrid perovskite field-effect transistors *Nat. Commun.* **9** 5354

[30] Chin X Y, Cortecchia D, Yin J, Bruno A and Soci C 2015 Lead iodide perovskite light-emitting field-effect transistor *Nat. Commun.* **6** 7383

[31] Eaton S W, Lai M, Gibson N A, Wong A B, Dou L, Ma J, Wang L W, Leone S R and Yang P 2016 Lasing in robust cesium lead halide perovskite nanowires *Proc. Natl. Acad. Sci. U. S. A.* **113** 1993–8

[32] Yang Z, Xu Q, Wang X, Lu J, Wang H, Li F, Zhang L, Hu G and Pan C 2018 Large and Ultrastable All-Inorganic CsPbBr 3 Monocrystalline Films: Low-Temperature Growth and Application for High-Performance Photodetectors *Adv. Mater.* **30** 1802110

[33] Gurarslan A, Yu Y, Su L, Yu Y, Suarez F, Yao S, Zhu Y, Ozturk M, Zhang Y and Cao L 2014 Surface-Energy-Assisted Perfect Transfer of Centimeter-Scale Monolayer and Few-Layer MoS 2 Films onto Arbitrary Substrates *ACS Nano* **8** 11522–8

[34] Wang K, Wu C, Yang D, Jiang Y and Priya S 2018 Quasi-Two-Dimensional Halide Perovskite Single Crystal Photodetector *ACS Nano* **12** 4919–29

[35] Zheng W, Xiong X, Lin R, Zhang Z, Xu C and Huang F 2018 Balanced Photodetection in

One-Step Liquid-Phase-Synthesized CsPbBr 3 Micro-/Nanoflake Single Crystals *ACS Appl. Mater. Interfaces* **10** 1865–70

[36] Song J, Xu L, Li J, Xue J, Dong Y, Li X and Zeng H 2016 Monolayer and Few-Layer All-Inorganic Perovskites as a New Family of Two-Dimensional Semiconductors for Printable Optoelectronic Devices *Adv. Mater.* **28** 4861–9

[37] Wu C, Peng W, Fang T, Wang B, Xie C, Wang L, Yang W and Luo L 2019 Asymmetric Contact-Induced Self-Driven Perovskite-Microwire-Array Photodetectors *Adv. Electron. Mater.* **5** 1900135

[38] Yoo T J, Kim Y J, Lee S K, Kang C G, Chang K E, Hwang H J, Revannath N and Lee B H 2018 Zero-Bias Operation of CVD Graphene Photodetector with Asymmetric Metal Contacts *ACS Photonics* **5** 365–70

[39] Zhang C, Fernando J F S, Firestein K L, von Treifeldt J E, Siriwardena D, Fang X and Golberg D 2019 Thermal stability of CsPbBr 3 perovskite as revealed by in situ transmission electron microscopy *APL Mater.* **7** 071110

[40] Wang Y, Wan Z, Qian Q, Liu Y, Kang Z, Fan Z, Wang P, Wang Y, Li C, Jia C, Lin Z, Guo J, Shakir I, Goorsky M, Duan X, Zhang Y, Huang Y and Duan X 2020 Probing photoelectrical transport in lead halide perovskites with van der Waals contacts *Nat. Nanotechnol.* **15** 768–75

[41] M A G and Rahman A 2022 Phase evolution of all-inorganic perovskite nanowires during its growth from quantum dots *Nanotechnology* **33** 085706

# Chapter 9

# Ferroelectric $CsPbBr_3$ Nanoplatelets

## 9.1 Introduction

Ferroelectric materials are a lucrative class of materials due to their ability to store and maintain electric polarization, which has enabled their application in various fields such as catalysts, sensors, memory devices, and actuators.[1–4] Although many ferroelectric materials have been discovered since their first discovery in Rochelle Salt, most of them are inorganic perovskites, such as Lead Zirconate Titanate (PZT) and Barium Titanate (BTO).[5] Despite most ferroelectric materials being inorganic perovskites, the converse is not true.[6,7] Most perovskites, particularly oxide perovskites, have a non-polar structure at room temperature and pressure, which inhibits them from being ferroelectric. Similarly, all inorganic halide perovskites, such as $CsPbBr_3$, share structural similarities to oxide perovskites and primarily exist in the non-polar phases, which lack ferroelectric nature. Despite lacking ferroelectricity, $CsPbBr_3$ has emerged as a promising future semiconductor material due to its amazing optical and electrical properties [8][9] and poses the potential for a range of applications, including broadband detectors, quantum sensors, energy harvesting, and catalysis.[10–14] The incorporation of ferroelectricity in $CsPbBr_3$ is expected to enhance its inherent properties and enable the development of innovative devices for energy harvesting and sensing. Therefore, the creation of a ferroelectric $CsPbBr_3$ crystal could represent a significant step toward harnessing the full potential of this versatile material.

Many methods were implemented to induce ferroelectricity into $CsPbBr_3$ crystals such as alloying n-Butylamine and applying high pressure.[15–17] There have also been reports that $CsGeX_3$ (X = Cl, Br, I) is the only class of inorganic halide perovskites to have a noncentrosymmetric crystal structure, which may lead to ferroelectric behavior.[18] However, Hongming Yuan et al. successfully demonstrated the existence of $CsPbBr_3$ quantum dots in a

ferroelectric phase at room temperature and pressure.[19] There exist a variety of approaches to synthesizing $CsPbBr_3$ crystals, however, there is no reports on the synthesis of large-size crystals of $CsPbBr_3$ in its ferroelectric phase.

In this chapter, a novel solvothermal method to synthesize $CsPbBr_3$ crystals is discussed. The method utilizes acids and peroxides to regulate the solubility of precursors in alcohol, facilitating the growth of $CsPbBr_3$ crystals. The resulting crystals were two types with varying thicknesses: smaller area thick crystals and large area thin crystals. Notably, crystals with a thickness of less than 300 nm exhibited ferroelectric properties. The non-centrosymmetric nature of the crystals was confirmed by second harmonic generation (SHG) studies. Further electrical measurements suggested the presence of an anomalous photovoltaic effect, while piezoresponse force microscopy (PFM) studies confirmed the existence of ferroelectric domains. We anticipate that our findings will pave the way for new research on combining the remarkable properties of $CsPbBr_3$ crystals with ferroelectricity.

## 9.2 A novel solvothermal technique

We discovered that the addition of a little peroxide like $H_2O_2$ can significantly improve the solubility of $PbI_2$ in polar alcohols. Building on this discovery, we have developed a new solvothermal method to synthesize single-crystal $CsPbBr_3$ nanoplates. The addition of organic acids to the alcohol solution containing $H_2O_2$ promotes the solubility of $PbI_2$ and increases the lateral size of the crystals.

### 9.2.1 Solubility of $PbI_2$

Reaction vials with 10 ml ethanol and 10 mg of $PbI_2$ and 40 mg of CsBr with different combinations of organic acids and $H_2O_2$. A photograph of the vials is given in Fig 9.1. The first vial (E+O) shows the solution with just 50 µl octanoic acid added to it. There was no visible change in the color indicating no change in the solubility of $PbI_2$. The second vial (E+H(0.02%)) shows the solution with 0.02% of $H_2O_2$ added to it. There was a slight change in the color indicating a minute change in the solubility of $PbI_2$. The third vial (E+H(0.2%)) shows the solution with 0.2% of $H_2O_2$ added to it. The color change was much more visible (pale yellow)

indicating that $PbI_2$ started to dissolve well in the solution. The fourth vial (E+O+H(0.2%)) shows the solution with added 0.2% $H_2O_2$ and 50 µl octanoic acid. There was a significant change in the color (deep orange) indicating a good solubility of $PbI_2$ in the solution. The addition of inorganic acids such as HBr and other organic ligands such as amines also improves the solubility of $PbI_2$, but the photoluminescence and size of the crystals are not as good as the ones made using organic acids. A comparison of the size and PL intensity from the crystals synthesized using various acids and amines are given in tables 9.1 and 9.2. The solubility of $PbI_2$ improves significantly in the presence of $H_2O_2$. The color of the solution can vary depending on the solubility of $PbI_2$ and is a very good indicator of the solubility of $PbI_2$ (Fig 9.1). If $PbI_2$ remains insoluble, the reaction mixture will stay transparent, while a highly soluble $PbI_2$ solution can cause the solution mixture to appear deep red

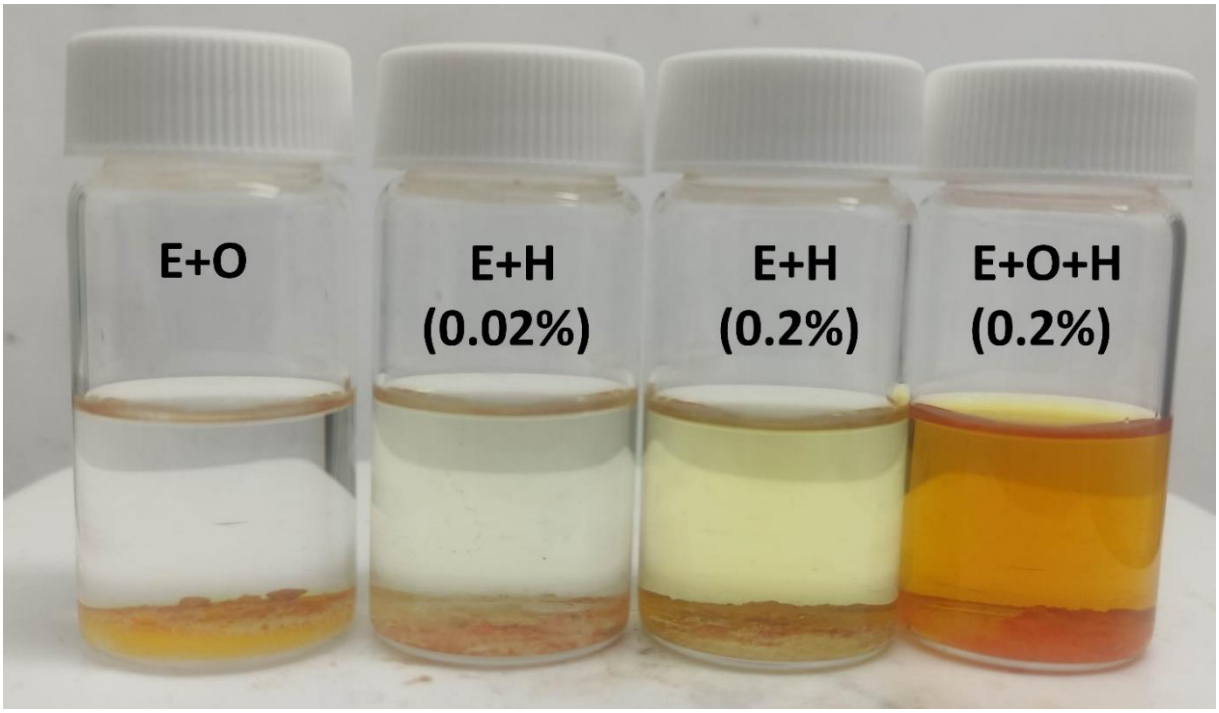


Figure 9.1: Different reaction vials with different combinations of peroxides and acids after 3 hrs. on a hot plate at 50 °C. The color difference indicates the difference in solubility of PbI2 in different solutions.

### 9.2.2 Growth of $CsPbBr_3$ nanoplatelets

A schematic of the growth is shown in Fig 9.2 a. The growth is accomplished by mixing 100 µl of $H_2O_2$ (3 wt% in water) with 10 ml of Ethanol in a glass vial, followed by the addition of 10 mg of $PbI_2$ and 40 mg of CsBr. A substrate is placed in the solution to collect the as-grown $CsPbBr_3$ crystals in the glass vial and 50 µl of Octanoic acid is added to enhance the growth. The vial is then sealed and heated on a hot plate between 45 – 65 °C causing both CsBr and $PbI_2$ to dissolve slowly. The ion concentration gradually increases over time, reaching an optimal concentration for the nucleation and growth of $CsPbBr_3$ crystals. As the crystals grow, they settle onto the substrate and continue to grow. After 3 – 4 hrs the growth is complete and the substrate with the crystals is washed in anhydrous IPA followed by blow drying with nitrogen gas and heating at 50°C.

Fig 9.2b displays an optical microscopy (OM) image of the as-grown sample, revealing crystals with lateral dimensions in the range of a few tens of micrometers. The FESEM images depicted in Fig 9.2c demonstrate that some crystals have stacked on top of one another, which aligns with our proposed mechanism. To further substantiate the growth mechanism, we introduced two substrates into the reaction vial, as illustrated in Fig 9.2d. Crystals were observed exclusively on the upward-facing sides of both substrates, while no crystals were observed on the sides that were facing down. Elimination of the gap between the substrates by stacking one substrate on top of the other resulted in the absence of crystals on the covered substrate, thus validating our proposed mechanism of crystals settling onto the substrate.

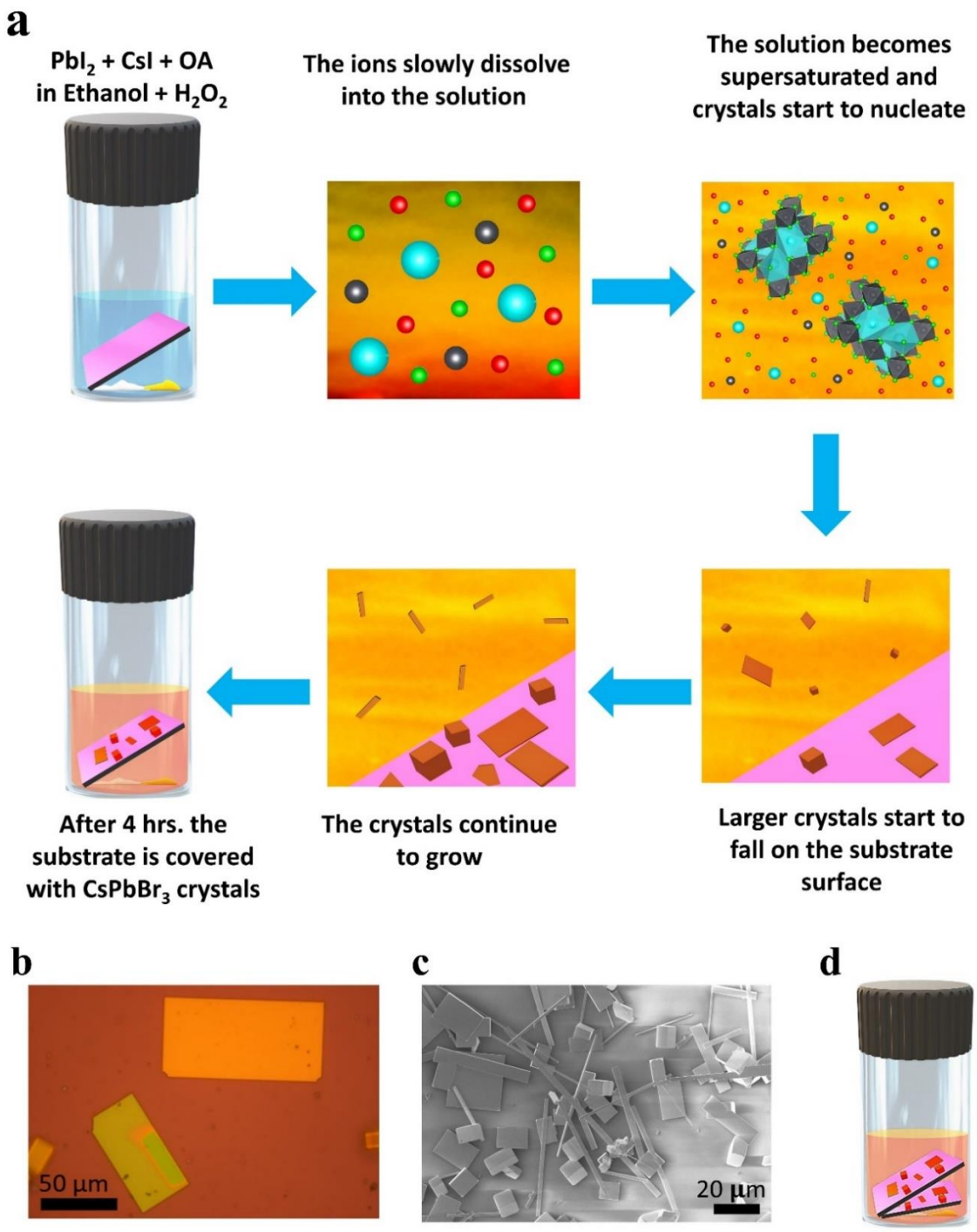


Figure 9.2: Growth of $CsPbBr_3$ nanoplatelets. (a) schematic of the growth mechanism involved in the solvothermal process. (b) is the optical microscope image of the synthesized $CsPbBr_3$ nanoplatelets, produced using the new technique described in (a). FESEM image of the samples, showcasing crystals that overlap on top of each other is shown in (c). (d) shows the schematic demonstrating the deposition of $CsPbBr_3$ crystals on multiple substrates.

### 9.2.3 Reaction with other combinations of alcohol mixtures

The reaction was also carried out using other combinations of acids and amines. A comparison of the size of the crystals and their PL are given in table 9.1 and 9.2. The addition of organic acids, inorganic acids, Amines, and Amides into the $H_2O_2$ added alcohol all improved the solubility. However, only certain combinations produced large crystals with good PL intensity. As can be seen from the table the size of the crystal is better for Methanol and Ethanol and is poor for Isopropyl-Alcohol (IPA) for all organic acids used. For inorganic acids, amines, and amides both the PL and size of the grown crystal go down. Whereas Organic acids retained good PL. We chose ethanol and octanoic acid for further study as this combination gave good results.

Table 9.1. Size of the crystals grown using different acids/ligands

| | Octanoic acid | Oleic acid | Hexanoic acid | Oleyl-amine | Octyl-amine | HBr |
|---|---|---|---|---|---|---|
| **Methanol** | **V. Good** | **V. Good** | **Good** | **Average** | **Average** | **Poor** |
| **Ethanol** | **V. Good** | **V. Good** | **Poor** | **Average** | **Average** | **Poor** |
| **IPA** | **Poor** | **Poor** | **Poor** | **Poor** | **Poor** | **Poor** |

Table 9.2. PL of the crystals grown using different acids/ligands

| | Octanoic acid | Oleic acid | Hexanoic acid | Oleyl-amine | Octyl-amine | HBr |
|---|---|---|---|---|---|---|
| **Methanol** | **V. Good** | **V. Good** | **V. Good** | **Poor** | **Poor** | **Poor** |
| **Ethanol** | **V. Good** | **V. Good** | **V. Good** | **Poor** | **Poor** | **Poor** |
| **IPA** | **V. Good** | **V. Good** | **V. Good** | **Poor** | **Poor** | **Poor** |

## 9.3 Characterization of the as-grown crystal

The crystal structure and composition of $CsPbBr_3$ crystals were investigated using XRD, EDX, HRTEM, and SAED. The XRD pattern of the $CsPbBr_3$ crystals was compared with the ICSD # 97851 as depicted in Fig 9.3a. The XRD showed strong diffraction peaks that can be assigned to the pure orthorhombic crystal structure, without any impurity peaks (such as CsBr or $PbI_2$). The clear splitting of (002)/(110) and (004)/(220) peaks in the spectrum indicate that the as-grown $CsPbBr_3$ crystals are in the orthorhombic phase and have large crystalline domains.[20,21]

The SEM image in Fig. 9.3b, highlights the existence of two distinct types of crystals. The first type comprises thin crystals with lateral sizes of a few tens of micrometers and is of such thinness that the shades of the crystals underneath them are visible in the SEM image (thin crystals). The second type is crystals with lateral sizes of a few micrometers that have a thickness of a few micrometers (bulk crystals). The difference in aspect ratios of the crystal indicates that the growth of the two crystals was different as the thin crystal preferred lateral growth and the thick crystal more or less grew uniformly as compared to the thin crystal. These findings suggest the possibility of a difference between the two crystal types. Both crystals are identified as being in the orthorhombic phase, as indicated by the absence of impurity peaks in the XRD pattern.

EDS elemental mapping, shown in Fig 9.3c indicates a uniform distribution of Cs, Pb, and Br in both crystal types.

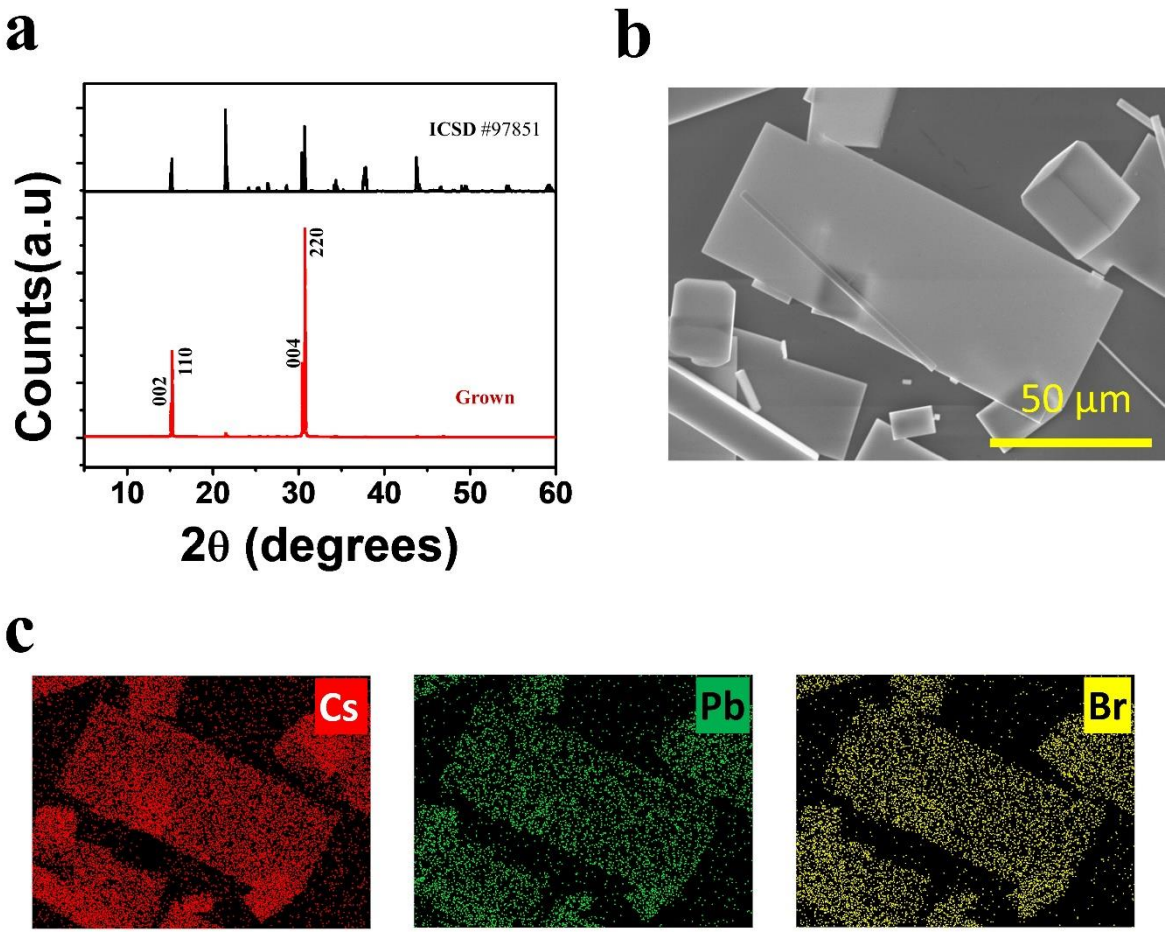


Figure 9.3: (a) the XRD of the as-synthesized crystals which match with the peaks of orthorhombic $CsPbBr_3$. (b) Shows the FESEM images of both thin and thick crystals of different aspect ratios. (c) is the EDS elemental maps showing Cs (red), Pb (green), and Br (yellow) of the sample shown in the SEM image in (b).

To analyze the crystal structure of the thin crystals we transferred the crystals on to a carbon-coated TEM grid. The bigger crystals were too thick for the beam to pass through and hence we focused on smaller crystals as they were thin enough and allowed the e-beam to pass through them. The HRTEM image of typical crystal in Fig. 9.4 showed lattice fringes at an angle of 90° with a spacing of 5.9 and 5.8 Å, corresponding to the (002) and (110) planes of orthorhombic $CsPbBr_3$.[19] The FFT pattern analysis indicates that the synthesized crystals are single crystalline and have an orthorhombic phase, which agrees with the XRD pattern.

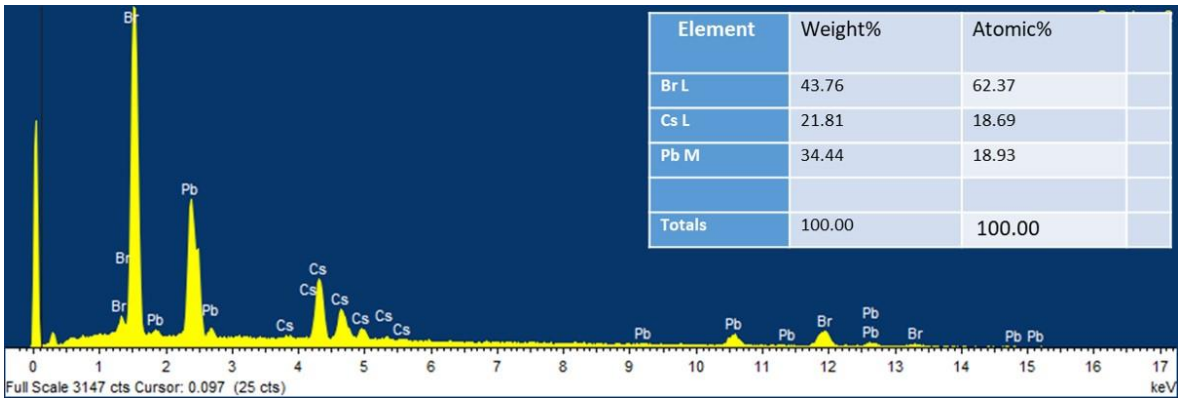


| Element | Weight% | Atomic% |
|---|---|---|
| Br L | 43.76 | 62.37 |
| Cs L | 21.81 | 18.69 |
| Pb M | 34.44 | 18.93 |
| | | |
| Totals | 100.00 | 100.00 |

Figure 9.4: EDX spectra of $CsPbBr_3$ showing a Cs:Pb:Br ratio as 1:1:3.

The crystals' composition was determined using EDX spectroscopy, which closely matches that of the $CsPbBr_3$ (with a Cs:Pb:Br ratio close to 1:1:3) as can be seen in supplementary Fig 9.4. The composition of the crystal along with the other characterizations points to the crystal being $CsPbBr_3$ in its orthorhombic phase.

The reflection conditions for the orthorhombic space group Pnma are indistinguishable from $Pna2_1$.[22] As a result, both crystal types will exhibit similar XRD and SAED patterns, implying that it is impossible to distinguish the two types based on these studies.[23] Historically this symmetry has led to the assigning of Pnma crystals in the $Pna2_1$ group which were later assigned back to the Pnma group.[24–27] Thus even if the crystals contain a mixture of both $Pna2_1$ and Pnma crystals, we would still get a purely orthorhombic crystal pattern. The observed difference in growth between the two crystal types could be attributable to this difference. This argument is supported by the report on the $Pna2_1$ $CsPbBr_3$ crystals by Hongming Yuan *et al.*[19]

## 9.4 Optical characterization of the crystals

To distinguish between the crystals, optical microscopic techniques like microscopic photoluminescence, Raman spectroscopy, and second harmonic generation were used. Fig. 9.5a depicts the PL microscopic images of the as-synthesized crystals. The crystals exhibit a very bright green PL. The PL spectrum of the two crystals, bulk and thin, are shown in Fig. 9.5b. Slight PL variations exist among different samples, making it challenging to reliably differentiate between the two crystals based solely on PL characteristics. In the case of the

thinner crystal, the PL spectrum reveals the presence of two distinct peaks, while the thicker crystal exhibits a broader single peak. These two distinct peaks were previously documented in orthorhombic CsPbBr3 by Stoumpos et al. at 46 K and by Zhang et al. at room temperature.[28,29] Our observation of PL peaks at 530 nm and 543 nm, each with a full width at half maximum (FWHM) of 10 nm and 17 nm, respectively, aligns with the findings reported by Zhang et al. Notably, Zhang et al. attributed the 530 nm peak to free exciton emission, while the peak close to 550 nm was ascribed to bound-exciton emission. We suspect that the appearance of the two peaks has to do with crystal quality and cannot be used to distinguish between the two crystals. Generally, the thin crystals were more PL active than the Bulk crystals and this might explain why the PL from the thinner sample had two distinct peaks.

The Raman signal however was very distinct for the two crystals. The bulk CsPbBr3 crystal exhibits a distinct Raman scattering pattern with a strong signal at 82 $cm^{-1}$ (assigned to the $B_{g1}$ mode), a weak signal at 132 $cm^{-1}$ (assigned to the $A_{1g}$ mode), and a very weak signal at 314 $cm^{-1}$ (corresponding to the second-order phonon Raman scattering).[30,31] These results suggest that the crystal is in the orthorhombic Pnma phase group. However, thinner crystals do not exhibit any distinct Raman scattering pattern.

The $Pna2_1$ crystals groups are non-centrosymmetric and only non-centrosymmetric crystals are capable of producing second-order nonlinear optical interactions.[32] Thus SHG studies can be used to distinguish them from the centrosymmetric Pnma crystal group. The SHG studies were performed using a Ti-Sapphire Laser (operating at 140fs, 80 Hz), with an excitation wavelength of 810 nm. We grew the crystals on a microscope cover slip and excited the thin and thick crystals with the laser. The thin crystals generated an SHG signal at 405 nm whereas the thick crystal gave no SHG (Fig. 9.5d). This suggests that only very thin crystals are in the non-centrosymmetric $Pna2_1$ group. The exact relation between the crystal thickness and SHG signal needs further study.

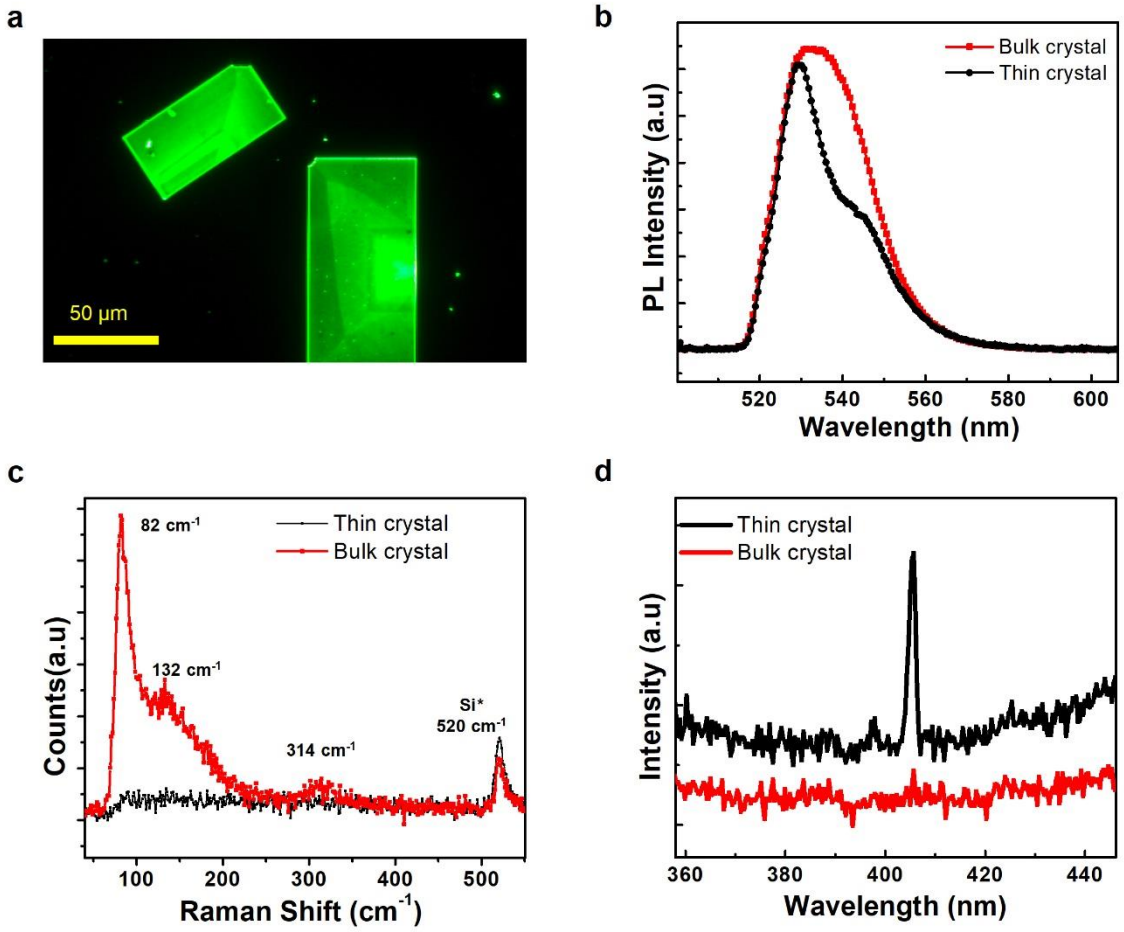


Figure 9.5: (a) PL images of the crystals grown show very bright green emission when excited with 465 nm. (b) the PL spectra obtained from bulk and thin crystals demonstrate distinct emission characteristics. In the thin crystal, two distinct peaks are observed, whereas the bulk crystal exhibits a single broader peak. (c) is the Raman from the two samples of different thicknesses. The thick samples show Raman peaks corresponding to the Pnma phase group whereas the thin nanoplatelets do not show any Raman signal in the given range. (d) SHG spectra from the two crystals when excited with an 810 nm femtosecond pulsed laser. The thin nanoplatelets gave SHG signal whereas the thick samples generated no SHG signal, suggesting that the bulk crystals are centrosymmetric whereas the thin crystals are non-centrosymmetric.

An interesting observation was made during the SHG experiments. To eliminate the possibility of low power causing the absence of SHG, we conducted an experiment by increasing the laser power. Surprisingly, the thick crystals showed no SHG signal, despite the higher power. Conversely, when studying thin crystals with the same experimental parameters, a strong SHG peak was observed. However, the higher laser power led to damage in the thin crystal.

Intriguingly, even thick crystals with lateral dimensions measuring tens of micrometers failed to show any SHG signal even when the accumulation time was increased to more than thrice that was used for thin crystal.

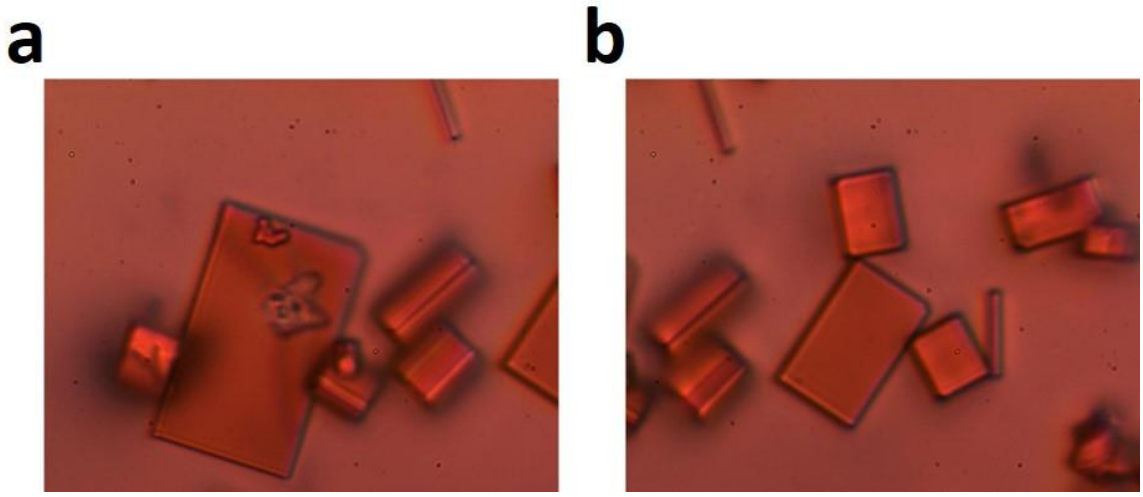


Figure 9.6: (a) is the OM image of the thinner crystal that got damaged under the laser and (b) is the OM image of the thicker crystal that showed no SHG even when accumulation time was increased to 10 seconds showed no visible signs of any damage.

## 9.5 Electrical characterization of the crystal

To explore the electrical properties of the $Pna2_1$ crystals, active devices were fabricated using the lithography technique reported earlier.[33] The technique is well suited for thin crystals and the ITO leads were deposited on a crystal that had a greenish appearance (Fig. 9.7a). The dark current of the device was in few femto-Amperes and exhibited current peaks similar to the ferroelectric switching current in ferroelectrics (Fig. 9.7b). A maximum $V_{oc}$ of around 0.4 V was observed when illuminated with a 470 nm LED with an intensity of 10 $mW/cm^2$ (Fig. 9.7c). The transient photocurrent response of the device at 0 V bias by switching 470 nm LED on and off periodically also exhibited good photocurrent generation is shown in Fig. 9.7d.

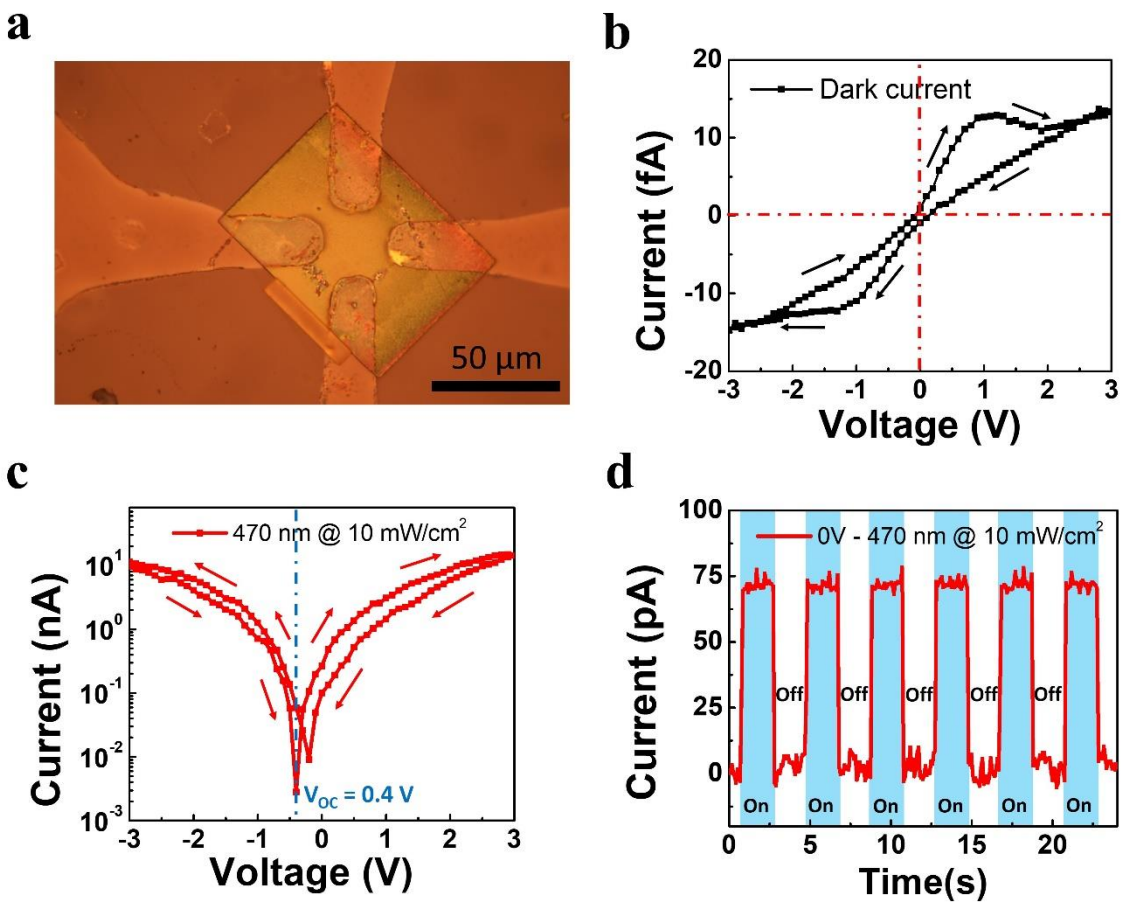


Figure 9.7: (a) Optical microscope image of the $CsPbBr_3$ nanoplatelet device used for the measurement. (b) Shows the dark current measurement on the device under test exhibiting I-V hysteresis loop similar to ferroelectric switching current. (c) is the photocurrent I-V scan of the device when illuminated with an LED of 470 nm excitation having 10 mW/cm$^2$ intensity. The device showed a $V_{oc}$ of nearly 0.4 V. Time-resolved photoresponse of the device at 0 V bias is shown in (d). The device generated significant photocurrent when the LED is turned on even at 0 V bias.

The photocurrent vs. wavelength scan of the device indicates that photocurrent is generated in the crystal if the incident wavelength is 550 nm or lower as seen in Fig. 9.8 a and d).

The on-off current ratio ($I_{on}/I_{off}$) and the responsivity (R) of the device were calculated using the relations,

$$I_{on}/I_{off} = I_{light}/I_{dark} \quad \text{and} \quad R = (I_{light}-I_{dark})/(P \times A)$$

Respectively.[34]

Here, $I_{light}$ is the current under illumination and $I_{dark}$ is the dark current, P is the intensity of the

incident light on the device, and A is the area of the device. The Dark current measured using the electrometer gives a current on/off ratio of $10^6$, and a responsivity above 0.3 A/W at 0 V bias in the wavelength range between 350 nm – 530 nm (Fig. 9.8 b and e). This value of responsivity increases to above 3.5 A/W at 1 V bias in the wavelength range between 350 nm – 520 nm and is comparable to that of thicker orthorhombic crystal-synthesized in other works.[20,33,35] and is better than multigrain detectors of $CsPbBr_3$.[36]

The detectivity is given by

$$D = R \times ((2eI_{dark})/A)^{-(1/2)}$$

Here, e is the charge of an electron.[34] The device's low dark current, in conjunction with its impressive photocurrent generation, results in a detectivity that is remarkably high. For a broad range of spectra (ranging from 350 nm to 530 nm), this detectivity is on the order of $10^{14}$ Jones at 0V bias and $10^{15}$ Jones at 1V bias (Fig. 9.8 c and f).

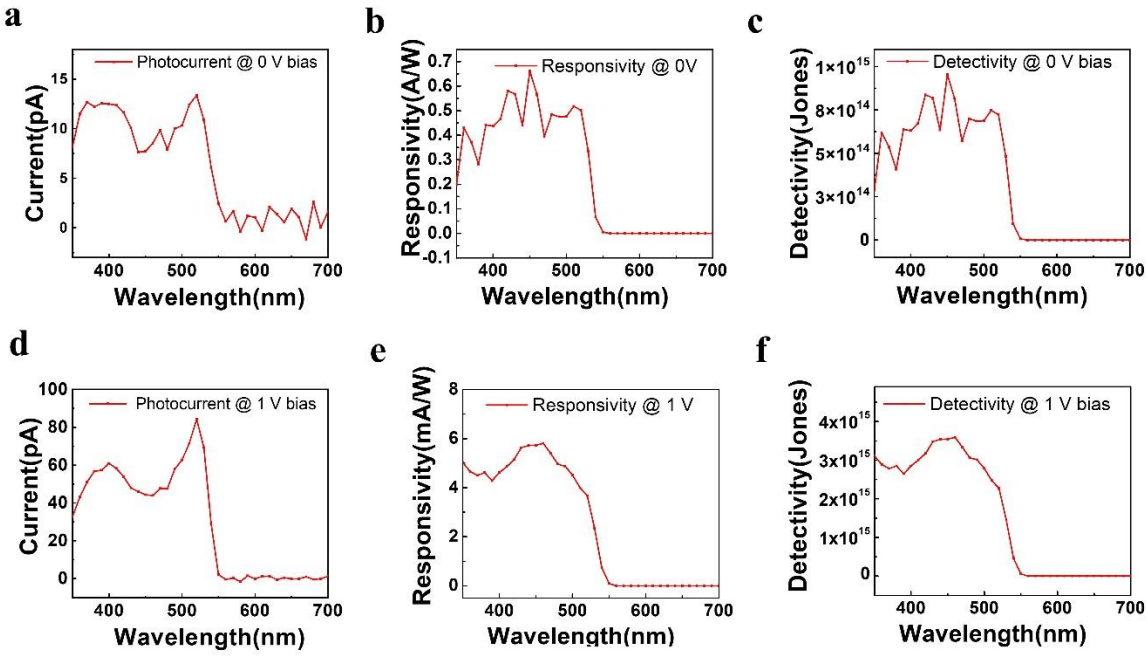


Figure 9.8: (a), (b), and (c) shows the photocurrent vs wavelength. The responsivity vs wavelength, and the detectivity vs wavelength of the device at 0 V. (d), (e), and (f) shows the photocurrent vs wavelength, The responsivity vs wavelength, and the detectivity vs wavelength of the device at 1 V respectively.

## 9.6 Piezoresponse Force Microscopy

The optical and electrical studies point towards the ferroelectric nature of the $CsPbBr_3$ crystals. Ferroelectric domains are present in a ferroelectric material and thus to validate the presence of ferroelectric domains in $CsPbBr_3$ crystal, we utilized piezoresponse force microscopy and spectroscopy.[37] For this, we grew $CsPbBr_3$ crystals on top of an ITO-coated glass substrate using our growth technique. Thin $CsPbBr_3$ nanoplatelets with a thickness close to 300 nm were identified (Fig. 9.9a). To corroborate the ferroelectric nature of these domains, we analyzed the spontaneous polarization and its response to externally applied electric fields by utilizing switching spectroscopy PFM. The phase of the PFM response signal is correlated with the direction of the domain's polarization, and the amplitude of the PFM response signal is related to the local electro-mechanical response magnitude. The obtained hysteresis behavior in the phase of the PFM signal (Fig. 9.9b) shows nearly 180° switching of electrical polarization, supporting the presence of ferroelectric domains.

Additionally, the butterfly-shaped loop in the amplitude of the PFM response signal (Fig. 9.9c) provides additional confirmation of the existence of localized ferroelectric domains. To provide additional evidence for the presence of ferroelectric domains, topographic, amplitude, and phase imaging of the crystals were taken ((Fig. 9.9d-e). The images confirmed the existence of localized ferroelectric domains, and the contrast variations in the phase image imply the presence of oppositely polarized domains in close proximity.

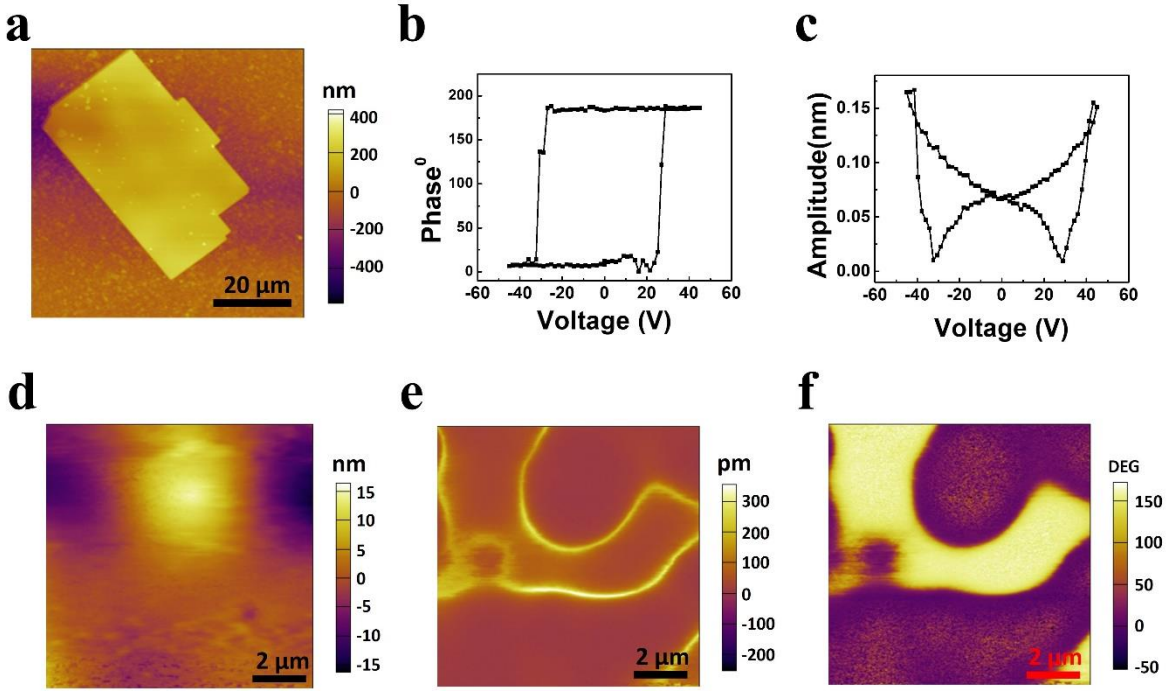


Figure 9.9: (a) shows the AFM topographic map of the crystal of interest (b) and (c) are the phase and amplitude switching spectroscopy loops of the crystal as a function of voltage. (d) shows the surface morphology of a small region of the crystal (e) and (f) are the PFM amplitude map and PFM phase map of the region shown in (d). The PFM mapping proves the existence of ferroelectric domains in the $CsPbBr_3$ nanoplatelets.

## 9.7 Summary

In this chapter, we present a novel technique for synthesizing ferroelectric $CsPbBr_3$, which demonstrates promising results with respect to its ferroelectric properties. The synthesis approach involves a simple, low-temperature, and cost-effective solvothermal method, which produces crystals with very low dark current in few femtoamperes. The thin nanoplatelets of $CsPbBr_3$ exhibited ferroelectric behavior and the self-powered devices made from them exhibited a very high detectivity of $10^{14}$ Jones. To gain a comprehensive insight into the structural and functional properties of $CsPbBr_3$, XRD, Raman spectroscopy, HRTEM, PL, SHG, electrical measurements, and PFM measurements were performed. The PFM measurements clearly established the presence of ferroelectric domains. The results shown in this chapter suggest that ferroelectric $CsPbBr_3$ could become a valuable addition to the scientific community's repertoire of advanced technologies. Moreover, the growth method

proposed in this study could be applied to other similar materials for various technological applications.

**Bibliography**

[1] Lines M E and Glass A M 2001 *Principles and Applications of Ferroelectrics and Related Materials* vol 14 (Oxford University Press)

[2] Dong W, Xiao H, Jia Y, Chen L, Geng H, Bakhtiar S U H, Fu Q and Guo Y 2022 Engineering the Defects and Microstructures in Ferroelectrics for Enhanced/Novel Properties: An Emerging Way to Cope with Energy Crisis and Environmental Pollution *Adv. Sci.* **9** 2105368

[3] Martin L W and Rappe A M 2016 Thin-film ferroelectric materials and their applications *Nat. Rev. Mater.* **2** 16087

[4] Scott J F 2007 Applications of Modern Ferroelectrics *Science (80-. ).* **315** 954–9

[5] Valasek J 1921 Piezo-Electric and Allied Phenomena in Rochelle Salt *Phys. Rev.* **17** 475–81

[6] Cohen R E 1992 Origin of ferroelectricity in perovskite oxides *Nature* **358** 136–8

[7] Benedek N A and Fennie C J 2013 Why Are There So Few Perovskite Ferroelectrics? *J. Phys. Chem. C* **117** 13339–49

[8] Kovalenko M V., Protesescu L and Bodnarchuk M I 2017 Properties and potential optoelectronic applications of lead halide perovskite nanocrystals *Science (80-. ).* **358** 745–50

[9] Yu J, Liu G, Chen C, Li Y, Xu M, Wang T, Zhao G and Zhang L 2020 Perovskite CsPbBr 3 crystals: growth and applications *J. Mater. Chem. C* **8** 6326–41

[10] Peng K, Tao R, Haeberlé L, Li Q, Jin D, Fleming G R, Kéna-Cohen S, Zhang X and Bao W 2022 Room-temperature polariton quantum fluids in halide perovskites *Nat. Commun.* **13** 7388

[11] Su R, Ghosh S, Wang J, Liu S, Diederichs C, Liew T C H and Xiong Q 2020 Observation of exciton polariton condensation in a perovskite lattice at room temperature *Nat. Phys.* **16** 301–6

[12] He Y, Petryk M, Liu Z, Chica D G, Hadar I, Leak C, Ke W, Spanopoulos I, Lin W, Chung

D Y, Wessels B W, He Z and Kanatzidis M G 2021 CsPbBr3 perovskite detectors with 1.4% energy resolution for high-energy γ-rays *Nat. Photonics* **15** 36–42

[13] Liu X, Tan X, Liu Z, Ye H, Sun B, Shi T, Tang Z and Liao G 2019 Boosting the efficiency of carbon-based planar CsPbBr3 perovskite solar cells by a modified multistep spin-coating technique and interface engineering *Nano Energy* **56** 184–95

[14] Zhu X, Lin Y, San Martin J, Sun Y, Zhu D and Yan Y 2019 Lead halide perovskites for photocatalytic organic synthesis *Nat. Commun.* **10** 2843

[15] Wu Z, Ji C, Li L, Kong J, Sun Z, Zhao S, Wang S, Hong M and Luo J 2018 Alloying n -Butylamine into CsPbBr 3 To Give a Two-Dimensional Bilayered Perovskite Ferroelectric Material *Angew. Chemie Int. Ed.* **57** 8140–3

[16] Ben Sadok R, Muñoz A, Rodríguez-Hernández P, Djani H and Hammoutène D 2022 Pressure-driven ferroelectric phase transition for the Pnma-CsPbBr3: Mechanical and dynamical stability study *J. Solid State Chem.* **314** 123402

[17] Zhao Y-Q, Ma Q-R, Liu B, Yu Z-L and Cai M-Q 2018 Pressure-induced strong ferroelectric polarization in tetra-phase perovskite CsPbBr 3 *Phys. Chem. Chem. Phys.* **20** 14718–24

[18] Zhang Y, Parsonnet E, Fernandez A, Griffin S M, Huyan H, Lin C-K, Lei T, Jin J, Barnard E S, Raja A, Behera P, Pan X, Ramesh R and Yang P 2022 Ferroelectricity in a semiconducting all-inorganic halide perovskite *Sci. Adv.* **8** eabj5881

[19] Li X, Chen S, Liu P-F, Zhang Y, Chen Y, Wang H-L, Yuan H and Feng S 2020 Evidence for Ferroelectricity of All-Inorganic Perovskite CsPbBr 3 Quantum Dots *J. Am. Chem. Soc.* **142** 3316–20

[20] Yang Z, Xu Q, Wang X, Lu J, Wang H, Li F, Zhang L, Hu G and Pan C 2018 Large and Ultrastable All-Inorganic CsPbBr 3 Monocrystalline Films: Low-Temperature Growth and Application for High-Performance Photodetectors *Adv. Mater.* **30** 1802110

[21] Rakita Y, Kedem N, Gupta S, Sadhanala A, Kalchenko V, Böhm M L, Kulbak M, Friend R H, Cahen D and Hodes G 2016 Low-Temperature Solution-Grown CsPbBr 3 Single Crystals and Their Characterization *Cryst. Growth Des.* **16** 5717–25

[22] Pu S, Zheng H, Chen Z, Li M, Hu Z, Wang J and Zou H 2015 The microstructure and ferroelectric property of Nd-doped multiferroic ceramics Bi0.85Nd0.15FeO3 *Ceram. Int.*

**41** 5498–504

[23] Tamari R, Grushko B and Meshi L 2021 Electron Diffraction Study of the Space Group Variation in the Al–Mn–Pt T-Phase *Symmetry (Basel).* **14** 38

[24] Poglitsch A and Weber D 1987 Dynamic disorder in methylammoniumtrihalogenoplumbates (II) observed by millimeter-wave spectroscopy *J. Chem. Phys.* **87** 6373–8

[25] Kay H F and Miles J L 1957 The structure of cadmium titanate and sodium tantalate *Acta Crystallogr.* **10** 213–8

[26] Ahtee M and Unonius L 1977 The structure of NaTaO 3 by X-ray powder diffraction *Acta Crystallogr. Sect. A* **33** 150–4

[27] Swainson I P, Hammond R P, Soullière C, Knop O and Massa W 2003 Phase transitions in the perovskite methylammonium lead bromide, CH3ND3PbBr3 *J. Solid State Chem.* **176** 97–104

[28] Zhang H, Liu X, Dong J, Yu H, Zhou C, Zhang B, Xu Y and Jie W 2017 Centimeter-Sized Inorganic Lead Halide Perovskite CsPbBr 3 Crystals Grown by an Improved Solution Method *Cryst. Growth Des.* **17** 6426–31

[29] Stoumpos C C, Malliakas C D, Peters J A, Liu Z, Sebastian M, Im J, Chasapis T C, Wibowo A C, Chung D Y, Freeman A J, Wessels B W and Kanatzidis M G 2013 Crystal Growth of the Perovskite Semiconductor CsPbBr 3 : A New Material for High-Energy Radiation Detection *Cryst. Growth Des.* **13** 2722–7

[30] Qin Z, Dai S, Hadjiev V G, Wang C, Xie L, Ni Y, Wu C, Yang G, Chen S, Deng L, Yu Q, Feng G, Wang Z M and Bao J 2019 Revealing the Origin of Luminescence Center in 0D Cs 4 PbBr 6 Perovskite *Chem. Mater.* **31** 9098–104

[31] Wang C, Wang Y, Su X, Hadjiev V G, Dai S, Qin Z, Calderon Benavides H A, Ni Y, Li Q, Jian J, Alam M K, Wang H, Robles Hernandez F C, Yao Y, Chen S, Yu Q, Feng G, Wang Z and Bao J 2019 Extrinsic Green Photoluminescence from the Edges of 2D Cesium Lead Halides *Adv. Mater.* **31** 1902492

[32] Robert W. BoyD 2003 *Nonlinear Optics* vol 13 (Elsevier)

[33] M. A. G and Rahman A 2023 Fabrication of High-Performance Devices on Water-Soluble Lead Halide Perovskites Using Water-Based Photolithography *Adv. Mater. Interfaces* **10**

2201749

[34] Wang K, Wu C, Yang D, Jiang Y and Priya S 2018 Quasi-Two-Dimensional Halide Perovskite Single Crystal Photodetector *ACS Nano* **12** 4919–29

[35] Zheng W, Xiong X, Lin R, Zhang Z, Xu C and Huang F 2018 Balanced Photodetection in One-Step Liquid-Phase-Synthesized CsPbBr 3 Micro-/Nanoflake Single Crystals *ACS Appl. Mater. Interfaces* **10** 1865–70

[36] Song J, Xu L, Li J, Xue J, Dong Y, Li X and Zeng H 2016 Monolayer and Few-Layer All-Inorganic Perovskites as a New Family of Two-Dimensional Semiconductors for Printable Optoelectronic Devices *Adv. Mater.* **28** 4861–9

[37] Jesse S, Baddorf A P and Kalinin S V. 2006 Switching spectroscopy piezoresponse force microscopy of ferroelectric materials *Appl. Phys. Lett.* **88** 062908

# Chapter 10

# Conclusion and future direction

## 10.1 Conclusion

In conclusion, this thesis has made significant contributions to the field of semiconducting materials and their heterostructures, with a specific focus on TMD monolayers and perovskites. The research began by providing a comprehensive introduction to semiconducting materials, emphasizing the potential of TMD monolayers and perovskites as promising candidates for future electronic devices. The exploration of various semiconducting heterostructures further highlighted their wide-ranging applications. Chapter 2 delved into the characterization techniques employed in this thesis to study the synthesized materials. Chapter 3 of this thesis presented a comprehensive account of the instrumentation employed throughout the research, highlighting the meticulous setup and the various homebuilt arrangements I had the opportunity to contribute to. The investigation in Chapter 4 explored the sensitivity of CVD growth of monolayers to flow fluctuations. This understanding was leveraged to develop a self-modulating effect that facilitated the controlled growth of monolayers under conditions favorable for bulk TMD growth. This novel approach holds significant promise for the synthesis of monolayers. Chapter 5 focused on the study of sodium silicate as a growth promoter for $MoS_2$ monolayers. Through a comparison of growth and field effect mobility with conventional salt, the superior performance of water glass in synthesizing TMDs was demonstrated. The impact of strain on the optoelectronic properties of $MoS_2$ was investigated in Chapter 6. The research revealed that strain induced by growing TMDs on textured substrates led to intriguing modulations in photoluminescence emission spectra. These findings contribute to the understanding of strain engineering in TMDs, opening avenues for the development of improved optoelectronic devices. Chapter 7 delved into the growth of $CsPbI_3$ nanowires using the Hot Injection method. Through meticulous experiments, including in-situ observation using an optical microscope, the growth

dynamics and morphology control of nanowires were comprehensively studied, providing valuable insights into the growth mechanism of $CsPbI_3$ nanowires in HI method. In Chapter 8, a novel sacrificial layer-assisted lithography technique was demonstrated, enabling the fabrication of electrical devices using water-soluble perovskite crystals and traditional water-based photolithography. This innovative approach expands the possibilities for device fabrication in perovskite-based electronics. Lastly, Chapter 9 introduced a low-temperature solvothermal technique for growing $CsPbBr_3$ nanoplatelets with large lateral dimensions and ultralow dark currents. The method also facilitated the synthesis of ferroelectric $CsPbBr_3$ platelets, possibly opening up new avenues for research. Overall, this thesis significantly contributes to the advancement of semiconducting materials and their heterostructures by investigating their properties, exploring novel growth techniques, and uncovering their optoelectronic capabilities. The findings and methodologies presented herein provide a solid foundation for future research and the development of innovative electronic devices with enhanced performance and functionality.

## 10.2 Future Direction

In semiconductors, the emergence of two-dimensional materials possessing dangling-bond-free surfaces and relatively weak van der Waals interactions has opened up new avenues for the assembly of high-quality heterostructures, alleviating the stringent requirement of lattice-constant matching that has traditionally constrained conventional semiconductor epitaxy processes. Consequently, the generation of dislocations at the heterostructure interface has been significantly reduced.[1]

Although monolayers of 2D materials exhibit extraordinary properties, such as exceptional mechanical strength and remarkable optical absorption coefficients, they suffer from a critical limitation: their ultrathin nature leads to minimal light absorption. Furthermore, the emergent properties observed in these monolayers tend to vanish at the bulk level.[2] [3] However, the formation of heterostructures comprising direct band gap materials, particularly lead halide perovskites, introduces a captivating opportunity to overcome these limitations and realize novel devices. Lead halide perovskites, known for their exceptional optical absorption coefficients, are a direct bandgap material even in bulk and can enhance the light absorption capabilities of the

heterostructures made with it.[4]

At the heart of these heterostructures lies the atomic interface, which holds immense intrigue and promise. The atomic-scale arrangement and interaction between the 2D materials and lead halide perovskites present an intriguing landscape for exploration. The reasons behind the captivating nature of this atomic interface are multifaceted. Firstly, the distinct properties exhibited by each material create opportunities for synergistic effects and emergent phenomena. Additionally, the interface plays a crucial role in modulating the transport of charge carriers and excitons, impacting the overall performance of the heterostructure. Understanding and manipulating the atomic interface hold the potential to unlock novel functionalities and device designs with enhanced optoelectronic properties.

In this chapter, we delve into the fascinating realm of heterostructures composed of 2D materials and lead halide perovskites. The chapter briefly touch upon the future direction of the work in this thesis, good progress has already been achieved in the transfer process for precisely transferring $CsPbBr_3$ and 2D materials. We have already successfully made photodiodes and LEDs using this technique. The preliminary results from the devices are promising and we intend to do a thorough study of their device property. Herein, we will discuss some of the relevant achievements and introduce the preliminary studies done on these heterostructures. By combining a deep understanding of the materials' properties with innovative approaches to interface engineering, we aspire to pave the way for future advancements in the development of next-generation optoelectronic devices with unprecedented capabilities.

### 10.2.1 Controlled Transfer of perovskite and TMDs

A pivotal hurdle encountered in the creation of heterostructure devices is the complex issue of transferring 2D materials and perovskite crystals. The process of transferring CVD-grown monolayer TMDs, for instance, is fraught with the risk of damage to the monolayer. Additionally, the transfer of perovskite crystals, given their solubility in a wide range of solvents, presents a distinct challenge that demands the development of a damage-free transfer technique.

While traditional methods such as organic polymer-assisted transfer and hBN-assisted transfer have proven effective for 2D materials, their applicability to perovskites is limited.[5][6] The

techniques, such as washing off the polymer make it a monumental challenge in fabricating these intricate heterostructures. This challenge has been surmounted by some researchers who have successfully fabricated 2D perovskite heterostructures through a different approach: they opt to grow these crystals directly on the 2D material, thus bypassing the aforementioned issue.[7][8] However, this approach lacks control over orientation and sometimes the quality of the heterostructures could also be affected. Other strategies like drop casting also suffer from similar issues and are not suited to study a very clean device interface.

We have recently tweaked the polymer-assisted transfer method to come up with a new protocol for a damage-free transfer technique to effectively transfer Perovskite and 2D materials. While the work is in progress a schematic of the same is given in Fig. 10.1.

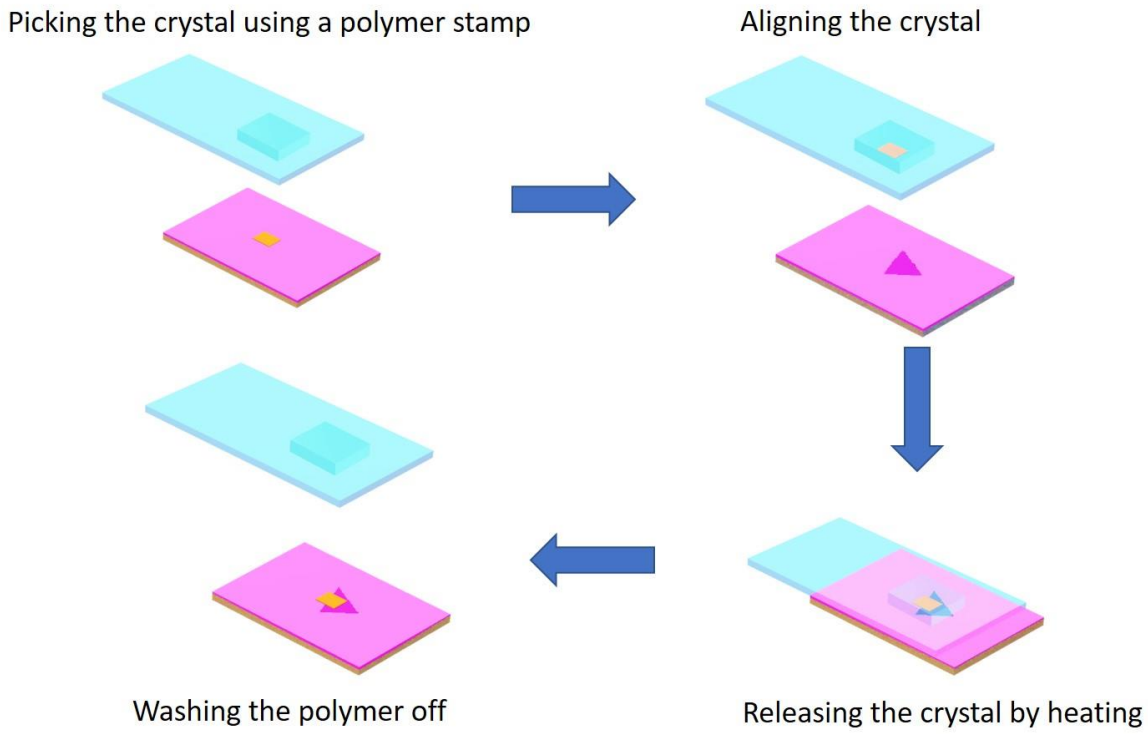


Figure 10.1: Common steps involved in the transfer techniques.

### 10.2.2 $WS_2$ - $CsPbBr_3$ micro-LED

We used our fabrication protocol to assemble 2D perovskite heterostructures step by step. This gave us great control over the orientation and quality of the assembled samples. Fig. 10.2 shows the different stages involved in the assembly of a Graphene - $CsPbBr_3$ - $WS_2$ heterostructure.

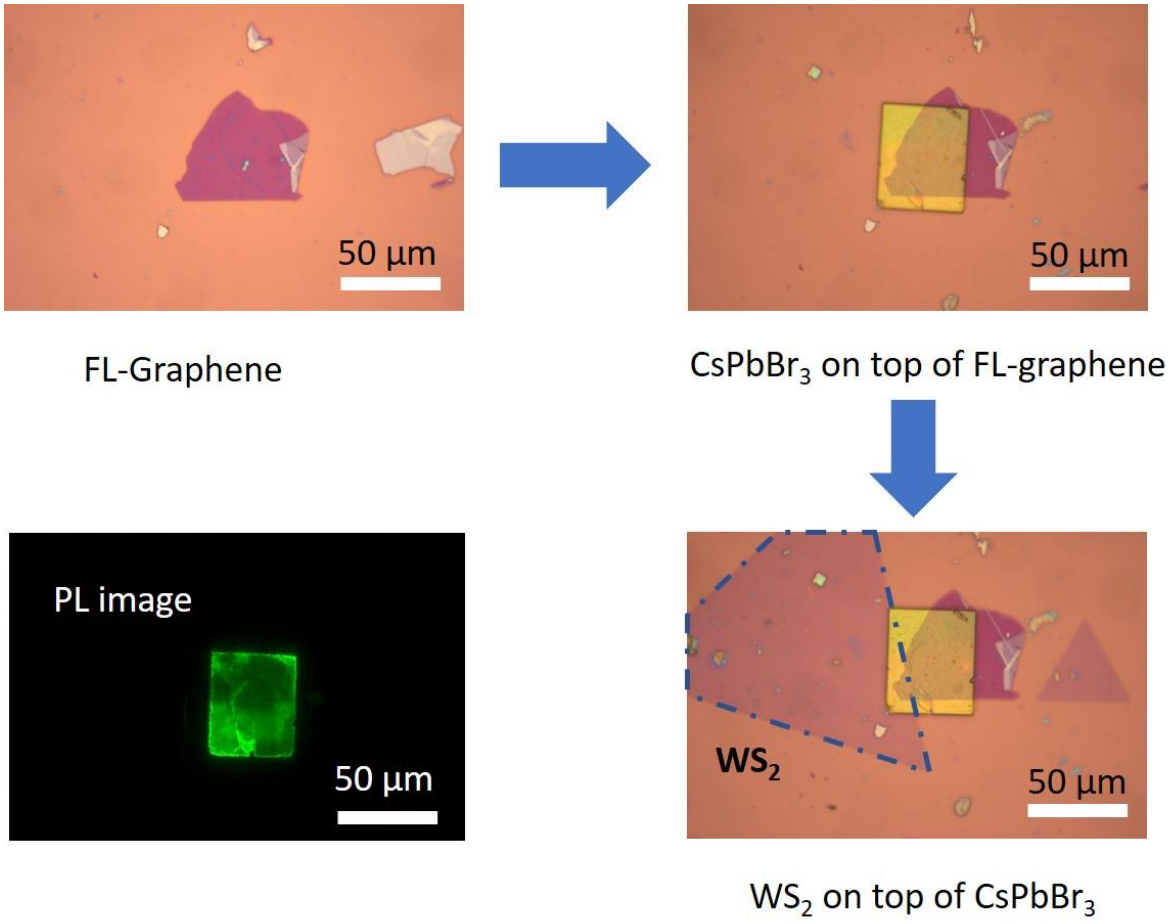


Figure 10.2: The transfer technique being implemented to make heterostructures of Graphene - $CsPbBr_3$ - $WS_2$ by assembling each layer at a time.

The assembled heterostructures were then used to fabricate a micro-LED. The preliminary results of the micro-LED exhibit a strong diodic behavior as can be seen from Fig. 10.3 a. The corresponding electroluminescence from the device at an applied voltage of 3 V is given in Fig. 10.3 b. There was a very strong emission from the device around 2.36 eV with an FWHM of 70 meV. This corresponds to the bandgap of $CsPbBr_3$ suggesting that most of the electron hole radiative recombination is happening in the perovskite material. Interestingly there is also an

emission at 2.02 eV corresponding to the band gap of $WS_2$. We believe that this is happening because of the type-1 band alignment of the $CsPbBr_3$ crystals.[9] A detailed study is needed to confirm this hypothesis and understand the underlying mechanism in detail.

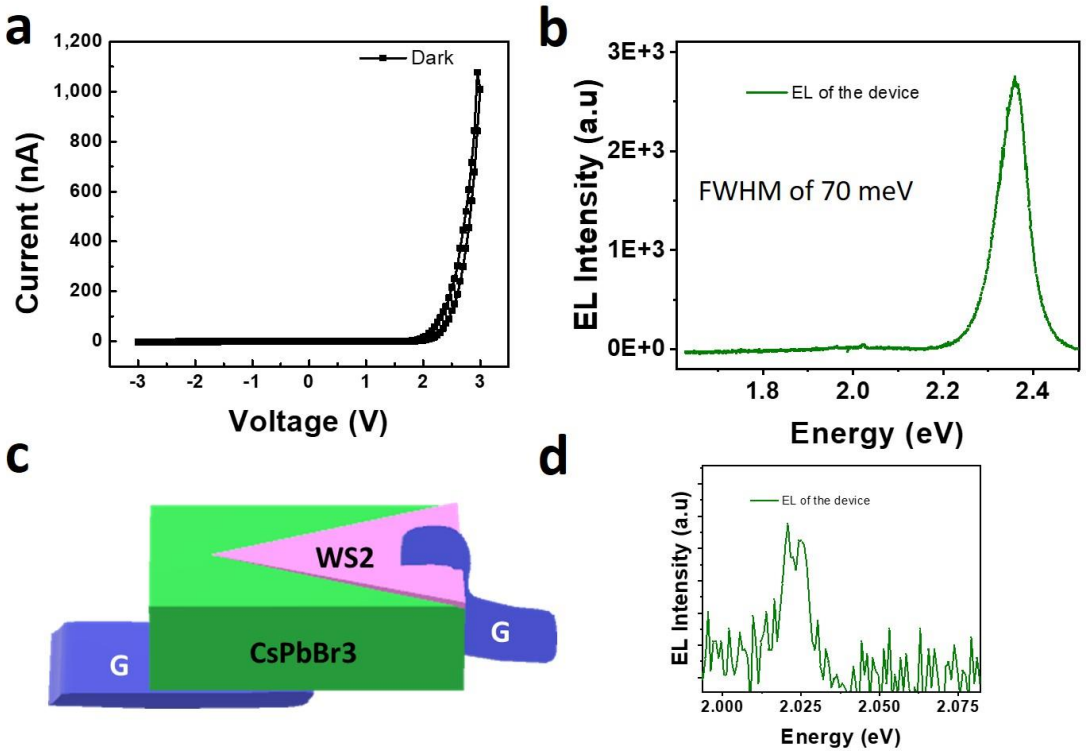


Figure 10.3: Preliminary results on $WS_2$-$CsPbBr_3$ heterostructure made using the transfer technique. (a) The dark I-V characteristics of the device. (b) The electroluminescence of the device with an emission at 2.36 eV (525 nm). (c) is the device geometry used for the measurement and (d) is the minor electroluminescence peak at 2.02 eV (613 eV) of the device.

### 10.2.3 $MoS_2$ - $CsPbBr_3$ Photodiodes

Similar to the Graphene - $CsPbBr_3$ - $WS_2$ heterostructure, we also fabricated Graphene - $CsPbBr_3$ - $MoS_2$ heterostructure. The image of the as fabricated device cab be seen in Fig. 10.4 a. The $CsPbBr_3$ - $MoS_2$ heterostructure is a type-2 heterostructure and thus exhibits a diodic behavior under light illumination as can be seen from Fig. 10.4 b.[10] Due to the highly insulating nature of the perovskite crystal, which lacked any charge carriers, the device exhibited exceptionally low levels of dark current. Intriguingly, as the temperature decreased, the device's reverse saturation current increased. This increase in photocurrent at low temperature can be attributed to the phonon interaction of the crystal.[11] The forward current decreases with the decrease in temperature most likely because of the shift in knee voltage associated with decreasing temperature. The existence of an effective field is evident from the zero bias photoresponse of the device as seen in Fig. 10.4. d.

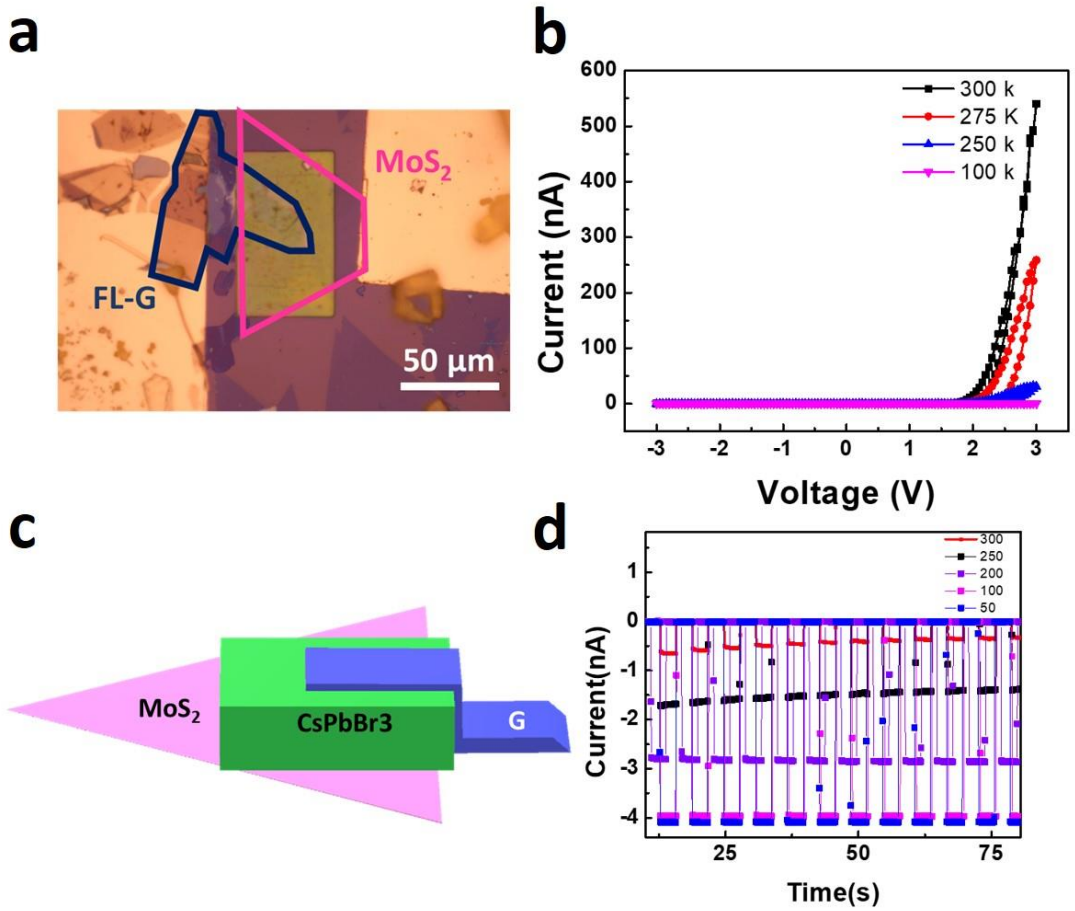


Figure 10.4: Preliminary results on $MoS_2$-$CsPbBr_3$ heterostructure made using the transfer technique. (a) The OM image of the device under test. (b) The I-V characteristics of the device. (c) is the device geometry used for the measurement. (d) is the zero bias photoresponse of the device at different temperatures.

### 10.2.4 The research objective

The primary goal of our research is to unravel the fundamental mechanisms underlying charge transfer properties and leverage this knowledge to design advanced optoelectronic devices for a wide range of applications. Our finely tuned polymer-assisted transfer method can help achieve damage-free transfer for the effective fabrication of various Perovskite - 2D material heterostructures. This technique offers precise control over their orientation and sample quality. The assembled heterostructures will be used to study various combinations and will ultimately help in deepening Our understanding of these heterostructures such as the nature of charge

transfer, the formation of interface, and ultimately the physics at play in these semiconductor junctions. As we delve into these results, we hope to gain a profound understanding of the mechanisms at play and leverage this knowledge to design superior optoelectronic devices for a multitude of practical applications.

**Bibliography**

[1] Zhang S, Liu J, Kirchner M M, Wang H, Ren Y and Lei W 2021 Two-dimensional heterostructures and their device applications: progress, challenges and opportunities—review *J. Phys. D. Appl. Phys.* **54**

[2] Splendiani A, Sun L, Zhang Y, Li T, Kim J, Chim C-Y, Galli G and Wang F 2010 Emerging Photoluminescence in Monolayer MoS 2 *Nano Lett.* **10** 1271–5

[3] Mak K F F, Lee C, Hone J, Shan J and Heinz T F F 2010 Atomically thin MoS2: A new direct-gap semiconductor *Phys. Rev. Lett.* **105**

[4] Sarritzu V, Sestu N, Marongiu D, Chang X, Wang Q, Masi S, Colella S, Rizzo A, Gocalinska A, Pelucchi E, Mercuri M L, Quochi F, Saba M, Mura A and Bongiovanni G 2018 Direct or Indirect Bandgap in Hybrid Lead Halide Perovskites? *Adv. Opt. Mater.* **6** 1701254

[5] Pizzocchero F, Gammelgaard L, Jessen B S, Caridad J M, Wang L, Hone J, Bøggild P and Booth T J 2016 The hot pick-up technique for batch assembly of van der Waals heterostructures *Nat. Commun.* **7** 11894

[6] Uwanno T, Hattori Y, Taniguchi T, Watanabe K and Nagashio K 2015 Fully dry PMMA transfer of graphene on h -BN using a heating/cooling system *2D Mater.* **2** 041002

[7] Huo C, Liu X, Wang Z, Song X and Zeng H 2018 High-Performance Low-Voltage-Driven Phototransistors through CsPbBr 3 –2D Crystal van der Waals Heterojunctions *Adv. Opt. Mater.* **6** 1800152

[8] Cheng H-C, Wang G, Li D, He Q, Yin A, Liu Y, Wu H, Ding M, Huang Y and Duan X 2016 van der Waals Heterojunction Devices Based on Organohalide Perovskites and Two-Dimensional Materials *Nano Lett.* **16** 367–73

[9] Li H, Zheng X, Liu Y, Zhang Z and Jiang T 2018 Ultrafast interfacial energy transfer and

interlayer excitons in the monolayer WS 2 /CsPbBr 3 quantum dot heterostructure *Nanoscale* **10** 1650–9

[10] Song X, Liu X, Yu D, Huo C, Ji J, Li X, Zhang S, Zou Y, Zhu G, Wang Y, Wu M, Xie A and Zeng H 2018 Boosting Two-Dimensional MoS 2 /CsPbBr 3 Photodetectors via Enhanced Light Absorbance and Interfacial Carrier Separation *ACS Appl. Mater. Interfaces* **10** 2801–9

[11] Shinde A, Gahlaut R and Mahamuni S 2017 Low-Temperature Photoluminescence Studies of CsPbBr 3 Quantum Dots *J. Phys. Chem. C* **121** 14872–8